Silk: a Biopolymer for Engineering Nanoparticles

Thidarat Wongpinyochit

University of Strathclyde

Strathclyde Institute of Pharmacy and Biomedical Sciences

A thesis presented in fulfilment of the requirements for the degree of

Doctor of Philosophy

November 2018

Declaration of Authenticity and Author's Rights

'This thesis is the result of the author's original research. It has been composed by the author and has not been previously submitted for examination which has led to the award of a degree.'

Signed: ______________________________________

(Thidarat Wongpinyochit)

Date:

Acknowledgements

I would like to express the deepest appreciation to my first supervisor, Dr. Philipp Seib for the continuous support since my master's degree then my PhD. I would like to thank him for his invaluable guidance, consistent encouragement, and immense knowledge throughout my PhD research. I also would like to thank my second supervisor, Dr. Blair Johnston, not only for giving me an excellent opportunity to do PhD, but also for his valuable time, insightful advice, and support in the modelling work. Additionally, I would like to thank Assoc Prof Samir Hemant Mushrif for his guidance and support in modelling work during my placement in Nanyang Technological University, Singapore and providing computational resources until I finished my work. This thesis would not have been possible without their excellent supervision.

I would like to gratefully acknowledge the financial support from the International Strategic Partnership between University of Strathclyde and Nanyang Technological University, Singapore for funding my PhD. I also would like to thank the EPSRC Future CMAC Research Hub and SIPBS to facilitate and support all equipment and resources throughout my research.

I would like to thank Dr. Antony Vassileiou for his help and suggestions for modelling work. I also thank my all colleagues in Seib group, especially John Totten, Anne Goudie and Osama Ibrahim and my lovely friends in SIPBS; Lina Akil and Nouf Abutheraa and in CMAC for their friendship and support. Special thanks also go to my Thai friends in SIPBS (P'Ple and P'M) and in Thailand for their friendship, help and encouragement.

Finally, my deep and sincere gratitude to my parents, aunt (Na'Nid) and my entire family member for all their love, help, support and believe in me. I would have not been able to complete this thesis without their support.

Abstract

Silk from *Bombyx mori* has a robust clinical track record for load bearing applications. It was hypothesized that the biopolymer silk would also have the potential to generate nanoparticles. Therefore, the aim of this thesis was to manufacture and assess these silk nanoparticles for drug delivery. First, silk nanoparticles were produced from aqueous silk stock by nanoprecipitation. The resulting nanoparticles were then surface grafted with polyethylene glycol (PEG), yielding nano-sized particles (104 to 116 nm) with a negative zeta potential (-56 to -46 mV). PEGylated silk nanoparticles showed a reduced macrophage response, high aqueous stability but low drug loading capacity. The drug loaded PEGylated silk nanoparticles showed improved cytotoxicity, cellular uptake and intracellular dynamics in cancer cells (Chapter 2). Next, the fate of native and PEGylated silk nanoparticles during various enzyme treatments was investigated to demonstrate the elimination of nanoparticles after administration. Native and PEGylated silk nanoparticles were degraded in protease enzymes *in vitro*, but showed faster degradation in protease XIV (degraded after a 1-day treatment) and slower degradation in papain and *ex vivo* lysosomal enzymes (degraded after a 5-day treatment) (Chapter 3). Next, the NanoAssemblr^{TM} microfluidic system was exploited to manufacture silk nanoparticles. Silk nanoparticles were generated using the commercial microfluidic chip that allowed rapid mixing of both the aqueous silk solution and the organic solvent. This microfluidic system allowed tuning of silk nanoparticle characteristics through adjusting processing parameters such as the total flow rate, the total flow rate ratio and solvent selection (Chapter 4). Finally, computational modelling was applied to better understand the impact of silk conformation and its subsequent interaction with the model drug doxorubicin at the atomic level. Well-tempered metadynamics, an enhanced sampling method for molecular dynamics simulations was used to explore the free energy surface of an amorphous-crystalline silk model structure in water. Next, silk with optimised secondary structures were used to study the interaction of the model drug doxorubicin at both pH 4 and 7.4. Here, the N-terminus was the predominant domain responsible for drug loading and release (Chapter 5). Overall, this thesis demonstrated that silk is a versatile biopolymer to generate nanoparticles for drug delivery (Chapter 6).

Table of Contents

List of Figures

List of Tables

List of Abbreviations

Abbreviation	**Explanation**
°C	Degrees Celsius
× g	G-force
ACPYPE	AnteChamber PYthon Parser interfacE
AFM	Atomic force microscopy
ANOVA	Analysis of variance
BCA	Bicinchoninic acid
CI	Combination index
CVs	Collective variables
DLS	Dynamic light scattering
DMEM	Dulbecco’s modified eagle medium
DMSO	Dimethyl sulphoxide
Dox	Doxorubicin
DS	Discovery studio
EDTA	Ethylenediaminetetraacetic acid
ELISA	Enzyme-linked immunosorbent assay
EPR	Enhanced permeation and retention effect
FBS	Fetal bovine serum
FDA	Food and Drug Administration
FES	Free energy surface
FSD	Fourier self-deconvolution
FTIR	Fourier transform infrared spectroscopy
FWHM	Full width at half-maximum
GPa	Gigapascal
GPUs	Graphics Processing Units
h	Hour
HCl	Hydrochloric acid
HEPES	4-(2-hydroxyethyl)-1-piperazineethanesulfonic acid
HMF	Heavy mitochondrial fraction
HPMA	N-(2-hydroxypropyl)methacrylamide

HRP	Horseradish peroxidase
IC_{50}	Half maximal inhibitory concentration
kDA	Kilodalton
kJ	Kilojoules
LiBr	Lithium bromide
LMF	Light mitochondrial fraction
log D	Distribution coefficient
log D MW^{-1}	Diffusion coefficient
log P	Partition coefficient
LPS	Lipopolysaccharide
MD	Molecular dynamics
min	Minute
MM	Molecular Mechanics
MPS	Mononuclear phagocytic system
MTT	3-(4, 5-dimethylthiazol- 2-yl)-2, 5-diphenyltetrazolium bromide
mV	Millivolt
MW	Molecular weight
N.D.	Not determined
$Na_2B_4O_7$	Sodium borate
Na_2CO_3	Sodium carbonate
NAG	N-acetyl-β-glucosaminidase
NaOH	Sodium hydroxide
NMR	Nuclear magnetic resonance
PBS	Phosphate buffer saline
PDB	Protein Data Bank
PDI	Polydispersity index
PEG	Polyethylene glycol
PEG-SNPs	PEGylated silk nanoparticles
pKa	Apparent acid dissociation constant
PLGA	Poly(lactic-co-glycolic acid)
PME	Particle mesh ewald
QM	Quantum Mechanics

REMD	Replica-exchange molecular dynamics
R_g	Radius of gyration
RMSD	Root-mean-square deviation
rpm	Revolutions per minute
RPMI	Roswell Park Memorial Institute
RSA	Relative specific activity
SD	Standard deviation
SDH	Succinate dehydrogenase
SEDS	Solution-enhanced dispersion
SEM	Scanning electron microscope
SNPs	Silk nanoparticles
TNF-α	Mouse tumour necrosis factor alpha
TST-activated mPEG	Methoxypolyethylene glycol activated with cyanuric chloride
U	Enzyme activity unit
vdW	Van der Waals
VEGF	Vascular endothelial growth factor
VMD	Visual Molecular Dynamics

Prologue

When we say “silk”, the mind leaps immediately to luxurious and smooth fabrics. It is not surprising that humans have been using silk for thousands of years both for textiles and medical applications. Some of the first examples were the use of silk medically by ancient Greeks and Romans, who bundled up spider silk to treat wounds. Claudius Galenus of Pergamon (c. 131 – c. 211 AD) was the first to document a potential medical application of the silk thread. Galenus noted in his book De Methodo Medendi (150 AD) the use of several materials as sutures, including silk (Holland et al., 2018). Currently, one promising application of silk in biomedical sciences is its use for drug delivery. The potential of silk-based nanoparticles for drug delivery has been reported previously (Kundu et al., 2010; Wenk et al., 2011; Seib, Jones, et al., 2013). Nonetheless, many questions remain that not only require dedicated laboratory experiments but also the use of computer simulation to advance the field. This thesis sets out to use both experimental and computational approaches to evaluate the ability of silk-based nanomedicines for drug delivery (Figure 1).

Experimental studies focused on the development and assessment of silk nanoparticles as drug carriers specifically examining (i) the manufacture of silk nanoparticles, (ii) the surface modification of silk nanoparticle with polyethylene glycol (PEG), (iii) the *in vitro* and *ex vivo* biodegradation of native and PEGylated silk nanoparticles and (iv) the evaluation of silk nanoparticle cellular responses (e.g. breast cancer cells and macrophages) as well as their intracellular trafficking.

Better understanding silk behaviour at the molecular level should aid the design of second generation carriers for drug delivery. Thus, computational modelling was applied to generate insight into the silk structure and its interaction with the model drug doxorubicin at atomic resolution. This work package was enabled through a placement at Nanyang Technological University (NTU), Singapore under the supervision of Assoc. Prof. Samir H. Mushrif.

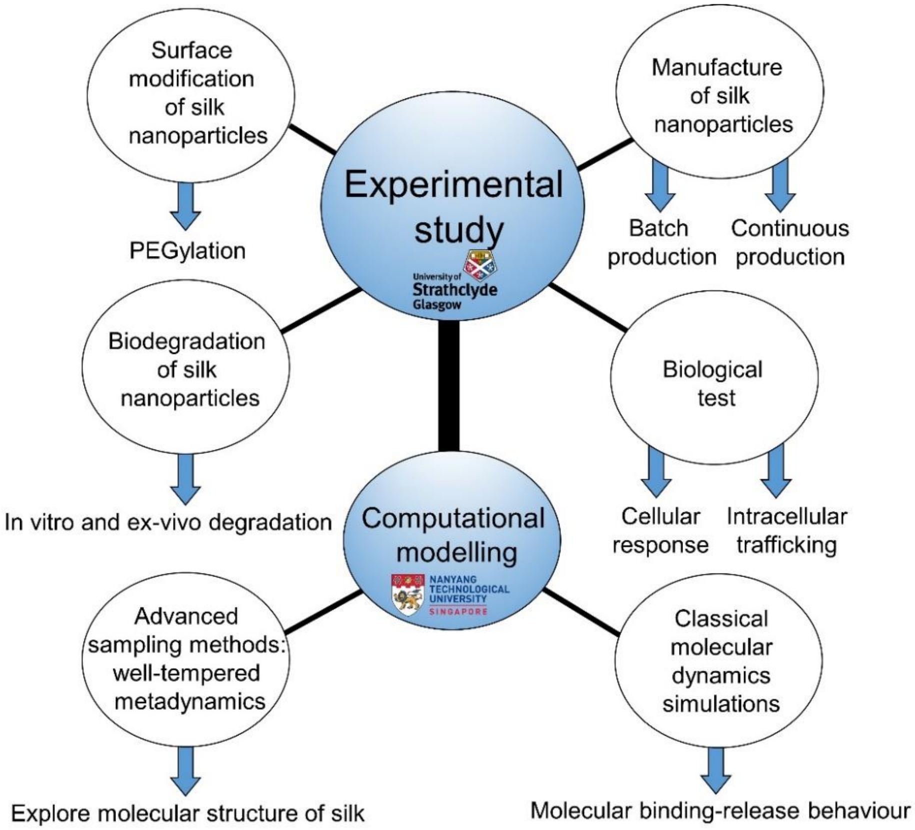

Figure 1 A schematic diagram of this PhD. This thesis contains two main parts; wet laboratory experiments carried out at the University of Strathclyde and computational modelling in collaboration with NTU, Singapore.

This thesis contains three experimental chapters and one computational chapter that form the basis of three peer-reviewed publications, one submitted manuscript and one in preparation. The chapters are organized as follows:

Chapter 1 is a general introduction to silk including its structure, properties and applications for drug delivery. This chapter also includes the theory to molecular dynamics (MD) simulation and an enhanced sampling method such as metadynamics, and an overview of MD simulation relating to silk.

Chapter 2 details the manufacture of native and PEGylated silk nanoparticles for anticancer drug delivery including characterisation of silk nanoparticles, drug loading, cytotoxicity towards cancer cells and intracellular trafficking. This chapter was published in Biomacromolecules, 2015, 16, 3712-22 (DOI: 10.1021/acs.biomac.5b01003) and in The Journal of Visualized Experiments, 2016, 116, e54669 (DOI: 10.3791/54669).

Chapter 3 describes the degradation behaviour of native and PEGylated silk nanoparticles exposed to protease enzymes and *ex vivo* lysosomal enzymes by measuring nanoparticles' properties such as particle size, surface charges, morphology, and secondary structures. This chapter was published in ACS Biomaterials Science & Engineering, 2018, 4, 942-51 (DOI:10.1021/acsbiomaterials.7b01021).

Chapter 4 describes the manufacture of silk nanoparticles using a microfluidic chip. This chapter details the effect of microfluidic processing parameters on silk nanoparticles' characteristics such as particle size, surface charges, morphology and secondary structures. The generated silk nanoparticles were determined cellular responses and intracellular distribution. This chapter has been submitted for publication (August 2018).

Chapter 5 details the computational modelling study which applied well-tempered metadynamics, an advanced sampling method to explore semi-crystalline silk structures in water. These data sets were then applied to classical MD simulations to investigate the silk-doxorubicin interaction at the molecular level. This chapter is the manuscript in preparation for publication.

Chapter 6 provides a summary of the outcomes for this thesis and suggestions for future work.

Chapter 1

Introduction

1.1 Introduction

Nanomedicines are defined as particularly engineered nanomaterials, nanosized drugs and drug delivery systems, which consist of at least two components, one of which is a pharmaceutical active ingredient (Duncan and Gaspar, 2011). Overall, nanomedicines are utilised for diagnosis, prevention, and treatments of many diseases, such as cancer. Many nanomedicines (>40) have now progressed into the clinic (Duncan and Gaspar, 2011; Uchegbu and Siew, 2013). In addition, there is an exponential increase in publications on nanomedicines over the last decade (Duncan and Vicent, 2013). However, the biopolymer silk has only recently been explored for nanomedicines.

Silk is an interesting biomaterial due to its outstanding mechanical properties and versatility (e.g. many different formats, triggered change in conformation etc.). Silk has demonstrated good biocompatibility and biodegradability across numerous applications (Seib and Kaplan, 2013). Therefore, silk has become a promising biopolymer to develop nanomedicines for drug delivery applications, especially in the context of cancer (Kundu et al. 2010; Seib et al. 2013; Gupta et al. 2009). There is emerging evidence that silk-based nanoparticles are stimuli-responsive anticancer nanomedicines by accessing cancer cells via endocytotic uptake and pH dependent drug release (Seib et al. 2013). Nonetheless, there have been relatively few experimental studies that have set out to improve the manufacture of silk nanoparticles, modify the particle surface and investigate silk biodegradation. Additionally, there are no reports that have used computational modelling to systematically understand silk's ability to adsorb a small molecular weight anticancer drug.

To understand the scope of this thesis it is important to have a background knowledge of ‘silk’ and ‘molecular dynamics’ which is described in the following sections.

1.2 Silk

Silk is a fibrous protein polymer spun by several insects, including mites, moths, silkworms and spiders for use outside the body (Hakimi et al., 2007). However, these silks serve different functions. For example, silkworms produce cocoons to protect themselves from a hazardous environment during metamorphosis; on the other hand, spiders generate orb webs to trap their prey and use the spider dragline for safety (Zhao et al., 2005). In addition, the structure, composition and properties of silk vary depending on source, environment and production processes.

The most popular silks used in research are from the domesticated silkworm *Bombyx mori* and spider silk (e.g. recombinant dragline silk from *Nephila clavipes*) (detailed in section 1.2.1.2). *B. mori* silk is licensed by the Food and Drug Administration (FDA) for use in humans for load bearing applications, namely sutures and surgical meshes (Seib and Kaplan, 2013). Due to the outstanding mechanical properties, biocompatibility, biodegradability and chemical modification potential, silk has become an interesting biomaterial for biomedical applications such as drug delivery and tissue engineering. For example, mechanical properties, such as tensile strength, extensibility and toughness outperform most other natural or man-made materials (e.g. albumin, collagen and chitosan) (detailed in section 1.2.2.1) (Koh et al., 2015).

1.2.1 Types of silk

1.2.1.1 Silkworm silk (*B. mori*)

The silkworm cocoon (*B. mori*) is generated during the fifth instar larval stage in order to protect the pupa (Pérez-Rigueiro et al., 2001). Large amounts of silk can be obtained from farming silkworms (i.e. sericulture). The global production of silk is currently >153 metric ton per year, and China is the largest silk producer (Padaki et al., 2015). *B. mori* silk is widely used for biomaterial applications unlike spider silks. Silkworm silk contains two proteins: silk and glue-like sericin, which is soluble in water. (Figure 1.1). Removal of sericin is necessary for biomedical applications, because sericin can cause inflammatory reactions *in vivo* by upregulation of inflammatory cytokines (Mathur and Gupta, 2010; Seib and Kaplan, 2013). However, boiling in water can only remove the outer layer of sericin. Therefore, the degumming process by boiling the cocoons pieces in aqueous alkaline solution (e.g. Na_2CO_3) is required to completely remove sericin. This step also decreases the molecular weight of the silk protein due to hydrolytic degradation of silk, resulting in fragmentation of the silk protein chains. The reduction of the silk molecular weight affects the silk structure, viscosity and degradation behaviour (Pritchard et al., 2013).

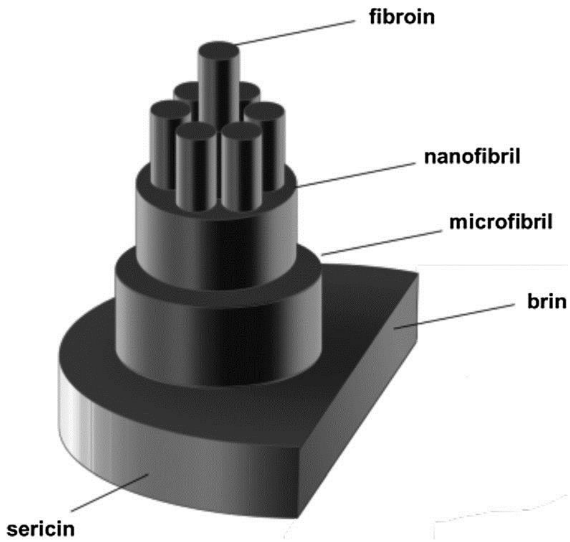

Figure 1.1 Structure of *B. mori* silk thread (Pereira et al., 2014).

Silk is a large protein (200 – 400 kDA). Silk is mainly composed of glycine (43%), alanine (30%) and serine (12 %) (Kaplan et al., 1998). The three amino acid residues are the main components of silk. Silk is composed of a heavy chain (390 kDa, 5263 amino acid residues), light chain (26 kDa, 262 amino acid residues) and glycoprotein (P25) (30kDa, 220 amino acid residues). The heavy chain, light chain and P25 are bounded in the ratio of 6:6:1, respectively. The heavy chain and light chain are connected by a single disulfide bond at cys-20 of heavy chain and cys-170 of light chain (Inoue et al., 2000) (Figure 1.2).

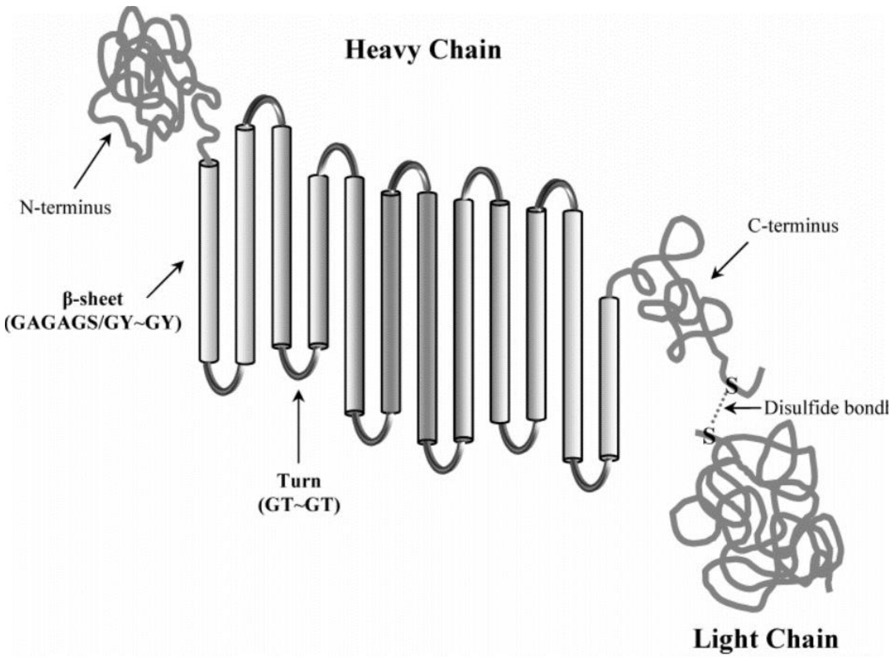

Figure 1.2 The schematic of heavy chain and light chain of *B. mori* silk. The heavy chain of silkworm silk consists of N-terminus, C-terminus, amorphous regions, and crystalline domains. The L-chain of silkworm silk links to the heavy chain using a single disulfide bond (Ha et al., 2005).

The heavy chain of silk contains 12 repetitive modular hydrophobic domains interrupted by 11 amorphous segments (spacers) (Figure 1.3). The hydrophobic segments allow for tight packing through hydrophobic interactions and hydrogen bonding. The repetitive core of the heavy chain can be classified into four types of motifs: GAGAGS, GAGAGY, GAGAGSGAAS, and non-repetitive segment (where G = glycine, A = alanine, S = serine, Y = tyrosine). The GAGAGS amino acid sequence is mainly repeated in the hydrophobic segment of the heavy chain resulting in a β-sheet formation (He et al., 2012). In addition, there are less repetitive amino acid sequences which make up the turns (GAAS) and helixes (Ma et al., 2013) The amorphous regions are hydrophilic and contain negative charges; these regions are the linker segments connecting the β-sheet domains (Zhou et al., 2001). The complete amino acid sequence of the heavy chain can be obtained from GenBank AF 226688-EMBL P05790.

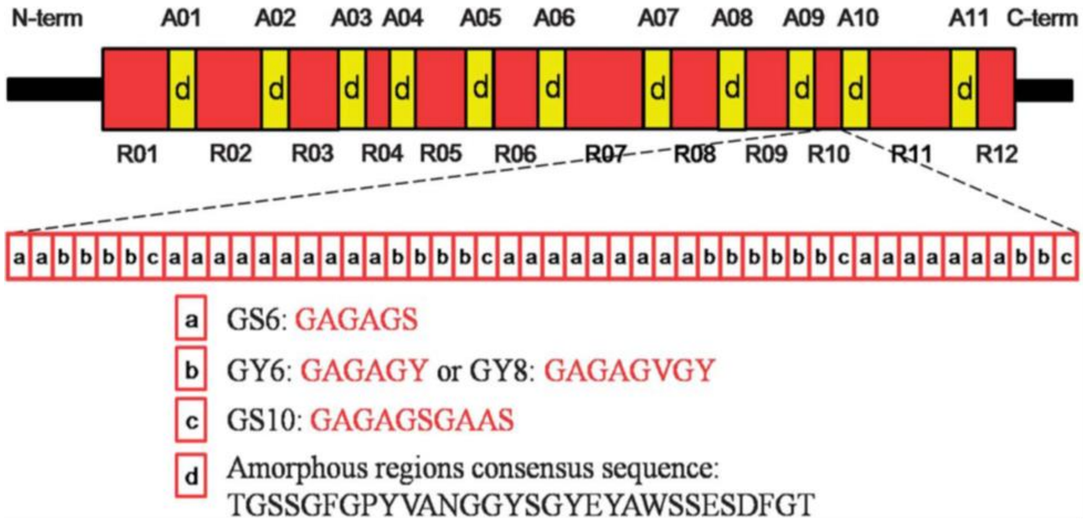

Figure 1.3 Schematic of the primary structure of silk heavy chain including N-term, C-term, repetitive regions and amorphous regions (Ma et al., 2013).

The secondary structure of silk is predominantly anti-parallel β-sheets (Figure 1.4), which are stabilised by hydrogen-bonding, resulting in a crystalline structure with outstanding mechanical properties.

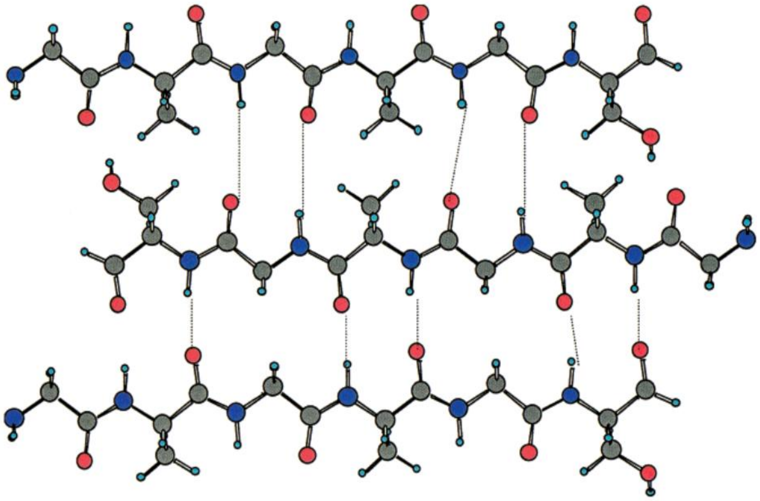

Figure 1.4 The two dimensional β-sheet structure (GAGAGS) in the heavy chain of silkworm silk (dash line = H-bonding) (Zhou et al., 2001).

Additionally, silk has three structural forms: silk I, silk II and silk III. Silk I is the format found in the silkworm gland. Silk I contains extended helixes or random coils: this form is completely water soluble. Subjecting silk I to external factors such as shearing, heating, pH reduction and organic solvent (e.g. ethanol and acetone), silk I is converted into silk II (Seib and Kaplan, 2013). Silk II is common and the most stable and organized structure. Silk III, a newly discovered silk structure, has threefold polyglycine II-like helices (Vepari and Kaplan, 2007).

1.2.1.2 Spider silk (*N. clavipes*)

Spiders produce various types of silks. The spider silks have different amino acid arrangements and sequences, which impacts their mechanical properties. The most common spider silk is dragline silk spun by *N. clavipes*. The dragline silk is produced for safety and web construction, and is strong and particularly tough. The tensile strength-to-weight ratio of the dragline silk provides up to five times and three times stronger than high tensile steel and Kevlar (a para-aramid synthetic fibre), respectively; however, extensibility of the silk are about equivalent to synthetic rubber (Omenetto and Kaplan, 2010). Because spiders cannot be farmed and access to the material is more restricted, domesticated silkworm silk (*B. mori*) is commonly used for drug delivery and tissue engineering applications (Vepari and Kaplan, 2007). However, spider silk can be produced using recombinant DNA technologies (more detailed in section 1.2.1.3).

Table 1.1 A comparison of properties between silkworm silks and spider silks (Hakimi et al., 2007; Wong et al., 2014).

Properties	**Silkworm silk (*B.mori*)**	**Spider silk**
Difference in production	Domesticated *B. mori* secretes silk threads from salivary glands	Spiders release silk from abdominal glands
Adverse effects	Sericin results in human immune response and asthma attacks in sensitive patients	None, considered antibacterial and reduces potential for infection
Thickness	Consistent thickness which is 10 times thicker than spider silk, measuring 0.08 mm	Depending on types of silk, the diameter range from 0.003 to 0.008 mm
Strength	Light and strong for their size and thickness	At least twice as strong as the type made by *B. mori*, it is also extremely elastic and stronger than steel or Kevlar
Crystalline region	$(GAGAGS)_n$, 40-50%	Spidrorin I and spidroin II (SP I and SP II)
Non-crystalline region	Tyr-rich domains	Gly-rich domains, 35%
Content (non-crystalline region)	Negatively charge, polar, bulk hydrophilic	Variable in length and composition, rich in glycine
Size	~ 350 kDa	275 – 320 kDa
Use	Textiles, scaffolds for tissue regeneration, drug delivery and cosmetics	No commercial products yet

1.2.1.3 Recombinant silk proteins

Although spider silks outperform the mechanical properties of many natural and synthetic materials, difficulties in generating this protein limits the wide use of spider silks. Due to the aggressive behaviour and territorial nature of spiders, they cannot be farmed, (unlike sericulture of the domesticated silkworm). However, silk-like biomaterials can be manufactured using recombinant technology; several companies (e.g. AMSilk GmbH, Bolt Threads Inc.) are developing large scale production processes to meet future demands. Recombinant expression results in a predictable and controllable silk protein. Cloning and expression of native and synthetic silks have succeeded in mimicking silk's structure in a range of expression hosts (e.g. bacteria (*Escherichia coli*), yeast, (*Pichia pastoris*), insects (silkworm larvae), plants (tobacco, soybean, potato, Arabidopsis), mammalian cell lines (BHT/hamster) and transgenic animals (mice, goats)) (Numata and Kaplan, 2010; Qin and Kaplan, 2011). *Escherichia coli* (*E. coli*) is the most popular host to express recombinant silk because it is easy to grow and low-cost. However, the low productivity of recombinant silk proteins in *E. coli* was observed because the highly repetitive core sequence of silk proteins (glycine-rich domain), large protein size (300-350 kDa) and the restricted glycyl-tRNA pool in the expression host. These factors resulted in the difficulty to yield full-length silk. However, a recent study discovered that using glycyl-tRNA metabolically engineered *E. coli* could overcome this limitation. As a result, the metabolic engineered expression host improved the overall silk size, which was similar to the natural spider silk and it also provided similar mechanical properties when compared to native *N. clavipes* silk (Xia et al., 2010).

Apart from *E. coli*, the multicellular organisms such as insects, plants and mammals have been employed as heterologous hosts for spider silk formations. For example, *B. mori* silkworms have become an excellent candidate as a genetically engineered host organism to generate novel silk (fibres) (Zhang et al., 2011; Teule et al., 2012).

1.2.2 Properties of silk

1.2.2.1 Mechanical properties

Mechanical properties of biomaterials are necessary for drug delivery and tissue engineering, especially for load-bearing purposes. Because of the robust β-sheet structure, mechanical performances of silk surpass most natural and synthetic materials, and do not require chemical crosslinking as other biomaterials (e.g. collagen). Silks provide unique mechanical properties by combining high tensile strength and extensibility, which result from the β-sheet crystallites and amorphous segments, respectively. In contrast, synthetic materials have high strength but limit toughness and extendibility (Table 1.2, Figure 1.5). In nature silk-producing species use a spectrum of amino acid sequences ultimately affecting silk performance. Furthermore, the process for preparing regenerated silk from silk cocoons influences the silk structure, which affects the mechanical properties (Cho and Um, 2010; Dou and Zuo, 2014; Wang et al., 2015). The relationship between the molecular structure and mechanical properties have been studied for silks using bottom-up computational simulations such as atomistic simulations and coarse-grained simulations (more detailed in section 1.4.1)

Table 1.2 A comparison of mechanical properties of silk and synthetic fibres (modified from Fu et al., 2009).

Materials	Strength (GPa)	Extensibility (ε_{max})	Toughness (MJ/m^3)
***B. mori* silk**	0.6	0.18	70
Spider silk (major ampullate)	1.1	0.27	180
Kevlar 49	3.6	0.027	50
Steel	1.5	0.008	6
Nylon	0.95	0.18	80

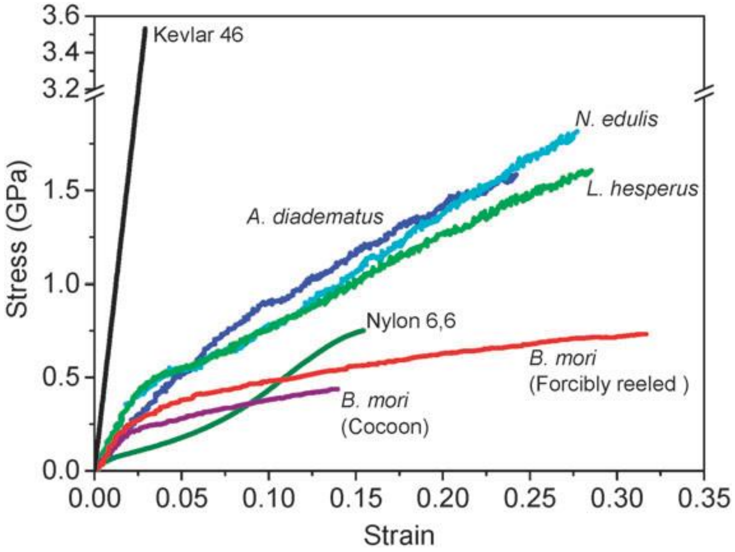

Figure 1.5 The stress-strain curve of different species of silks compared to synthetic fibres (Kevlar 46 and Nylon 66) (Fu et al., 2009).

1.2.2.2 Biocompatibility and biodegradation properties

Biocompatibility of a polymer refers to its ability to accomplish its desired purposes (e.g. drug delivery and tissue engineering) while promoting the appropriate cellular or tissue response without adverse effects (Williams, 2008). Over millennia, silk has been used in human as suture materials because it is robust and easy to handle (Rajak et al., 2011). However, biocompatibility studies are needed for silk-based nanoparticles because their intended function goes beyond silk's traditional uses. For example, silk nanoparticles designed for intravenous dosing are expected to be compatible with blood. Therefore, silk-based biomaterial for drug delivery requires specific biocompatibility studies.

The biodegradability of a biomaterial is important for drug delivery and tissue engineering in order to control pharmacokinetics and tissue replacement, respectively. For example some poly lactic-*co*-glycolic acid polymers (PLGA) hydrolyse quickly producing acidic residues, which results in loss of PLGA's mechanical stability and an inflammatory reaction due to acidic degradation products (Makadia and Siegel, 2011). In contrast, there is emerging evidence that the degradation process of silk caused by proteolytic enzyme (e.g. protease, chymotrypsin, actinase, and carboxylase) and enzyme-catalysed hydrolysis reactions (Cao and Wang, 2009) proceeds without toxic or irritant by-products. A recent study proposed a mechanism of silks' proteolytic degradation driven by the breakdown of β-sheet crystals (Numata and Kaplan, 2010). Therefore, the degradation rate can be modified by regulating the crystalline state (Numata and Kaplan, 2010).

1.2.2.3 Payload stabilisation

Proteins and small molecular weight drug molecules have been commonly used in therapeutics; however, some of them have low stability that in turn needs to be improved. Silk-based biomaterials can be used as carriers to stabilise proteins from degradation (Seib and Kaplan, 2013). There is evidence that silk biomaterial can stabilise many sensitive biological molecules such as vaccines (Zhang et al., 2012), horseradish peroxidase (HRP) (Lu et al., 2009), glucose oxidase (GOx) and lipase (Lu et al., 2009). For example, HRP is commonly used as an indicator enzyme in enzyme immunoassays and enzyme electrodes (or as a model protein drug). However, HRP has a low solution stability. Lu and co-workers showed that HRP activity increased 30-40% when HRP was added to a silk solution (Lu et al., 2009). In addition, the half-life of the HRP activity was 25 days at 25 °C in silk solution compared to 2.5 h in PBS. Additionally, HRP activity retained >90 % of its initial activity when HRP was encapsulated in a silk films and exposed to accelerated aging conditions (4 °C, 25 °C, and 37 °C over 60 days) (Lu et al., 2009). There are three main working hypothesis to explain the silk's mechanism of action with respect to payload stabilisation (Pritchard et al., 2012). First, silk forms a protective barrier that protects proteins or small molecules from exogenous enzymes which can inactivate the payload. Second, silk reduces mobility effects; silk "freezes" proteins or small molecules in their optimal and native structure as a result of immobilization of the molecules in the silk structure. Thus, this effect can reduce protein unfolding and enhance thermal stability. Thirdly, silk's ability to regulate microenvironmental effects. Silks (e.g. films and micro- or nanoparticles) can buffer changes in the bulk environment that affords a stable microenvironment in silk matrices. In addition, silks provide suitable hydration and low water content of β-sheet structure in nanoscale size. Overall, these properties set silks apart from other pharmaceutical excipients used in drug delivery (Pritchard et al., 2012).

1.3 Applications of silk-based biomaterial

Silk is a versatile biomaterial, as it can be generated into many types of formulations such as films, scaffolds, hydrogel and micro or nanoparticles (Figure 1.6). For the purpose of this thesis only nanoparticles are examined.

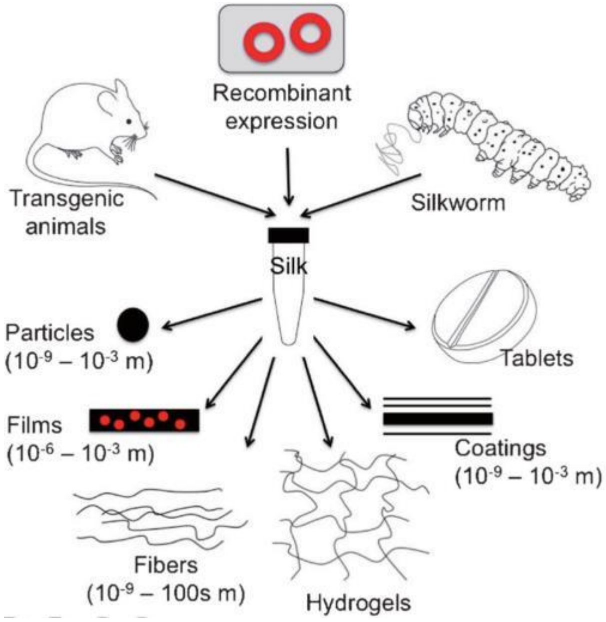

Figure 1.6 Diagram of silk sources and various silk-based formulations (Seib and Kaplan, 2013).

1.3.1 Silk nanoparticles

The concept of nanoparticles started with Paul Ehrlich in 1891. He developed the concept of targeted drug delivery, which is known as “magic bullet” (Strebhardt and Ullrich, 2008). In the late 1960s and early 1970s, Professor Peter Paul Speiser and his colleagues developed first generation nanoparticles for vaccination. They focused on sustained drug release properties to achieve single-injection vaccines. After this development, there were many studies examining nanoparticles for pharmaceutical and medical applications.

Abraxane, human serum albumin nanoparticles loaded with paclitaxel, was the first nanoparticle product that reached the market in 2005 (Kreuter, 2007).

“Nanoparticles are submicron-sized polymeric colloidal spheres that can entrap an active agent within the polymeric matrix, or the active agent can be adsorbed or conjugated to the outside of particles” (Betancourt et al., 2009). According to Duncan and Gaspar, nanoparticles used for medical applications are nanosized particles in the range of 1 nm to 1,000 nm (Duncan and Gaspar, 2011). Silk can be formulated into nanoparticles and subsequently studied as potential therapeutic drug delivery system.

There are many studies focusing on the production of silk nanoparticles using various methods. For example, polyvinyl alcohol silk blends (Wang et al., 2010), spray drying (Qu et al., 2013), salting out (Lammel et al., 2010), capillary microdot printing (Gupta et al., 2009), and desolvation (Seib et al., 2013; Tudora, et al., 2013) (Table 1.3).

Table 1.3 Examples of silk based nanoparticles for drug delivery applications.

Type of silk	Preparation method	Particle size (± SD)	Zeta potential (mV) (± SD)	Model drug (% encapsulation efficiency)	*In vitro* drug release	References
B. mori	Capillary microdot	< 100 nm	N.D.	Curcumin (>96 %)	>8 weeks	(Gupta et al., 2009)
B. mori	Phase separation	500 nm – 2 µm	-26.3 (pH 4) to -46 (pH 9)	Crystal violet (>95%) Alcian blue (>95%) Rhodamin B (~ 50%)	1 week	(Lammel et al., 2010)
B. mori	Desolvation	98 nm	-33.6 ± 5.8	Doxorubicin (>95%)	6 days	(Seib et al., 2013)
B. mori	Desolvation	50 – 300 nm	N.D.	N.D.	N.D.	(Tudora et al., 2013)
B. mori	Desolvation	35-125 nm	N.D.	N.D.	N.D.	(Zhang et al., 2006)
B. mori	Desolvation	154.3 ± 15 nm	-21.2 ± 1.2	Methotrexate (75%)	12 days	(Subia and Kundu, 2013)
B. mori	SEDS	50 nm	N.D.	Indomethacin (30.52 %)	2 days	(Zhao et al., 2012)
B. mori ***A. mylitta***	Desolvation	150 ± 4 nm 177 ± 3 nm	-24 to -26	VEGF (~ 100%)	3 weeks	(Kundu et al., 2010)
A. mylitta	Reverse microemulsion	167-169 nm	N.D.	Rhodamin B	360 minutes	(Myung, et al., 2008)

A number of silk-based nanoparticles for cancer therapy has been described to date (Table 1.3). Nanosized carriers can gain access into cells via endocytosis and then traffick to lysosomes to release their payload (known as lysosomotropic delivery (Duncan and Richardson, 2012). For example, Gupta et al. (2009) studied the properties of curcumin loaded silk nanoparticles as cancer drug delivery to improve the retention time in cancer cells, efficacy and bioavailability *in vitro* breast cancer cells (MCF-7 (Her2-) and MDA-MB-453 (HER2+)). The result showed that curcumin loaded silk nanoparticles provided high loading efficiency (9.6 wt %) and sustained release over 8 days which led to high intracellular uptake and cytotoxicity. Moreover, Seib et al. (2013) found that drug loaded silk nanoparticles could be used as a lysosomotropic anticancer nanomedicine. Doxorubicin, pKa = 8.3, log P = 1.3, is a weak base that was proposed to bind to the negatively charged hydrophilic spacers of silk by electrostatic interaction. At low pH (e.g. pH 4.5), the electrostatic interaction of the drug and silk changes which can trigger drug release and can be exploited for lysosomal drug delivery.

1.4 Molecular dynamics (MD) simulation on silks

1.4.1 Mechanical properties investigation of silks using MD simulation

Although the hierarchical structures of *B. mori* silk fibres and dragline silk are similar (Figure 1.7), the latter shows stronger mechanical properties than the former. The exceptional mechanical properties of dragline silk were investigated by laboratory experiments and *in silico* studies.

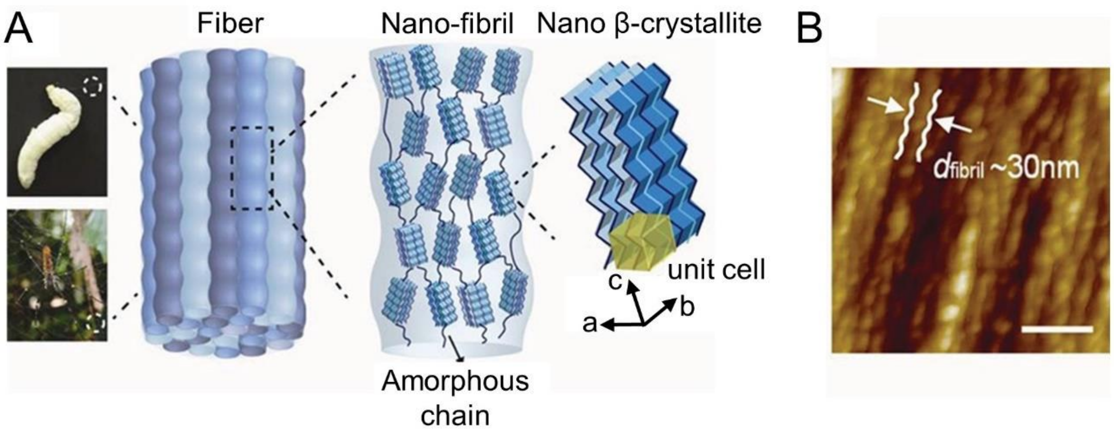

Figure 1.7 The hierarchical structure of silkworm and spider dragline silk**.** (A) Both silkworm silk and spider dragline silk consist of a bundle of inter-locking nano-fibrils, which contain stacked β-sheet crystals connecting by amorphous chains. (B) Diameter of nano-fibrillar structure in silkworm silk using AFM (scale bar = 100 nm) (Xu et al., 2013).

Most MD simulation studies focused on spider silk (dragline silk; MaSp1 and MaSp2) rather than silkworm silk (Table 1.4). The relationship between nanostructure silk and mechanical performances has been extensively studies (Termonia, 1994; Keten and Buehler, 2010; Bratzel and Buehler, 2012a; Tarakanova and Buehler, 2012; Cheng et al., 2014). The outstanding mechanical properties of silk are of great interest due to the silk structure containing simple building blocks of amino acids and weak chemical interactions such as H-bonding.

There is evidence that H-bonding between β-sheet stands could form interlocking interactions after stretching. This stress loading transfer between chains results in high toughness (Keten et al., 2010). There are many studies investigated silk crystalline size

(Keten et al., 2010; Nova et al., 2010) and the properties of amorphous region in relation to mechanical properties (Nova et al., 2010). A reduced β-sheet nanocrystal size (<10 nm) resulted in high strength, stiffness and extensibility outperforming materials such as steel. The amorphous regions broke first when silk was stretched. However, β-sheet crystalline is a predominant structure that controls tensile strength and large-deformation mechanical properties.

Table 1.4 The overview of mechanical properties studies of silk using MD simulation.

Type of silk	MD method	Aims	Studies	Ref
Spider dragline silk (Amorphous and crystalline part)	Coarse-grained and atomistic simulation	Investigate the impact of β-sheet size on its mechanical properties	**Mechanical studies** Amorphous regions play a key role in extensibility; while β-sheet enhances the mechanical properties where a small β-sheet showed high strength and toughness	Nova et al., 2010
Spider dragline silk (MaSp1)	Atomistic simulation	Study the effect of the unit length of poly-Ala on crystal formation	**Structure studies** The minimum length of Poly-Ala to obtain β-sheet nanocystals is six residues	Bratzel and Buehler, 2012
Spider dragline silk (MaSp1 and MaSp2)	Atomistic simulation	Identify nanostructure of spider silk to mechanical properties	**Mechanical and structure studies** Nanoscale behaviour of spider silk is controlled by the crystalline and semi-amorphous regions, and H-bonding	Keten and Buehler, 2010

Spider dragline silk	Coarse-grained simulation	Determine the mechanical properties in macroscopic scale	**Mechanical studies**	Giesa et al., 2011
***B.mori* silk (β-sheet)**	Atomistic simulation	Examine strength, elastic, toughness capacity of β-sheet nanocrystal in variety size	**Mechanical studies** Smaller nanocrystal provide stronger and tougher due to uniform shear and self-healing ability	Keten et al., 2010
***B.mori* silk (β-sheet)**	Atomistic simulation	The effect of water on H-bond of β-sheet	**Mechanical properties** Water affects mechanical properties of β-sheet crystallite by reducing strength of H-bond	Cheng et al., 2014
Spider silk and *B.mori* silk (anti and parallel β-sheet)	Atomistic simulation	-Determine mechanical resistance of anti- and parallel β-sheet of spider silk and *B. mori* silk - Determine the effect of H-bond on mechanical properties	**Mechanical properties** - Spider silk outperform silkworm. Antiparallel > parallel. - H-bond is a major element for force bearing	Xiao et al., 2009

1.5 Models and computational methods

Computational techniques have become principal tools to study energetic, structural and dynamic properties of molecular systems. These methods have been utilised over four decades in molecular modelling from simple small molecules to complex molecular systems. Such simulations enable comparison with laboratory studies and can help rationalise experimental results (Leach, 2001).

The computational methods used in molecular modelling can largely be divided into two groups: Quantum Mechanics (QM) and Molecular Mechanics (MM) (Lewars, 2011). QM is a mathematical technique that is used for calculating the energy in an atomistic system. This method provides accurate results due to consideration of entire electrons and nuclei in the system. However, this is the most computationally expensive method, which makes it difficult to study biological systems with large numbers of atoms in tractable timescales. MM is an alternative method for computational modelling of large systems, such as proteins, DNA and other cellular constructs. This is because MM uses simpler equations to solve classical mechanics, in which molecules energies (force fields) and their interactions are described by bonded and non-bonded interactions (more detailed in section 1.5.1.2) using equations similar to those used in physics to describe to spherical masses joined by a spring. Unlike QM methods, electrons are not explicitly modelled in MM; the energy of the system is calculated based on the nuclear position only. This results in reduction in the number of “particles” in a simulation system, and with simpler equations to solve, reduced computational overheads and access to simulations with larger numbers of atoms or simulations over longer timescales. MM is commonly used to identify stable molecular conformations with the lowest energy. The principles of MM can be expanded to include dynamic effects which allow systems to be studied as they evolve over time using thermodynamic theories such as MD simulations (Goodman, 1998), which will be discussed in more detailed in the following sections.

1.5.1 Molecular dynamics (MD)

MD is a computer simulation technique that uses the classical equations of motion of atoms to provide time dependent behaviour of molecular structure, thermodynamics in a simulation system. The MD simulation was firstly performed by Alder and Wainwright in 1957 (Alder and Wainwright, 1957) using a hard-sphere model. This study provided trajectories of particles in solid and fluid phases at a microscopic scale. In the 1970s, computers were widely used for numerical computation, which subsequently resulted in MD simulation development. The first MD simulation of a protein was firstly carried out in 1976 (McCammon, 1976). MD simulation has been extensively applied in both scientific and engineering applications due to high-performance computing and improvement of novel algorithms; calculations can be parallelised and can now run on Graphics Processing Units (GPUs) for further significant speed improvements. In addition, MD simulations at the meso- and nanoscale are contributing to the developing fields of micro- and nanotechnology (Buehler et al., 2008).

In particular, computational simulations are crucial for scientific work because they can show the detailed picture in micro- and nanoscales helping to relate the physical performance and chemical behaviour of molecules. This also can verify experimental predictions and propose hypothesis to be checked in the experiment (Buehler et al., 2008). The simplest form of MD simulations uses Newton's laws of motion (equation (1.1)) to adjust acceleration, velocity, and position of molecules - called trajectory (Leach, 2001).

$$F_i = m_i a_i(t) \tag{1.1}$$

Where m and a represent the mass and acceleration of the ith atom in the system, respectively.

Due to the complexity of systems containing huge numbers of atoms in the MD system, using only the Newton equation to analyse positions and velocities is impossible. Therefore, the numerical methods used to integrate Newton's equations of motion are required. There are many integration methods used in MD simulations, such as the verlet algorithm, the leapfrog algorithm and the velocity verlet algorithm. The velocity verlet algorithm is more accurate in terms of the trajectories produced than other methods because this algorithm allows the calculations of positions, velocities and accelerations at the same time (Leach, 2001).

1.5.1.1 Integration algorithms for constrained molecules

Reducing the number of degree of freedom (potential movements) of the system can enhance the efficiency of an MD simulation. This can be done by limiting certain movements within the molecule which require short time steps to properly resolve; these would include fixing certain bonds involving a hydrogen atom as the low mass of H results in higher frequency bond vibrations which would require shorter time steps to properly capture in a simulation. For example, the bond vibrations of O-H bonds of water molecules can be approximated and explicitly ignored. Thus, implementation of constrained algorithms is useful. The SHAKE algorithm is the most common used method to constraint the length of hydrogen bonds (Ryckaert et al., 1977) making it possible to increase the time step of the MD simulation (Adcock and McCammon, 2006).

1.5.1.2 Molecular force field

Unlike QM, MM considers the energy of a simulated molecule in terms of all the atoms in the system and as a function of their nuclear positions and by ignoring the electronic behaviour. The MM potential energy of a system is derived using a force field incorporating terms which approximate either intra or intermolecular interactions within the system. The force field is a crucial component in the molecular simulation because it can reflect behaviour and structure of molecules in the modelled system (Leach, 2001).The force field in molecular simulations is calculated from the energy from both bonded and non-bonded interaction as shown in equation (1.2).

$$E_{total} = E_{bonded} + E_{unbonded} \tag{1.2}$$

Where E_{bonded} refers to chemical bonds, angles and torsion, and $E_{unbonded}$ describes the non-bonded interactions that contributed from electrostatic and van der Waals contributions.

1.5.1.3 Periodic boundary conditions

Periodic boundary conditions are the most common boundary conditions applied in MD simulations because they enable large numbers of particles to be simulated using a smaller number and periodically repeating cells. In addition, this method can mimic an infinite computational domain despite a finite number of atoms in a cell. The identical atoms in the cubic box are copied in all directions to give a periodic array (Figure 1.8). The coordinate of the atoms in the cubic boxes can be computed simply by adding or subtracting integral multiples of the box sides. For example, the periodic boundary conditions allow the leaving atoms from the grey box to enter to the opposite side of the grey box at the same time. Therefore, the number of atoms in the system is kept constant (Leach, 2001).

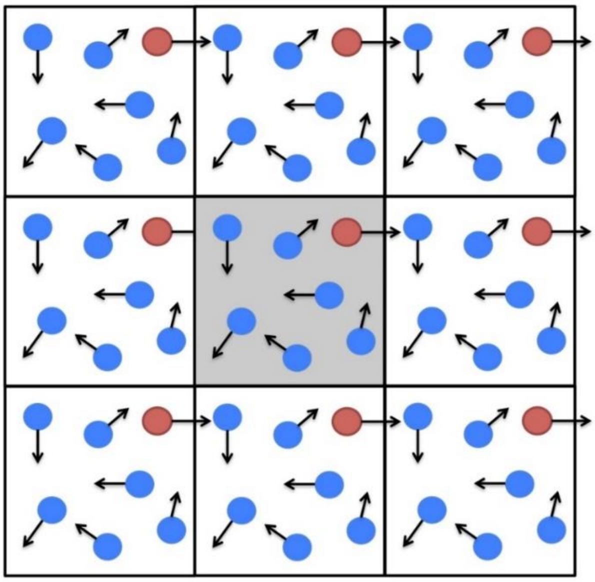

Figure 1.8 Periodic boundary condition in two dimensions. The grey cell in the middle is infinitely repeated in three dimensions.

1.5.1.4 The MD simulation process

To start a MD simulation, an initial structure of the molecule being studied is required. Protein structures are obtained from experimental techniques, such as X-ray diffraction and nuclear magnetic resonance (NMR). Fortunately, many protein and biomolecular structures are available in the Protein Data Bank (PDB) database (Berman et al., 2000). However, the initial structure needs to be chosen carefully because it can affect the quality of MD simulation; if the starting molecular conformation is unrealistic then it will take longer for the MD simulation to reach a stable equilibrium. Next, the Tleap program is used for preparation of topology and coordinate files. The program specifies force field, solvate molecules for the system (e.g. TIP3P water model), type of period cell, and subsequently provides topology and coordinate files ready for running the simulation.

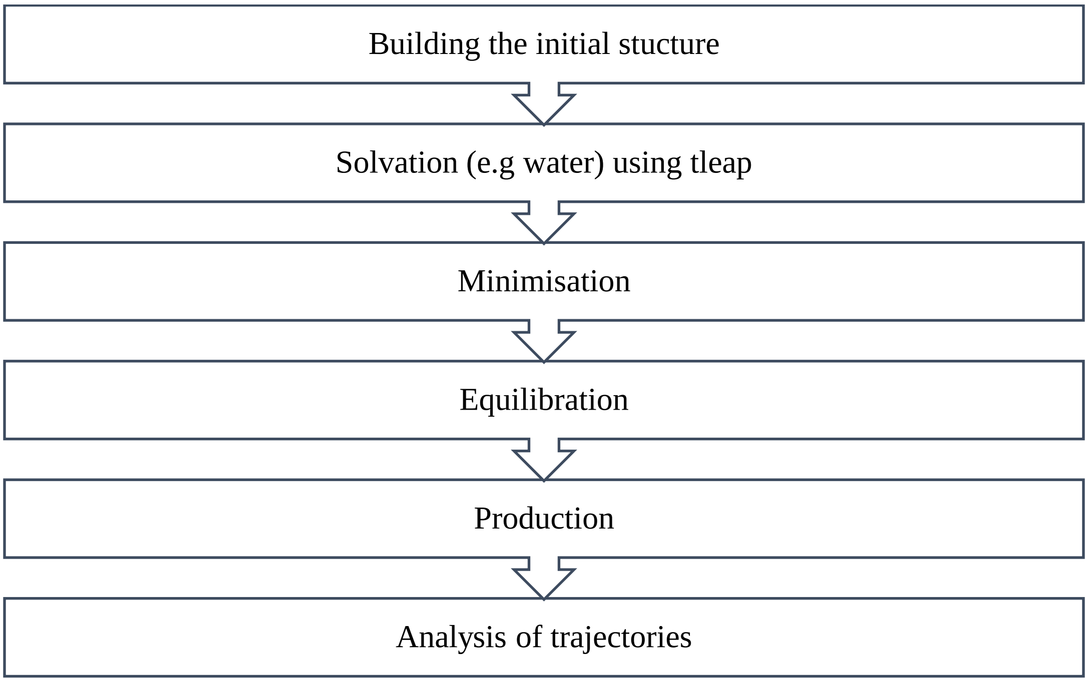

Figure 1.9 A schematic representation of a MD simulation workflow.

Next, an energy minimisation step is carried out to remove structural artefacts resulting from the model-building process; this might include structural errors introduced during experimental structure refinement or through bad contacts made when adding hydrogen atoms to x-ray structures in the previous simulation step. The most common minimisation method is positional restraint. This method initially fixes each atom in the model to a reference position with a weak spring. In the minimisation cycles, atoms in the system are moved away from the reference position; the new position is used as the reference position for the next cycle. The conformation of the modelled structure after several energy minimisation cycles should resemble a low-energy structure where the positions of atoms are optimally placed to minimise the energy arising from the forcefield. Subsequently, an equilibration or heating process is used to simulate heating the system to a desired temperature (equilibration phase) so that it can further equilibrate during what is known as the production phase. In the equilibration step the idea is to run the simulation until the properties (e.g. structure, pressure and temperature) are stable with respect to time. The production step then provides the final atomic/molecular trajectories which are used in the analysis of results. In order to visualise and analyse the simulation results, the most popular graphic programs; Visual Molecular Dynamics (VMD) and PyMOL can be used. These programs can provide three-dimensional (3D) renderings of the MD trajectories and are useful for visualising complicated conformational data.

1.5.2 Enhanced sampling techniques

MD simulations have been used in a broad range of biological sciences, from small systems such as small peptides (Buchete and Hummer, 2008; Rhinehardt et al., 2015) to large complex systems such as the cell membrane (Zhang et al., 2017), protein folding (Chen et al., 2015) and protein-protein interaction (Abriata and Peraro, 2015). However, one of the greatest challenges of MD simulations used for biological molecules is the limitation of conformational sampling owing to the relevant configurations in metastable states separated by high-energy barriers (Figure 1.10). Therefore, to observe rare events in biological systems, long simulation run and supercomputers are required, which results in high computational cost (Onuchic, Luthey-Schulten and Wolynes, 1997).

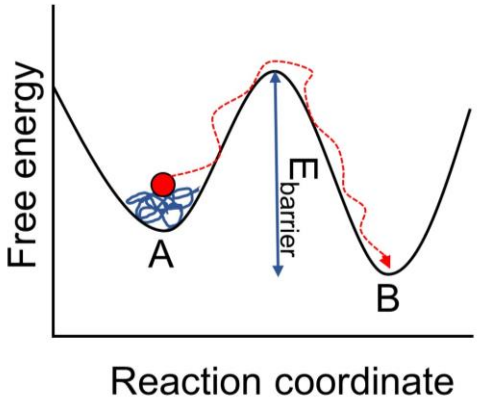

Figure 1.10 Schematic of free energy landscape containing two metastable states A and B. The system (red circle) starts its dynamics in state A and it can be trapped in A for long period of time due to high free energy barrier ($E_{barrier}$) between A and B.

Over the past decade, remarkable improvements have been made in the development of enhanced sampling techniques to overcome this limitation, such as the umbrella sampling method (Torrie and Valleau, 1977), replica-exchange molecular dynamics (REMD) method (Sugita and Okamoto, 1999), accelerated molecular dynamics (Hamelberg et al., 2004), steered molecular dynamics (Isralewitz et al., 2001) and metadynamics (Laio and Gervasio, 2008). In this thesis, metadynamics was chosen to enhance the conformational sampling of silk structure in water. The theory of metadynamics and the choice of collective variables (CVs) are described in the following sections.

1.5.2.1 Metadynamics

Metadynamics was first introduced by Alessandro Laio and Michele Parrinello in 2002 (Laio and Parrinello, 2002). Metadynamics is a powerful and reliable technique for enhanced sampling in MD simulations; it has been employed successfully in many systems, from chemistry to biology (Ensing et al., 2006; Bealing et al., 2009; Cavalli et al., 2015; Comitani et al., 2015; Leva et al., 2018). This method can be used for (i) reconstructing the free energy landscape, (ii) exploring the transition states and the lowest minima, and (iii) accelerating rare events in simulations (Laio and Gervasio, 2008). Metadynamics enhances conformational sampling and speeds up the simulation by constructing an external history-dependent bias potential (sum of Gaussians) along free energy landscape in a properly chosen set of collective variables (CVs) (Figure 1.11B) (more detailed in section 1.5.2.3) (Laio and Gervasio, 2008). In metadynamics, the set of CVs (S) is described in the microscopic coordinate (R) of the system.

$$S(R) = (S_1(R),\ldots S_n(R) \qquad (1.3)$$

At the time point t, metadynamics bias potential ($V_G(S,t)$) is

$$V_G(S,t) = \int_0^t dt'\omega \exp(-\sum_{i=1}^{d} \frac{(S_i(R)-S_i(R(t')))^2}{2\sigma_i^2}) \qquad (1.4)$$

Where ω is an energy rate, which is described by Gaussian height (W) and a time step of deposition (τ_G) (equation (1.5)), σ_i is the width of the Gaussian for the *i*th CV.

$$\omega = \frac{W}{\tau_G} \qquad (1.5)$$

The bias potentials from metadynamics are able to fill up a free energy minima where the system is stuck enabling the system moves away from the local minima to visit another region of CVs space. However, the main drawback of the standard metadynamics is poor convergence because it is difficult to predict when to terminate the simulation. This leads to overfill of the underlying free-energy resulting in irrelevant conformations and time loss (Figure 1.11B). To dissolve this problem, well-tempered metadynamics was developed.

1.5.2.2 Well-tempered metadynamics

The well-tempered metadynamics has been proposed to alleviate the problem from the original metadynamics by reducing the error from overfilling free energy landscape (Barducci et al., 2008). Well-tempered metadynamics has the advantage of ensuring convergence of the energy landscape by reducing Gaussian height (W) over simulation time (Figure 1.11C), according to equation (1.6)

$$W = W_0 e^{\frac{-V_G(S,t)}{k_B \Delta T}} \tag{1.6}$$

Where W_0 is the initial Gaussian height, k_B is the Boltzmann constant and ΔT is an input parameter with the dimension of a temperature.

The reduction rate of Gaussian height over simulation time can be controlled by bias factor (γ) $\frac{T+\Delta T}{T}$ that enables the construction of free energy landscape (F(S)) smoothly converge (equation (1.7)).

$$V_G(S, T \rightarrow \infty) = -\frac{\Delta T}{T+\Delta T} F(S) + C \tag{1.7}$$

Where $T \rightarrow \infty$ corresponds to the standard metadynamics, T is the temperature of the system, $T + \Delta T$ indicates the higher temperature used to sampling CVs of the system over simulation time, C is irrelevant constant.

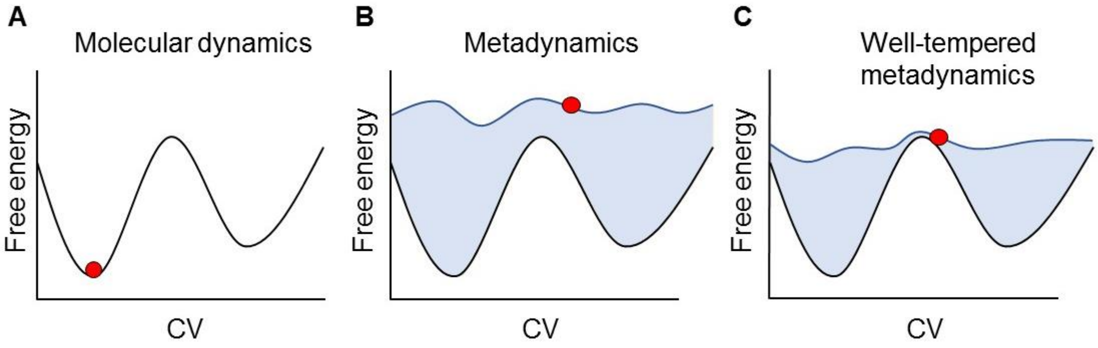

Figure 1.11 Schematic of free energy profile of molecular dynamics, matadynamics and well-tempered metadynamics. The red circle represents the system position, the blue area is the added external bias potential. The well-tempered metadynamics showed the reduction of the error from overfilling of the bias potential during simulation.

1.5.2.3 The choice of collective variables

As mentioned above, the bias potential was added into trajectory of a few selected degrees of freedom or CV's space. Therefore, the reliability of metadynamics relies on the selection of CVs. There are three criteria of ideal CVs for accurate and reliable metadynamics simulations (Laio and Gervasio, 2008).

(i) CVs should be able to distinguish between metastable states of free energy landscape.

(ii) CVs should be able to define all slow events that relate to the process of interest.

(iii) The number of CVs should be kept low to avoid long simulation time due to exploration of the high number of dimensional space.

There are various available CVs that can be selected. For this project, the conformation space of amorphous-crystalline silk structure was explored and the free energy landscape was reconstructed (Chapter 5). ANTIBETARMSD and ALPHARMSD were selected as CVs in this project. These CVs have been successfully used for exploring conformational space of protein systems (Cossio et al., 2010; Baftizadeh et al., 2012; Granata et al., 2013). ALPHARMSD and ANTIBETARMSD are able to determine the secondary structures of proteins that can form α-helix and antiparallel β-sheet, respectively (Pietrucci and Laio, 2009). These CVs calculate how many fragments of the six residues in a protein (six contiguous residues for α-helix and 3 + 3 residues for an antiparallel β-sheet) belong to α-helix and β-sheet. For ANTIBETARMSD, the 3 + 3 residues block can be from two protein chains or the same protein chain separated by two residues to generate a turn. The number of secondary structure segments are computed by the root-mean-square deviation (RMSD) calculation with respect to an ideal structure of α-helix and β-sheet from Protein Data Bank (PDB) database, according to equation (1.8) and Figure 1.12.

$$S = \sum_{\alpha} n\left[RMSD\left(\{R_i\}_{i\epsilon\Omega_\alpha,}\{R^0\}\right)\right] \tag{1.8}$$

$$n(RMSD) = \frac{1-(RMSD/0.1)^8}{1-(RMSD/0.1)^{12}} \tag{1.9}$$

Where n is a function switching smoothly between 0 and 1. The RMSD is measured in the distance (nm) between protein structure models and the ideal secondary structures $\{R_i\}_{i\epsilon\Omega_\alpha}$ is the atomic coordinates of a set Ω of six protein residues. $\{R^0\}$ is the corresponding atomic position of the ideal α-helix and β-sheet conformations.

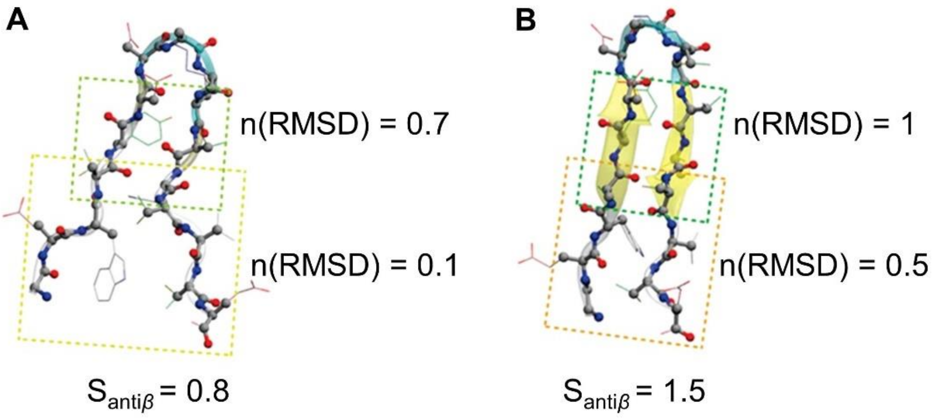

Figure 1.12 Schematic of C-terminal β-hairpin of protein GB1 representing RMSD calculation of antiparallel β-sheet conformation. $S_{anti\beta}$ is a value calculated by ANTIBETARMSD calculated. (A) Partial (B) complete formed antiparallel β-sheet conformation **(**modified from Pietrucci and Laio, 2009).

To sum up, silk from *B. mori* is an excellent candidate as a biomaterial in drug delivery applications due to (i) high silk yields from sericulture, (ii) long clinical track record in humans, (iii) remarkable mechanical properties due to its crystalline structure, (iv) biocompatibility, (v) ability for therapeutic payload stabilisation and (vi) a tuneable fabrication process allowing manufacture of various forms, including nanoparticles. Silk nanoparticles are emerging as interesting (anticancer) drug carriers. Additionally, the knowledge of molecular dynamics simulations enables enhanced understanding of silk at the molecular level, which can provide a platform to better understand silk performance for drug delivery. This will ultimately support advanced material design strategies. Silk is a fascinating biopolymer and thus this thesis aims to contribute to the silk knowledge base. The thesis aims are detailed in the following section.

1.6 Hypothesis and thesis aims

The main hypothesis of this thesis is that silk nanoparticles can be used as a potential nanomedicine for lysosomotropic anticancer drug delivery. To fulfil this hypothesis, silk nanoparticles need to have specific properties such as a nanoscale particle size, high stability, adequate drug loading capability, biodegradability and ability to traffic to lysosomes and release their payload.

Therefore, the aim of this thesis is to exploit a range of experimental and computational approaches for the development and evaluation of silk nanoparticles as a potential drug delivery carrier. The specific thesis aims are:

(i) The manufacture and surface modification of silk nanoparticles (Chapter 2).

(ii) Assessment of native and PEGylated silk nanoparticles for combination drug loading and delivery (Chapter 2).

(iii) Assessment of the biodegradation of native and PEGylated silk nanoparticles *in vitro* and *ex vivo* (Chapter 3).

(iv) Manipulating silk nanoparticle’s characteristics using microfluidics (Chapter 4).

(v) Assessment of the silk atomic structure as well as drug binding using advanced sampling methods of molecular dynamics simulation (Chapter 5)

Chapter 2

Native and PEGylated silk nanoparticles for anticancer drug delivery

This chapter contains the results from the published articles in Biomacromolecules (DOI: 10.1021/acs.biomac.5b01003) and in the Journal of Visualized Experiments (DOI: 10.3791/54669). Some results such as stability, drug loading characterisations and drug release of native and PEGylated silk nanoparticles were included in my MRes thesis with the title "Silk nanoparticles for drug delivery applications"; therefore, these data sets are not shown in this chapter. My contribution of this work was that I acquired, analysed and interpreted all data and generated the manuscript draft. Prof Andrew Urquhart performed FTIR curve-fitting.

2.1 Introduction

The term "nanomedicine" was coined in the early 2000s and is essentially an umbrella descriptor for specifically engineered, nano-sized therapeutics and imaging agents composed of multiple components (Duncan and Gaspar, 2011). Over the past three decades, more than 40 nanomedicines have entered routine clinical use (Duncan and Gaspar, 2011; Duncan and Vicent, 2013). The majority of these nanomedicines serve as imaging agents (Duncan and Gaspar, 2011; Duncan and Vicent, 2013), but interest continues in nanomedicines for drug delivery applications (Yin et al., 2014). For example, more than a dozen nanoparticles are currently in clinical trials for a broad spectrum of indications (Sheridan, 2012; Veiseh et al., 2015), including targeting of solid tumours (Hrkach et al., 2012). Nanoparticles are particularly well suited for tumour targeting because they can exploit the leaky neo-vasculatures and poor lymphatic drainage of solid tumours, thereby enabling their passive accumulation (Fang et al., 2011; Maeda et al., 2013). This phenomenon is widely described as the enhanced permeation and retention effect (EPR) (Matsumura and Maeda, 1986); this effect can increase the retention time of nanoparticles in tumours (Torchilin, 2011).

The payloads of nanomedicines differ widely but they must reach the tumour microenvironment and often must deliver their payload to a specific intracellular compartment to elicit the desired pharmacological effect (Duncan, 2006). For example, anticancer nanomedicines designed for intracellular activation must complete their journey from the extracellular space to the desired intracellular destination via endocytic pathways (Seib et al., 2006, 2007). Following endocytic uptake of a nanomedicine, the default destination is the lysosome, where the nanomaterial is exposed to low pH (typically 4.5) and lysosomal enzymes (Duncan and Richardson, 2012). The use of stimulus-responsive polymers (e.g., pH-triggered) in the design of the macromolecular drug carrier can therefore promote drug release (i.e., lysosomotropic drug delivery) (De Duve et al., 1974).

The vast majority of anticancer nanomedicines are designed for parenteral administration, which means that the nanomedicine must come into direct contact with the blood. This can trigger nanomedicine opsonisation; a process that is one of the most significant biological barriers for controlled drug delivery (Owens and Peppas, 2006). Specifically, unmodified nanomedicines are “tagged” by opsonins, subsequently recognised by the mononuclear phagocytic system (MPS), and eventually removed (Owens and Peppas, 2006). Therefore, surface modification of macromolecular drug carriers is a well-established strategy to minimise this effect (Pasut and Veronese, 2012; Rabanel et al., 2014). Surface modification of particles provides many benefits: increased biocompatibility, decreased immune response, improved stability, and delayed clearance by the MPS (Veronese and Pasut, 2005; Rabanel et al., 2014). Therefore, PEGylated nanoparticles have a greater chance of reaching the tumour microenvironment when compared to uncoated nanoparticles. (Bae and Park, 2011; Rabanel et al., 2014).

Biopolymers ranging from biological active polymers (e.g., heparin) to macromolecular drug carriers (e.g., dextrin, dextran, alginates, chitosan) and multifunctional materials are being used for a broad spectrum of medical applications (Spiess et al., 2010; Werner and Meinel, 2015). One natural biopolymer, silk, has been used for millennia for suturing, and is licensed by the Food and Drug Administration (FDA) for use in humans for load bearing applications. Nevertheless, silk has only recently emerged as promising biopolymer for drug delivery (Seib and Kaplan, 2013).

Silk has a robust clinical track record and excellent mechanical properties (Omenetto and Kaplan, 2010; Seib and Kaplan, 2013). In addition, silk is biodegradable and can be processed under mild aqueous conditions to generate various material formats (Wenk et al., 2008). A number of studies have detailed the manufacture of *B. mori* silk nanoparticles using poly(vinyl alcohol) blends (particle size range 300 nm to 10 μm) (Wang et al., 2010), emulsification (>6000 nm) (Xie et al., 2008), capillary microdot printing (25−140 nm) (Gupta et al., 2009), salting out (486−1200 nm) (Lammel et al., 2010), supercritical CO_2 (50−100 nm) (Zhao et al., 2013; Xie et al., 2015), or organic solvent precipitation (35−170 nm) (Zhang et al., 2007; Kundu et al., 2010; Seib, Jones, et al., 2013) (reviewed in Zhao, Li and Xie, 2015). Some of these studies examined the ability of silk nanoparticles to entrap and release (model) drugs (Kundu et al., 2010; Lammel et al., 2010; Wang et al., 2010). Nanoparticles prepared from spider silks (Heim et al., 2009; Borkner et al., 2014) and chimeric silks (e.g., silk-elastin-like protein polymers) (Price et al., 2014) are typically formed using a self-assembly process; these engineered silk nanoparticles have been used for a range of drug delivery applications including small molecular weight (model) drugs (Xia et al., 2014) and biologics (e.g., peptides, proteins and therapeutic plasmids; reviewed in Numata and Kaplan, 2010; Pritchard et al., 2012). For example, bioengineered spider silk nanoparticles functionalized with a HER2 binding peptide and loaded with doxorubicin showed preferential uptake via receptor-mediated endocytosis in HER2$^+$ breast cancer cells resulting in improved intracellular drug delivery when compared to non-targeted nanoparticles (Florczak et al., 2014). However, none of the described silk nanoparticles has been specifically refined to avoid the MPS. The optimum use of nanoparticles *in vivo*, however, typically requires “stealth” design principals. Therefore, the aim of this chapter was to manufacture PEGylated silk nanoparticles and characterise their drug loading, coupled with preliminary *in vitro* studies.

2.2 Materials and Methods

Throughout this thesis chemicals were supplied by Sigma Aldrich (Poole, Dorset, UK) with a minimum purity of > 98% and used as supplied unless otherwise stated.

2.2.1 Preparation of a reverse-engineered silk solution from *Bombyx mori* cocoons

B. mori silk (Tajima Shoji, Kanagawa, Japan) was extracted from dried cocoons as described previously (Rockwood et al., 2011). Briefly, 5 g of cocoons were cut with scissors into 5 mm × 5 mm pieces, any soiled layers were removed, boiled in 0.02 M Na_2CO_3 for 60 min and then fibres were rinsed in ultrapure water and air-dried. This typically yields 3.6 g of degummed silk fibres. The fibres were then dissolved in 9.3 M LiBr solution at 60 °C up to 4 h, yielding a 5 wt % solution. This solution was dialysed (Slide-A-Lyzer Dialysis cassettes with 3.5 kDa molecular weight cut-off, Thermo Scientific, Paisley, UK) against 1 L of ultrapure water for 72 h to remove the LiBr salt. The silk solution was collected from the dialysis cassette and centrifuged for 20 min at 5 °C at 9,500 x g (Avanti J-E, Rotor J20, Beckman Coulter, Brea, CA, USA). The supernatant was recovered and the process was repeated twice more. The concentration of silk solution (w/v) was determined by weighing of an empty weighing boat (W1) and then adding 1 mL of the silk solution (W2). The sample was dried at 60 °C overnight. Next, the total dry weight (W3) (dried silk and weighing boat) was determined. Therefore, the concentration of the silk solution (w/v) is:

$$\text{Silk solution (\% w/v)} = \frac{(W3-W1)}{(W2-W1)} \times 100 \tag{2.1}$$

2.2.2 Preparation of silk nanoparticles

Silk nanoparticle preparation has been reported elsewhere (Seib, Jones, et al., 2013). Briefly, the silk (5 wt %) solution was added dropwise (20 µL/drop) to acetone, maintaining >75% v/v acetone volume. Precipitated silk was then centrifuged at 48,400 × g for 2 h, the supernatant was aspirated, and the pellet was resuspended in ultrapure water, vortexed, and subsequently sonicated twice for 30 s at 30% amplitude with a Sonoplus HD 2070 sonicator (ultrasonic homogenizer, Bandelin, Berlin, Germany). The centrifugation, washing and resuspension steps for the silk nanoparticle preparation were repeated at least twice more. The particles were analysed as detailed below and stored at 4 °C until use. A calibration curve was generated to measure the amount of silk nanoparticles in suspension by measuring the scatter light at 600 nm (Figure 2.1).

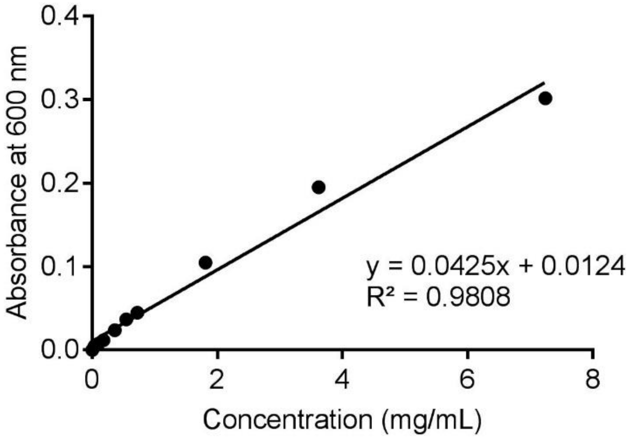

Figure 2.1 Calibration curve to calculate the amount of silk nanoparticles suspended in water. The silk nanoparticles were suspended in ultrapure water and the scatter lights was measured at 600 nm. The data represents the mean ± SD, error bars are hidden in the plot-symbol when not visible, n = 3.

2.2.3 Preparation of PEGylated silk nanoparticles

For PEGylation, an aqueous 50 mg/mL silk nanoparticle stock was prepared. Next, 50 mg of silk nanoparticles and 50 mg of methoxypolyethylene glycol activated with cyanuric chloride (TST-activated mPEG, 5000 g/mol, Sigma-Aldrich, St. Louis, MO, U.S.A.) were allowed to react in 2 mL of 50 mM $Na_2B_4O_7$ pH 9.4 overnight under constant stirring at 4 °C. After the reaction, the sample was centrifuged for 30 min at 194,000 × g. The absorbance of the collected supernatant was measured at 240 nm

(Vepari et al., 2010). A calibration curve of activated PEG in 50 mM $Na_2B_4O_7$ was used to determine the amount of PEG conjugated to silk nanoparticles (Figure 2.2).

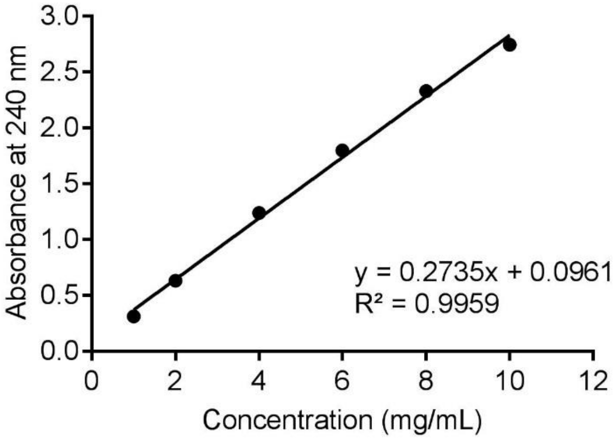

Figure 2.2 Calibration curve to calculate the amount of PEG conjugated to silk nanoparticles. The absorbance of PEG in 0.05 M $Na_2B_2O_7$, pH 9.4 was measured at 240 nm. The data represents the mean ± SD, error bars are hidden in the plot-symbol when not visible, n = 3.

2.2.4 Silk nanoparticle size and zeta potential analysis

Particle size and zeta potential of native and PEGylated silk nanoparticles were determined by dynamic light scattering (DLS, Zetasizer Nano-ZS Malvern Instrument, Worcestershire, U.K.) in ultrapure water, unless otherwise stated. The samples were sonicated twice at 30% amplitude for 30 seconds prior to the measurements. The particle size represented by the Z-average value and the width of particle size distribution known as the polydispersity index (PDI). All samples were diluted to the concentration of 1 mg/mL, subsequently filled into disposable polystyrene cuvettes (Thermo Scientific, Paisley, UK). Refractive indices of 1.33 for ultrapure water and 1.60 for protein were taken for computation of particle size. Each measurement was determined in triplicate and averaged. The impact of pH on the zeta potential of native and PEGylated silk nanoparticles was determined by suspending them in 0.01 M phosphate buffer saline (PBS) at pH 4.5 to 8.5 and measuring the resulting zeta potential.

2.2.5 Fourier transform infrared spectroscopy

Untreated silk films, autoclaved silk films, freeze-dried native and PEGylated silk nanoparticles were used to determine the secondary structure of silk. Fourier transform infrared spectroscopy (FTIR) was carried out using a PerkinElmer Spectrum 100 instrument over the wavenumber range of 550 to 4000 cm^{-1} by running 128 scans at 4 cm^{-1} resolution for each measurement. All spectra were normalised and corrected for water signals. In order to determine the secondary structure of silk, Fourier self-deconvolution (FSD) was used and performed by OriginPro 9.0 software as indicated in Hu et al., 2006; Yang et al., 2015. First, the FTIR spectra at the amide I region (1595−1705 cm^{-1}) were selected as the most sensitive spectral region to protein secondary structure compositions. Second, deconvolution was performed by maintaining peak full width at half-maximum (FWHM) at a fixed value (10 cm^{-1}) to avoid overfitting the data (Mains et al., 2013). Next, the amide I region was assigned to 1605−1615 cm^{-1} as side chain, 1616−1621 cm^{-1}, 1622−1627 cm^{-1}, 1628−1637 cm^{-1}, and 1697−1703 cm^{-1} as β-sheet structure, 1638−1646 cm^{-1} and 1647−1655 cm^{-1} as random coil structure, 1656−1662 cm^{-1} as α-helical bands, and 1663−1670 cm^{-1}, 1671−1685 cm^{-1}, and 1686−1696 cm^{-1} as β-turns. The 11 peaks at 1611, 1619, 1624, 1630, 1640, 1650, 1659, 1666, 1680, 1691, and 1698 cm^{-1}, which are the centre of the secondary structure regions were selected and fitted to the FTIR spectra using

Gaussian curve fitting (dotted curves in Figure 2.3). The ratio of the individual peak area to the total amide I band area was determined and served as the amount of the secondary structures of silk samples. Silk films with a low and high crystallinity were generated by air-drying 2 ml of a 4 % w/v silk solution. High crystallinity was induced by autoclaving the film at 121 °C while low crystallinity silk films were left untreated. These films were used as a reference for the silk nanoparticle studies (Figure 2.3 and Figure 2.8).

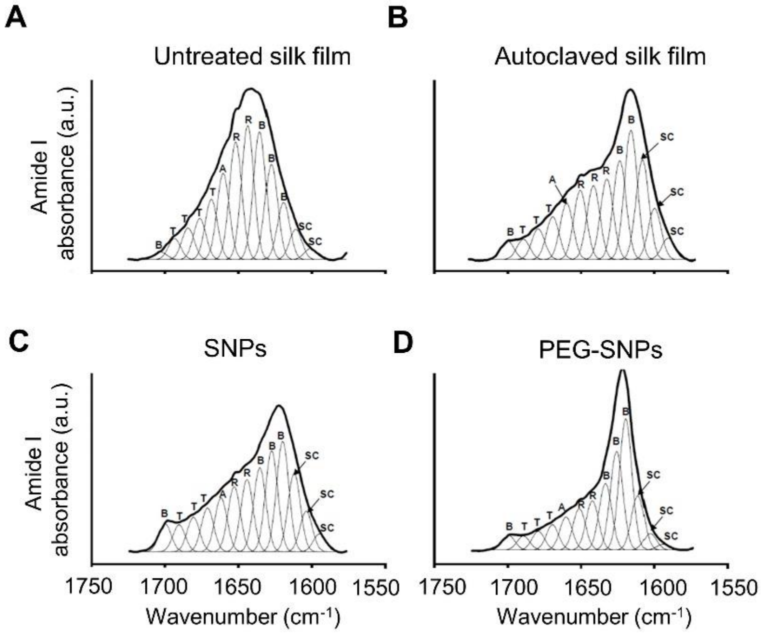

Figure 2.3 Absorbance spectra of silk's amide I region after Fourier self-deconvolution. (A) Untreated silk film, (B) autoclaved silk film, (C) native silk nanoparticles (SNPs) and (D) PEGylated silk nanoparticles (PEG-SNPs). The heavy line represents the deduced absorbance band. The light lines represent the contributions to the amide I band and are marked as (A) α-helix, (B) β-sheet, (R) random coil, (SC) side chain and (T) turn.

2.2.6 *In vitro* response of macrophages toward native and PEGylated silk nanoparticles

The murine macrophage RAW 264.7 cell line was purchased from ATCC (Manassas, VA, U.S.A.). Cells were cultured in DMEM (4.5 g glucose, 110 mg sodium pyruvate, 10%v/v FBS), grown in a humidified 5% CO_2 atmosphere at 37 °C and routinely subcultured every 2−3 days by scraping cells off the flask and replating them at a split ratio of 2−10 on tissue culture treated polystyrene (Corning, New York, NY, U.S.A.). Macrophage activation was assessed by seeding the cells at a density of 1.4×10^4 cells/cm^2 and allowing them to recover overnight. Next, the culture medium was aspirated and replaced with fresh containing either (i) 5 ng of lipopolysaccharide (LPS, Sigma-Aldrich, St. Louis, MO, U.S.A.), (ii) 50 µg of native silk nanoparticles, (iii) 50 µg of PEGylated silk nanoparticles, and (iv) control medium. Cultures were incubated for 24 h and then the medium was collected and centrifuged at 6,000 × g for 5 min. Assay samples were stored at −80 °C and analysed using mouse tumour necrosis factor alpha (TNF-α) DuoSet ELISA (R&D Systems, Minneapolis, MN, U.S.A.), according to the manufacturer’s instructions.

2.2.7 Drug loading of native and PEGylated silk nanoparticles

The drug loading strategy used for doxorubicin HCl (LC Laboratories, Boston, MA, U.S.A.) and propranolol HCl (Sigma-Aldrich, St. Louis, MO, U.S.A.) was identical for native and PEGylated silk nanoparticles. Briefly, a 200 µL nanoparticle suspension containing 5 mg of silk nanoparticles was mixed with 200 nmol drug in 1 mL of ultrapure water. After a 24 h incubation period at room temperature, the sample was centrifuged for 30 min at 194,000 × g. The supernatant was collected and the pellet was washed three times with ultrapure water. The combined supernatant was analysed for free drug in order to determine the encapsulation efficiency (%) and weight percentage (%w/w) loading. With the aid of propranolol HCl and doxorubicin HCl calibration curves the amount of free drug remaining in solution was calculated using absorbance (289 nm) and fluorescence (excitation 480 nm, emission 590 nm) measurements, respectively (Figure 2.4). Subtracting the residual amount left in the supernatant from the initial starting amount allowed us to deduce nanoparticle drug loading. The encapsulation efficiency was calculated using the following equation (2.2):

$$\text{Encapsulation efficiency (\%)} = \frac{W1}{W2} \times 100 \qquad (2.2)$$

Where W1 is the actual nanoparticle drug loading and W2 is the theoretical nanoparticle drug loading.

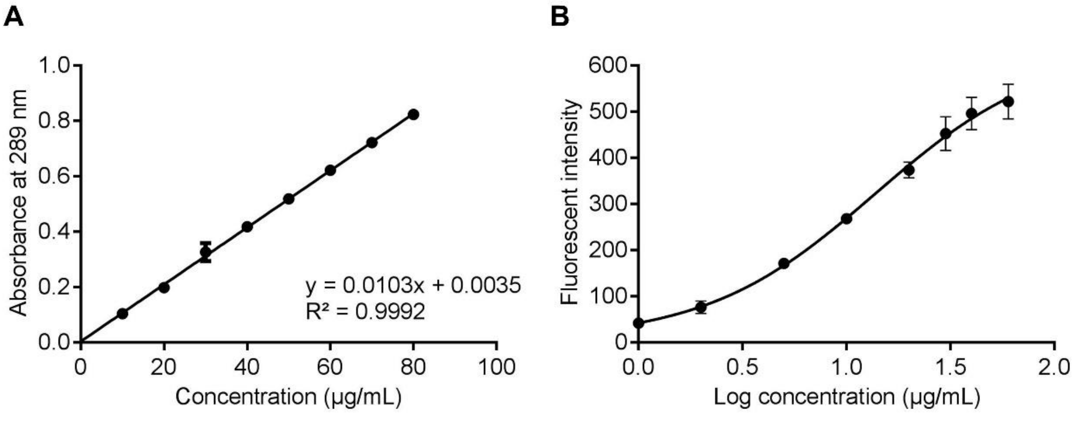

Figure 2.4 Calibration curves of model drugs in ultrapure water. (A) Propranolol HCl at 289 nm. (B) Doxorubicin HCl at 480 nm (Ex), 590 nm (Em). The data represents the mean ± SD, error bars are hidden in the plot-symbol when not visible, n = 3.

2.2.8 *In vitro* cytotoxicity and analysis of freely diffusible drug combinations

The human breast cancer cell lines MCF-7 was purchased from ATCC (Manassas, VA, U.S.A.). Cells were cultured in DMEM (4.5 g glucose, 110 mg sodium pyruvate, 10%v/v FBS, 10 µg/ mL insulin), plated on tissue culture treated polystyrene, grown in a humidified 5% CO_2 atmosphere at 37 °C and routinely subcultured every 2−3 days. Cells were seeded in 96-well plates at a density of 2×10^4 cells/cm^2 (for a typical growth curve, Figure 2.5) and allowed to recover overnight. Next, propranolol HCl and doxorubicin HCl stock solutions were filter sterilised (0.22 µm, polyethersulfone membrane, Merck Millipore, Billerica, MA, U.S.A.) and cells were treated using freely diffusible (i) doxorubicin HCl, (ii) propranolol HCl, and (iii) doxorubicin and propranolol combinations. Following a 72 h incubation period during the exponential growth phase, cell viability was determined using 3-(4, 5-dimethylthiazol- 2-yl)-2, 5-diphenyltetrazolium bromide (MTT at 5 mg/mL in PBS); 20 µL of MTT was added to each well and cultures were incubated for 5 h. The formazan product was solubilized with 100 µL of dimethyl sulfoxide (DMSO) and absorbance was measured at 570 nm. Untreated control cells represented 100% cell viability. For treatment groups the half maximal inhibitory concentration (IC_{50}) was calculated.

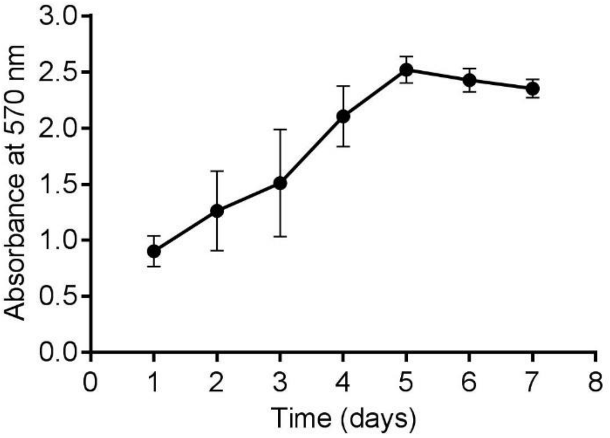

Figure 2.5 Growth curve of MCF-7 cells plated at an initial density of 2 × 10^4 cells/cm^2. The cell viability was assessed using MTT assay. The data represents the mean ± SD, error bars are hidden in the plot-symbol when not visible, n = 3.

The impact of freely diffusible doxorubicin and propranolol drug combinations on MCF-7 cells was determined with an isobologram and combination index (CI) methods using CompuSyn Software (Combo-Syn Inc., Paramus, NJ, U.S.A.). First, the IC_{50} for each drug on its own was determined as detailed above. Next, an isobologram was generated by plotting the propranolol IC_{50} on the abscissa and doxorubicin IC_{50} on the ordinate. The straight line fit connecting these IC_{50} values generated the additive line. Combination data points that fell on the line represented an additive effect, while data points that fell below or above the line represented synergism or antagonism, respectively. The CI of doxorubicin and propranolol was calculated with CompuSyn software (version 1.0), where a $CI < 1$ indicated synergism, $CI = 1$ was additive, and $CI > 1$ showed antagonism (Chou, 2006). The most promising drug combination was used for nanoparticle experiments.

2.2.9 *In vitro* cytotoxicity of drug loaded native and PEGylated silk nanoparticles

MDA-MB-231 and MCF-7 cell viability was assessed by exposing cells to control, doxorubicin-loaded and propranolol-loaded native and PEGylated silk nanoparticles. MDA-MB-231 cells were cultured in RPMI 1640 with 10% v/v FBS, plated on tissue culture treated polystyrene, grown in a humidified 5% CO_2 atmosphere at 37 °C and routinely subculture at 80% confluence every 2−3 days. Cells were seeded in 96-well plates at a density of 2×10^4 cells/cm^2 and allowed to recover overnight. Next, 0.1 µg freely diffusible doxorubicin, 0.001-0.5 mg silk nanoparticles and 0.1 mg silk nanoparticles loaded with 0.1 µg doxorubicin HCl were added into 96-well plates (final volume 100 µL per well). The cell viability and the IC_{50} were determined with MTT as detailed above.

MCF-7 cells were cultured as detailed in section 2.2.8. The combination therapy delivered via native and PEGylated silk nanoparticles used fixed ratios of 0.01 µg doxorubicin HCl and 2.1 µg of propranolol HCl for every 0.5 mg of silk nanoparticles. Nanoparticles were prepared and loaded with the respective drug (100% loading efficiency). Next, doxorubicin-loaded and propranolol-loaded nanoparticles were mixed to obtain the desired doxorubicin and propranolol combination. MCF-7 cells were treated with (i) 0.5 mg native silk nanoparticles, (ii) 0.5 mg PEGylated silk nanoparticles, (iii) 0.5 mg silk nanoparticle containing the fixed drug combination of 0.01 µg doxorubicin HCl and 2.1 µg propranolol HCl, or (iv) the combination of freely diffusible drugs at the equivalent doses. Following a 72 h incubation period, cell viability was assessed with the MTT as detailed above.

2.2.10 Scanning electron microscopy of breast cancer cells exposed to drug loaded silk nanoparticles

MDA-MB-231 and MCF-7 cells and were seeded on sterile glass coverslips and allowed to recover as detailed above. Cells were exposed to the treatments for 72 h and then fixed with 2% v/v glutaraldehyde in PBS, washed with ultrapure water twice, dehydrated with an increasing ethanol series (10%, 30%, 60%, 80%, 90% and absolute ethanol), and critical point dried (EM CPD300, Leica Microsystems, Wetzlar, Germany). Samples were then sputter-coated with 15 nm of gold and analysed by SEM at 5 kV at 300-, 700-, and 2000-fold magnification.

2.2.11 Labelling native and PEGylated silk nanoparticles with Alexa Fluor 488

A total of 10 mg of native and PEGylated silk nanoparticles were fluorescently labelled. First, silk nanoparticles were resuspended in 0.1 M $NaHCO_3$, pH 8.3. Next, 1 mg of Alexa Fluor 488 succinimidyl ester (Life Technologies, Carlsbad, CA, U.S.A.) was dissolved in anhydrous DMSO at 1 mg/mL and 100 μL of this solution was added to the native and PEGylated silk nanoparticles and allowed to react for 24 h at room temperature in the dark while stirring. Silk nanoparticles were then centrifuged, and the pellets were washed four times with acidified water (pH 4.6) to remove unbound dye, followed by three washes with ultrapure water. The samples were stored at 4 °C in the dark until use.

2.2.12 Cellular uptake of native and PEGylated silk nanoparticles

MCF-7 cells were seeded in complete phenol-red-free medium at a density of $2 \times 10^4/cm^2$ and allowed to recover for 24 h. Next, the cultures were incubated for 5 h with

(i) 0.3 μg/mL doxorubicin HCl or the equivalent amount of doxorubicin HCl loaded in (ii) 0.5 mg/mL Alexa Fluor 488 labelled native silk nanoparticles or (iii) 0.5 mg/mL Alexa Fluor 488 labelled PEGylated silk nanoparticles. Immediately prior to live cell imaging, the culture medium was replaced with fresh complete DMEM medium containing 25 mM HEPES. Cells were imaged for up to 20 min using a Leica TCS-SP5 confocal laser scanning microscope (Leica Microsystems GmbH, Wetzlar, Germany) equipped with a 40× magnification water objective with a numerical aperture of 1.25. Alexa Fluor 488 and doxorubicin-associated fluorescence was tracked using a 485 nm excitation wavelength and acquired sequentially to minimise bleed-through at an emission wavelength of 500−545 and 590−635 nm, respectively. The data were exported to ImageJ 1.48 (National Institute of Health, U.S.A.) for contrast enhancement and were assembled for colocalisation.

2.2.13 Statistical analyses

Data were analysed using GraphPad Prism 5.0b (GraphPad Software, La Jolla, CA, U.S.A.). Sample pairs were analysed with the Student's t test. Multiple samples were evaluated by one-way analysis of variance (ANOVA) followed by Bonferroni's multiple comparison post hoc test or Dunnett's post hoc tests to compare between the control and samples. An asterisk denotes statistical significance as follows: *$P < 0.05$, **$P < 0.01$, ***$P < 0.001$. All data are presented are as mean values ± standard deviation (SD) and the number of independent experiments (n) is noted in each figure legend.

2.3 Results

2.3.1 Characterisation of native and PEGylated silk nanoparticles

Regenerated silk solution was prepared and subsequently added dropwise to acetone to generate silk nanoparticles via nanoprecipitation (Figure 2.6). Nanoprecipitation generated uniform silk nanoparticles that were of a spherical size (104.20 nm ± 1.7, polydispersity 0.11) and had a net negative charge, resulting in a zeta potential of −56.38 mV ± 5.6 in water (Table 2.1). The presence of amine, hydroxyl and imidazole groups in the silk's primary structure rendered this biopolymer amenable to TsT-activated mPEG conjugation (Figure 2.7A). Here, silk nanoparticles were PEGylated using activated PEG and the process was tailored to maximise yields. Pilot studies used a constant weight-based 1:1 ratio of activated PEG to silk nanoparticles, employing 20 mg and 50 mg silk nanoparticle batch sizes. The amount of surface-grafted PEG was significantly higher ($P < 0.05$) for the 50 mg silk nanoparticle batch (19.4 % ± 1.93) than for the 20 mg batch (12.1 % ± 2.2; Figure 2.7B). Therefore, a 50 mg silk nanoparticle batch size was routinely used for all subsequent studies. In addition to spectrophotometric measurements to quantify PEGylation, the impact of PEGylation on particle size and zeta potential was measured (Table 2.1). PEGylation significantly increased the apparent size of the silk nanoparticles from 104.2 to 116.4 nm (Figure 2.7C) and significantly decreased the negative surface charge from −56.38 to −46.71 mV (paired t test, $P < 0.001$; Table 2.1).

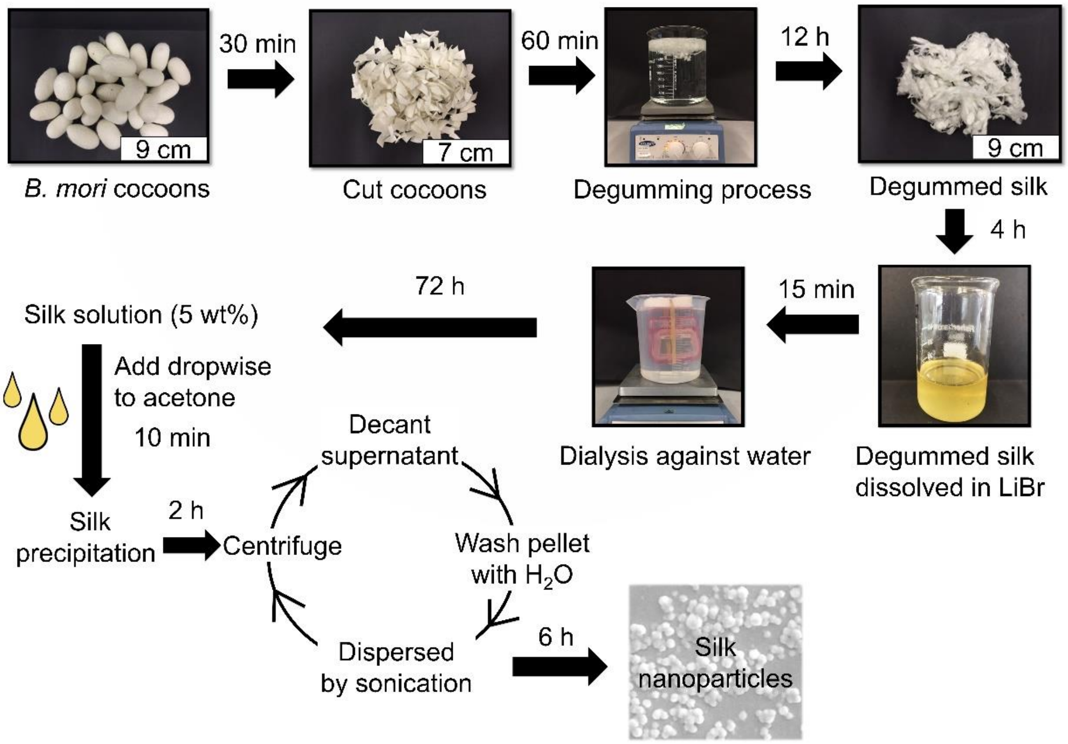

Figure 2.6 The key steps to generate a reverse engineered silk solution and silk nanoparticles. First, silk cocoons are reverse engineered by cutting and then degumming them for 60 min (i.e. boiling) to yield degummed silk fibres. The fibres are dissolved in 9.3 M LiBr and then dialysed against water for 72 h. An aqueous 5% w/v silk solution is used to generate silk nanoparticles. The dropwise addition of silk into acetone leads to silk nanoprecipitation. Silk nanoparticles are washed and collect for subsequent use.

Table 2.1 Summary of silk nanoparticle characteristics[a]

Samples	Particle size (nm)	PDI	Zeta potential[b] (mV)
SNPs	104.20 ± 1.70	0.11 ± 0.01	-56.38 ± 5.60
PEG-SNPs	116.40 ± 3.23	0.12 ± 0.02	-46.71 ± 2.59

[a]Data sets are ±SD, n ≥ 3. [b]Measurement were performed in ultrapure water

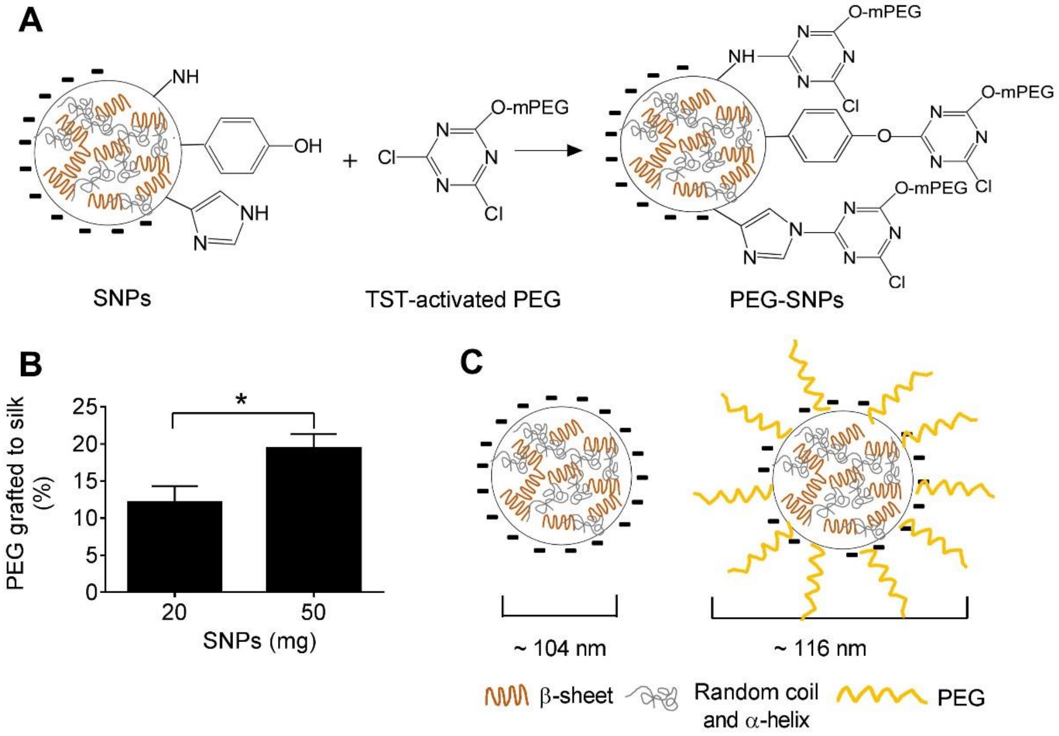

Figure 2.7 Formation and characterisation of PEGylated silk nanoparticles. (A) Reaction between activated PEG and the silk nanoparticle surface. (B) PEG grafting efficiency (%) to the silk nanoparticle surface for 20 and 50 mg/mL batches (equivalent to 20 and 50 mg of silk, respectively). An asterisk denotes statistical significance as follows: *P < 0.05, **P < 0.01, ***P < 0.001. The data represents the mean ± SD, n = 3. (C) Schematic representation of native (left) and PEGylated silk nanoparticles (right). Diagram not drawn to scale.

2.3.2 Surface analysis of native and PEGylated silk nanoparticles

Zeta potential measurements over a range of pH using 0.01 M PBS were used to study surface charge characteristics of native and PEGylated silk nanoparticles. The zeta potentials of PEGylated silk nanoparticles were not substantially different over the pH

4.5−8.5 range. In contrast, the surface charges of unmodified silk nanoparticles were sensitive to ion exchange; this was evident as they became more strongly charged at higher pH values (Figure 2.8A). The FTIR spectra of the amide I region of native and PEGylated silk nanoparticles were compared to untreated and autoclaved silk films and PEG (Figure 2.8B) serving as negative and positive controls for β-sheets, respectively. The PEGylated silk nanoparticle secondary structure was dominated by β-sheets. In turn, PEGylated silk nanoparticles had the lowest α-helices and turns content of all studied samples. Overall, spectra of native and PEGylated silk nanoparticles showed a high β-sheet content and substantially lower α-helix and random coil structures when compared to untreated, water-soluble silk films (Figure 2.8B).

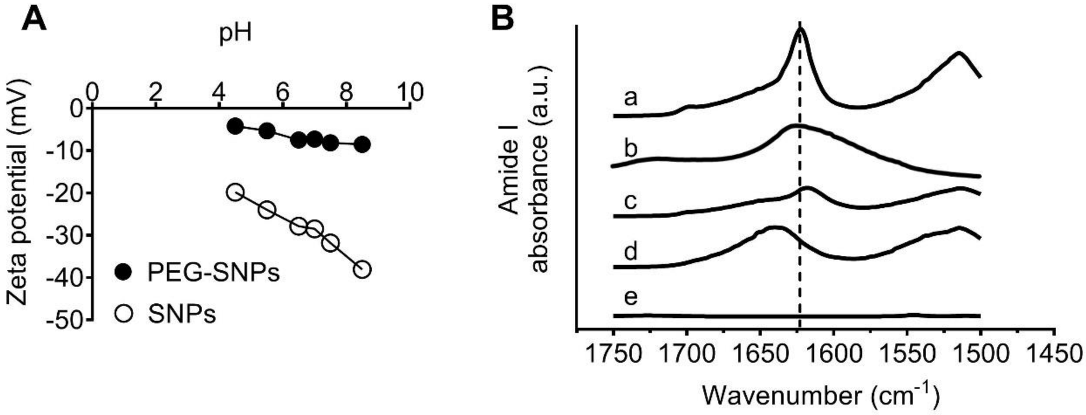

Figure 2.8 Characteristics of native and PEGylated silk nanoparticles. (A) Zeta potential measurements for silk nanoparticles in 0.01 M PBS at pH 4.5 to 8.5. (B) FTIR absorbance spectra of native and PEGylated silk nanoparticles and reference samples: (a) PEGylated silk nanoparticles; (b) silk nanoparticles; (c) autoclaved silk film; (d) untreated silk film; and (e) PEG. Dashed line indicates β-sheet.

2.3.3 PEGylated silk nanoparticles: modulating macrophage response

The macrophage response to native and PEGylated silk nanoparticles was determined by quantifying the secreted amounts of TNF-α in the culture medium (Figure 2.9). While native silk nanoparticles induced a significant amount of TNF-α release, PEGylated silk nanoparticles showed no differences in secreted TNF-α levels when compared to negative control macrophages. Overall, the highest macrophage response was observed for LPS stimulated cells.

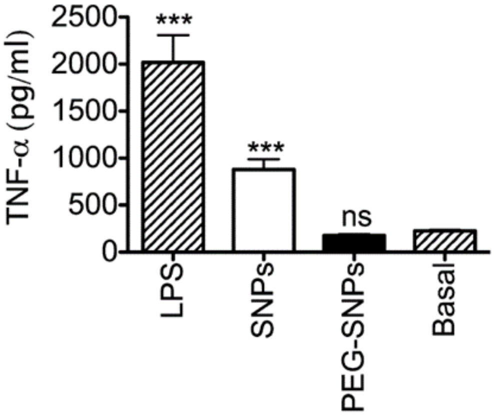

Figure 2.9 Macrophage response to silk nanoparticles. Quantification of TNF-α in culture supernatants following 24 h exposure to 5 ng of lipopolysaccharide (LPS, positive control), 50 μg of native or PEGylated silk nanoparticles, and untreated control cells (basal TNF-α levels). An asterisk denotes statistical significance as follows: *P < 0.05, **P < 0.01, ***P < 0.001. The data represents the mean ± SD, error bars are hidden in the plot-symbol when not visible, n = 3.

2.3.4 Drug loading of native and PEGylated silk nanoparticles

Pilot studies were conducted using 200 nmol propranolol HCl and 2, 5, and 10 mg silk nanoparticles to determine silk's loading and encapsulation efficiency (Figure 2.10A, B). The encapsulation efficiency of 2 mg silk was 46%, which was significantly lower than that of 5 mg and 10 mg of silk nanoparticles, where 93% and 98% of the drug was adsorbed, respectively (Figure 2.10B). No statistically significant difference was found between 5 and 10 mg silk nanoparticles, so all subsequent studies were conducted with 5 mg silk nanoparticles (i.e. 1.1% w/w drug loading capacity). The overall propranolol HCl loading profile for 5 mg of silk nanoparticles indicated a 50% encapsulation efficiency for 1420 nmol propranolol HCl (Figure 2.11). Next, the loading capacity of PEGylated silk nanoparticles was determined. A 5 mg sample of PEGylated silk nanoparticles showed significantly better propranolol HCl loading than 2 mg of PEGylated silk nanoparticles (Figure 2.10B). The use of 5 mg of PEGylated silk nanoparticles increased the loading efficiency for propranolol HCl from 93 to 98% when compared to native silk nanoparticles (Figure 2.10B). The use of 5 mg of both native and PEGylated silk nanoparticles resulted in loading of 100% of 200 nmol doxorubicin HCl (Figure 2.10C).

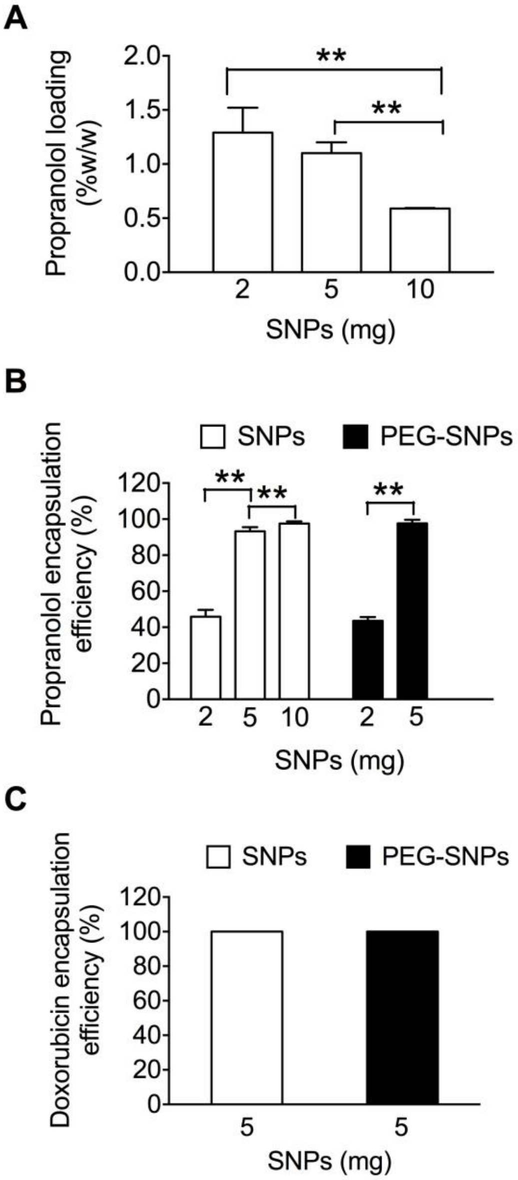

Figure 2.10 Characterisation of the loading capacity of native and PEGylated silk nanoparticles. (A) Loading efficiency (% w/w) and (B) encapsulation efficiency (%) for propranolol HCl in relation to different amounts of silk nanoparticles. (C) Ability of native and PEGylated silk nanoparticles to adsorb doxorubicin. An asterisk denotes statistical significance as follows: *P < 0.05, **P < 0.01, ***P < 0.001. The data represents the mean ± SD, error bars are hidden in the plot-symbol when not visible, n = 3.

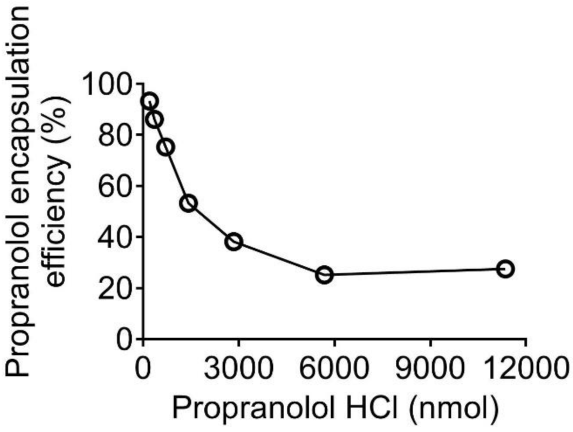

Figure 2.11 Encapsulation efficiency of 5 mg native silk nanoparticles over a range of propranolol HCl amounts. The data represents the mean ± SD, error bars are hidden in the plot-symbol when not visible, n = 3.

2.3.5 *In vitro* cytotoxicity

The ability of drug-loaded silk nanoparticles to deliver doxorubicin and subsequently kill cancer cells was assessed *in vitro*. Human breast cancer MDA-MB-231 cells were exposed to silk nanoparticles, freely diffusible doxorubicin HCl or doxorubicin-loaded silk nanoparticles. Cell viability was assessed after a 72 h exposure period. The IC_{50} values of freely diffusible doxorubicin and doxorubicin-loaded silk nanoparticles were 0.48 µg/mL and 0.24 µg/mL, respectively while the silk nanoparticles had an $IC_{50} > 5$ mg/mL (Figure 2.12A). At equivalent drug doses of 0.1 µg, freely diffusible doxorubicin and doxorubicin-loaded silk nanoparticles caused significant decreases in cell viability of 83% ± 11 and 65% ± 11, respectively (Figure 2.12B). However, freely diffusible doxorubicin showed a substantial greater cytotoxicity than doxorubicin-loaded silk nanoparticles. These quantitative measurements were corroborated by qualitative SEM imaging (Figure 2.12C). Here, control cultures showed high cellular density and a predominating mesenchymal MDA-MB-231 phenotype; similar observations were made for cultures exposed to silk nanoparticles. However, cultures exposed to doxorubicin showed a markedly different cell phenotype. At the equivalent doxorubicin dose, MDA-MB-231 cells treated with freely diffusible doxorubicin and doxorubicin-loaded silk nanoparticles showed a substantial reduction in cell numbers. Furthermore, many cells had a very broad and spread out morphology. Cultures exposed to doxorubicin-loaded silk nanoparticles showed evidence of nanoparticles (and their aggregates) associated with the plasma membrane (Figure 2.12C).

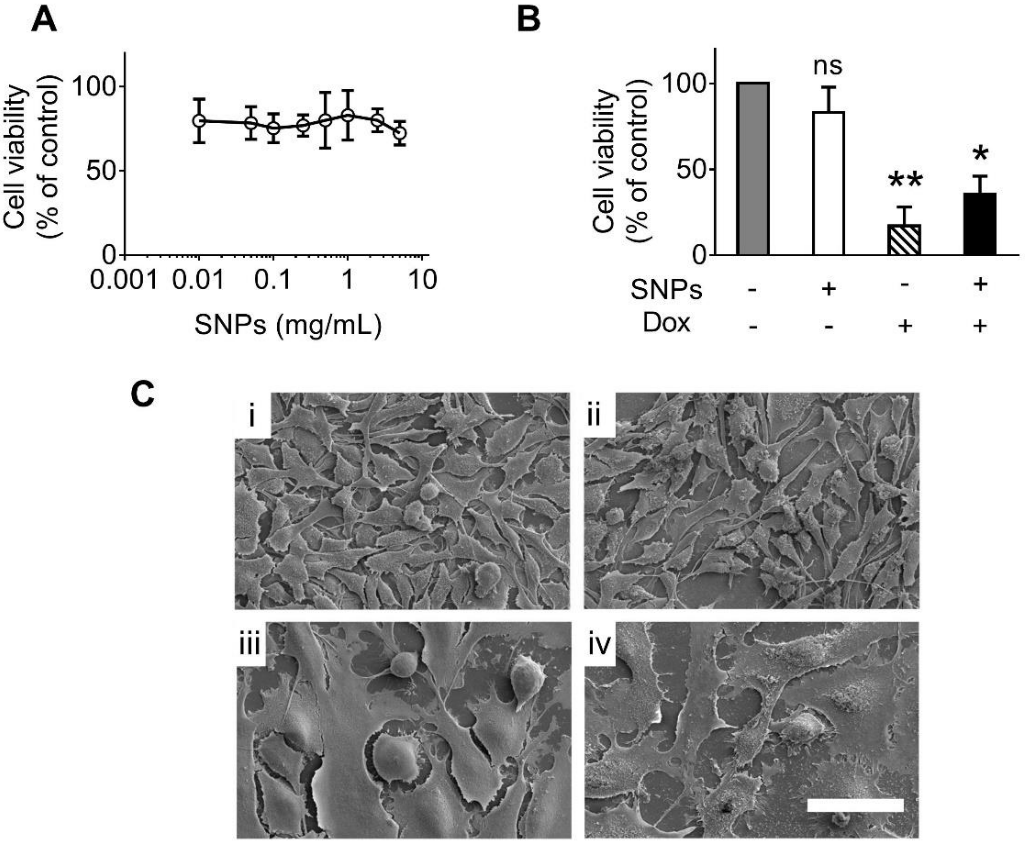

Figure 2.12 *In vitro* cytotoxicity of silk nanoparticles and doxorubicin-loaded silk nanoparticles in MDA-MB-231 human breast cancer cells. (A) Cell viability of MDA-MB-231 cells after a 72 h treatment cycle with silk nanoparticles (SNPs) (0.01-5

mg/mL containing 0.001-0.5 mg SNPs). (B) Cell viability of MDA-MB-231 cells after a 72 h treatment cycle with 0.1 mg silk nanoparticles, 0.1 µg of freely diffusible doxorubicin HCl (Dox) or 0.1 mg of silk nanoparticles loaded with 0.1 µg of doxorubicin HCl (Dox-SNPs). (C) SEM images of MDA-MB-231 cells exposed to (i) medium (control), (ii) 0.1 mg silk nanoparticles, (iii) 0.1 µg of freely diffusible doxorubicin, and (iv) doxorubicin-loaded silk nanoparticles at equivalent doses (scale bar = 50 µm). An asterisk denotes statistical significance as follows: $^{*}P < 0.05$, $^{**}P < 0.01$, $^{***}P < 0.001$. The data represents the mean ± SD, error bars are hidden in the plot-symbol when not visible, $n = 3$.

Next, the cytotoxicity of native and PEGylated silk nanoparticles were determined using MCF-7 human breast cancer cells (Figure 2.13A, B); both nanoparticle types had an $IC_{50} > 5$ mg/mL. Silk nanoparticles loaded either with propranolol HCl or doxorubicin HCl were assessed as monotherapy and as a combination therapy. As controls, analogous experiments with equivalent dose levels and combinations were performed with unbound, freely diffusible drug. Dose−response curves were established for the freely diffusible drugs and IC_{50} was calculated for each drug (Figure 2.14A). These IC_{50}s were used to assess freely diffusible drug combinations with an isobologram and gave a subsequent CI value of 0.94 for the doxorubicin (0.01 µg) and propranolol (2.1 µg) drug combination (Figure 2.14B).

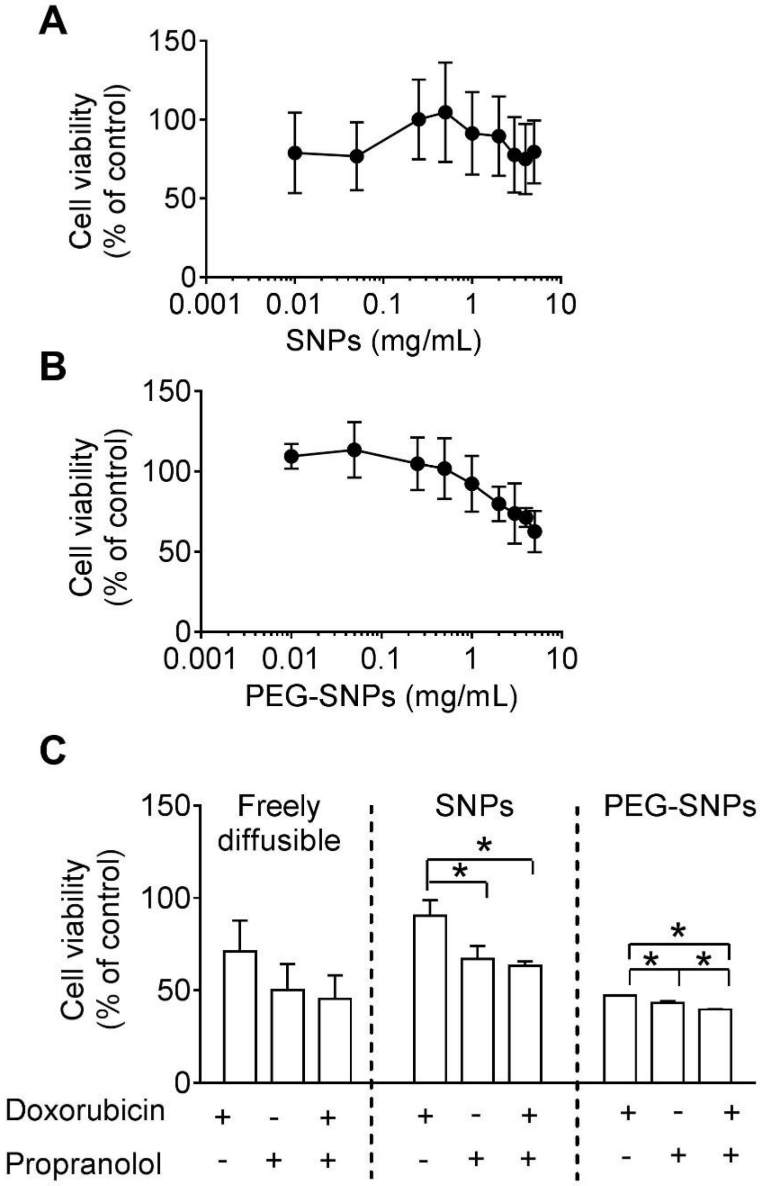

Figure 2.13 *In vitro* cytotoxicity of silk nanoparticles against MCF-7 human breast cancer cells. The MCF-7 cells were exposed for 72 h to (A) silk nanoparticles, (B) PEGylated silk nanoparticles, and (C) doxorubicin HCl (0.01 μg) and propranolol HCl (2.1 μg) drug combination of freely diffusible and nanoparticle delivered drug combinations. An asterisk denotes statistical significance as follows: *P < 0.05, **P < 0.01, ***P < 0.001. The data represents the mean ± SD, error bars are hidden in the plot-symbol when not visible, n = 3.

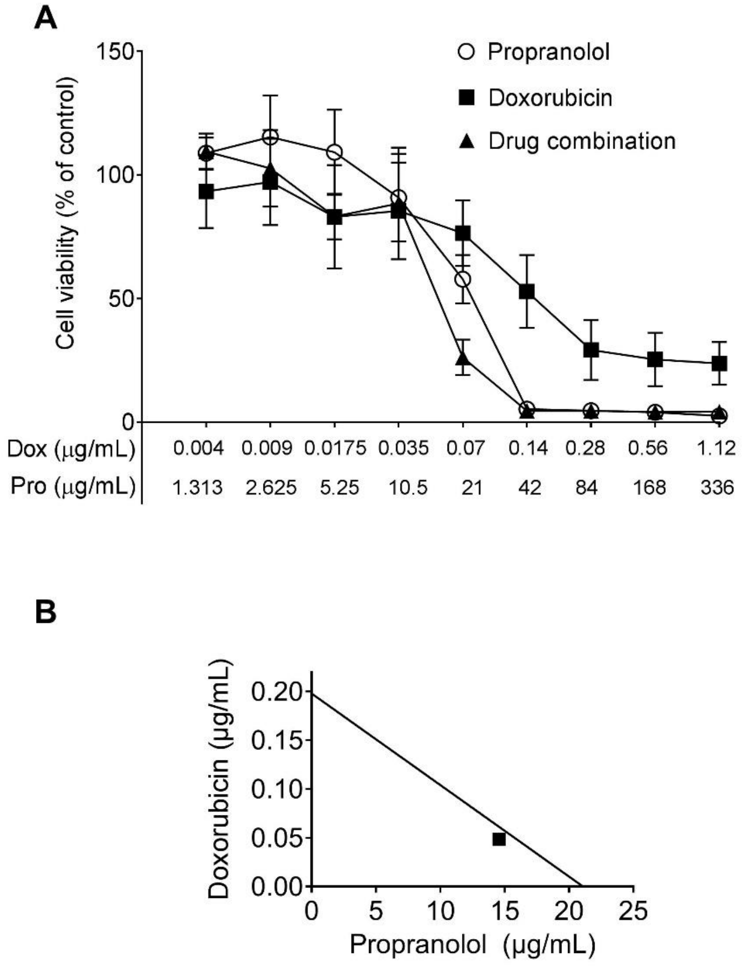

Figure 2.14 *In vitro* cytotoxicity of freely diffusible doxorubicin HCl, propranolol HCl and drug combinations against MCF-7 breast cancer cells. (A) Growth inhibitory effect of combination of doxorubicin and propranolol in MCF-7 cell lines after 72 h exposure. (B) Isobologram of doxorubicin and propranolol. Experimental data point represented by square located close to the additive line; for doxorubicin (0.1 μg/mL containing 0.01 μg doxorubicin HCl) and propranolol (21 μg/mL containing 2.1 μg propranolol HCl) drug combination. The data represents the mean ± SD, error bars are hidden in the plot-symbol when not visible, n = 3.

The data sets obtained for freely diffusible drug combinations were then used to inform nanoparticle studies. First, silk nanoparticles were loaded with either propranolol HCl or doxorubicin HCl, next drug loaded silk nanoparticles were mixed to yield the most promising drug combination (i.e., 0.01 μg doxorubicin HCl and 2.1 μg propranolol HCl) that was then tested *in vitro*. The combination of propranolol- and doxorubicin-loaded silk nanoparticles significantly reduced cell viability when compared to the equivalent amount of doxorubicin (Figure 2.13C). The greatest reduction in cell viability was observed for drug loaded PEGylated silk nanoparticles; they outperformed the freely diffusible treatment groups and showed a significant greater cytotoxicity than drug loaded native silk nanoparticles (Figure 2.13C). These cytotoxicity measurements were underpinned by SEM analysis of MCF-7 (Figure 2.15). Cells exposed to doxorubicin- and propranolol-loaded native and PEGylated silk nanoparticles showed substantial morphological changes when compared to control cells (Figure 2.15A−H). Control MCF-7 cells had a large number of plasma membrane microvilli (Figure 2.15E, I) that were not found in drug-treated cells; overall, the drug-treated cells had a smoother appearance (Figure 2.15F−H), with evidence of plasma membrane-associated native and PEGylated silk nanoparticles (Figure 2.15G, H). SEM images were quantitatively analysed by determining the number of cell neighbours (Figure 2.15J). Cells treated with either freely diffusible drug or the silk nanoparticle−drug combination showed a similar reduction in neighbouring cells when compared to untreated cells (Figure 2.15J).

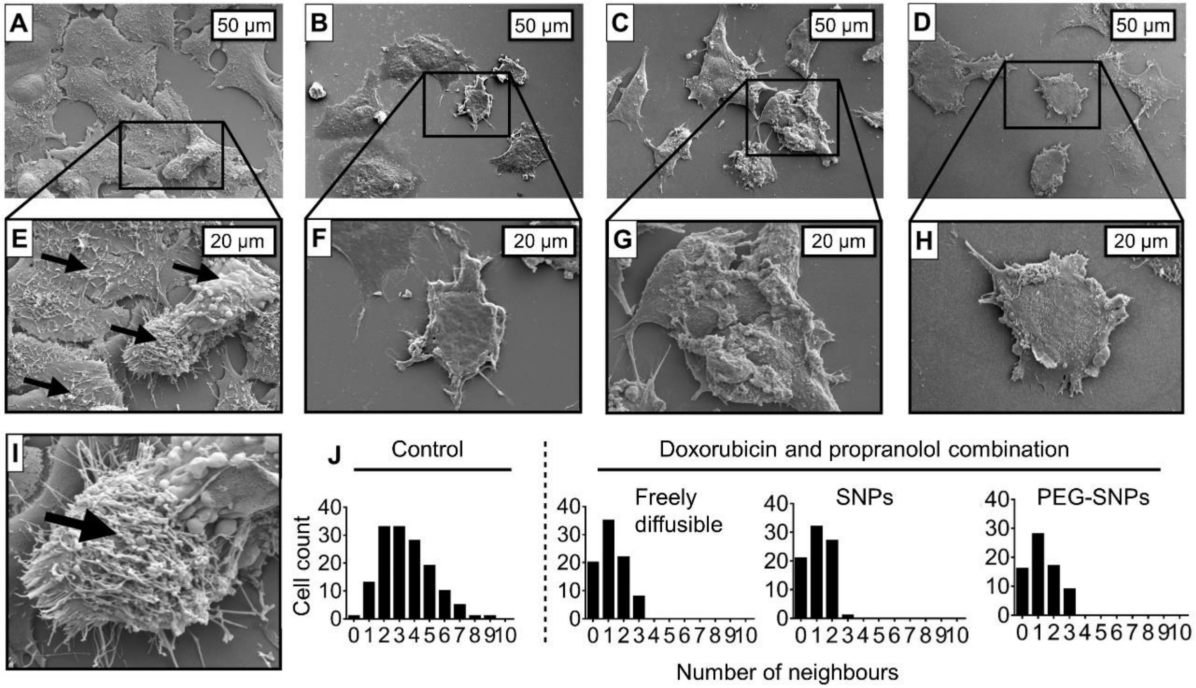

Figure 2.15 Scanning electron microscopy of human breast cancer cells exposed to drug combinations. (A, E, I) MCF-7 control cells displaying typical cluster-like arrangements with plasma membrane microvilli (arrows E and I). Cells treated with the drug combination of (B, F) freely diffusible propranolol (2.1 μg) and doxorubicin (0.01 μg) and the drug combination at the equivalent amounts delivered using (C, G) native and (D, H) PEGylated silk nanoparticles. (J) Qualitative analysis of cell neighbours; MCF-7 control cells, cells treated with the freely diffusible drug combination, and the drug combination at the equivalent doses delivered using silk nanoparticles.

2.3.6 Cellular uptake of native and PEGylated silk nanoparticles

The intracellular distribution of doxorubicin-loaded native and PEGylated silk nanoparticles was visualised by confocal live cell imaging. Native silk nanoparticles had a propensity to form aggregates in the culture medium, resulting in substantial amounts of doxorubicin-loaded silk nanoparticles attaching to the cell plasma membrane (Figure 2.16A). Nonetheless, cytoplasmic doxorubicin and both doxorubicin- and nanoparticle-associated fluorescence were evident in endocytic vesicles (Figure 2.16A−D). In contrast, doxorubicin-loaded PEGylated silk nanoparticles showed no aggregation and extensive perinuclear accumulation was evident in endocytic vesicles following a 5 h incubation. Furthermore, tracking of the doxorubicin-associated fluorescence showed substantial doxorubicin-associated fluorescence in the nucleus (Figure 2.16G), but no nanoparticle-associated fluorescence (Figure 2.16F).

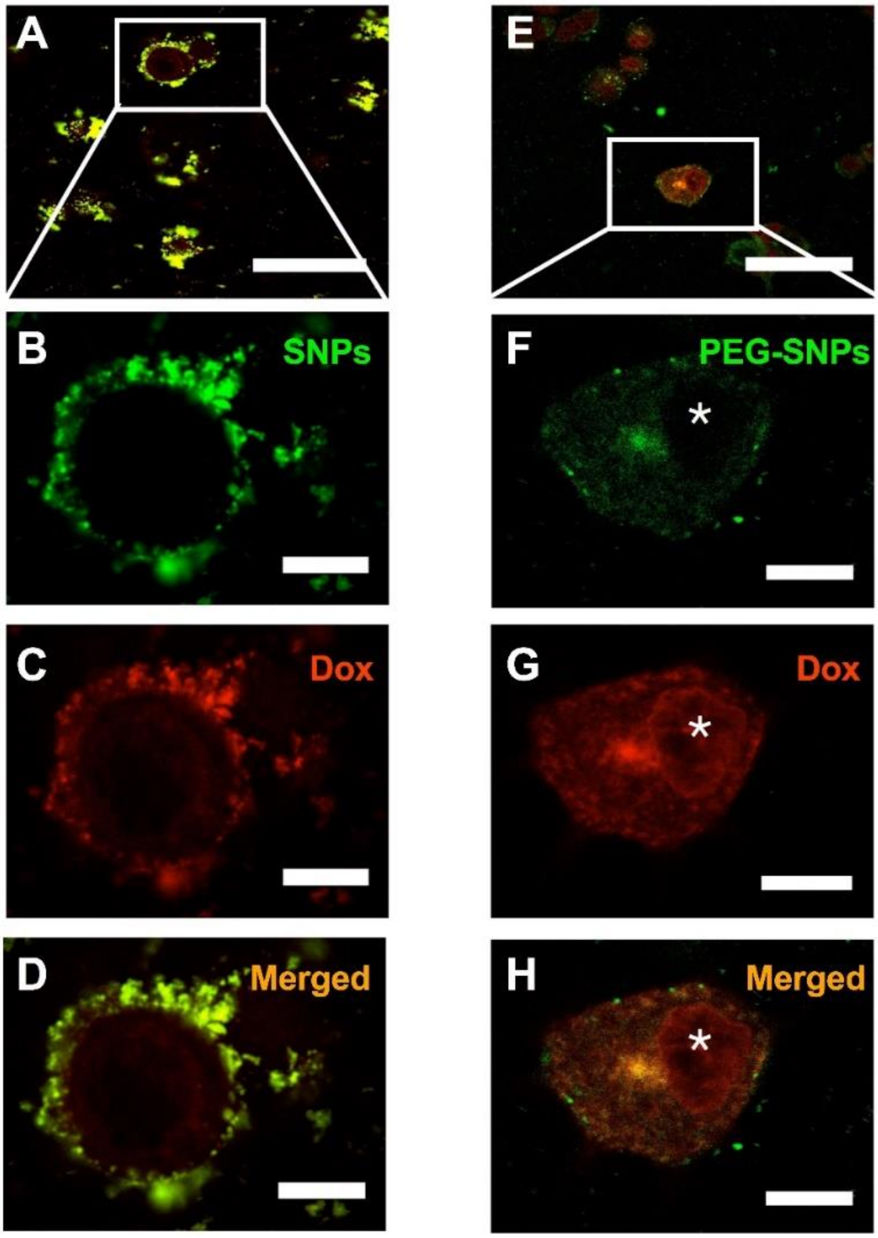

Figure 2.16 Live cell confocal fluorescence microscopy of doxorubicin loaded native and PEGylated silk nanoparticles in MCF-7 cells. Cells were incubated with Alexa Fluor 488 labelled nanoparticles for 5 h and imaged for doxorubicin-associated and nanoparticle-associated fluorescence. (A−D) Doxorubicin-loaded native silk nanoparticles and (E−H) PEGylated silk nanoparticles. Asterisk (*) denotes doxorubicin accumulation in the nucleus. The scale bars for low and high magnification are 10 and 50 µm, respectively.

2.4 Discussion

Cancer therapy typically uses drug combinations to maximise clinical outcomes. Many anticancer drugs are small molecular weight compounds, where pharmacokinetics, tissue distribution, intracellular drug concentrations and elimination are governed by the physicochemical properties of the drug. Drug administration is typically based on the maximum tolerated dose and drug combinations are often concocted using this principle. However, emerging evidence suggests that cellular drug concentrations are critical for maximising any synergistic effects, because drug combinations can vary from antagonistic to synergistic (Cortes et al., 2015). For example, CPX-351 (Vyxeos, Jazz Pharmaceuticals), a liposomal formulation containing the synergistic 5:1 cytarabine/daunorubicin molar ratio, has been approved by FDA in 2017 for the treatment of adults with acute myeloid leukaemia (AML) (Cortes et al., 2015; Talati and Lancet, 2018). The use of this macromolecular drug carrier approach endows the payload with a predesigned whole body, organ, cellular, and subcellular pharmacokinetic profile.

Besides using drugs that have known anticancer indications, an effort is ongoing to repurpose other drugs for use in oncology (Pantziarka et al., 2015). Emerging evidence indicates that β-adrenergic signalling regulates multiple cellular processes, including cell proliferation, differentiation, and migration pathways that are implicated in cancer. Epidemiological studies also suggest that β-blockers favourably affect cancer progression and metastasis in patients (Ji et al., 2012). Therefore, this chapter set out to determine the ability of silk nanoparticles to deliver both propranolol and doxorubicin in combination. However, the development of a combination nanomedicine that would also be applicable in *in vivo* applications first required refinement of the carrier to minimise MPS accumulation.

PEGylation is one of the most popular ways to modify biomaterial surfaces. PEG is frequently used to modify macromolecular drug carriers such as nanoparticles and liposomes, as well as proteins, antibodies and aptamers (Pasut and Veronese, 2012; Rabanel et al., 2014). The overall result of PEGylation is an improved pharmacokinetic profile when compared to the unmodified parent molecule. PEGylated macromolecules have been used clinically for more than 20 years with a remarkable safety track record (Webster et al., 2006). PEG is non-biodegradable and predominately eliminated via urinary clearance; therefore, the selected molecular weight must be below the renal threshold (typically < 30000 g/mol) to ensure adequate elimination (Webster et al., 2006).

A linear 5000 g/mol PEG was used because many clinical products employ this type of PEG molecule (Greenwald et al., 2003; Webster et al., 2006). Cyanuric chloride-activated PEG (5000 g/mol) has previously been surface-crafted for macro-scale silk films (18.9 cm^2) using a reaction of cyanuric chloride to the amine and hydroxyl groups of silk (Vepari et al., 2010) at a 1:2.5 silk:PEG ratio; this resulted in a grafting efficiency of 3.5%. These PEG grafted silk films displayed low cell adhesion when compared to the unmodified silk surface (Vepari et al., 2010).

In pilot studies both the silk:PEG ratio and the actual concentration of silk nanoparticles used during the conjugation reaction were varied. Here, a 1:1 silk/PEG ratio and a 50 mg silk nanoparticle batch size were selected, which resulted in a 19.39% grafting efficiency (Figure 2.7B). Although these conditions are quite different from the work reported for silk films (Vepari et al., 2010), the final results are not surprising; the nanoscale nature of our particles substantially increases the relative surface area to mass and the overall dynamics of the conjugation reaction. Successful PEG grafting was determined by physical measurements of nanoparticle size (104 nm and 116 nm for native and PEGylated silk nanoparticles, respectively) and zeta potential (−56 mV to −45 mV for native and PEGylated silk nanoparticles in ultrapure water, respectively). These results are in line with the values reported in the literature because PEG is known to increase the apparent particle size and to shield surface charges (Rabanel et al., 2014), leading to a reduced zeta potential. Surface-tethered PEG can adopt different configurations. For example, high PEG grafting densities typically lead to a brush-like conformation, while lower densities result in a mushroom-like conformation (Rabanel et al., 2014). These different conformations are reflected in hydrodynamic layer thickness measurements. The radius of gyration (R_g) for PEG 5000 g/mol is 2.8 nm (Thierry and Griesser, 2012), and in the present study, the measured hydrodynamic layer thickness was >2-fold the R_g. This suggested that the most likely conformation of PEG chains extending from the surface of silk nanoparticles adopted a brush conformation (Thierry and Griesser, 2012). Although PEG reduced the zeta potential, the retention of some negative surface charge is desirable to provide sufficient electrostatic repulsion to prevent nanoparticle aggregation during storage and handling in addition to PEGs' ability to stabilise nanoparticles. Surface-grafted PEG typically results in a more neutral zeta potential of nanoparticles (reviewed in Rabanel, Hildgen and Banquy, 2014); for example, PEGylated poly(lactic-coglycolic acid) copolymer (PLGA) nanoparticles showed effective charge reduction across a broad pH range (Stolnik et al., 1994). In the present study, the surface of PEG-modified silk nanoparticles was effectively shielded from protonation and deprotonation over the studied pH range; an observation that was not made with native silk nanoparticles (Figure 2.8A). Because the zeta potential is dependent on the solvent system used, the measured zeta potentials are different for those reported in Table 2.1 and Figure 2.8A.

PEGylation to synthetic nanoparticles is typically supported by FTIR and/or NMR analysis (Rabanel et al., 2014). Successful verification of this type of covalent linkage for the biopolymer silk is a recognised challenge (Murphy and Kaplan, 2009); this also includes the reaction of cyanuric chloride-activated PEG with silk (Vepari et al., 2010). Furthermore, cryo-transmission electron microscopy studies performed on my behalf by Dr Petr Formanek (Leibniz Institute of Polymer Research Dresden, Germany) did not show a PEG corona; these are typically only seen for PEG > 20,000 g/mol and thus the absence of the corona here was expected (in hindsight). Although the lack of FTIR and NMR measurements is a limitation of the current study, the evidence presented (Table 2.1, Figure 2.7 and 2.8A) strongly suggests the successful covalent grafting of PEG onto silk nanoparticles.

Next, the macrophage response toward silk nanoparticles was assessed. Previous studies have clearly demonstrated that TNF-α release from macrophages in response to nanoparticles is a valuable marker for assessing the status of the MPS (Thomas et al., 2012; Pondman et al., 2014; Bancos et al., 2015). The amount of TNF-α measured for the positive control was several fold higher than the levels determined for native silk nanoparticles (Figure 2.9), whereas the macrophage response to native silk nanoparticles was comparable to that observed with PLGA nanoparticles (data not shown). More importantly, PEGylation of silk nanoparticles reduced the TNF-α amounts to levels seen with the untreated resting macrophages (Figure 2.9). This clearly demonstrated that PEGylation of silk nanoparticles further improved their biocompatibility; the applied “stealth” technology successfully evaded the MPS system using the TNF-α assay as a marker.

Next, the ability of PEGylated silk nanoparticles to bind drugs was assessed. Silk carries a negative charge at pH 7.4 in both native and PEGylated form, as verified here, which facilitates loading of positively charged drugs via electrostatic interactions leading to an overall reduced zeta potential (data shown in MRes thesis) (Wongpinyochit, 2014). Propranolol HCl (pKa 9.1) and doxorubicin HCl (pKa 8.3) are weakly basic drugs that are protonated at a pH below their respective pKa values. The Scheibel laboratory demonstrated that the distribution coefficient (log D) and diffusion coefficient (log D MW^{-1}) are two useful parameters for estimating the loading and encapsulation efficiency of weakly basic, small molecular weight molecules onto recombinant spider silk (eADF4(C16)) particles (Lammel et al., 2011). Log D is a useful indicator for predicting physical properties because it is based on the calculated ratio of unprotonated and protonated states of a molecule in octanol (hydrophobic) and water (hydrophilic), which in turn relates to both log P and pKa of the payload molecule.

The presented experiments supported the conclusion that eADF4-(C16) particle loading was best for weakly basic payloads with a high log D and diffusion coefficient (expressed by the inverse proportionality of molecular weight). However, silk nanoparticles showed a greater encapsulation efficiency for doxorubicin HCl than for propranolol HCl at pH 7.4 despite a lower log D 0.35 and log D MW^{-1} 6×10^{-4} values than propanol's log D 1.47 and log D MW^{-1} 5×10^{-3} values. This discrepancy is likely due to structural differences between *B. mori* silk and spider silk eADF4(C16). *B. mori* silk consists of hydrophilic blocks in the heavy chain with negative charges while spider silk eADF4(C16) is very hydrophobic due to its lack of hydrophilic spacers in the silk backbone (Lammel et al., 2011). Therefore, structural differences in *B. mori* silk are likely to affect drug loading through a number of mechanisms, including hydrophilic−hydrophilic interactions and π−π stacking of adsorbed doxorubicin HCl resulting in high encapsulation efficiency. The work with eADF4(C16) (Lammel et al., 2011) and this *B. mori* silk nanoparticle study used an equivalent amount of propranolol HCl. However, *B. mori* silk nanoparticles gave a 93% propranolol HCl encapsulation efficiency while eADF4(C16) particles encapsulated only 45%. This discrepancy could be due to structural differences of the silks; this is also supported by the relatively high negative zeta potential (−56 mV) of *B. mori* silk when compared to the low negative zeta potential (−22 mV) of eADF4(C16) of spider silk. Therefore, *B. mori* silk nanoparticles are expected to have a better drug loading capacity than eADF4(C16) spider silk systems. Overall, native and PEGylated *B. mori* silk nanoparticles showed low drug loading capacity which, without further improvement, is not suitable for *in vivo* studies.

Next, human breast cancer cells were used to examine the ability of drug-loaded silk nanoparticles to deliver single and combination drugs. Emerging evidence suggests that propranolol has anticancer properties and synergistic effects are observed with chemotherapy. Furthermore, *in vitro* studies indicated that these effects were dose-dependent and cell-type specific (Pasquier et al., 2011). For example, increasing the concentration of 5 nM paclitaxel to 10 nM could modify the interaction effect from subadditive to synergistic in MCF-7 human breast cancer cells when combined with 10−50 μM propranolol (Pasquier et al., 2011); MCF-7 cells are luminal A with an immunoprofile of ER^+, $PR^\pm$, and $HER2^-$ (Holliday and Speirs, 2011). However, this synergistic effect of paclitaxel and propranolol was not observed with HBL-100 cells (a putative human “breast cancer cell line” that has been discontinued) or SK-BR-3 (invasive ductal carcinoma, ER^-, PR^-, HER^+), where an antagonist dose−response was evident (Pasquier et al., 2011). Based on these data, MCF-7 cells were used to examine the biological response of doxorubicin and propranolol drug combinations. Additionally, doxorubicin-loaded silk nanoparticles exposed to MDA-MB-231 cells were examined. These cells are derived from a highly invasive triple negative breast cancer (ER-/PR-/HER2-) that is difficult to treat in the clinic (Holliday and Speirs, 2011). Therefore, designing a drug delivery system tailored to this patient population is expected to yield tremendous benefits.

For MDA-MB-231 cells, in the absence of drug loading, silk nanoparticles did not affect cell viability (IC_{50} values > 5 mg/mL) (Figure 2.12A, C). However, at equivalent doses, significantly greater cytotoxicity was observed with freely diffusible doxorubicin than with doxorubicin-loaded silk nanoparticles (Figure 2.12B). The differences between the *in vitro* cellular pharmacokinetics of freely diffusible and particle bound drug explain this observation. The freely diffusible drug can rapidly cross the plasma membrane via diffusion, whereas uptake of the drug-loaded nanoparticles relies on endocytosis. Nonetheless, endocytic uptake of nanoparticles can enhance drug retention and overcome drug resistance mechanisms (Davis et al., 2008). However, the true benefit of nanoparticle-mediated anticancer drug delivery is that it exploits the EPR effect to facilitate passive tumour targeting and to improve pharmacokinetics. Therefore, the use of a nanoparticle-based drug delivery approach can only be fully assessed *in vivo*. *In vitro* studies have limitations (i.e. the absence of the EPR-mediated targeting and an energy-dependent process that has a limited cargo uptake capacity) that preclude the full characterisation of these types of drug delivery systems (Duncan and Richardson, 2012).

For MCF-7 cells, freely diffusible drug combinations showed no synergism but an additive anticancer effect (Figure 2.14); a similar observation was made for silk nanoparticle combinations. The lack of synergism is a limitation of the present study and requires additional optimization to uncover the full potential of silk nanoparticles for combination therapy. Nonetheless, combination therapy significantly reduced cell viability when compared to single drug treatment (Figure 2.13) and changed MCF-7 morphology and organization (Figure 2.15). Overall, PEGylated silk nanoparticle outperformed native silk nanoparticles for the delivery of single and combination therapy. One possibility for this observation is that PEGylated silk nanoparticles did not aggregate and thereby enabled efficient endocytic uptake and subsequent lysosomal accumulation of the carrier (Figure 2.16). PEGylated silk nanoparticle delivering doxorubicin also induced greater cytotoxicity than freely diffusible controls at the equivalent doxorubicin concentration (Figure 2.13C). This observation is encouraging but unexpected. Typically nanomedicines designed for intracellular activation do not show their full potential *in vitro*.

This chapter reports preliminary uptake studies of silk nanoparticles into MCF-7 breast cancer cells using live cell confocal microscopy. Live cell imaging was preformed to minimise the fixation artefacts typically seen with doxorubicin (Seib et al., 2006). Furthermore, a 5 h incubation time was used to allow the accumulation of silk nanoparticles throughout the entire endocytic pathway. Default trafficking from the plasma membrane into lysosomes typically takes 1 h (Seib et al., 2007), so additional time was allowed to provide sufficient exposure of silk nanoparticles to the lysosomes. Emerging evidence indicates that the cellular uptake of the PEGylated nanoparticles can be decreased due to the steric interaction between grafted PEG chains and the cell membrane (Soenen et al., 2014). However, this study showed that PEGylated silk nanoparticles improved cellular uptake and lysosomotropic drug delivery compared to the native silk nanoparticles because PEGylation minimised silk nanoparticle aggregation in the culture medium and thereby modulated endocytic uptake and lysosomal trafficking of discrete silk nanoparticles (Figure 2.16 E−H). Nevertheless, the cellular uptake of PEGylated silk nanoparticles can be improved by conjugating PEG with targeting moieties such as cell-penetrating peptides (CPPs) (Nativo et al., 2008), arginylglycylaspartic acid (RGD) peptides (de la Zerda et al., 2012), or anti-HER2 antibodies (Wartlick et al., 2004).

2.5 Conclusion

In this chapter, PEGylated silk nanoparticles were developed, characterised and tested as a potential anticancer drug delivery system. PEGylated silk nanoparticles showed low drug loading and release capacity and were subsequently assessed for their *in vitro* antitumor efficacy. This chapter demonstrates the first example of silk nanoparticle combination therapy. These findings, when combined with prior *in vitro* data on silk, supported the assessment of the silk nanoparticle degradation; these data are reported in the following chapter.

Chapter 3

Degradation behaviour of silk nanoparticles – enzyme responsiveness

This chapter contains the results from the published article in ACS Biomaterials Science & Engineering (DOI:10.1021/acsbiomaterials.7b01021). For this work, I designed, analysed and carried out all experiments, as well as generated the manuscript draft.

3.1 Introduction

The biopolymer silk has a long clinical track record, as silk from domesticated silkworms (*B. mori*) has been used in medical applications for many centuries (Seib and Kaplan, 2013). Even today, silk remains the preferred material for specialised suture applications (e.g., eye surgery) (Seib and Kaplan, 2013) due to its exquisite handling and toughness (Holland et al., 2007; Omenetto and Kaplan, 2010). Recently, silk has been approved for human use in surgical meshes (Allergan Inc., USA) designed for soft tissue repair and reconstruction (Jewell et al., 2015). However, silk is also a promising biopolymer for emerging biomedical applications, because of (i) the extensive clinical experience with silk, (ii) the all-aqueous silk processing technology, (iii) the ability of silk to stabilise and protect therapeutic payloads, and (iv) the capacity to reverse engineer silk into films, scaffolds, hydrogels, and micro- and nanoparticles (reviewed in (Werner and Meinel, 2015; Seib, 2017b, 2017a). Silk nanoparticles can be surface decorated with polyethylene glycol (PEG) to improve colloidal stability in physiological fluids and to allow evasion of immune recognition (Wongpinyochit et al., 2015; Maitz et al., 2017) (Chapter 2).

Native and PEGylated silk nanoparticles (size approx. 100 nm) are often proposed for solid tumour drug targeting (reviewed in Seib, 2017b). Following intravenous dosing, these nanoparticles circulate in the blood, extravasate at the tumour site due to leaky blood vessels and accumulate due to impaired lymphatic drainage. This phenomenon is commonly referred to as the EPR effect (Matsumura and Maeda, 1986; Nakamura et al., 2015), but full clinical exploitation of the EPR effect remains to be realised (Wilhelm et al., 2016; Natfji et al., 2017). The payloads of nanoparticles can differ widely, but the nanoparticles must reach the tumour microenvironment and must often deliver the payload to a specific intracellular destination to elicit the desired pharmacological effect. For example, native and PEGylated silk nanoparticles are typically designed for lysosomotropic drug delivery (Seib, Pritchard, et al., 2013; Wongpinyochit et al., 2015); therefore, they need to traffic into lysosomes, where the low pH and lysosomal enzymes trigger payload release (Totten et al., 2017). However, the subsequent fate and the material properties of the native and PEGylated silk nanoparticles that accumulate within lysosomes is unknown.

The silk protein is considered biodegradable because it is sensitive to proteolytic enzymes (e.g., protease K, protease XIV, collagenase, and α-chymotrypsin) and enzyme-catalysed hydrolysis reactions (Altman et al., 2003). The hydrophilic amorphous segments within the silk heavy chain, as well as the C- and N-terminal sequences (which consist of completely non-repeating amino acid residues), are particularly susceptible to proteolytic degradation. The degradation of monolithic silk films (Meinel et al., 2005) and porous silk scaffolds (Wang et al., 2008) been studied extensively both *in vitro* and *in vivo.* However, the degradation behaviour is influenced by a number of factors, including (i) silk secondary structures (e.g., β-sheet content), (ii) silk format (e.g., monolithic film versus porous scaffold), (iii) exposure time, and

(iv) enzyme types (these vary among cells as well as subcellular locations) (Meinel et al., 2005; Wang et al., 2008; Rajkhowa et al., 2012; Brown et al., 2015).

The degradation products of silk-based biomaterials are expected to be non-cytotoxic (Cao and Wang, 2009). However, the enzymatic degradation behaviour of silk nanoparticles is poorly defined, especially for silk nanoparticles intended for lysosomotropic drug delivery. The goal of this chapter was therefore to investigate the degradation of native and PEGylated silk nanoparticles by monitoring the secondary structure, zeta potential, particle size, mass loss and morphology following exposure to protease enzymes (protease XIV and α-chymotrypsin) and a cysteine protease, papain, which resembles the mammalian lysosomal enzymes, cathepsins B, H, L, and S (Stoka et al., 2005). The morphology and particle size distribution of native and PEGylated silk nanoparticles were also examined following *ex vivo* exposure to enzymes from lysosomes isolated by subcellular fractionation of rat liver.

3.2 Materials and Methods

3.2.1 Preparation of reverse engineered silk solution

Silk was extracted from *B. mori* silk cocoons using a 60 min degumming time and was fully reverse engineered to yield an aqueous silk solution, as described in Chapter 2 (section 2.2.1).

3.2.2 Preparation of native and PEGylated silk nanoparticles

Silk nanoparticles were generated using nanoprecipitation and then were surface modified with TST-activated mPEG 5000, as described in Chapter 2 (section 2.2.2 and 2.2.3). The native and PEGylated silk nanoparticles were stored at 4 °C until use.

3.2.3 Degradation of native and PEGylated silk nanoparticles by protease enzymes and a lysosomal-like enzyme

Protease XIV from *Streptomyces griseus* (3.5 units per mg enzyme), α-chymotrypsin from bovine pancreas (40 units per mg enzyme), and papain (lysosomal-like enzyme) from *Carica papaya* latex (10 units per mg enzyme) were purchased from Sigma-Aldrich (St. Louis, MO, U.S.A.). The enzymatic activities were fixed at 3.5 enzyme units (U) for all subsequent degradation studies. Therefore, 1 mg/mL protease XIV, 0.0875 mg/mL α-chymotrypsin, and 0.35 mg/mL papain were freshly prepared by dissolving the respective enzyme powder in ultrapure water. The 10 mg/mL native and PEGylated silk nanoparticles were exposed to these enzymes, and the enzymes were recharged (i.e. keeping enzyme activity at 3.5 U) every five days for up to 20 days. All samples were incubated at 37 °C and analysed at 1, 3, 5, 10, and 20 days.

3.2.4 Isolation of lysosomes from rat liver using gradient centrifugation

The subcellular fractionation methods were based on published protocols (Graham, 1993). Briefly, three male Sprague-Dawley rats (typical weight 250 g) were sacrificed and the livers were immediately removed and kept on ice. Each rat liver was weighed and minced with scissors, pushed through a sieve and then transferred to a Potter-Elvehjem homogeniser with the homogenisation buffer (using 10 mL for every 2.5 g of wet tissue). The homogenisation buffer contained 0.25 M sucrose, 1 mM EDTA, 20 mM Hepes-NaOH, pH 7.4. The tissue homogenate was homogenised using 6 strokes of the pestle at 500–700 rpm. The homogenate was then fractionated by differential centrifugation. First, the homogenate was centrifuged at 1,000 x g for 5 min to pellet the nuclei. The supernatant was then collected and was centrifuged at 3,000 x g for 10 min to pellet the heavy mitochondrial fraction (HMF). Next, the supernatant was aspirated and centrifuged at 17,000 x g for 15 min and the pellet of the light mitochondrial fraction (LMF) was collected (Figure 3.1). The fraction containing highly enriched lysosomes was then isolated from LMF. First, a discontinuous gradient was prepared using OptiPrep^{TM} (Fresenius Kabi Norge AS, Oslo, Norway) (60% iodixanol) diluted with homogenisation buffer to 19%, 22%, 25% and 27% iodixanol. First, 2.5 mL of 27% iodixanol was added to a clear Ultra-Clear$^{®}$ Open-Top Tube (capacity of 14 mL) followed by progressive layers of lower densities (25%, 22% and 19%). The tube was sealed with ParaFilm$^{®}$ M film (Bemis, Neenah, WI, USA), carefully rotated to a horizontal position and stored at 4 °C overnight to form the gradient. The LMF obtained by differential centrifugation was adjusted to 30% iodixanol and 2.5 mL of the sample was layered underneath the gradient using a narrow metal cannula. The gradient was centrifuged in a swing out bucket rotor (SW 40 Ti rotor, Beckman Coulter, Brea, CA, USA) at 70,000 × g for 2 h at 4 °C using fast sample acceleration and a slow deceleration. The gradient was collected in 0.8 mL fractions from the top using a narrow metal cannula. The protein content and enzyme activity was assessed for each fraction.

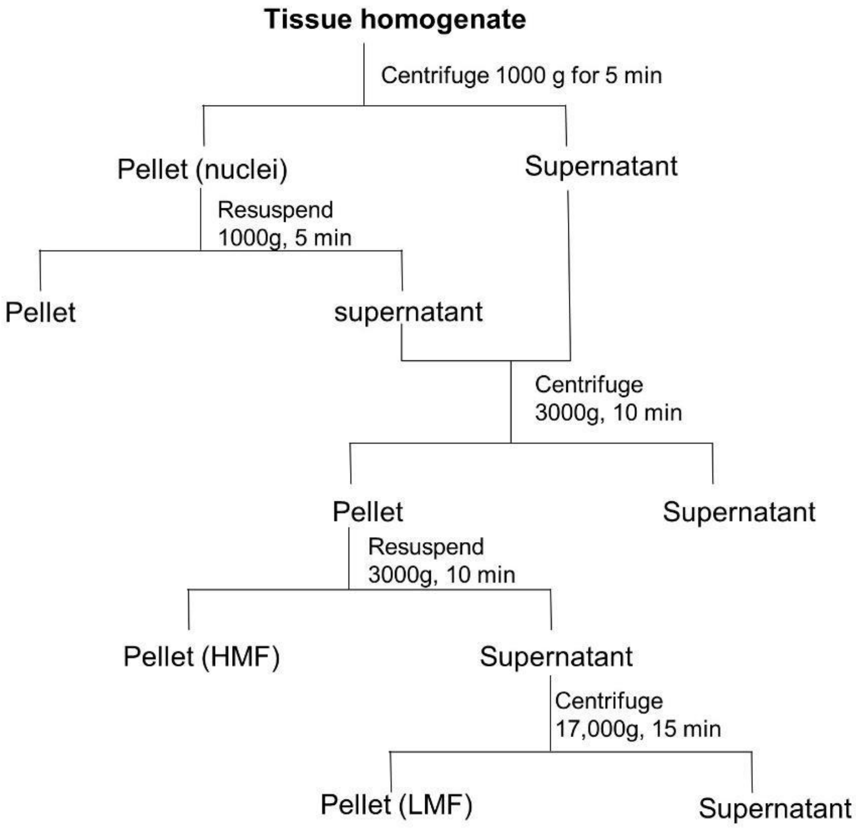

Figure 3.1 Subcellular fractionation process using differential centrifugation for rat liver.

3.2.5 Evaluation of subcellular fractions

Evaluation and quality control of the subcellular fractions were based on our previous studies (Seib et al., 2006). Briefly, the total amount of protein in the crude homogenate and all the lysosomal fraction was determined using Pierce BCA Protein Assay Kit (Thermo Scientific, Waltham, MA, USA) using bovine serum albumin as the protein standard. N-acetyl-β-glucosaminidase (NAG; a marker for lysosomes) (Klemm et al., 1998) and succinate dehydrogenase (SDH; a marker for contaminating mitochondria) (Rickwood, 1992) were selected as markers to characterise the subcellular fractions. The NAG assay was conducted by mixing 50 μL of each subcellular fraction with 30 μL of assay buffer containing 5 mM 4-methylumbelliferyl N-acetyl-β-D-glucosaminide, 250 mM sucrose and 200 mM sodium citrate-HCl (pH 5.0). The samples were incubated for 5 min at 25 °C in the dark. The reaction was stopped by adding 200 μL of 250 mM glycine NaOH, pH 10.4. The sample was centrifuged at 22,500 × g for 2 min and 200 μL was transferred to a black 96 well plate. The fluorescence of the liberated 4-methylumbelliferone was measured (excitation/emission wavelength 360/448 nm). For the SDH assay, 50 μL of crude homogenate (or fraction) was mixed with 250 μL reaction buffer (Tris-HCl EDTA buffer, 50 μL 200 mM sodium succinate, pH 7.5 and 50 μL 2.5 mg/mL 2-(4-iodo-phenyl)-3-(4-nitrophenyl)-5-phenyl tetrazolium chloride). The sample was incubated for 10 min at 25 °C. The reaction was stopped with ethyl acetate/ethanol/trichloroacetic acid stopping buffer. The sample was then centrifuged at 22,500 × g for 2 min, 200 μL of the supernatant was transferred to a 96 well plate, and absorbance of the formazan product was measured at 500 nm. The recovery was calculated from the total enzyme activity in the fractions divided by the activity of the homogenate. The latency of the isolated lysosomes was determined. To present the distribution of the markers in individual fractions, histograms were plotted with the fractions presented on the abscissa in the order they were isolated, with the lengths of the blocks proportional to their protein content. The ordinate displayed the enrichment of the respective marker, which was expressed as the relative specific activity (RSA). The RSA is the percentage of activity/content recovered in the fraction over the percentage of protein of the same fraction. Enrichment of the marker is indicated by a RSA value >1 (Seib et al., 2006).

3.2.6 *Ex vivo* degradation of native and PEGylated silk nanoparticles exposed to lysosomal enzymes

A 0.5 mL lysosome-rich fraction was added to a 0.1 mL Slide-A-Lyzer Mini Dialysis Device (MWCO 3500 g mol^{-1}; Thermo Scientific, Waltham, MA, U.S.A.) and was dialysed against 1 L ultrapure water at 4 °C for 24 h to remove the buffer. The functional capacity of this buffer-free lysosomal-rich fraction was verified with the NAG assay (Figure 3.11). Native and PEGylated silk nanoparticles were treated with 3.5 U/mL lysosomal enzymes (enzyme activity 0.105 U/mL): 30 µl of 3.33 mg/mL native and PEGylated silk nanoparticles containing 0.1 mg nanoparticles were treated with 333 µL of lysosomal enzymes in 400 µL of acidified water, pH 5.5, containing 5 mM glutathione and 2 mM EDTA. The samples were incubated at 37 °C with the enzymes for 5 days. Silk nanoparticle morphology and particle size distribution were then studied by scanning electron microscopy (detailed in section 3.2.10).

3.2.7 Nanoparticle mass loss

Native and PEGylated silk nanoparticles were exposed to model enzymes and incubated at 37 °C in 2 mL Eppendorf tubes. The controls were (i) native silk particles in water, (ii) PEGylated silk nanoparticles in water, and (iii) respective model enzymes in water; the control samples were treated identically to the respective enzyme-treated samples. All Eppendorf tubes were weighed before adding the sample (W1). At treatment day 1, 3, 5, 10, and 20, the samples were centrifuged at 16,000 × g for 40 min. The pellet and supernatant were collected, frozen, and lyophilized. The tubes containing freeze-dried pellets were weighed (W2) to determine the nanoparticle mass remaining after the treatment using (equation 3.1) (silk nanoparticles in water served as the control; i.e., 100% weight).

$$\% \text{ Mass remaining} = \frac{(W2\text{-}W1)}{\text{Weight of control nanoparticles}} \times 100 \qquad (3.1)$$

3.2.8 Particle size and zeta potential

The changes in particle size and zeta potential were determined by dynamic light scattering (DLS, Zetasizer Nano-ZS Malvern Instrument, Worcestershire, U.K.) for native and PEGylated silk nanoparticles treated with and without enzymes for 1, 3, 5, 10 and 20 days as detailed in Chapter 2 (section 2.2.4).

3.2.9 Secondary structure measurement

Untreated and enzyme-treated silk nanoparticles were centrifuged, washed with ultrapure water, frozen and then freeze-dried. The samples were subjected to Raman and Fourier transform infrared (FTIR) spectroscopy to determine the secondary structure of silk. Raman spectra measurements were performed using a Raman XploraA microscope (Horiba Jobin Yvon, Villeneuve d'Ascq, France). The 50 × objective lens was used and the laser wavelength was 532 nm. The spectrum was recorded between 50 and 3500 cm^{-1}, with 2 accumulations for 20 seconds per acquisition using a grating with 1200 grooves mm^{-1}. FTIR was carried out using a TENSOR II FTIR spectrometer (Bruker Optik GmbH, Ettlingen, Germany). Each measurement was run for 128 scans at 4 cm^{-1} resolution over the wavenumber range of 400 to 4000 cm^{-1}. OriginPro 9.2 software was used to correct baselines and peak fits at the amide I region (1595–1705 cm^{-1}). The amide region was identified as detailed in Chapter 2 (section 2.2.5). Additionally, deconvolution was applied for peak fitting. Gaussian line shapes were used for curve fitting. Overfitting of the data was avoided by fixing FWHM at 10 cm^{-1}.

3.2.10 Scanning electron microscopy

The morphology of native and PEGylated silk nanoparticles before and after enzyme treatment was imaged by scanning electron microscopy (SEM) using a FE-SEM SU6600 instrument (Hitachi High Technologies, Krefeld, Germany) at 5 kV. Samples were pipetted onto a silicon wafer and lyophilised overnight. The specimens treated with model enzyme were sputter-coated with carbon using a vacuum coater (Polaron Division E6100, Bio-Rad, Birmingham, UK), while the specimens of *ex vivo* lysosomal-treated nanoparticles were sputter-coated with 15 nm of gold using an ACE200 low vacuum sputter coater (Leica Microsystems, Wetzlar, Germany). The subsequent SEM images were analysed using ImageJ v1.50i software (National Institutes of Health, Bethesda, MD, USA).

3.2.11 Statistical analyses

Data were analysed using GraphPad Prism 7.0 (GraphPad Software, La Jolla, CA, U.S.A.). The statistical methods were described in Chapter 2 (section 2.2.13).

3.3 Results

3.3.1 Nanoparticle mass loss in response to enzymes

The mass of native and PEGylated silk nanoparticles exposed to protease XIV dropped rapidly to 40% and 60%, respectively, of the original mass within one day. The degradation rate subsequently slowed after the 3-day treatment cycle. The mass loss of native and PEGylated silk nanoparticles treated with papain gradually decreased from day 1 to day 5, resulting in a loss of more than 50% of their mass after 10 days of treatment. By contrast, no significant change was noted in the mass of the native or PEGylated silk nanoparticles after chymotrypsin treatment (Figure 3.2).

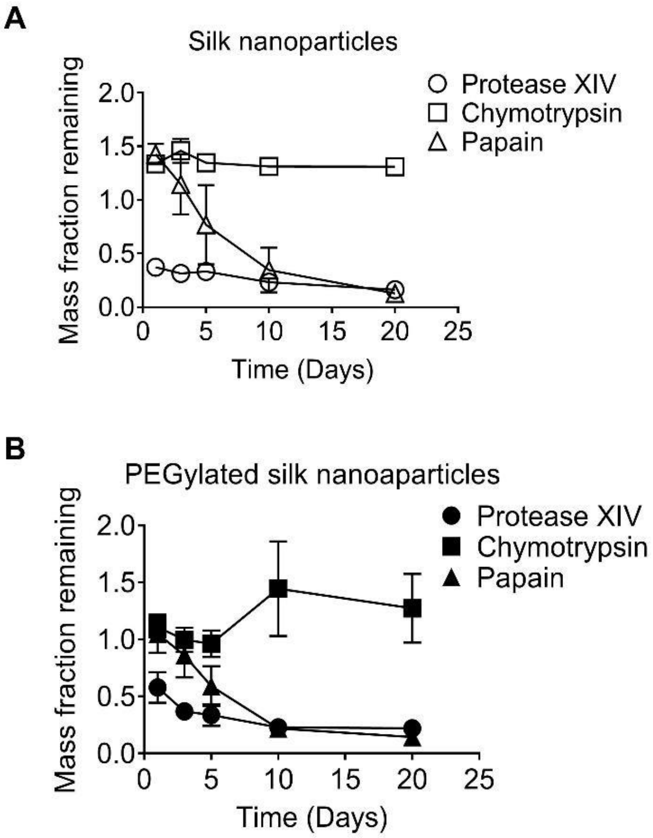

Figure 3.2 Nanoparticle mass loss after enzyme treatment of native and PEGylated silk nanoparticles. (A) The native silk nanoparticles and (B) PEGylated silk nanoparticles were treated with the respective enzymes and the remaining mass of nanoparticles over 20 days was measured. The data represents the mean ± SD, error bars are hidden in the plot-symbol when not visible, n = 3.

3.3.2 Impact of enzymes on particle size and zeta potential changes

The particle size and zeta potential of control native silk nanoparticles were 94.44 nm ± 3.03 and -45.2 mV ± 1.6, respectively, whereas the particle size and zeta potential of the control PEGylated silk nanoparticles were 108.5 nm ± 3.72 and -37.3 mV ± 1.4, respectively. The particle size slightly increased over the 20-day treatment cycle for the native and PEGylated silk nanoparticles treated with protease XIV (Figure 3.3A, C). The negative zeta potentials for silk nanoparticles were shifted toward a less negative value over the treatment period (Figure 3.3B, D). The size of the silk nanoparticles exposed to papain significantly increased and had reached 2.2 µm and 1.5 µm for native and PEGylated silk nanoparticles, respectively, by day 10 (Figure 3.3A, C). The zeta potential of silk nanoparticles treated with papain was considerably shifted toward a more neutral value after the 10-day treatment cycle. By contrast, no change was noted in the size or surface charge of the nanoparticles exposed to chymotrypsin (Figure 3.3).

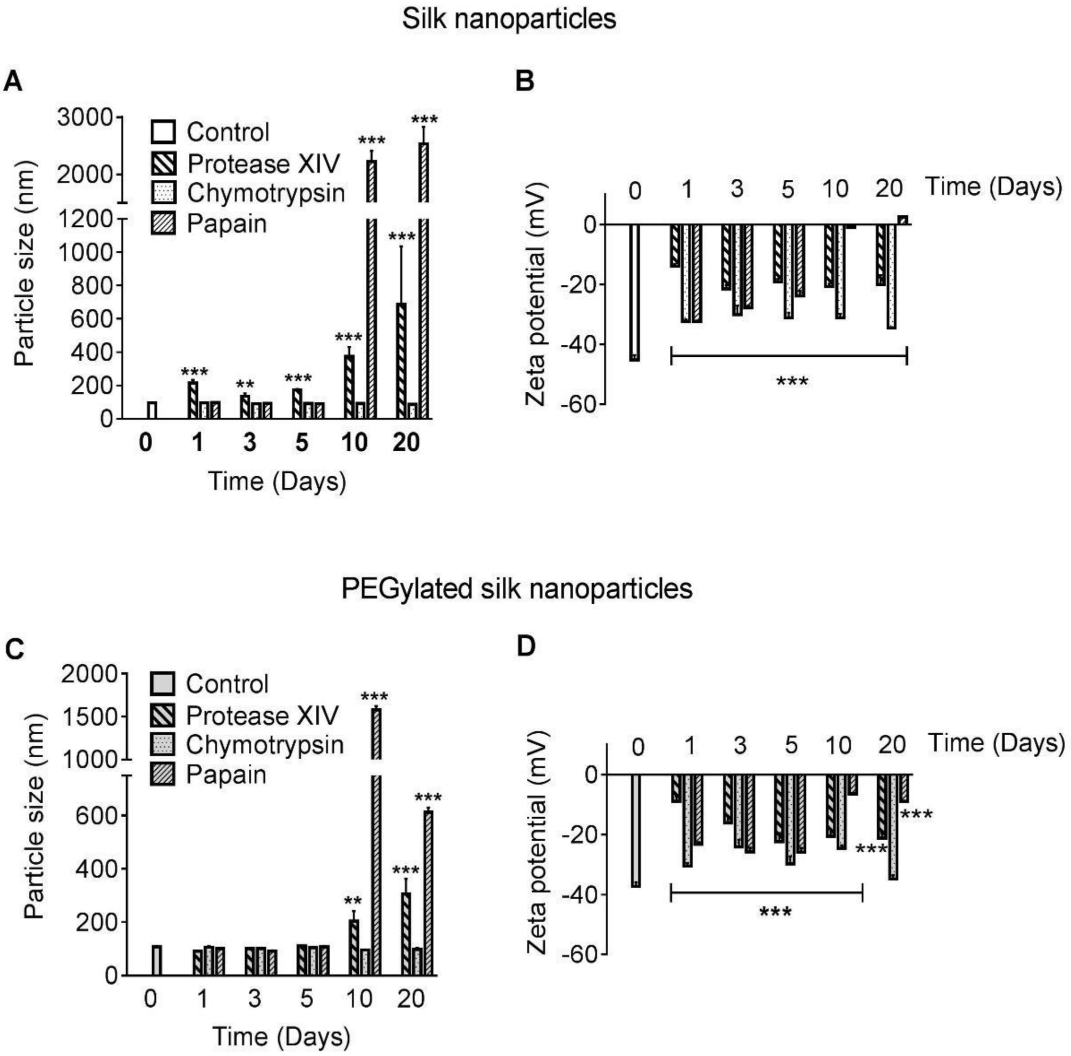

Figure 3.3 Particle size and zeta potential measurement of native and PEGylated silk nanoparticles following exposure to enzymes. Shifts in particle size and zeta potential of enzyme-treated (A), (B) native silk and (C), (D) PEGylated silk nanoparticles over the 20-day treatment cycle at 37 °C. An asterisk denotes statistical significance as follows: *P < 0.05, **P < 0.01, ***P < 0.001. The data represents the mean ± SD, error bars are hidden in the plot-symbol when not visible, n = 3.

3.3.3 Effect of proteolytic enzymes on the secondary structure of silk

The secondary structure of native and PEGylated silk nanoparticles before and after enzyme exposure was analysed by FTIR and Raman spectroscopy (Figure 3.4 and 3.5). The Raman bands at 1665 cm^{-1} and 1229 cm^{-1} represent β-sheet structure in the amide I and amide III regions, respectively. The two bands at 1104 cm^{-1} and 1084 cm^{-1} are due to alanine in coils/helix and β-sheet conformations, respectively (Monti et al., 2001). The Raman spectra showed similar results for both native and PEGylated silk nanoparticles treated with model enzymes. The amide I (1665 cm^{-1}) and amide III (1229 cm^{-1}) region of the nanoparticles did not change following enzyme treatment. However, silk nanoparticles treated with protease XIV and papain showed peak broadening at 1104 cm^{-1} and 1084 cm^{-1} over the 20-day treatment cycle (Figure 3.4).

For FTIR analysis, the amide I bands at 1621 cm^{-1} and 1640 cm^{-1} are attributed to β-sheet and amorphous structures, respectively (Hu et al., 2006). The amide I region of the native and PEGylated silk nanoparticles did not change over the 20-day enzyme treatment cycle, when compared with the control (Figure 3.5).

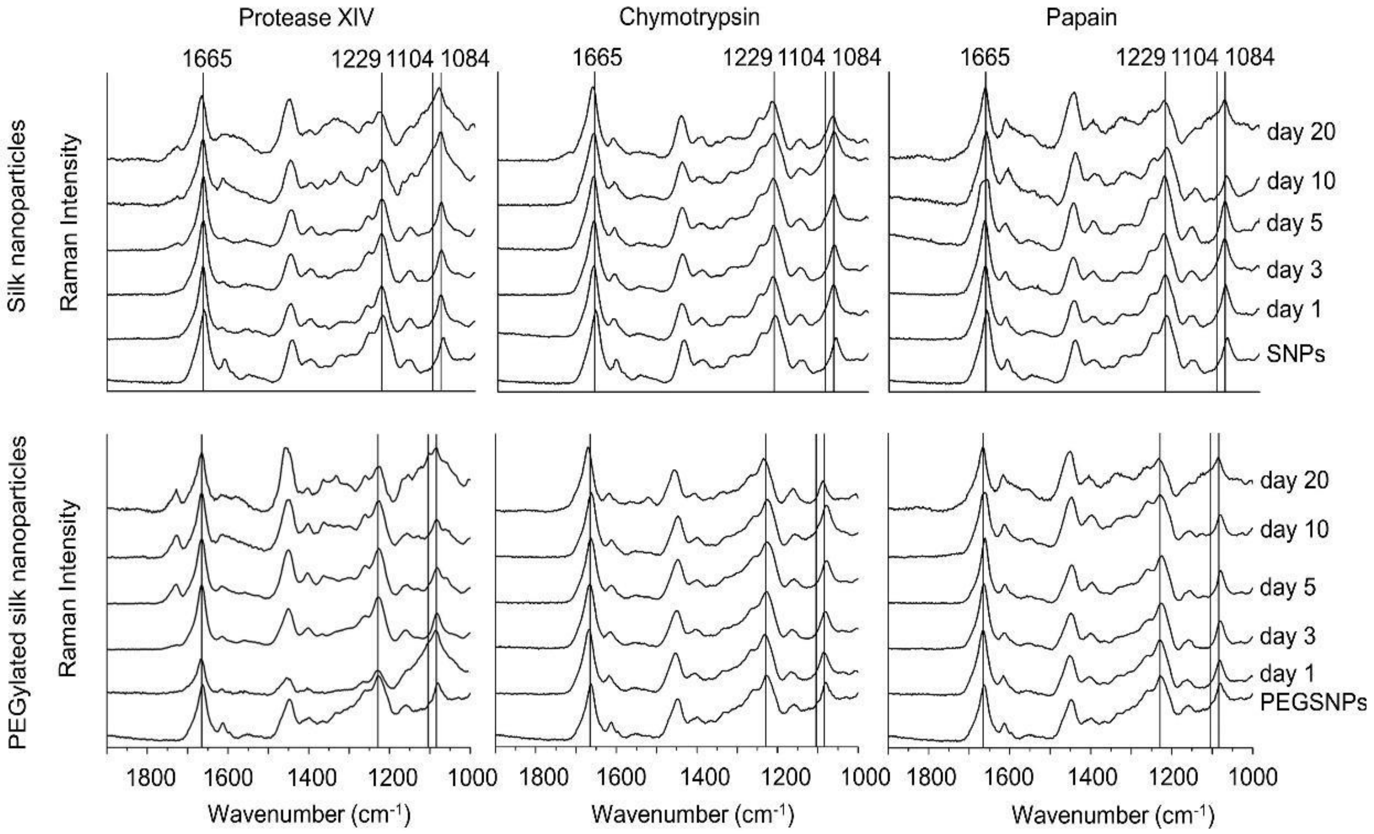

Figure 3.4 Raman spectra of native and PEGylated silk nanoparticles after enzyme degradation. The lines in the Raman spectra at 1665 cm^{-1}, 1229 cm^{-1} and 1084 cm^{-1} represent β-sheets, while 1104 cm^{-1} represents the amorphous segments.

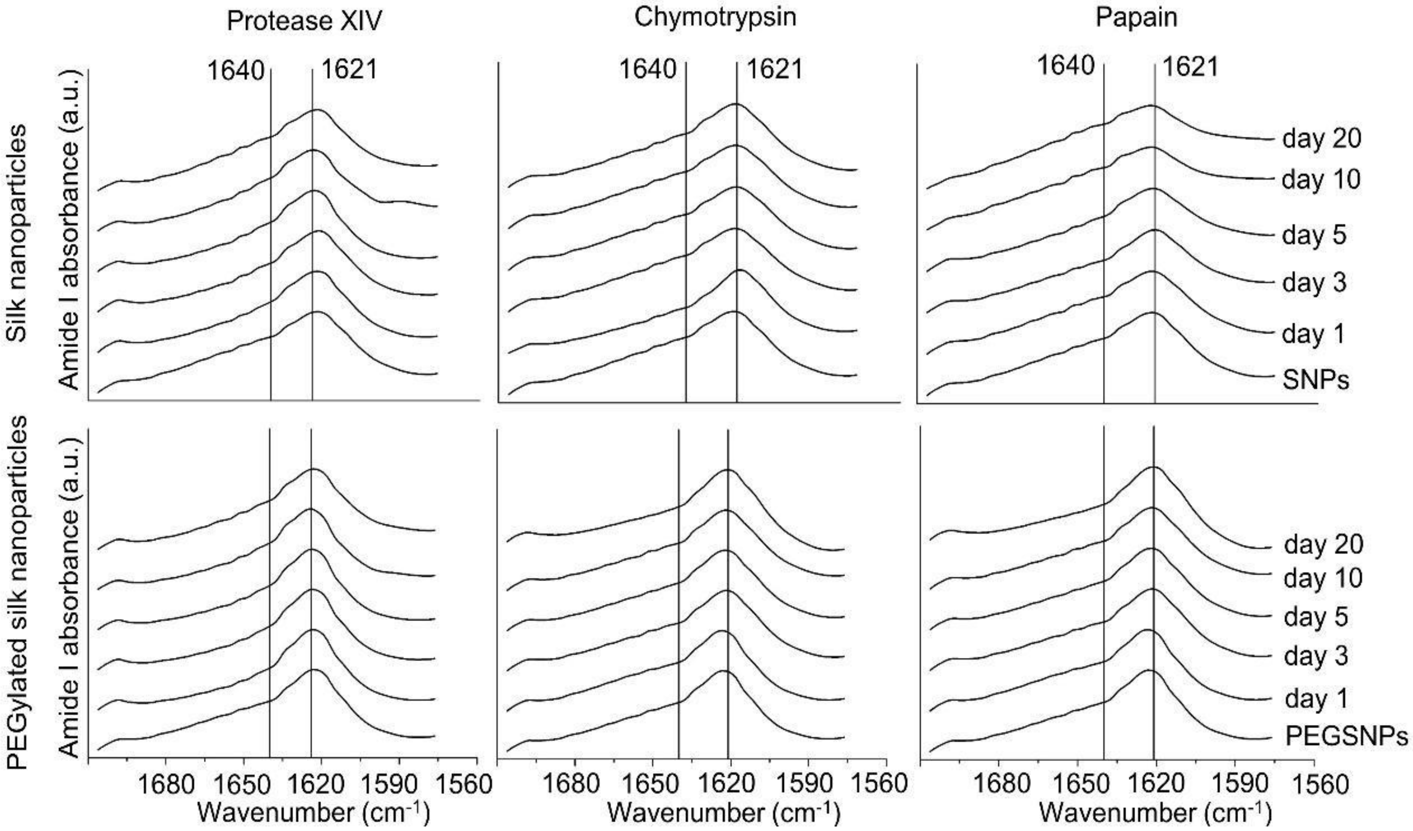

Figure 3.5 Determination of FTIR absorbance spectra of the amide I region of enzyme-treated native and PEGylated silk nanoparticles over time. The lines mark the absorbance band at 1621 cm^{-1} and 1640 cm^{-1}, representing β-sheets and random coils/helixes, respectively.

Fourier self-deconvolution (FSD) was applied to extract the secondary structure content (%) from the FTIR spectra of the enzyme-exposed silk nanoparticles (Figure 3.5). The percentage contribution to the secondary conformation of the structural elements was derived from the area under the individual deconvoluted peaks (Figure 3.6). The observed changes were similar for both native and PEGylated silk nanoparticles. However, marked differences were evident, depending on the enzymes tested. Protease XIV reduced random coil/α-helix structure and β-turns, which resulted in a proportional increase in β-sheet structure of the silk nanoparticles (Figure 3.7). The increase in β-sheets was attributed to the increase in intermolecular β-sheet content over the 20-day treatment cycle (Figure 3.8). Papain decreased the overall β-sheet content after 10 days of enzyme treatment due to a reduction in the content of intermolecular β-sheets within the silk nanoparticles (Figure 3.8). Consequently, a proportional increase was observed in the random coil/α-helix structure. Chymotrypsin treatment decreased the random coil and α-helix content of silk nanoparticles at day 1, but the content was restored to control values by day 3 and was maintained until day 20 (Figure 3.7). By contrast, chymotrypsin did not affect the secondary structure of PEGylated silk nanoparticles over the 20-day treatment cycle (Figure 3.7).

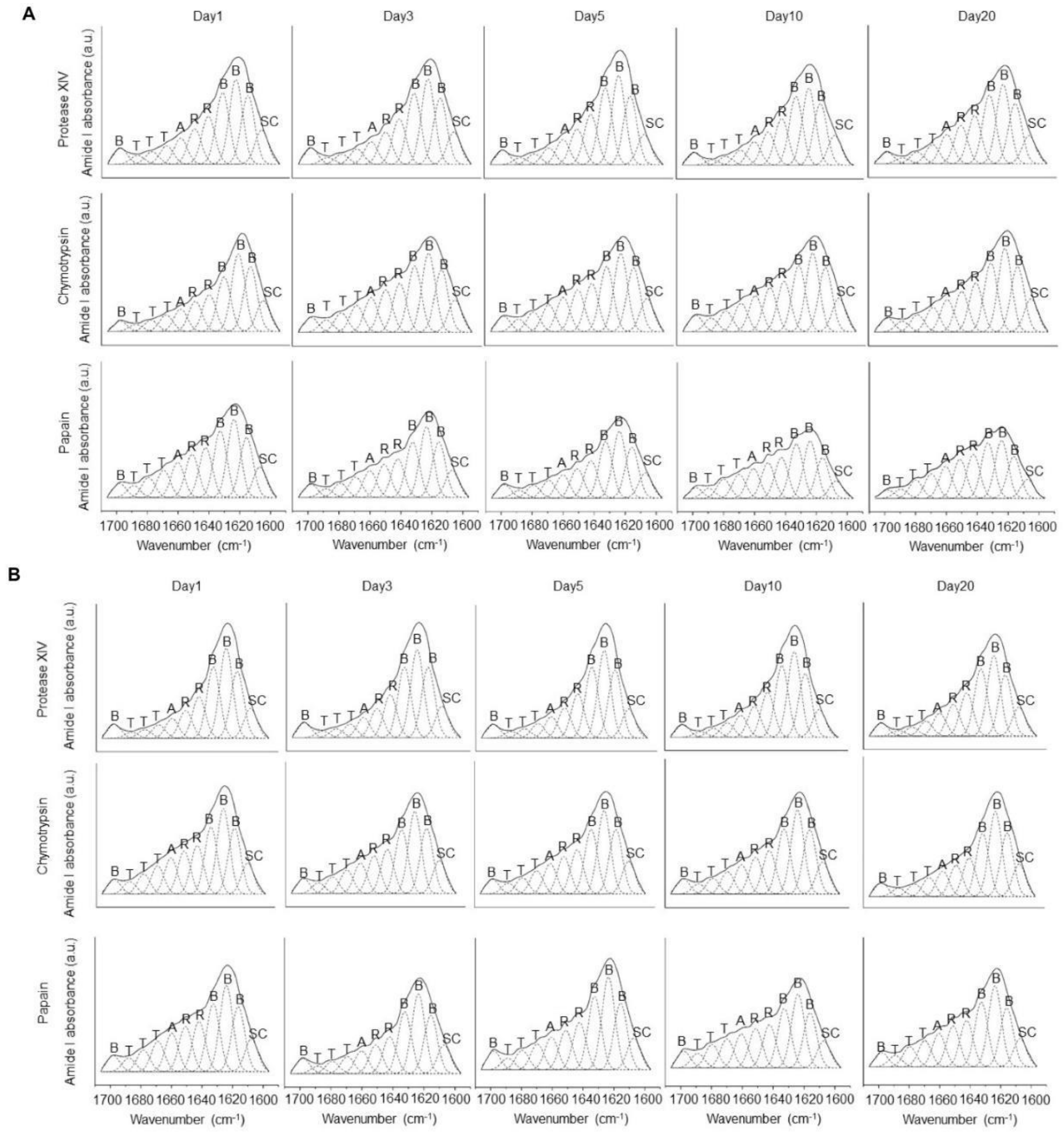

Figure 3.6 Fourier self-deconvolution absorbance spectra. Absorbance spectra of (A) native silk nanoparticles and (B) PEGylated silk nanoparticles treated three enzyme models. The dash lines represent the individual deconvoluted peaks of turns (T), α-helix (A), random coil (R), β-sheet (B) and side chains (SC).

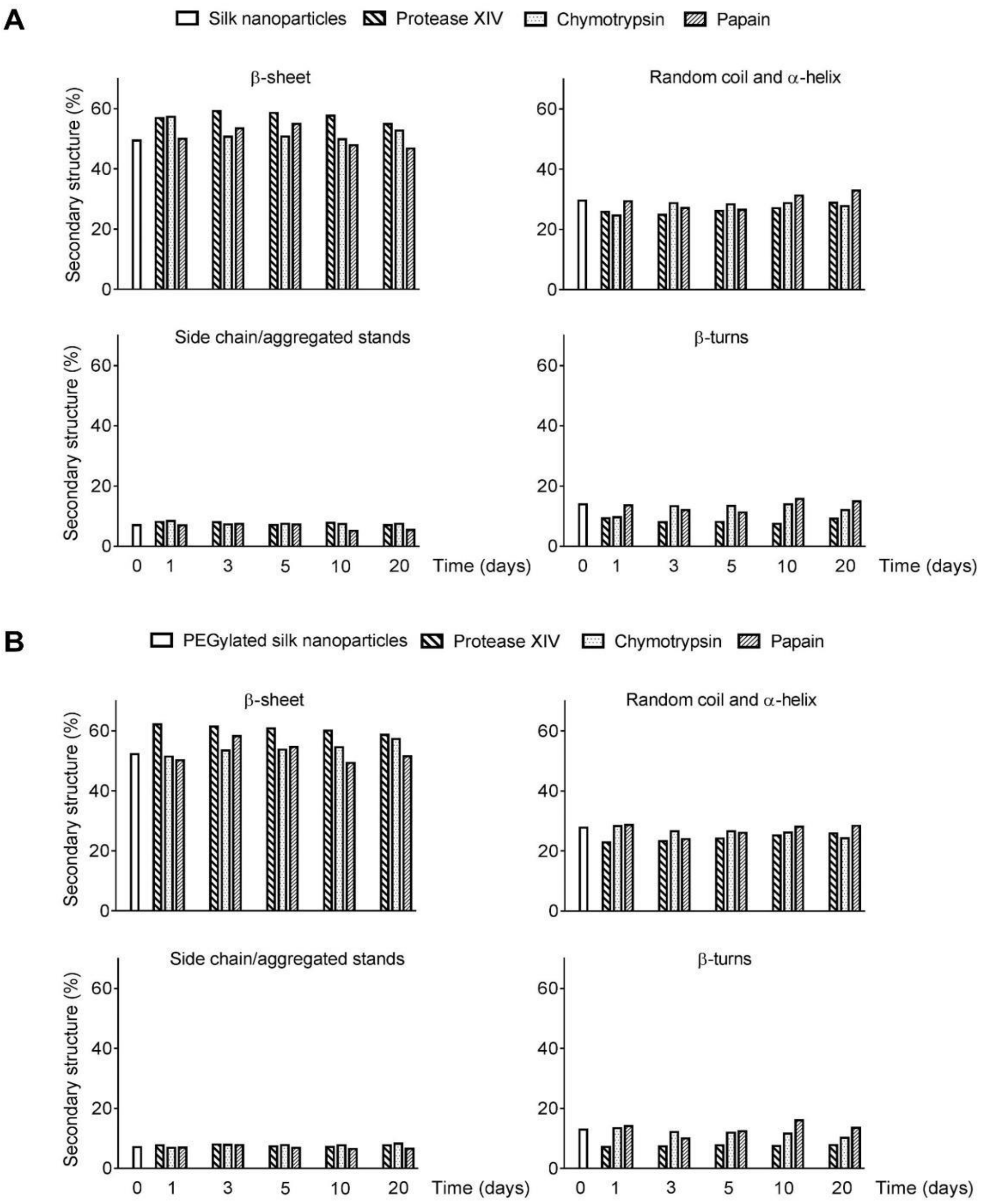

Figure 3.7 Quantification of the secondary structure (%) of enzyme-treated native and PEGylated silk nanoparticles over time. Secondary structures: β-sheets, random coil, and α-helix, side chain/aggregated stands and β-turns of (A) silk nanoparticles and (B) PEGylated silk nanoparticles over the 20-day enzyme treatment cycle.

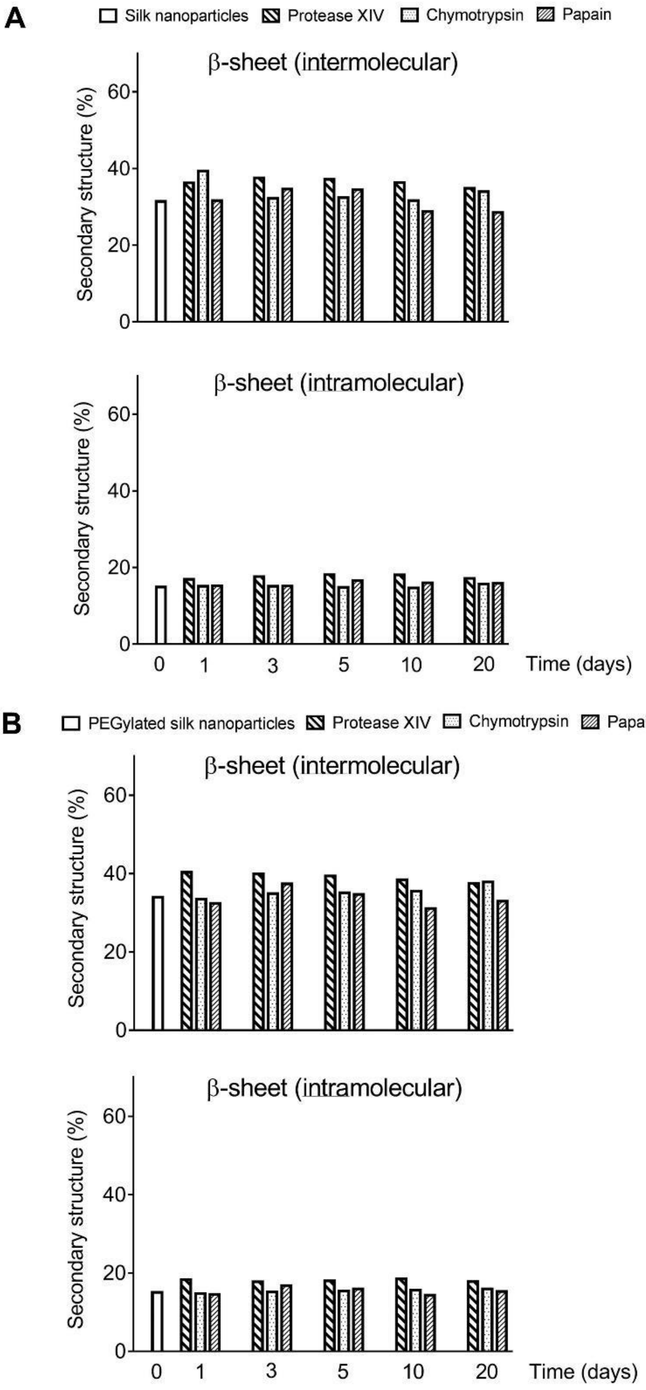

Figure 3.8 The percentages of β-sheet content (%) of enzyme-exposed native and PEGylated silk nanoparticles. (A) Silk nanoparticles (B) PEGylated silk nanoparticles after enzymes treatment were determined inter and intramolecular β-sheets compared to control nanoparticles and silk film references over 20 days enzyme treatment.

3.3.4 Morphology changes of nanoparticles

Electron microscopy studies indicated that native and PEGylated silk nanoparticles were spherical particles in the nanometer size range (100 to 120 nm) (Figure 3.9). The morphological changes were similar for both native and PEGylated silk nanoparticles following enzyme treatment. Nanoparticles exposed to protease XIV for 1 day aggregated and appeared swollen, porous, and irregularly shaped. The continuous degradation of silk by protease XIV was accompanied by a change to a more compact morphology. Nanoparticles treated with papain remained within the nanometer size range and retained a spherical shape after 1 day of treatment; however, the particles were significantly degraded and were closely packed into micrometer sized particles without visible pores after the 20-day enzyme exposure. By contrast, nanoparticles exposed to chymotrypsin did not change in shape or size over the 20-day treatment cycle (Figure 3.9).

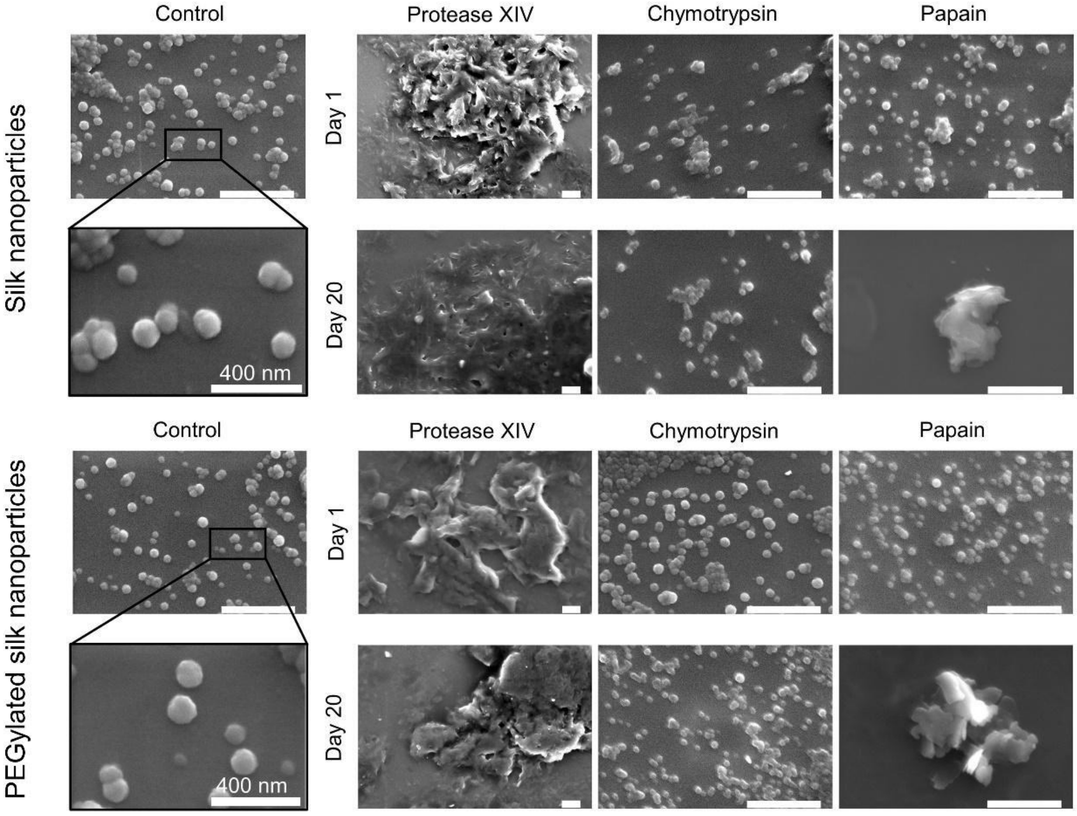

Figure 3.9 Scanning electron microscopy (SEM) images of native and PEGylated silk nanoparticles after 20 days of treatment with or without enzymes (scale bar = 1 μm).

3.3.5 Characterisation of subcellular fractionation produced by differential centrifugation

Lysosomal preparations are often contaminated with mitochondria, which makes assessment of the quality of the isolated lysosomes particularly important. The LMF homogenate was analysed to estimate the total amount of contaminating mitochondria, using SDH as a marker. The LMF was layered under the gradient and centrifuged. The subcellular fractions were then collected and analysed for the total amount of protein using the Pierce BCA protein assay kit (Seib et al., 2006) and the enrichment of lysosomes was determined using the NAG assay. The mitochondrial content in the crude homogenate and fractions was negligible (RSA = 0.01), indicating low mitochondrial contamination. Lysosomal enrichment was consistently observed in fractions 5 to 8 (tubes A to D) (Figure 3.10). These fractions showed low protein content (narrow bar graph) and high RSA values (Figure 3.10). Therefore, these lysosomal-rich fractions were combined and the overall lysosomal enzyme activity (U/mL) was compared before and after -80 °C freezing. The enzyme activity increased substantially (>30%) following -80 °C freezing (or with the addition of 1% v/v Triton X-100 to the fresh lysosomal preparation) (Figure 3.11). This latency indicated that isolated lysosomes were intact and the lysosomal membrane was successfully ruptured by freezing and thawing. In addition, the lysosomal-rich fraction obtained following buffer removal by 24 h dialysis against water retained its full enzyme activity (Figure 3.11).

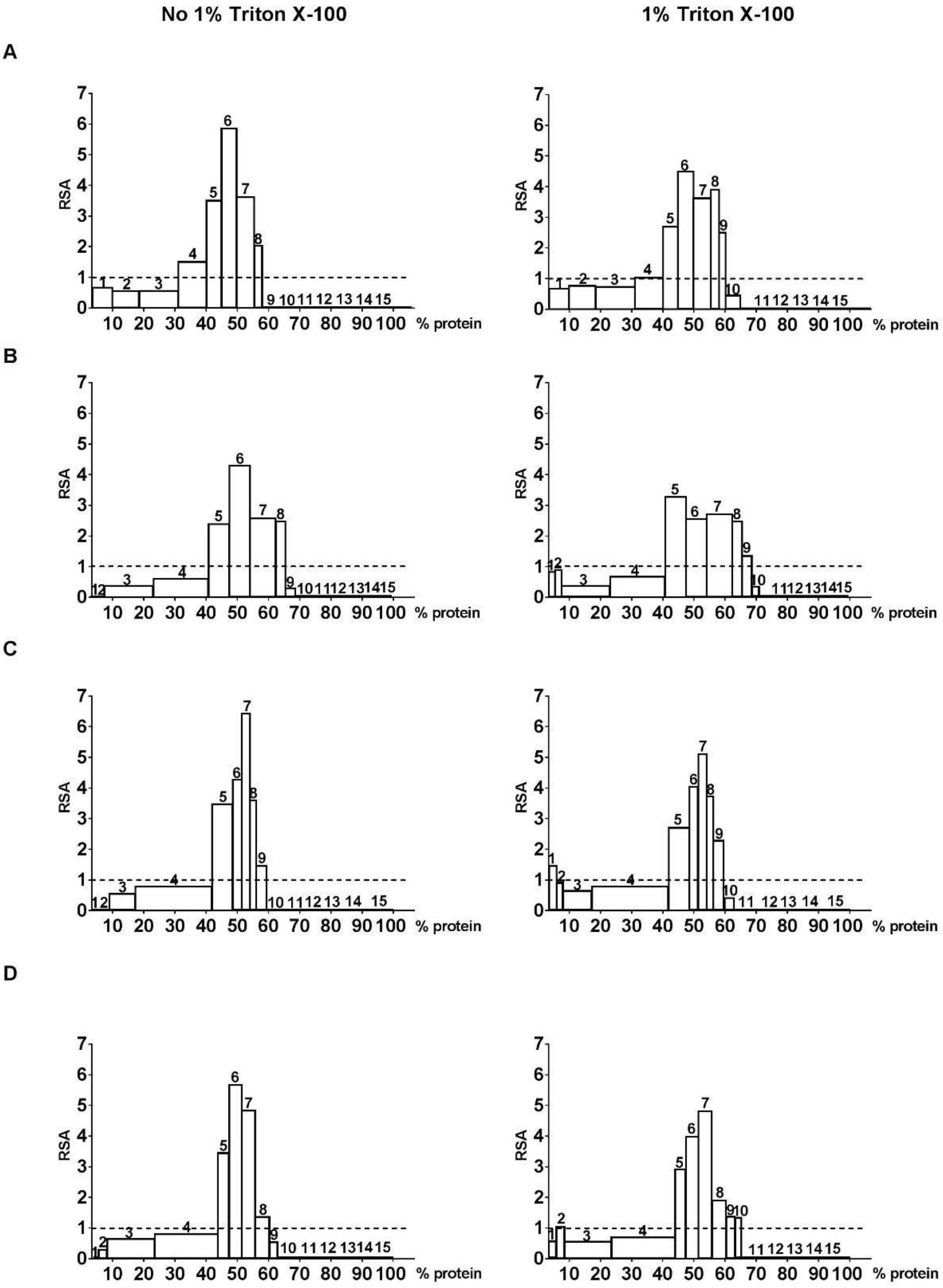

Figure 3.10 The relative specific activity (RSA) of N-acetyl-β-glucosaminidase in subcellular fractions of 4 tubes (A to D) in the presence and absence 1% v/v Triton X-100. The number on the top of each column indicates fraction number. The length of

each column is proportional to its protein content. An RSA > 1 shows enrichment of N-acetyl-β-glucosaminidase in the fraction.

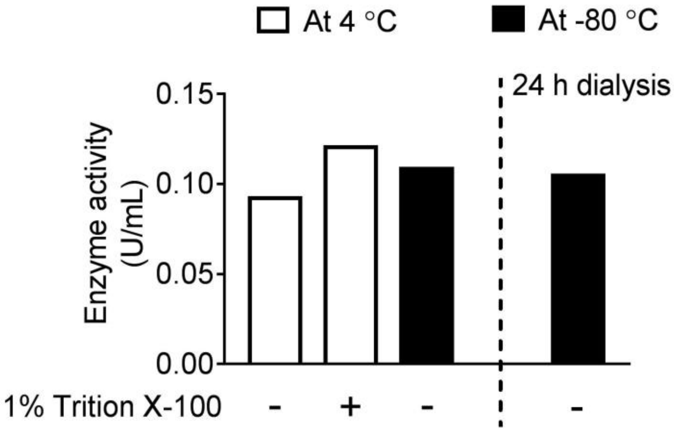

Figure 3.11 Enzyme activity (U/ml) of the combined lysosome-rich fractions at 4 °C and -80 °C in presence and absence of 1% Triton X-100 and after dialysis against water for 24 h.

3.3.6 Characterisation of the nanoparticles exposed to lysosomal enzymes

The morphological changes of native and PEGylated silk nanoparticles were investigated by SEM following a 5-day *ex vivo* lysosomal enzyme treatment. The particle size of enzyme-degraded silk nanoparticles was heterogeneous and averaged 75.7 nm ± 27.9 (Figure 3.12A). The silk nanoparticles aggregated after enzyme exposure and showed irregular shapes; evidence of residual material was visible on the mica surface (Figure 3.12A open arrow). By contrast, the particle size distribution remained more homogeneous (64.9 nm ± 14.7) for the enzyme-treated PEGylated silk nanoparticles, which showed little aggregation and less residual material overall on the surface (Figure 3.12B).

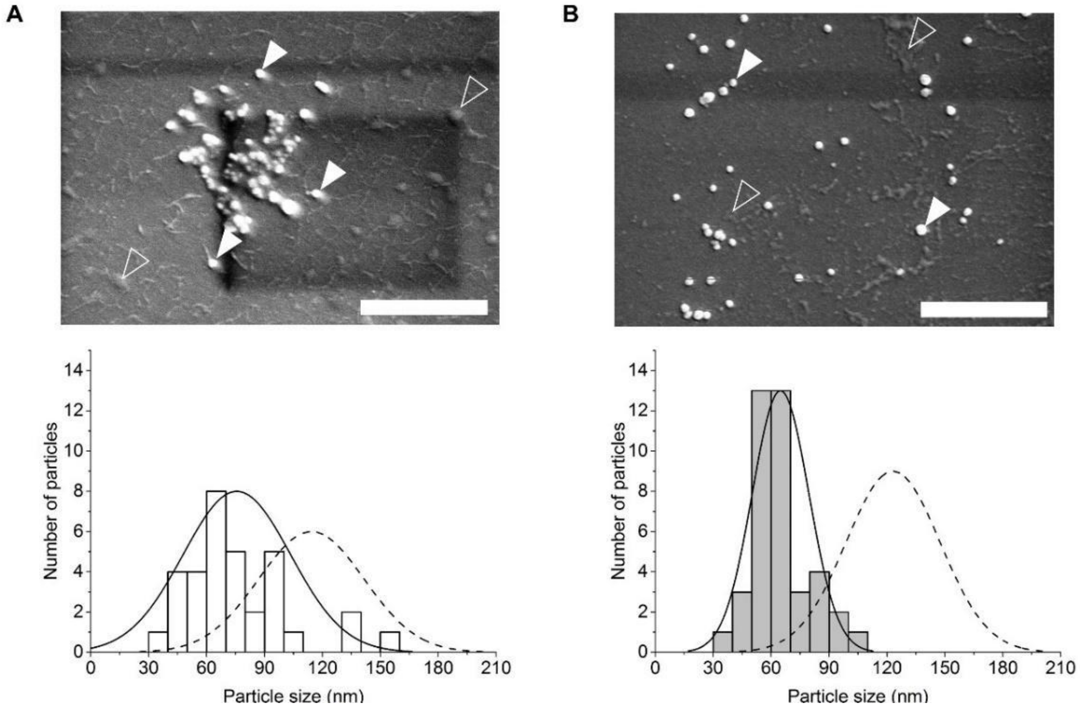

Figure 3.12 Qualitative and quantitative analysis of native and PEGylated silk nanoparticles following lysosomal enzyme exposure. Scanning electron microscopy (SEM) images and particle size distribution of (A) native silk nanoparticles and (B) PEGylated silk nanoparticles after a 5-day exposure to *ex vivo* lysosomal enzymes (scale bar = 1 μm). Closed arrows denote the remaining nanoparticles and open arrows denote degradation products. The normal distributions show the particle size distribution of nanoparticles (dashed line) and enzyme-treated nanoparticles (solid line).

3.4 Discussion

Nanoparticles designed for lysosomotropic drug delivery need to successfully navigate from the injection site to their final destination (i.e., the lysosomes) to elicit the desired therapeutic response (Seib, 2017b). Silk nanoparticle are readily trafficked *in vitro* to lysosomes, where the acidic environment and proteolytic enzymes trigger drug release (Totten et al., 2017). However, the impact of the lysosomal environment on the fate and material properties of native and PEGylated silk nanoparticles is unknown. The accumulation of PEGylated nanoparticles in lysosomes imposes a potential risk of evoking a "lysosomal storage disease-like" response, when the material destined for lysosomal degradation is not degraded at a sufficient rate but instead accrues and perturbs organelle function (Duncan and Richardson, 2012; Appelqvist et al., 2013).

Clinical experience with non-biodegradable polymers, such as *N*-(2-hydroxypropyl)methacrylamide (HPMA) (Duncan, 2009) and polyethylene glycol (PEG) (Ivens et al., 2015), has been encouraging. Nonetheless, the safety window for HPMA- and PEG-based nanomedicines depends on a multitude of factors, including (but not limited to) dosing frequency (i.e., chronic versus acute), polymer dose, and polymer characteristics (e.g., architecture, end group functionality, molecular weight, polydispersity, etc.). Non-clinical toxicology studies with clinically approved PEGylated biopharmaceuticals have shown evidence of (transient) vacuolation, primarily in phagocytic cells (Turecek et al., 2016). Furthermore, metabolic reprogramming of macrophages with (silk) nanoparticles has recently been reported (Saborano et al., 2017).

Silk has a remarkable clinical track record and it is degraded by proteolytic enzymes (Thurber et al., 2015), but the response to enzymes when silk is in nanoparticle form is unknown. Simply assuming that silk nanoparticles will behave similarly to other macro-sized silk formats is not scientifically rigorous (Seib, 2017b). Furthermore, material performance is context specific and thus requires dedicated assessments. The present study represents the first inroads into the assessment of silk nanoparticle degradation by proteolytic enzymes.

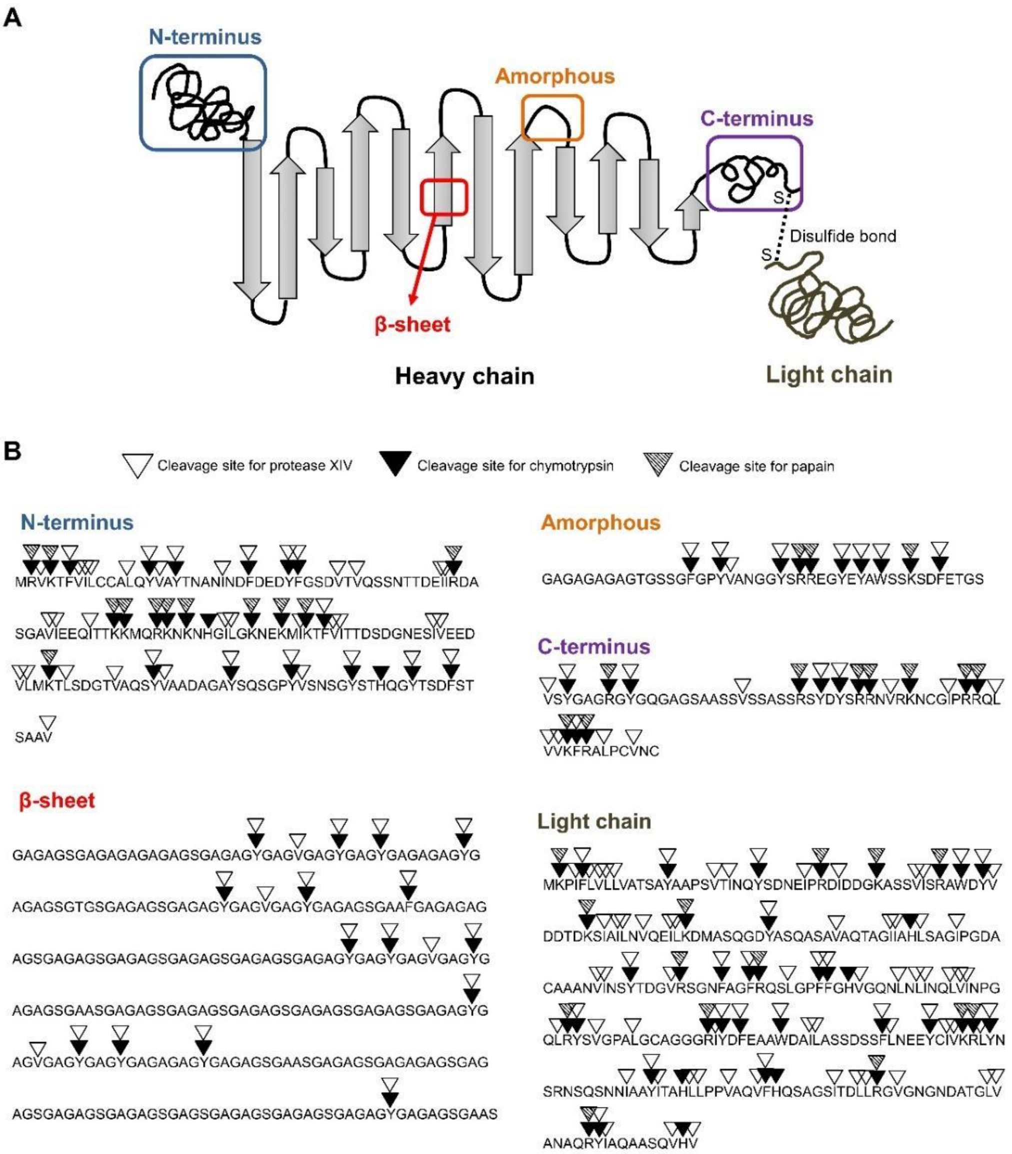

C

		Number of cleavage sites					
Enzymes	**Cleavage sites**	**Heavy chain**	N-terminus	β-sheet	Amorphous	C-terminus	**Light chain**
Protease XIV	Typ, Phe,Trp, His, Lys, Arg	348	27	222	84	15	41
Chymotrypsin	Typ, Phe,Trp, Val, Ile, Leu	434	41	291	88	14	81
Papain	Lys, Arg	26	12	0	4	10	15

Figure 3.13 *B. mori* schematic and cleavage sites of proteolytic enzymes of the silk amino acid sequence. (A) Two dimensional schematic of silk structure including the heavy chain (i.e. N-terminus, crystalline β-sheets, amorphous and C-terminus) and light chain. (B) Enzymatic specificities of proteolytic enzymes for the silk sequences. The silk amino acid sequences was extracted from Prot/TrEMBL accession numbers

P05790 and P21828. (C) Number of cleavage sites of proteolytic enzymes on different silk domains.

A

	Heavy chain			
	No treatment	Protease XIV	Chymotrypsin	Papain
Size (No. of amino acid)	5263	4915	4829	5237
pI	4.39	2.46	4.39	3.29
No. of Negative charges	55	55	55	55
No. of Positive charges	26	0	26	0

B

	Light chain			
	No treatment	Protease XIV	Chymotrypsin	Papain
Size (No. of amino acid)	262	221	181	247
pI	5.06	2.73	5.06	3.64
No. of Negative charges	22	22	22	22
No. of Positive charges	15	0	15	0

Figure 3.14 Physicochemical properties of (A) heavy chain and (B) light chain of silk before and after enzyme exposure.

The proteolytic susceptibility of both native and PEGylated silk nanoparticles was determined by assessing the mass loss in response to enzyme exposure. Both silk nanoparticle types showed a similar rank order (protease XIV > papain >> α-chymotrypsin) (Figure 3.2). Previous studies with silk films and hydrogels also demonstrated that silk degradation was significantly faster with protease XIV than with α-chymotrypsin (Brown et al., 2015). The silk sequence alignment indicates 434 α-chymotrypsin cleavage sites in the silk heavy chain and 81 in the light chain and 348 and 41 Protease XIV cleavage sites in the heavy and light chains, respectively (Brown et al., 2015) (Figure 3.13 and 3.14). Thus, the differences in silk degradation are not governed only by the number of cleavage sites but are critically dependent on enzyme accessibility, the silk format and the secondary structure of the silk.

In the current study, degradation was slower at the early time points (i.e. day 1 enzyme exposure and the resulting mass loss and particle size) for PEGylated silk nanoparticles than for native silk nanoparticles for all the tested enzymes (Figure 3.2 and 3.3). This relatively lower degradation rate for PEGylated silk probably reflects the ability of PEG to shield the silk surface and thus hinder the access of the proteolytic enzymes. This protective effect concurs with indirect observations in single breast cancer cells (Totten et al., 2017), where a slower therapeutic payload release was observed from PEGylated silk nanoparticles than from native silk nanoparticles, suggesting a reduced proteolytic degradation.

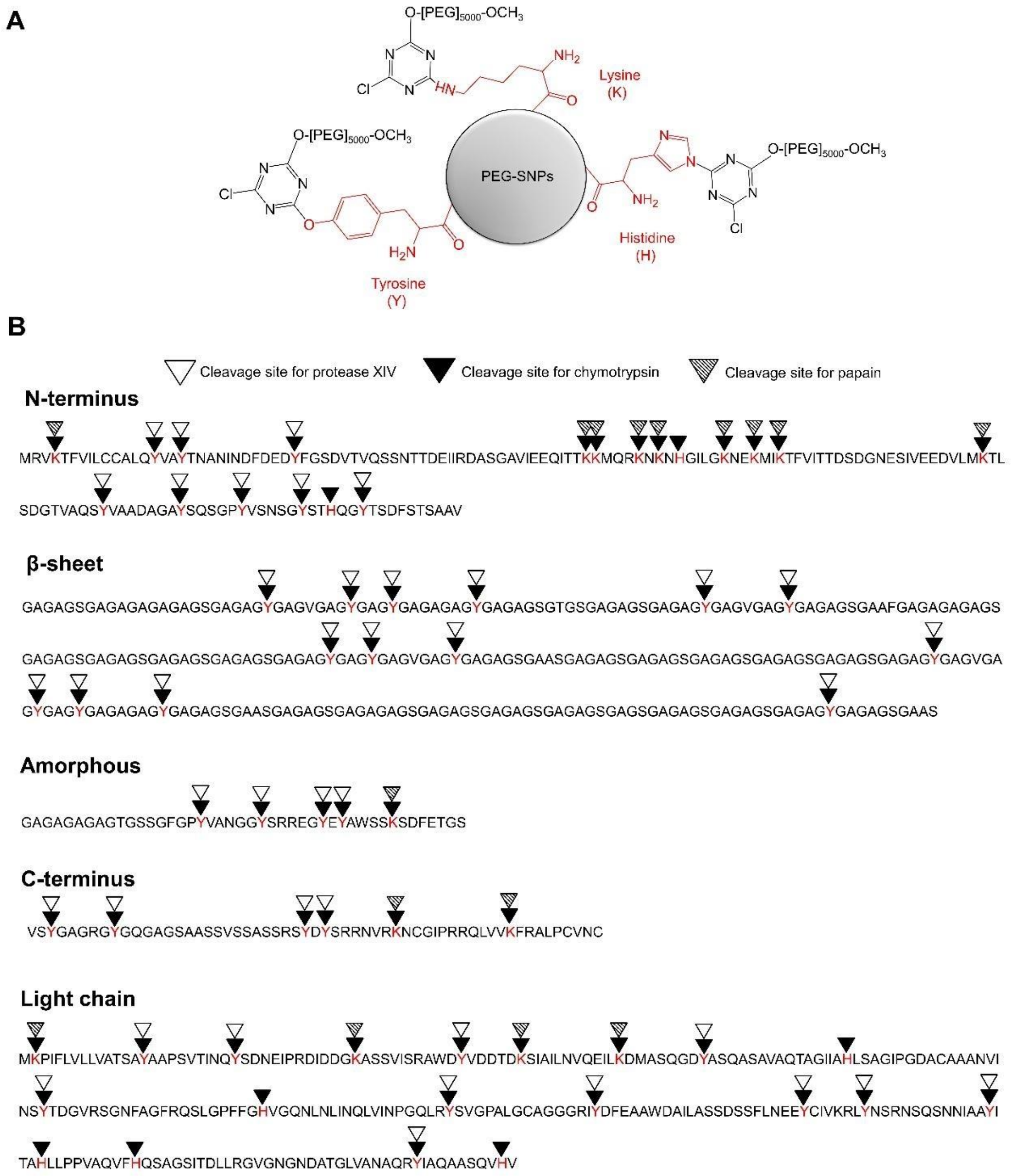

C

		Number of cleavage sites					
Enzymes	**Cleavage sites**	**Heavy chain**	N-terminus	β-sheet	Amorphous	C-terminus	**Light chain**
Protease XIV	His, Tyr, Lys	294	19	221	48	6	21
Chymotrypsin	Tyr	277	8	221	44	4	11
Papain	Lys	12	9	0	1	2	5

Figure 3.15 Schematic of PEGylated silk nanoparticles (PEG-SNPs) and cleavage sites by proteolytic enzymes. (A) PEGylated silk nanoparticles with the amino acids exploited for PEG conjugation (labelled in red). (B) Enzymatic cleavage sites patterns

and (C) the number of remaining cleavage sites of silk assuming that all the reactive amino acids have been involved in PEG conjugation.

The particle size and charge in response to enzyme treatment was also measured. A significant swelling of silk nanoparticles was observed, as reported for other protein-based nanoparticles (Magee et al., 1993, 1995). Increases in particle size were readily observed from day 10 onwards and these changes were particularly evident for the papain-treated silk nanoparticles (Figure 3.3). Papain exposure progressively changed the negative zeta potential of silk nanoparticles towards more positive values. This was particularly evident for the native silk nanoparticles and less so for the PEGylated ones, which suggested that PEGylation could provide steric hindrance and protection against proteolytic degradation (Figure 3.15). Silk sequence alignment showed that 26 sites in the silk heavy chain and 15 sites in the light chain are susceptible to cleavage by papain (Figure 3.13 and 3.14). Papain cleaves arginines and lysines of the silk sequence; the latter one is also exploited for PEGylation in addition to histidine and tyrosine (Seib, 2017b). Papain cleavage of lysines and arginines would be expected to lead to a net loss of positive charge. Thus the observed overall loss of the negative zeta potential is counterintuitive and requires more work to explain the experimental data. Similar considerations apply for protease XIV (Figure 3.3). By contrast, α-chymotrypsin treatment did not change the particle size or zeta potential of either the native or the PEGylated silk nanoparticles over the 20 day treatment cycle, as reflected by the maintenance of a consistent nanoparticle mass (Figure 3.2). Previous studies using silk films and hydrogels also reported minimal degradation by α-chymotrypsin (Brown et al., 2015).

Raman and FTIR spectroscopy was used to obtain a better understanding of the changes in native and PEGylated silk nanoparticles following enzyme treatment. The amide I band in FTIR and the amide I and III bands in Raman are well suited for assigning secondary structures to proteins (Pelton and McLean, 2000) and they are also widely applied to silk (Lefèvre et al., 2007). The typical wavenumbers in Raman spectroscopy for protein secondary structure are 1662–1655 cm^{-1}, 1272–1264 cm^{-1}, 1104 cm^{-1} for random coils/α-helixes and 1674–1672 cm^{-1}, 1242–1227 cm^{-1}, 1084 cm^{-1} for β-sheets (Monti et al., 2001; Rygula et al., 2013). The Raman spectra of native and PEGylated silk nanoparticles showed signal intensities at 1665 cm^{-1}, 1229 cm^{-1}, and 1084 cm^{-1}, which indicated a β-sheet conformation for silk (Figure 3.4). No changes were evident in the amide I spectra of the enzyme-treated nanoparticles due to the lower sensitivity of the Raman versus the FTIR spectra (Chen et al., 2016). However, the band at 1104 cm^{-1} and 1084 cm^{-1} was used to analyse secondary structure changes of silk nanoparticles. The bandwidth in this region became progressively broader for silk nanoparticles exposed to protease XIV and papain, from five days onwards, indicating that these enzymes digested β-sheet sequences.

The FTIR measurements confirmed that both native and PEGylated silk nanoparticles had high β-sheet contents (i.e., high amide I absorbance at 1621 cm^{-1}). The overall silk FTIR spectra bands did not show visible changes following enzyme exposure (Figure 3.5), so Fourier self-deconvolution (FSD) was applied to quantify the secondary structure (Hu et al., 2006). Protease XIV emerged as the most powerful proteolytic enzyme, as it caused significant changes in the secondary structure of both native and PEGylated silk nanoparticles. Protease XIV can cleave many amino acids (e.g., histidine, phenylalanine, tryptophan, tyrosine, lysine and arginine) that are found in the crystalline (222 sites) and amorphous regions (84 sites) (Figure 3.13). Overall, protease XIV has a low specificity, which facilitates its degradation of the crystalline and amorphous regions of silk (Brown et al., 2015). Conceivably, protease XIV first degraded the surface residues, which are expected to be present as random coils/α-helixes, followed by β-sheets, which are found in the core of the silk nanoparticle.

Papain was also included in this study because it is a cysteine protease enzyme that mimics the activity of lysosomal enzymes (Turk et al., 1997; Stoka et al., 2005). It can hydrolyse peptide bonds formed by the carboxyl groups of lysine and arginine and adjacent amino acid residues (Turk et al., 1997; Stoka et al., 2005). These lysine and arginine amino acid residues are found both in the heavy and light silk chain. However, they are not found in the crystalline domains, but four sites are present in the amorphous segments of the silk heavy chain and 22 sites in the C- and N-termini, as well as 15 sites in the silk light chain (Figure 3.13). By contrast, secondary structure analysis of silk nanoparticles treated with α-chymotrypsin showed no evidence of silk structural changes in either the crystalline or the random coil/α-helix structures. These observations were supported by morphological studies and the absence of loss of mass over the 20-day treatment cycle. The resistance of silk to α-chymotrypsin digestion over short time frames has also been reported by others (Brown et al., 2015).

Next, the morphological changes following enzymatic degradation of native and PEGylated silk nanoparticles were examined (Figure 3.9). Protease XIV effectively digested both native and PEGylated silk nanoparticles and elicited gross changes in morphology within 24 h. A slower, but similar, degradation pattern was observed following the papain treatment. The morphologies observed in the present study differed from those previously reported for silk films treated with protease XIV (Numata, Cebe and Kaplan, 2010; Lu et al., 2011). Our experience with silk films suggests that the silk format (i.e., nanoparticle versus film) as well as the processing parameters (e.g., water annealing, slow drying, and stretching) affects the degradation (Lu et al., 2011). The generation of nanofilaments (up to 10 nm thick and with a 10 m^2 surface area) (Numata et al., 2010) has been reported following protease XIV treatment of silk crystals, but no nanofilaments were observed in the present study. This chapter also did not observe any noticeable silk degradation in response to α-chymotrypsin treatment. The SEM images confirmed that α-chymotrypsin treatment had no detectable effect on the silk nanoparticle morphology (Figure 3.9).

Protease XIV is a useful model enzyme for studying the fundamental principles of silk degradation (and for direct comparison with many previous reports that typically use protease XIV). In the current study, also α-chymotrypsin was included because it is a relevant mammalian enzyme (unlike protease XIV which is a non-mammalian enzyme) (see Seib, 2017a for discussion). However, silk nanoparticles are typically designed for lysosomotropic drug delivery; thus, the degradation behaviour of silk nanoparticles in response to lysosomal enzymes is most relevant. This chapter reports the lysosomal model enzyme papain (discussed above and used at equivalent enzymatic units to permit direct comparisons), as well as lysosomes isolated from mammalian tissue. First, isolated lysosomes were extensively characterised (Figure 3.10 and 3.11). The preliminary results from *ex vivo* lysosomal degradation studies showed that native and PEGylated silk nanoparticles were slowly degraded over the initial five days, as evidenced by a reduction in particle size as well as by the formation of visible degradation products (Figure 3.12). Technical limitations (e.g., the difficulty of keeping a constant 3.5 U ratio of nanoparticles to enzymes while working with limited amounts of lysosomes, but also ensuring sufficient amounts of silk to permit detection and visualization by SEM) precluded the extension of these degradation studies beyond the 5-day time point. However, the lysosome-like model enzyme, papain (Stoka et al., 2005), also showed an initially slow silk nanoparticle degradation similar to that seen with the isolated enzymes; therefore, it is reasonable to speculate that silk nanoparticles would be fully degraded in lysosomes given longer exposure cycles.

3.5 Conclusion

The presence of surface PEGylation hindered enzyme accessibility and slowed silk degradation. Overall, silk nanoparticles showed a differential degradation behaviour in response to proteolytic enzymes, including lysosome-like enzymes (rank order: protease XIV > papain >> α-chymotrypsin). Preliminary studies with isolated lysosomal enzymes support the notion that silk nanoparticles will be degraded within lysosomes. In summary, this chapter provides the first insight into the proteolytic susceptibility of silk nanoparticles. In addition to modifying silk nanoparticle surface characteristics (Chapter 2) and ascertain their biodegradation (Chapter 3), controlling silk nanoparticle size is a fundamental parameter required when exploring silk nanoparticle capabilities. Therefore, the next chapter describes the manufacture of silk nanoparticles of different sizes.

Chapter 4

Microfluidic-assisted silk nanoparticle tuning

This chapter contains the results from the accompanying manuscript submitted in August 2018. In this study, I designed the study, performed all experiments and analysed all data sets as well as wrote the manuscript draft. John Totten performed confocal microscopy studies.

4.1 Introduction

Everyday silk from the domesticated silk moth (*B. mori*) is used both in the textile industry and in medical applications (most notably as a surgical suture material) (Holland et al., 2018). Over the past 30 years, a renewed interest has grown in the silk biopolymer for use in medical devices, including its recently approved use as a surgical scaffold for supporting and repairing soft-tissue damage in humans (Jewell et al., 2015). Silk is consistently viewed as a promising biopolymer for biomedical applications across a broad range of applications.

Silk has several important and exploitable characteristics, including (i) excellent mechanical properties, (ii) a long term track record of its safe use in humans, (iii) broad biocompatibility and biodegradability, (iv) mild aqueous processing conditions and (v) the ability to stabilise and protect therapeutic payloads (e.g., proteins and small molecular drugs) (Wenk et al., 2011; Li et al., 2015). In addition, a reversed engineered silk solution can be processed into numerous material formats, including hydrogels, scaffolds, films, microspheres and nanoparticles (reviewed in Seib, 2017b, 2018). For these reasons, silk nanoparticles are emerging as interesting carriers for drug delivery and are now often proposed for solid tumour drug targeting (Seib, Jones, et al., 2013; Tian et al., 2014; Wongpinyochit et al., 2015; Totten et al., 2017). Silk nanoparticles can be refined—for example, by surface decorating with polyethylene glycol (PEG)—to further tailor their performance by improving their colloidal stability and tuning their immune recognition (Wongpinyochit et al., 2015; Maitz et al., 2017) (Chapter 2). Both native and PEGylated silk nanoparticles have demonstrated drug loading, pH-dependent drug release, and selective degradation by protease enzymes as well as by *ex vivo* lysosomal enzymes (Wongpinyochit et al., 2018).

Silk nanoparticles can be manufactured by a broad spectrum of methods (reviewed in Mottaghitalab et al., 2015; Seib, 2017b), including poly(vinyl alcohol) blending (size range 300 nm to 10 μm) (Wang et al., 2010), emulsification (170 nm) (Myung et al., 2008), capillary microdot printing (25–140 nm) (Gupta et al., 2009), salting out (486–1200 nm) (Lammel et al., 2010), supercritical fluid technologies (50–100 nm) (Zhao, Xie, et al., 2015), ionic liquid dissolution (180 nm) (Lozano-Perez et al., 2015), electrospraying (59–80 nm) (Gholami et al., 2011), vibrational splitting of a laminar jet (up to 400 μm) (Wenk et al., 2008), electric fields (200 nm to 3 μm) (Lu et al., 2011), milling technologies (200 nm) (Rajkhowa et al., 2008) and organic solvent desolvation (35–170 nm) (Kundu et al., 2010; Seib, Jones, et al., 2013; Wongpinyochit et al., 2015, 2016). Among these methods, the manufacture of silk nanoparticles using desolvation is a robust and reproducible method that produces stable and uniform nano-sized particles. This method involves mixing an aqueous silk solution with a water-miscible organic solvent (e.g., methanol, isopropanol, acetone, etc.) to cause the nanoprecipitation of silk and the formation of silk nanoparticles. However, the current desolvation methods used to generate silk nanoparticles are time-consuming batch processes that allow little in-process control for tuning nanoparticle characteristics such as particle size. The ability to control the particle size and polydispersity of nanoparticles designed for drug delivery applications is important, as these particle attributes affect performance factors such as loading capacity (and thus drug dosage), targeting capabilities, cellular uptake and both whole body and cellular pharmacokinetic characteristics (Smith et al., 2008).

Over the past decade, remarkable progress has been made in the development of microfluidic-based fluid handling systems that can be applied to particle production for drug delivery applications (e.g. lipid, solid, tuned shape, etc.). Microfluidics enable the precise manipulation of liquids by allowing control of process parameters, such as the total flow rate, flow rate ratios between different phases, particle geometry, drug loading, etc., by design (Kastner et al., 2015; Guimarães et al., 2017; Gdowski et al., 2018). Nevertheless, despite the advantages of microfluidics, only a few studies have thus far exploited the technology to generate silk particles. The technologies have included glass capillary-based microfluidics (resulting in particles 145–200 μm in size) (Breslauer et al., 2010), double junction microfluidics (10–200 μm particles) (Toprakcioglu et al., 2017) and single and double T-junction droplet microfluidics (colloids 5–80 μm) (Shimanovich et al., 2017). However, these previous studies produced micro-sized particles that are too large size for use as carriers in many drug delivery applications (e.g., tumour targeting following intravenous dosing, endocytic uptake, intracellular trafficking, etc.).

The aim of this chapter was therefore to manufacture silk nanoparticles by desolvation using the NanoAssemblr^{TM} microfluidic setup. This chapter describes the impact of several process parameters, such as the total flow rate, flow rate ratios (i.e., aqueous to organic solvent) and organic solvent choices (acetone and isopropanol) on silk nanoparticle physical characteristics (e.g., yield, particles size, polydispersity, zeta potential, stability, secondary structure, and morphology). These bespoke silk nanoparticles were assessed to demonstrate the impact of silk nanoparticle size on uptake and intracellular trafficking.

4.2 Materials and Methods

4.2.1 Manufacturing of silk nanoparticles by microfluidics

The reverse engineered silk solution was firstly prepared as described in Chapter 2 (section 2.2.1). Silk nanoparticles were manufactured using a benchtop NanoAssemblr^{TM} instrument version 1.5 (model number: SN: NA-1.5-16) (NanoAssemblr^{TM}, Precision Nano-Systems Inc. Vancouver, Canada) equipped with a microfluidic cartridge (product code: NIT0012) (Figure 4.1). A 3% w/v aqueous silk solution and organic solvent (either acetone or isopropanol) were injected into separate chamber inlets, the silk nanoprecipitated in the microfluidic mixer, and the resulting nanoparticles were collected in the outlet (Figure 4.1). The total flow rates of the organic solvent and silk solution were varied from 1 to 12 mL/min, and the flow rate ratio was varied at 1:1, 3:1 and 5:1 (Figure 4.1). The collected silk nanoparticles were centrifuged at 48,400 × g for 2 h, the supernatant was aspirated and discarded. The pellet was resuspended in ultrapure water, vortexed, and subsequently sonicated twice for 30 s at 30% amplitude with a Sonoplus HD 2070 sonicator (ultrasonic homogenizer, Bandelin, Berlin, Germany). These centrifugation, washing, and resuspension steps were repeated at least twice more to produce the final silk nanoparticle preparation. The nanoparticles were characterised as detailed below and stored at 4 °C until use.

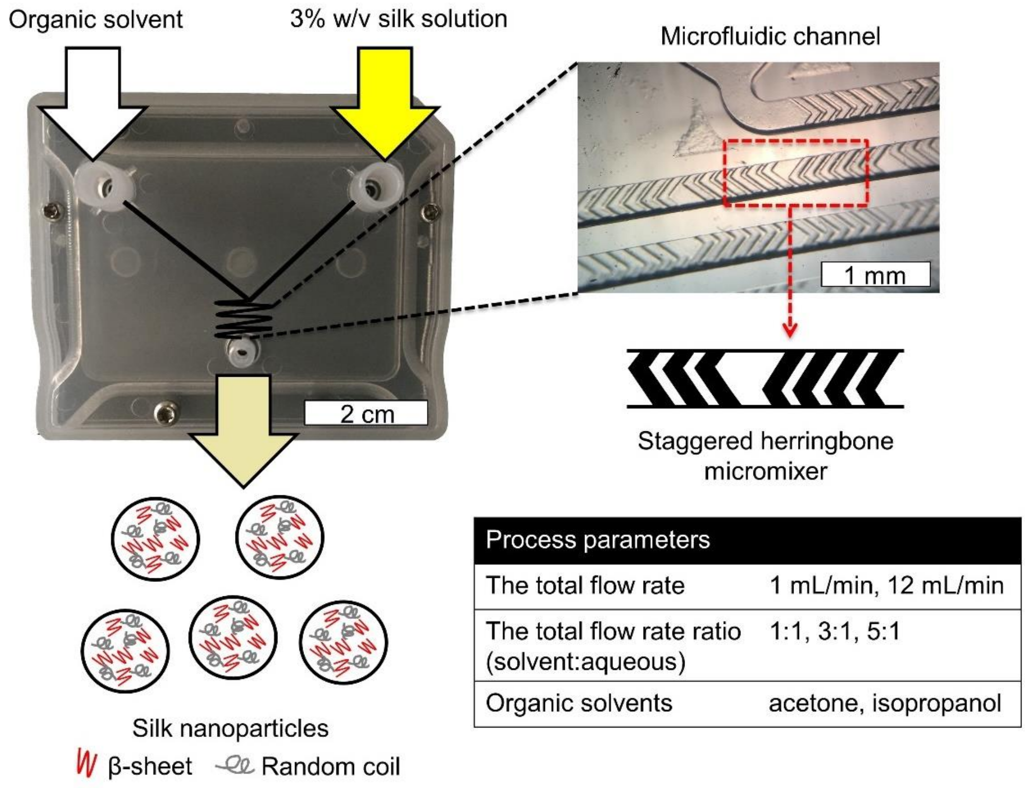

Process parameters	
The total flow rate	1 mL/min, 12 mL/min
The total flow rate ratio (solvent:aqueous)	1:1, 3:1, 5:1
Organic solvents	acetone, isopropanol

Figure 4.1 Schematic of silk nanoparticles manufacture using a microfluidic cartridge coupled with a benchtop NanoAssemblr^{TM} instrument. Organic solvent and a 3% w/v silk solution are pumped into two inlets and rapidly mixed, which leads to silk nanoparticle formation by nanoprecipitation. The microfluidic cartridge contains a micromixer channel, which is designed as staggered herringbone structure. The total flow rate, the total flow rate ratio, and solvent choice were the process parameters for this study.

4.2.2 The yield of silk nanoparticles

Several 2 mL Eppendorf tubes were weighed before adding silk nanoparticles (W1). The manufactured silk nanoparticles were then added, frozen and lyophilised overnight. The tubes containing the resulting freeze-dried silk nanoparticles were weighed again (W2) to determine the amount of silk nanoparticles using equation (4.1).

$$\%\ \text{yield of silk nanoparticles} = \frac{(W2-W1)}{\text{Amount of silk passed through the microfluidic system}} \times 100 \qquad (4.1)$$

4.2.3 Silk nanoparticle characterisation and stability in water

The particle size, PDI, and zeta potential of silk nanoparticles in ultrapure water were determined at 25 °C by dynamic light scattering (DLS, Zetasizer Nano-ZS Malvern Instrument, Worcestershire, UK) as detailed in Chapter 2 (section 2.2.4). The silk nanoparticles were stored in water at 4 °C and 37 °C and the size, PDI and zeta potential were determined at days 0, 14, 28, 35, and 42. All measurements were conducted in triplicate.

4.2.4 Secondary structure measurements of silk nanoparticles

The silk nanoparticles were frozen and then lyophilised overnight. The samples were subjected to secondary structure analysis by Fourier transform infrared (FTIR) spectroscopy (TENSOR II FTIR spectrometer, Bruker Optik GmbH, Ettlingen, Germany). The measurement and deconvolution method showed in Chapter 2 (section 2.2.5) and Chapter 3 (section 3.2.9).

4.2.5 Scanning electron microscopy of silk nanoparticles

The morphology of silk nanoparticles was assessed by scanning electron microscopy (SEM) using a FE-SEM SU6600 (Hitachi High Technologies, Krefeld, Germany) at 5 kV. Samples were pipetted onto a silicon wafer and lyophilised overnight. The specimens were coated with gold (15 nm thickness) using an ACE200 low vacuum sputter coater (Leica Microsystems, Wetzlar, Germany). The SEM images were processed using ImageJ v1.51j8 (National Institutes of Health, Bethesda, MD) (Schneider et al., 2017).

4.2.6 Manufacture of silk nanoparticles for *in vitro* assays

Silk nanoparticles were manufactured by the automated microfluidic benchtop NanoAssemblr^{TM} instrument, as detailed above. The total flow rate and ratio of isopropanol and 3% w/v aqueous silk solution were varied depending on the formulations: (i) 5:1 at 1 mL/min for 110 nm size and (ii) 5:1 at 12 mL/min for 215 nm size.

4.2.7 Macrophage responses toward silk nanoparticles

The murine macrophage RAW 264.7 cell line was cultured as detailed in Chapter 2 (section 2.2.6). For cytotoxicity studies, cells were seeded in 96-well plates at a density of 1.5×10^4 cells cm^{-2} and allowed to recover 24 h. Next, cells were treated with 2.5 to 100 µg/mL of 110 nm and 215 nm silk nanoparticles. After 48 h of incubation, cell viability was determined using MTT at 5 mg/mL in PBS; 20 µL of MTT was added to each well and cultures were incubated for 5 h. The formazan product was solubilized with 100 μL of DMSO and absorbance was measured at 570 nm. Untreated control cells represented 100% cell viability.

For TNF-α release, cells were seeded in petri dishes at a density of 1.5 × 10^4 cells cm^{-2} and allowed to recover overnight. Next, the culture medium was aspirated and replaced with fresh one containing either (i) 15 ng of LPS (Sigma-Aldrich, St. Louis, MO, U.S.A.), (ii) 10 μg/mL and 500 μg/mL of either 110 nm or 215 nm silk nanoparticles, and (iii) control medium. Cultures were incubated for 24 h and then the medium was collected, centrifuged at 6,000 × g for 5 min and assay supernatants were stored at −80 °C until analysis. Culture supernatants were assayed for TNF-α release using a DuoSet ELISA (R&D Systems, Minneapolis, MN, USA) according to the manufacturer's instructions. All measurements were derived from three biological replicates.

4.2.8 Labelling silk nanoparticles with fluorescent probes

A total of 3.5 mg of 110 and 215 nm silk nanoparticles were fluorescently labelled with Alexa Fluor 488 succinimidyl ester and Alexa Fluor 594 succinimidyl ester, respectively (Life Technologies, Carlsbad, CA, USA). The preparation process was described in Chapter 2 (section 2.2.11).

4.2.9 Cellular uptake and intracellular distribution of silk nanoparticles

RAW 264.7 cells were seeded in petri dishes at a density of 1.5 × 10^4 cells cm^{-2} and cultured in complete DMEM medium without phenol red. The cells were washed three times with PBS and the culture medium was replaced with either (i) control DMEM or (ii) 0.5 mg/mL mixed Alexa Fluor 488 (Life Technologies, Carlsbad, CA, U.S.A.) labelled 110 nm silk nanoparticles and Alexa Fluor 594 (Life Technologies, Carlsbad, CA, U.S.A.) labelled 215 nm silk nanoparticles. The cells were either (i) incubated for 1 h or (ii) incubated 1 h followed by three washes with PBS and chased in the culture medium for 3 h. The incubation was stopped by placing the cells on ice, aspirating all the medium and washing three times with ice-cold PBS. The cells were then stained with 1 µg/mL Hoechst 33342 (Thermo Scientific, Waltham, MA, USA) for 10 min at room temperature in the dark, washed three times with ice-cold PBS and live cells were imaged immediately with a Leica TCS-SP5 confocal laser scanning microscope (Leica Microsystems GmbH, Wetzlar, Germany) equipped with a 40× magnification water objective with a numerical aperture of 1.25. The data were exported to ImageJ 1.51j8 (National Institute of Health, U.S.A.) (Schneider et al., 2017) for image analysis and colocalisation.

4.2.10 Statistical analyses

Data were analysed using GraphPad Prism 7.0 (GraphPad Software, La Jolla, CA, U.S.A.). The statistical methods were described in Chapter 2 (section 2.2.13).

4.3 Results

4.3.1 The yield of silk nanoparticles

The percentage yield of silk nanoparticles was dependent on the total flow rate, the solvent ratio and the actual solvent used. A solvent:aqueous total (flow rate) ratio of 5:1 gave the best yield for both solvent systems (Figure 4.2). The yield of silk nanoparticles was higher when prepared from isopropanol than from acetone, especially at the 1 mL/min flow rate. The highest silk nanoparticle yield (11.7% w/w of silk) was obtained from isopropanol with the isopropanol:silk (i.e., aqueous phase) ratio of 5:1 and a 1 mL/min flow rate (Figure 4.2B).

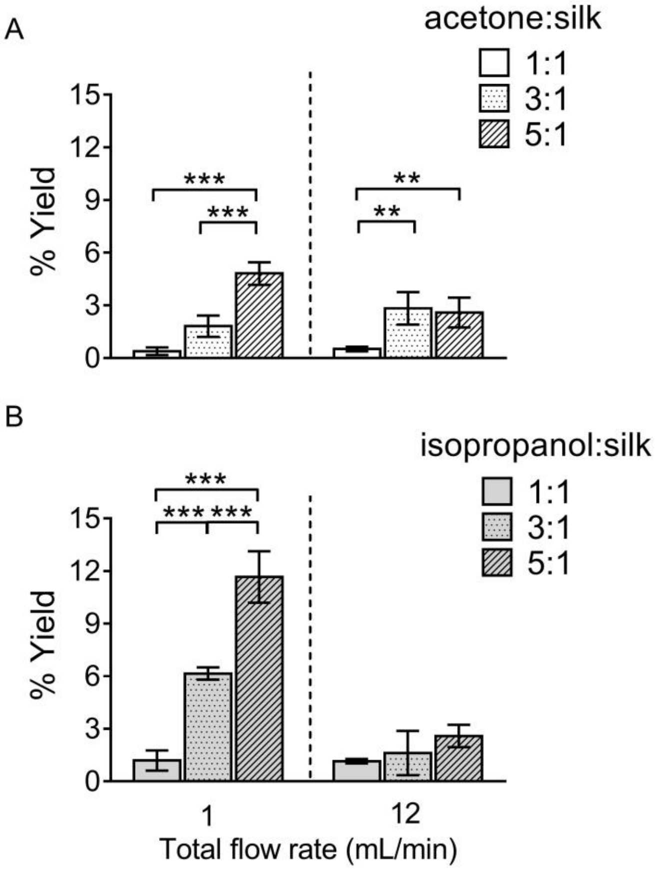

Figure 4.2 Percentage yield of silk nanoparticles produced with a NanoAssemblr^{TM} benchtop platform by varying the total flow rate and the flow rate ratios. The percentage yield of silk nanoparticles using the organic solvents (A) acetone, and (B) isopropanol. An asterisk denotes statistical significance as follows: $*P < 0.05$, $**P < 0.01$, $***P < 0.001$. The data represents the mean ± SD, error bars are hidden in the plot-symbol when not visible, n = 3.

4.3.2 Silk nanoparticle characterisation and their stability in water

For DLS measurement, the overall particle size of silk nanoparticles ranged from 110 to 310 nm, with a polydispersity ranging from 0.1 to 0.25 and a negative surface charge ranging from -20 to -30 mV (Figure 4.3). The acetone/aqueous total flow rate ratio of 3:1 generated the smallest size (110 nm), while the acetone/aqueous total flow rate ratio of 1:1 generated larger particles (200 nm) (Figure 4.3A). By contrast, the isopropanol/aqueous ratio of 5:1 at a 1 mL/min flow rate generated the smallest size (110 nm) and the isopropanol/aqueous total flow rate ratio of 1:1 at 12 mL/min generated the largest particle size (310 nm) (Figure 4.3A). However, a solvent/aqueous ratio of 1:1 showed higher polydispersity (>0.2), indicative of a wider particle size distribution (Figure 4.3B). The solvent/aqueous total flow rate ratio of 5:1 generated higher negative charges of silk nanoparticles when compared with a lower ratio of solvents (Figure 4.3C).

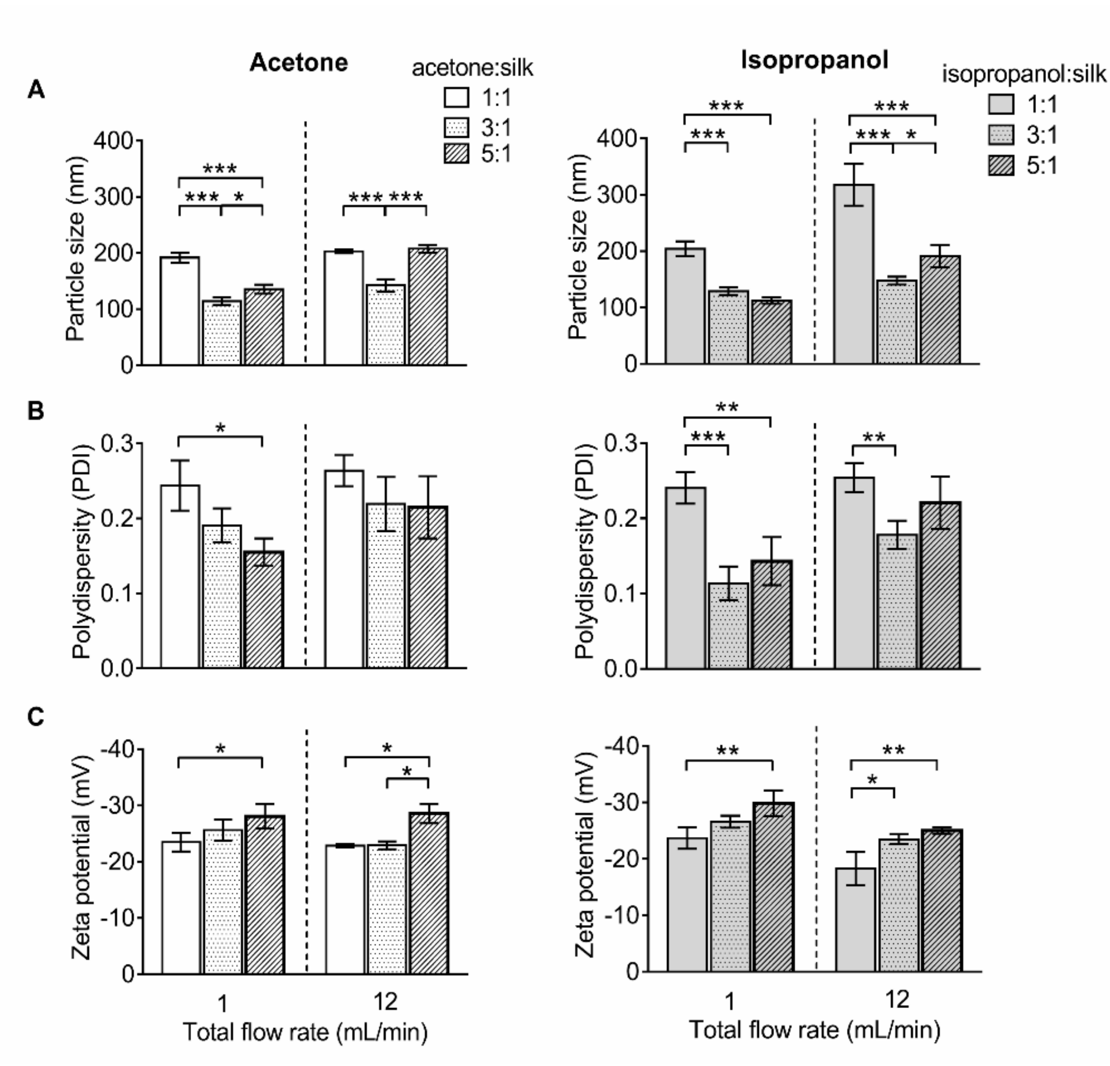

Figure 4.3 Characterisation of silk nanoparticles produced with acetone and isopropanol using a NanoAssemblr^{TM} benchtop platform with different total flow rates and ratios. (A) Particles size (nm), (B) Polydispersity index (PDI), and (C) Zeta potential of silk nanoparticles. An asterisk denotes statistical significance as follows: *P < 0.05, **P < 0.01, ***P < 0.001. The data represents the mean ± SD, error bars are hidden in the plot-symbol when not visible, n = 3.

The particle size stability was also determined for up to 42 days. For the acetone system, all formulations were stable in water at 4 °C for up to 42 days. Silk nanoparticles generated with a ratio of solvent to silk of 5:1 at 12 mL/min showed a statistical significant increase in particle size after storage at 37 °C for 42 days (Figure 4.4). The polydispersity of the silk nanoparticles did not change at 4 °C and 37 °C for up to 42 days (Figure 4.5). For the isopropanol system, silk nanoparticles generated with the ratios of solvent/silk of 3:1 and 5:1 were stable at 4 °C and 37 °C for up to 42 days. However, silk nanoparticles generated with a silk/isopropanol flow rate ratio of 1:1, especially at the total flow rate of 12 mL/min, were not stable after 14 days (Figure 4.4). The polydispersity of the silk nanoparticles from an isopropanol/silk flow rate ratio of 5:1 increased after 28 days (Figure 4.5). The negative surface charges of the silk nanoparticles from all formulations significantly decreased after 14 days at 37 °C (Figure 4.6).

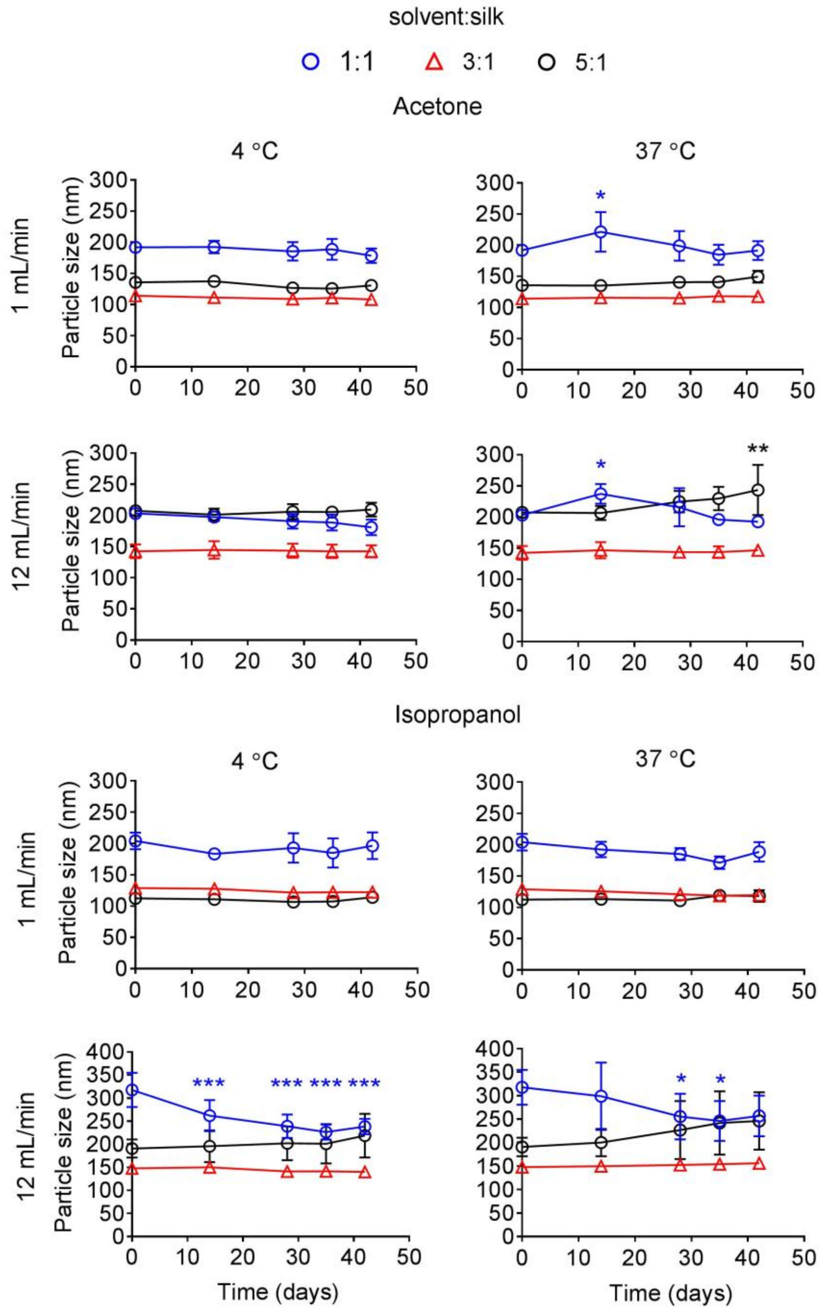

Figure 4.4 Stability of silk nanoparticles manufactured with a microfluidic-based method by varying solvents, the total flow rate, and the flow rate ratios. The particle size of the silk nanoparticles in water at 4 °C and 37 °C was measured over 42 days. An asterisk denotes statistical significance as follows: *P < 0.05,

**P < 0.01, ***P < 0.001. The data represents the mean ± SD, error bars are hidden in the plot-symbol when not visible, n = 3.

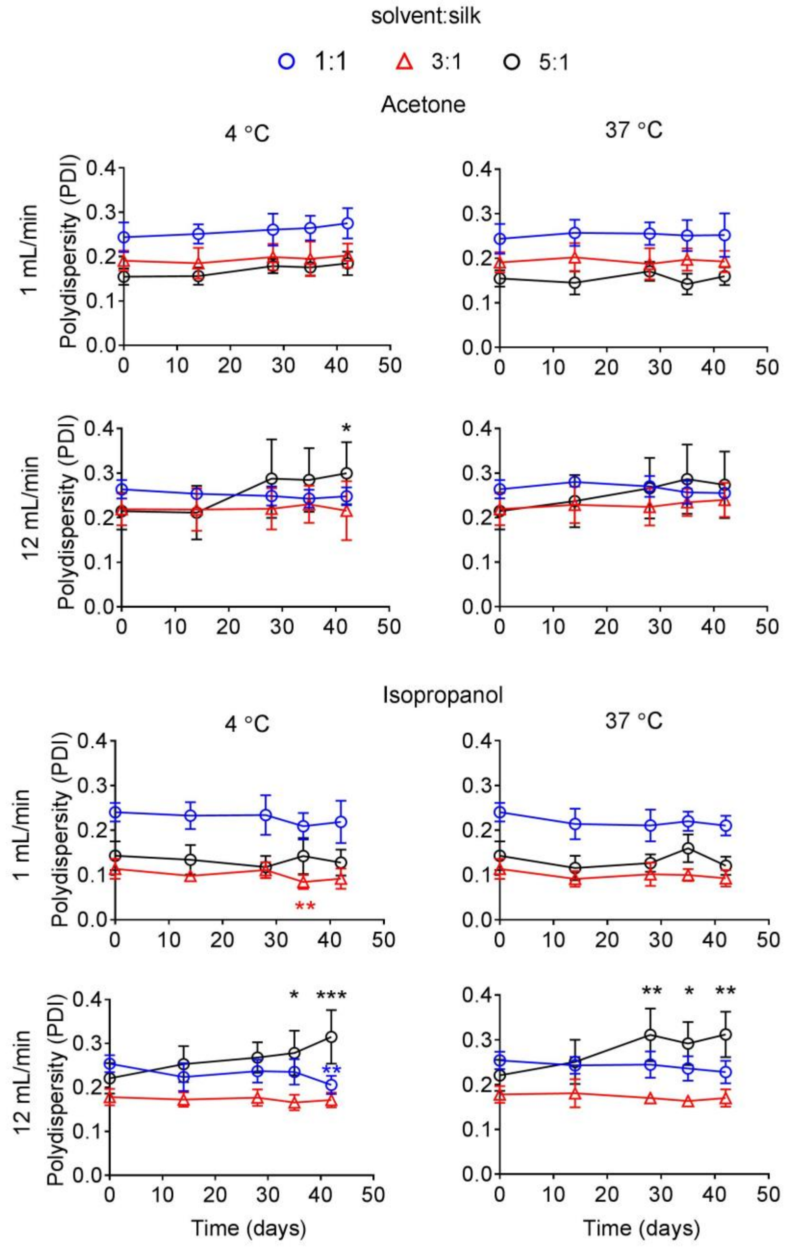

Figure 4.5 Stability of silk nanoparticles manufactured with the microfluidic-based method by varying solvents, the total flow rate and the total flow rate ratio. Polydispersity (PDI) of silk nanoparticles in water at 4 °C and 37 °C was measured at day 0, 14, 28, 35 and 42. An asterisk denotes statistical significance

as follows: *P < 0.05, **P < 0.01, ***P < 0.001. The data represents the mean ± SD, error bars are hidden in the plot-symbol when not visible, n = 3.

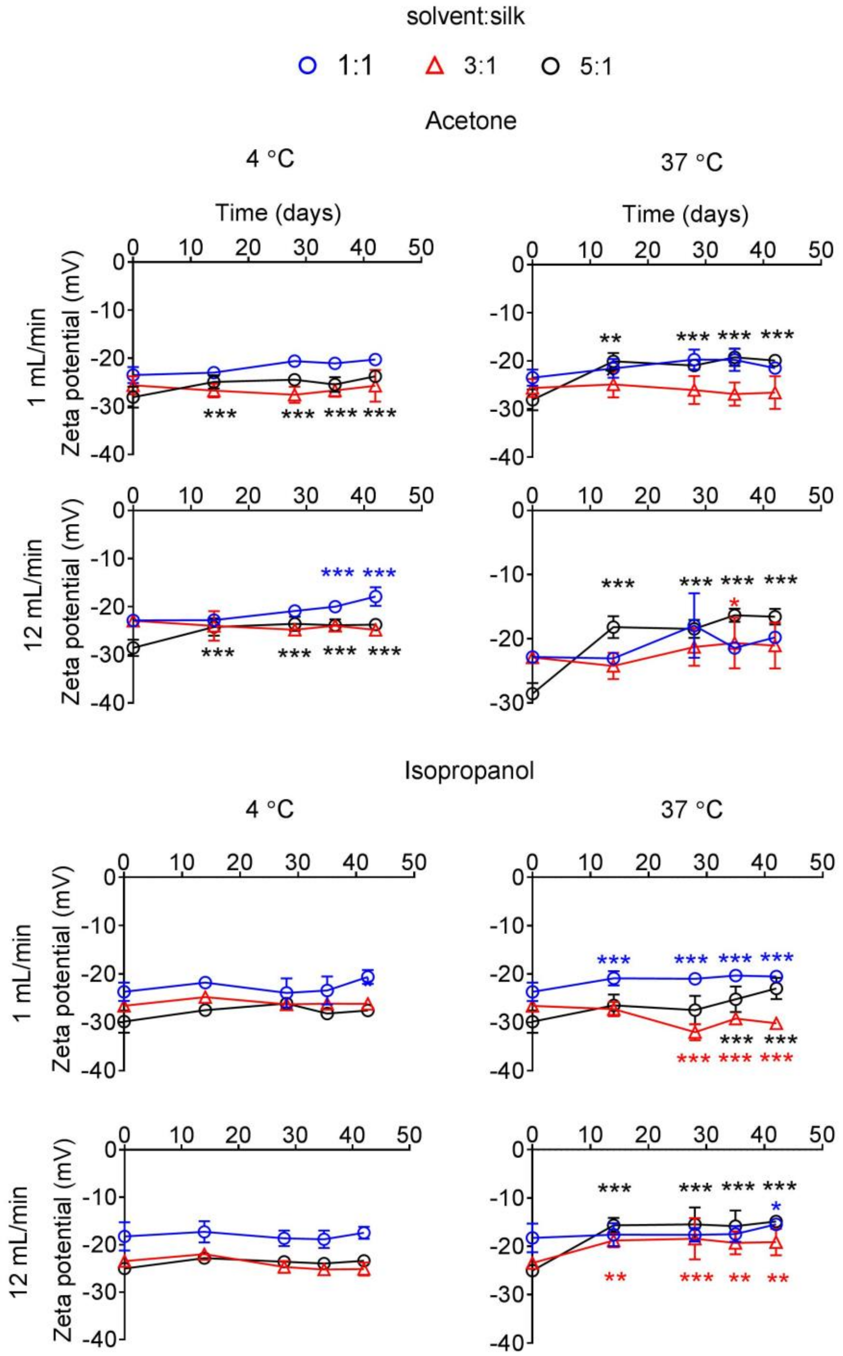

Figure 4.6 Stability of silk nanoparticles manufactured with the microfluidic-based method by varying solvents, the total flow rate and the total flow rate ratio. Zeta potential of silk nanoparticles in water at 4 °C and 37 °C was measured at

day 0, 14, 28, 35 and 42. An asterisk denotes statistical significance as follows: *P < 0.05, **P < 0.01, ***P < 0.001. The data represents the mean ± SD, error bars are hidden in the plot-symbol when not visible, n = 3.

4.3.3 Secondary structure measurement

The secondary structure of the silk nanoparticles produced under different process conditions was determined by FTIR measurement following peak analysis. Overall, silk nanoparticles manufactured using microfluidics contained high β-sheet content (48–51%) with no significant effect from the microfluidic parameters (Figure 4.7).

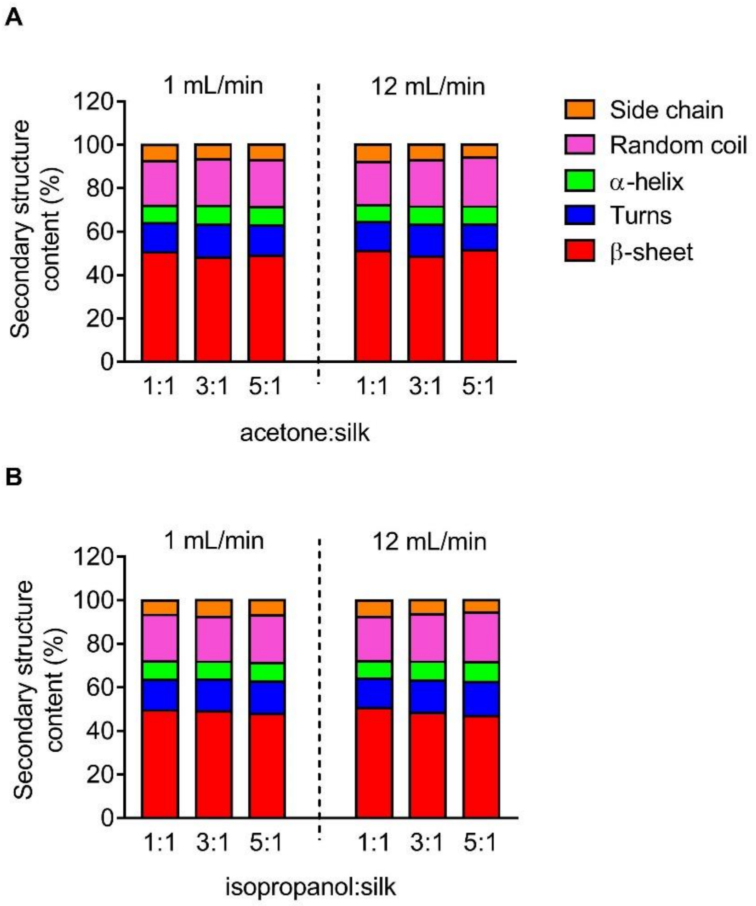

Figure 4.7 Secondary structure analysis of silk nanoparticles produced by microfluidics by varying the total flow rate, flow rate ratio, and solvents.

Secondary structure content (%) of silk nanoparticles using (A) acetone and (B) isopropanol as the organic solvent.

4.3.4 Scanning electron microscope of silk nanoparticles

Next, the morphology of silk nanoparticles was analysed by SEM (Figure 4.8). The silk nanoparticles generated by the solvent/aqueous total flow rate ratios of 3:1 and 5:1 had spherical shapes and uniform distributions, which correlated with the DLS measurements. Silk nanoparticles obtained using a total flow rate ratio of 1:1, especially at the total flow rate of 12 mL/min, showed larger sizes (up to 400 nm), irregular shapes, and wide particle distributions (particles ranging from 200 nm to 400 nm) (Figure 4.8).

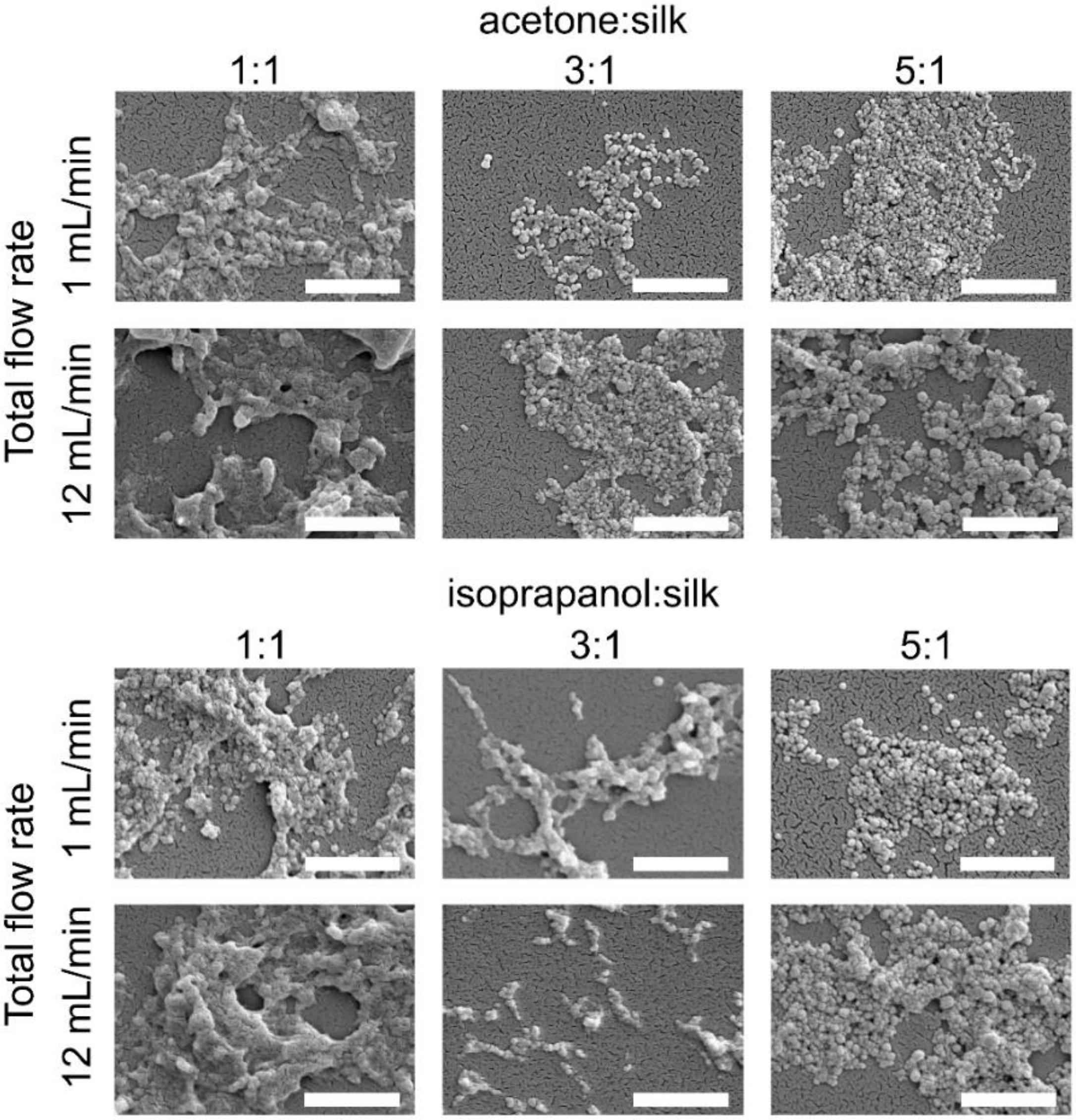

Figure 4.8 Scanning electron microscopy (SEM) images of silk nanoparticles produced using the NanoAssemblr^{TM} benchtop platform with different total flow rates and ratios of organic solvents (scale bar = 1 μm).

4.3.5 *In vitro* cytotoxicity and macrophage responses to silk nanoparticles

For cytotoxicity studies, two different sizes of silk nanoparticles (110 and 215 nm) were generated. No significant differences were noted in cytotoxicity between the two different sizes of silk nanoparticles (Figure 4.9A). The IC_{50} of 110 nm and 215 nm silk nanoparticles towards RAW 264.7 cells was >100 μg/mL. The TNF-α release by macrophages exposed to silk nanoparticles and lipopolysaccharide (LPS, positive control) was also measured (Figure 4.9B). TNF-α release in response to 110 nm silk nanoparticles (at both 10 μg/mL and 500 μg/mL) was not significantly different from the release by control cultures. However, treatment of the cells with 500 μg/mL of 215 nm silk nanoparticles caused a small, but statistically significant, increase in TNF-α release when compared to 110 nm nanoparticles at the equivalent dose (Figure 4.9B). There was a statistical difference TNF-α release between concentration of 10 μg/mL and 500 μg/mL of the silk nanoparticles (Student's t-test).

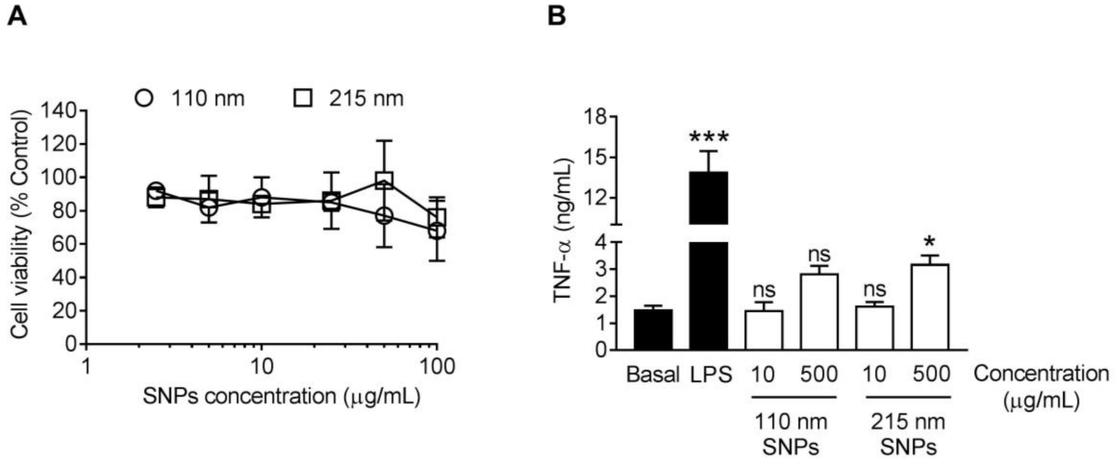

Figure 4.9 *In vitro* cytotoxicity and TNF-α release of silk nanoparticles in macrophages (RAW 264.7 cells). (A) For cytotoxicity tests, 2.5 to 100 μg/mL of 110 nm and 215 nm silk nanoparticles (SNPs) were incubated with the cells for 48 h. (B) The TNF-α release into culture supernatants was quantified following 24 h of exposure to 15 ng of LPS (positive control) or 10 μg/mL and 500 μg/mL of 110 nm and 215 nm silk nanoparticles and compared to release by untreated control cells (basal TNF-α levels). Dunnett's post hoc test was used to evaluate statistical differences between the basal levels and the samples. An asterisk

denotes statistical significance as follows: *P < 0.05, **P < 0.01, ***P < 0.001. The data represents the mean ± SD, error bars are hidden in the plot-symbol when not visible, n = 3.

4.3.6 Cellular uptake and intracellular distribution of silk nanoparticles in macrophages

Cellular uptake and intracellular distribution of 110 nm and 215 nm silk nanoparticles were qualitatively studied using live cell confocal microscopy (Figure 4.10). Following a 1 h pulse, 110 nm silk nanoparticles and 215 nm silk nanoparticles were internalised into different early endosome compartments. However, after a 3 h chase, both sizes of silk nanoparticles were localised in the same late endocytic compartments. These results were corroborated by profile plots that showed high co-localisation after the 3 h chase (Figure 4.10).

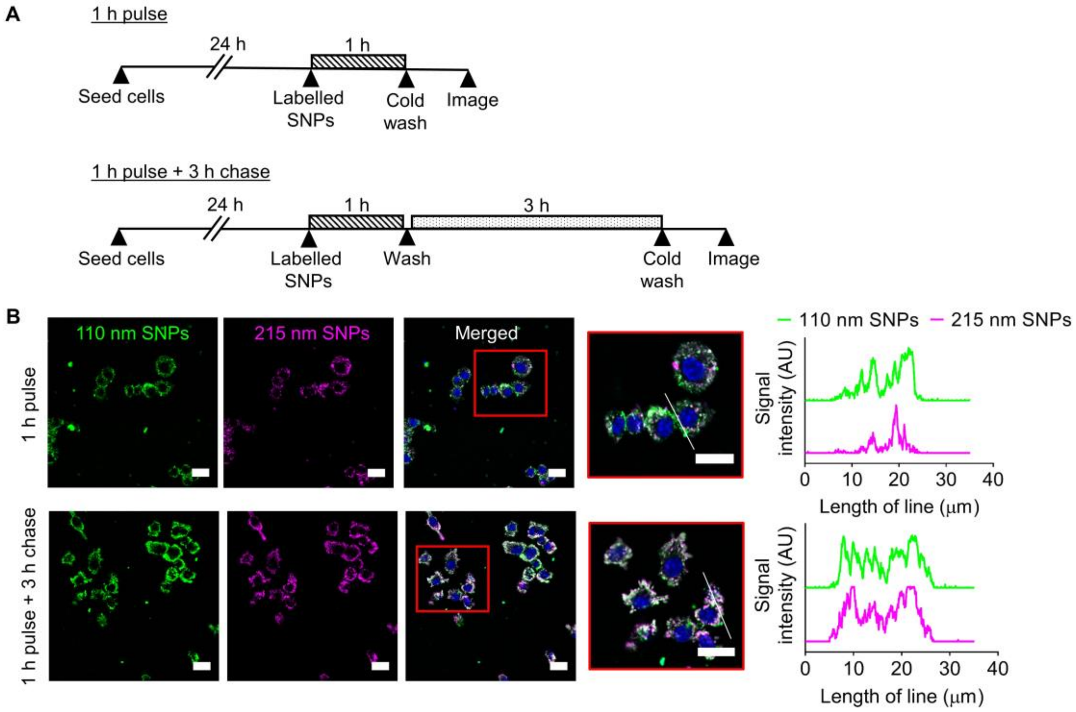

Figure 4.10 Impact of silk nanoparticle size on trafficking in macrophages. (A) Experimental outline. Cells were either (i) pulsed with a mixture of 110 nm and 215 nm labelled silk nanoparticles for 1 h and imaged or (ii) pulsed with the labelled silk nanoparticles for 1 h and then chased for 3 h and imaged. (B) Live cell confocal fluorescence microscopy of the mixture of Alexa Fluor 488-labelled 110 nm silk nanoparticles (green) and Alexa Fluor 594-labelled 215 nm silk nanoparticles (magenta) in RAW 264.7 cells. The scale bars are 20 μm. The white lines in the high magnification images are used in profile plots to highlight the colocalisation of 110 nm and 215 nm silk nanoparticles in the cells.

4.4 Discussion

Silk from *B. mori* has a strong clinical track record (Holland et al., 2018) and is currently emerging as a promising biomaterial for drug delivery (e.g. Yucel, Lovett and Kaplan, 2014; Seib, 2017, 2018). An increasing number of studies have now reported the manufacture of silk nanoparticles (typically in the 100 nm size range), often for (anticancer) drug delivery applications (e.g., Kundu et al., 2010; Tian et al., 2014; Montalban et al., 2018). The use of silk nanoparticles described in this thesis has specifically focused on drug loading and release, surface modification (Chapter 2) (Wongpinyochit et al., 2015), intracellular drug delivery (Totten et al., 2017), and the degradation of silk nanoparticles in cells (Chapter 3) (Wongpinyochit et al., 2018) as well as on the impact of these nanoparticles on metabolism and blood compatibility (Maitz et al., 2017; Saborano et al., 2017). However, in all of these previous studies, 100 nm silk nanoparticles were used, which were fabricated using a "conventional" nanoprecipitation method; i.e., manually adding the reverse-engineered silk solution to the organic phase (Chapter 2 and Chapter 3) (Wongpinyochit et al., 2016). This production method is a batch-based process and affords no in-process control to fine tune the particle properties. Therefore, a manufacturing method that enables rapid silk nanoparticle production while providing control over the nanoparticle characteristics would represent a substantial improvement and would open up the use of these silk nanoparticles in a wider spectrum of biomedical applications.

Microfluidic-based technologies have successfully been used for liposome and nanoparticle production (e.g., using 1,2-diplmitoylphosphatidylcholine, phosphatidylcholine, polycaprolactone-block-poly(ethylene oxide) and poly(lactide-co-glycolide)-b-polyethyleneglycol), which allow scalable production and control over particle characteristics (Zhigaltsev et al., 2012; Lim et al., 2014; Joshi et al., 2016; Xu et al., 2016). Many different microfluidic platform designs have been introduced, but the most important feature is the mixer channel layout, which have included, for example, droplet based (Teh et al., 2008) as well as T and Y shaped mixers (Wang, 2013; Liu et al., 2015). The staggered herringbone structure is a highly efficient micromixer and is now one of the commonest designs; it enhances the mixing of aqueous and solvent phases due to chaotic advection phenomena (Stroock, 2002). In the present study, the fully automated NanoAssemblr^{TM} platform was used in combination with a commercially available microfluidic chip that incorporates the staggered herringbone structure design (Figure 4.1).

This chapter describes the first study to report the “continuous” manufacture of silk nanoparticles. The determination of the production efficiency for generation of silk nanoparticles showed that a total flow rate at 1 mL/min at a 5:1 solvent/aqueous ratio was optimal for achieving the highest silk nanoparticle yields (Figure 4.2). One might speculate that this slow total flow rate (versus 12 mL/min) and high solvent concentration allows more time for interaction between the aqueous and solvent phases, thereby enabling a better removal of solvating water from the silk structure and ultimately resulting in silk nanoparticle formation through β-sheet formation (Zhang et al., 2007). Therefore, solvents with a high capacity to form hydrogen bonds with water are predicted to be good candidates for silk nanoparticle formation. Therefore, isopropanol was selected (a polar protic organic solvent), which has a greater ability than acetone (or DMSO) (polar aprotic organic solvents) to form hydrogen bonds with water. Previous batch-based studies have also successfully used isopropanol for silk nanoparticle formation (particle size ranging from 100 to 400 nm) (Zhang et al., 2007; Tudora et al., 2013). In the current study, the low flow rate of 1 mL/min, the selection of isopropanol and the high organic to aqueous ratio (i.e. 5:1) in particular allowed significant improvements in yield (Figure 4.2). Both the solvent/aqueous ratio and the flow rate had a significant impact on the particle size, PDI, and zeta potential (Figure 4.3). The high solvent/aqueous ratio (i.e., ≥ 3:1) generated small particles (110 to 200 nm) with a low polydispersity index (0.1 to 0.2) and high negative surface charge (-23 to -30 mV). Overall, these data highlight the importance of using sufficient amounts of solvent to extract the solvating water from the silk to initiate uniform nanoparticle nucleation and ultimately to narrow the particle size distribution. The zeta potential of silk nanoparticles produced using the microfluidic setup was less negative (-20 to -30 mV) when compared to those produced by a standard batch method (-40 to -50 mV as shown in Chapter 2). This comparatively low negative zeta potential could be a consequence of the continuous flow during particle formation, which could ultimately result in a different packing arrangement.

This chapter also examined silk nanoparticle stability in water over 42 days, because (medical) applications of these silk nanoparticles required them to have long-term stability during storage (Figure 4.4, 4.5 and 4.6). Silk nanoparticles generated from microfluidics using the total flow rate ratio of solvent/aqueous ≥ 3:1 were stable at 4 °C and 37 °C over the entire study period. This finding confirms the importance of the desolvating solvent concentration for silk nanoparticle formation and stability because low solvent to silk concentration ratios resulted in nanoparticles with compromised stability. Therefore, it was also expected to see differences in secondary structure because silk nanoparticles with a low β-sheet content have been reported (Xiao et al., 2016). However, the secondary structure content of the silk nanoparticles prepared by microfluidics had a comparable amount of β-sheet structure (Figure 4.7) and this content was therefore independent of the process parameters. Overall, all the silk nanoparticles generated were highly crystalline and essentially identical with respect to their secondary structure to nanoparticles that have previously reported (Wongpinyochit et al., 2015; Totten et al., 2017).

Morphological assessment by electron microscopy indicated that the total flow rate and the flow rate ratio were key parameters that influenced the particle appearance (Figure 4.8). Silk nanoparticles generated with a slow flow rate (1 mL/min) showed a more globular shape and appeared as discrete nanoparticles when compared with those generated using a flow rate of 12 mL/min, suggesting that the fast flow rate could disrupt the spherical morphology during particle formation and result in a greater tendency of these particles to undergo a loose fusion. Overall, a more discrete globular shape and uniformity required a solvent/aqueous flow rate ratio ≥ 3:1 (and a slow flow rate). This minimum solvent to water ratio for the formation of silk nanoparticles is consistent with previous batch-based silk particle work (Tudora et al., 2013).

The nanosize range of silk nanoparticles is expected to result in solid tumour targeting in medical applications because the passive accumulation of nanoparticles (e.g. 100 to 200 nm) is facilitated by the tumour pathophysiology, which includes a leaky vasculature and impaired lymphatic clearance that results in EPR effect of nanomedicines (Matsumura and Maeda, 1986). However, even EPR-mediated targeting typically results in only a small fraction of the administered dose reaching the tumour (Natfji et al., 2017), with most medicine accumulating in other tissues, predominantly in macrophages of the mononuclear phagocytic system (Gustafson et al., 2015). Macrophages are intimately associated with solid tumour development (Mantovani et al., 2017); therefore, the macrophage response towards nanomedicines is an important consideration. Previous work by the Seib lab demonstrated that silk nanoparticles can prime macrophages towards a M1-like phenotype (Saborano et al., 2017). Emerging evidence indicates that nanoparticle size is important for macrophage recognition and subsequent particle internalisation (Kusaka et al., 2014). This chapter therefore examined the relationship of silk nanoparticle size to cytotoxicity, TNF-α release, cellular uptake and intracellular distribution. Cytotoxicity was absent at the doses studied (i.e., keeping the amount of silk constant), with no obvious size-dependent cytotoxicity (Figure 4.9A). Low and high doses of 110 nm and 215 nm silk nanoparticles was selected and TNF-α release was monitored. At the maximum tested concentration, only a small increase was noted, but a statistically significant difference in TNF-α release was observed for 215 nm silk nanoparticles when compared to 110 nm particles (Figure 4.9B). However, the biological relevance of this difference is currently not known. Preliminary intracellular trafficking studies showed that 110 nm and 215 nm silk nanoparticles were both internalised by endocytosis within 1 h, but they were localised into different early endocytic structures. Following a 3 h chase, both silk nanoparticles accumulated in late endosomal/lysosomal compartments, as suggested by their peri-nuclear localisation (Figure 4.10). The observed differences in trafficking at the early time point could suggest that endocytic compartments were size-selective, as reported previously for labelled erythrocytes (Berthiaume et al., 1995). However, more detailed studies are needed to better characterise the intracellular trafficking of silk nanoparticles.

4.5 Conclusion

The use of a microfluidic setup enabled the rapid, reproducible and controllable manufacture of silk nanoparticles. The total flow rate and the flow rate ratio were the two key process parameters that affected silk nanoparticle characteristics. A total flow rate of 1 mL/min and a solvent to aqueous phase ratio of 5:1 provided the smallest particle size, the highest yield and best stability of silk nanoparticles. Subjecting the optimized silk nanoparticles to preliminary biological assessment indicated that they induced a particle-mediated macrophage response. In summary, microfluidic-assisted manufacturing enables the fine tuning of silk nanoparticles.

It is important to note that this chapter only described the manufacture of silk nanoparticles but not drug loading. Similar approaches as described in Chapter 2 can be used to load these silk nanoparticles. Alternatively, *in situ* loading strategies are envisaged to be suitable to incorporate drug into these silk nanoparticles (detailed in Chapter 6). However, it is currently not known where the payload binds within the silk secondary/tertiary structure. Therefore, *in silico* modelling studies were performed to advance our understanding (Chapter 5).

Chapter 5

Exploring native amorphous-crystalline silk structures and molecular binding behaviour in response to pH

This chapter contains the results from the manuscript in preparation. In this study, I designed, analysed and carried out all modelling work, as well as prepared the manuscript draft.

5.1 Introduction

Silk is a fascinating biopolymer because it combines high tensile strength with extensibility resulting in tough materials (Omenetto and Kaplan, 2010). Silk has been used in a wide range of applications from luxury fabrics to medical applications such as tissue regeneration. Silk consists of two main proteins, which are silk fibroin and sericin as detailed in Chapter 1. The silk fibroin contains a heavy chain (5,263 amino acid residues, 390 kDa) and a light chain (26 kDa), which is linked by a single disulphide bond at the C-terminus. The amino acid composition of the heavy chain is dominated by glycine (46%), alanine (30%), serine (12%) and tyrosine (5.3%) (Zhou et al., 2000). The primary structure of the heavy chain contains a (i) C-terminus, (ii) N-terminus, (iii) 11 non-repetitive sequences and (iv) 12 highly repetitive sequences (Figure 5.2A). The repetitive sequences of heavy chain are hydrophobic regions which are rich in GAGAGS and GAGAGY motives (G = glycine, A = alanine, S = serine and Y = Tyrosine). These blocks can be crystallised into β-sheets providing silk with its strength and stability. The non-repetitive amino acid sequences are hydrophilic groups forming amorphous structures responsible for the elasticity of silk (Zhou et al., 2001).

To date there are two main silk structure models: silk I and silk II. These structures are primarily based on X-ray diffraction and NMR studies (Wilson et al., 2000). Silk I is water soluble and naturally occurs in the posterior silk gland of silkworms. Silk I contains a high amorphous structure content such as random coils, along with ordered regions of GAGSGAGA as called silk I* (Asakura et al., 2015). The silk I* structure at the atomic level is determined using NMR (Suzuki et al., 2014). The NMR chemical shifts of the silk structure can be converted into torsion angles of the backbone of silk using the TALOS-N programme (Shen and Bax, 2013). The torsion angles describe the rotation of polypeptide chain around the two bonds in a protein including the phi (ϕ) angle, an angle around the Cα-N bond, and the psi (ψ) angle, an angle around the Cα-C (Figure 5.1A). The torsion angles of the silk structure derived from the TALOS-N programme are then plotted on a Ramachandran plot (Figure 5.1B), which can be defined the secondary structure of silk as a type II β-turn (Figure 5.1C).

In contrast, silk II refers to the water insoluble structure (e.g. β-sheet); the transition of silk I to II is triggered by environmental factors such as a drop in pH (as occurs in the anterior silk gland). Current evidence suggests that silk stored in the gland adopts a reversible micelle-like structure (100-200 nm) with a shell of hydrophilic domain and a core of hydrophobic crystallites (Jin and Kaplan, 2003). The silk micellar structure is assumed to contribute to the overall shape and properties of silk nanoparticles after exposure to organic solvents such as acetone.

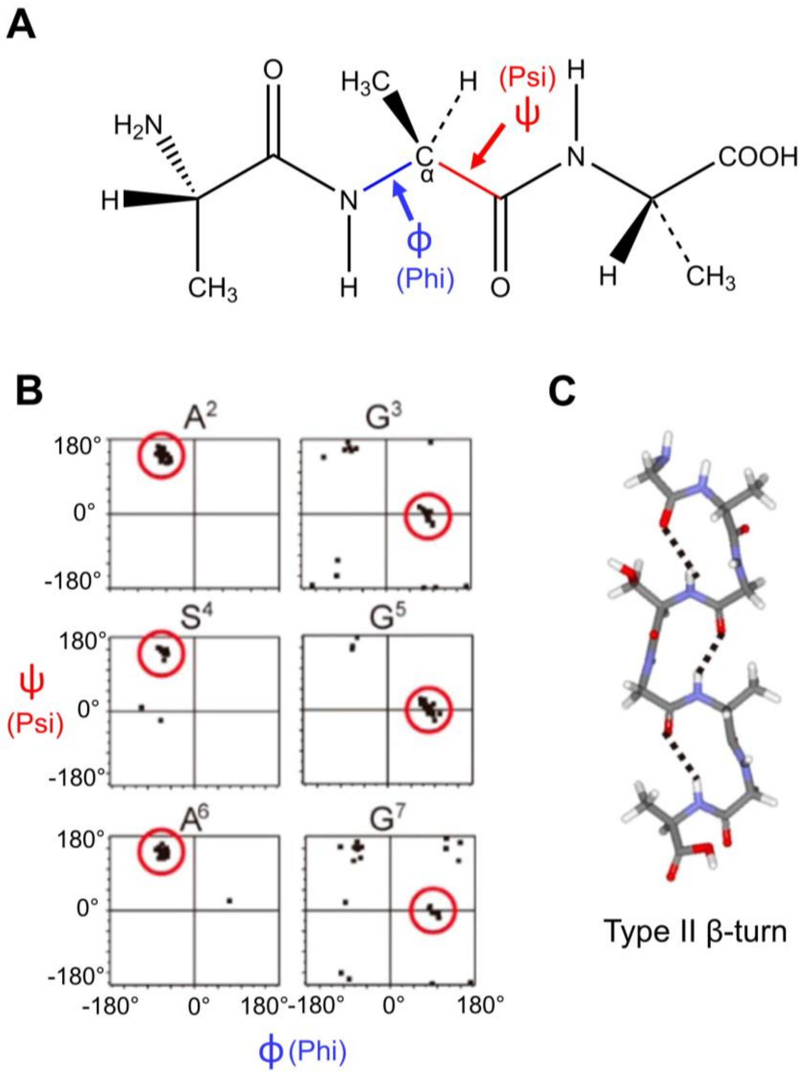

Figure 5.1 The torsion angles (ϕ, ψ) map and the type II β-turn structure. (A) A tripeptide of alanine shows location of phi and psi angles (B) Torsion angles for GAGSGAG motifs of silk obtained from the TALOS-N programme are plotted on a Ramachandran plot (Shen and Bax, 2013). (C) The ideal type II β-turn structure constructed using the averaged torsion angle in the red circle from the map (B). The red circles indicate area of torsion angles of ideal type II β-turn structure.

The potential of silk nanoparticles for drug delivery applications is being studied, especially for solid tumour targeting (Wongpinyochit et al., 2015; Totten et al., 2017).

Doxorubicin, a common chemotherapeutic agent, has previously been successfully loaded into silk nanoparticles (Chapter 2) and films (Seib and Kaplan, 2012). The ability of silk nanoparticles to support doxorubicin adsorption from solution is believed to be due to electrostatic interactions between negative charges of the silk structure and positive charges of doxorubicin at pH 7.4. Support for this hypothesis comes from *in vitro* studies where it was shown that doxorubicin release could be accelerated by placing silk nanoparticles in physiologically relevant acidic environments (doxorubicin release pH 4.5 >> 6.0 > 7.4) (Seib, Jones, et al., 2013; Wongpinyochit et al., 2015). There is evidence that the N-terminal domain of silk is the pH-sensitive region driving silk self-assembly (Lammel et al., 2010; He et al., 2012); it is therefore plausible that this region also interacts with positively charged, low molecular weight drugs. However, the precise mechanism between silk and doxorubicin is currently not known at the atomic level.

Molecular dynamics (MD) simulations have been widely used to investigate the motion of large molecules such as proteins (e.g. protein folding and ligand binding at the nanoscale) (Arinaminpathy et al., 2002; Beck and Daggett, 2004). Over the past 10 years, MD simulation has been used to study the silk structure, its mechanical properties (Keten et al., 2010; Xiao et al., 2013; Cheng et al., 2014) and the interaction with other molecules (e.g. graphene) (Cheng et al., 2015). However, the silk structure used previously was small (e.g. a stack of poly(GA) β-sheet 90 amino acids long) (Xiao et al., 2009; Cheng et al., 2014; Zhao et al., 2017). Furthermore, the amino acid composition did not faithfully reflect key components of the silk structure. In this chapter, a 300 amino acid long silk fragment containing both amorphous and crystalline domains was generated. However, the use of such a structure for MD simulation is challenging because of the time scales required to fully explore the conformation space as well as the conformational energy barriers (e.g. a 1 μs simulation of a small system using 24 processors takes several months to complete) (Durrant and McCammon, 2011). Nevertheless, this limitation can be addressed by using advanced sampling algorithms such as well-tempered (WT) metadynamics (Barducci et al., 2008; Laio and Gervasio, 2008). WT-metadynamics method improves the configurational sampling during MD simulations by adding external history-dependent potential along the selected collective variables (CVs) enabling enhanced sampling and reconstructed free energy surfaces (FES) (Barducci et al., 2008; Dama et al., 2014).

This chapter used WT-metadynamics to explore conformational free energy profiles of amorphous-crystalline silk structures in water. In this work CVs were the number of β-sheet and α-helix segments which are key secondary structure components of silk. The simulation provided realistic three-dimensional amorphous-crystalline silk structures that were compared to known structures derived from NMR measurements. Next, silk structures were selected to investigate silk-doxorubicin interactions in response to pH using classical MD simulations. These data were compared to previously reported experimental studies.

5.2 Materials and Methods

5.2.1 Preparation of initial silk structure

In this study, the representative silk structure contained the antiparallel chains of the linker 5 (L5), subdomain 6.5 (R6.5) and linker 6 (L6) of silk structure (Figure 5.2B). These structure were used in a previous study (Cheng et al., 2015). The antiparallel silk structure was manually built in Discovery Studio (DS) (Accelrys Inc., San Diego, CA, USA).

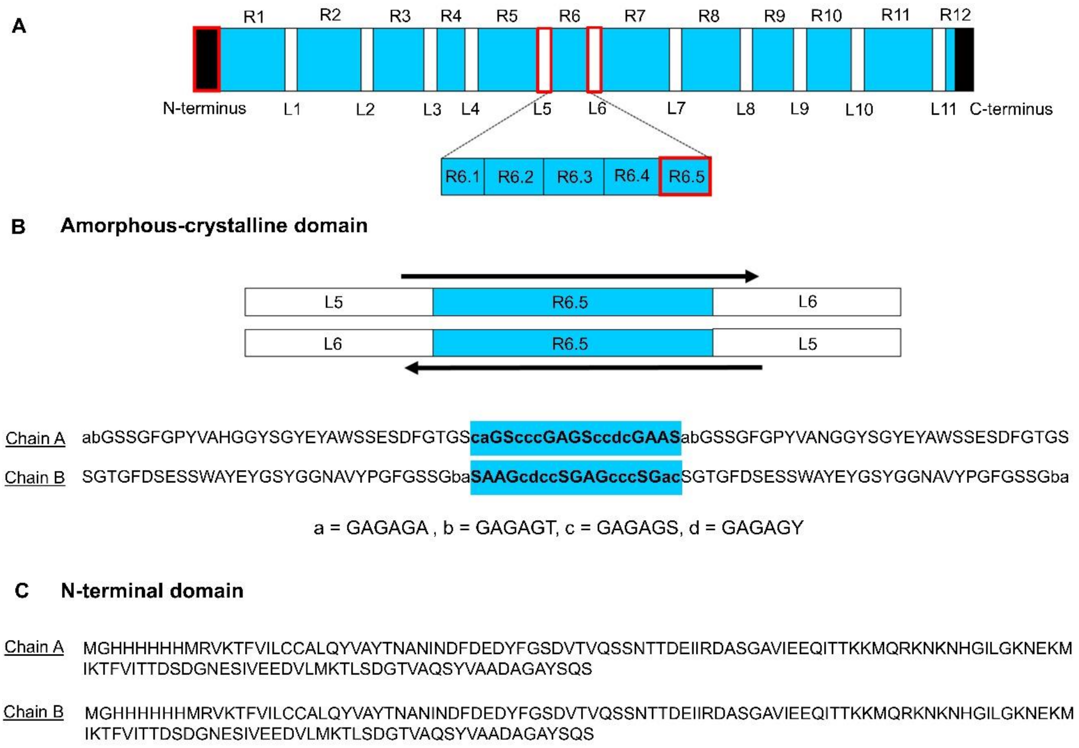

Figure 5.2 Primary structure of *B. mori* silk fibroin heavy chain and amino acid sequences for MD simulations. (A) Schematic representation of the primary structure of *B. mori* silk fibroin heavy chain. R1-R12 represent 12 repeated crystalline domains and L1-L11 represent 11 linkers (amorphous regions). Additionally, the subdomain L5, R6.5, L6 and N-terminus (red squares) are used in this study. (B) Schematic

representation of antiparallel silk structure (arrows show the directions) and their amino acid sequences. (C) Amino acid sequences of N-terminal domain (available in Protein Data Bank (3UA0) (He et al., 2012).

5.2.2 Equilibration of amorphous-crystalline silk structure

In order to obtain the equilibrated structure, the antiparallel structure was run in implicit water using the stochastic dynamic simulation for 1000 ns. All equilibrated simulations started with the use of the same structure and were run in parallel with 16 different random seeds. From each series, the equilibrated conformations at the last 100 ns (md901-1000 ns) were averaged to obtain one averaged structure.

The steepest descent in the energy minimisation was used to find the most stable and lowest energy of each averaged structure. Prior to minimisation, the averaged structure was solvated in TIP3P water model with a minimal distance of 10 Å between the box boundary and the silk structure. The equilibrated silk structure with the lowest minimised energy and a high number of amino acid in the allowed region of the Ramanchandran plot was used as an initial structure for well-tempered metadynamics simulations.

5.2.3 Well-tempered metadynamics

Exploring the free-energy landscape of the silk structure was carried out using the WT-metadynamics algorithm implemented in the PLUMED 2.1.1 plugin of the GROMACS 5.0.4 package (Bonomi et al., 2009). The Amber12sb and TIP3P models were used for protein and water, respectively. The system was accommodated in a box of 567 nm^3 with periodic boundary conditions. Two biased collective variables were chosen to define the conformational change along trajectories. The CVs were ANTIBETARMSD and ALPHARMSD (Pietrucci and Laio, 2009). ANTIBETARMSD and ALPHARMSD detect the number of the set of possible six amino acid residues that could conceivably form antiparallel β-sheet and α-helix, respectively as detailed in Chapter 1, section 1.5.2.3.

The Gaussian potentials with a height of 2 kJ/mol and width of 0.35 Å were added every 100 time steps along trajectories in the direction of selected collective variables. The Gaussian hill height was rescaled with a biasfactor of 25 and with a temperature of 300 K. Time evolution profiles of CVs, the Gaussian hill height profile and contour plot of free energy landscape were generated in OriginPro 9.2 Software. The silk structures at the global minimum and at the highest secondary structures (i.e. β-sheet and α-helix) were extracted using the Visual Molecular Dynamics (VMD) software package (Humphrey et al., 1996).

The extracted silk structures were subjected to energy minimisation until the maximum force value was less than 10 kJ mol^{-1} nm^{-1}. The 14 repetitive GAGSGAGA motifs were extracted from the most stable structure and torsion angles of each residue in the motif were displayed with a Ramachandran plot using the Ramachandran plot plug in for VMD and compared to the literature (Suzuki et al., 2014).

5.2.4 Molecular structures for molecular dynamics simulations

The amorphous-crystalline silk structures including the highest β-sheet content, the highest α-helix content and the most stable structure were obtained the free energy profile after WT-metadynamics simulation following minimisation. The molecular structure of N-terminal domain was extracted from Protein Data Bank with the code entry:3UA0 (He et al., 2012). The structure contains double-layered antiparallel β-sheet with 153 amino acid residues (Figure 5.2C).

5.2.5 Doxorubicin structure preparation

The initial doxorubicin structure was obtained from ChemSpider databases and then geometrically optimized by Gaussian 09W package using HF/6-31G basic set Pop=MK iop(6/33=2). The pKa of doxorubicin is 8.3; therefore, doxorubicin is protonated at pH lower than 8.3 (e.g. 4 and 7.4). To protonate doxorubicin structure, the DS software was used to add +1 charge (H+) at the amine group. Next, the antechamber program in AMBER 12 packages (University of California, CA, USA) was used to assign atom types and atomic charge (+1) of the optimized doxorubicin molecule. The output file (e.g. dox.mol2) after running antechamber was loaded into ‘tleap’ to create topology and coordinate files. The ‘parmchk’ was used to test if all parameters are available and the missing parameters were loaded into ‘tleap’. The parameters such as topology (.prmtop) and coordinate files (.inpcrd) of doxorubicin were converted into GROMACS format (.gro and .top) using ACPYPE (AnteChamber PYthon Parser interfacE).

5.2.6 Residue pKa calculation and protein ionisation corresponding to pHs

The pKa values for all ionisable residues presented in the model silk structure were calculated using Protein Ionisation and Residue pKa in DS. This method, developed by Spassov and Yan (Spassov and Yan, 2008), employs CHARMm-based algorithm to determine pKa and modifies charges of ionisable amino acids at pH 4 and pH 7.4. The protein and solvent dielectric constants used in these calculation were 10 and 80, respectively. The ionic strength was set at 0.145.

5.2.7 Molecular dynamics simulations for silk-doxorubicin interaction corresponding to pHs

The molecular dynamics simulation was executed in GROMACS 4.6.5 with amber12sb force field and TIP3P water model. The protonation states and charges of ionisable residues of model silk structures at pH 4 and pH 7.4 were fixed using pdb2gmx module of GROMACS by utilizing calculated pKa values from DS. The silk structures were added into a box with a 10x10x10 nm^3 size. Next, 31,500 water and 20 doxorubicin molecules were added into the systems. The systems were subsequently minimised within 5,000 steps of steepest descant algorithms (Fmax < 10 kJ/mol). Afterwards, 100 ps of NPT equilibration at a temperature of 300 K was conducted. The MD simulation was then carried out in NVT ensemble with temperature 300 K for 50 ns. Periodic boundary conditions were used in all dimensions. The particle Mesh Ewald (PME) method was used to determine electrostatic interactions.

5.2.8 Post-processing analysis

The number of hydrogen bonds between silk and doxorubicin for the 50 ns MD simulations were calculated using g_hbond tool in GROMACS. The interaction energies including electrostatic interactions and van der Waals interactions were extracted using g_energy from energy output file. The distance of each doxorubicin to silk at 50 ns was calculated using g_mindist module which compute the minimum distance of each doxorubicin to the model silk structure. The 2-dimentional silk-doxorubicin diagram was generated using LIGPLOT program (Wallace et al., 1995). All the graphs were plotted by GraphPad Prism 7 (GraphPad Software, La Jolla, CA, U.S.A.).

5.3 Results and Discussion

5.3.1 Exploring amorphous-crystalline silk structures using WT-metadynamics

The critical step for the WT-metadynamics simulations was the selection of CVs. The CVs should be able to distinguish between relevant metastable states and describe the key features of the structure (Barducci et al., 2011). Thus, in this chapter, the number of β-sheets and α-helix segments were the CVs because the secondary structure of silk contains primarily these two structures. These CVs can be detected and tracked to assess the conformation changes of the silk structure in water along their trajectories.

To monitor convergence of the system, time evolution profiles of CVs, Gaussian hill height and free energy landscapes were reconstructed. At the convergence, there are three main questions to be considered (i) Are the CVs values fully explored over simulation time? (ii) Does the hill height reach zero? and (iii) Are the reconstructed free energy profiles similar? (Barducci et al., 2008). In this chapter the WT-metadynamics simulations of the silk structure in water were converged after a 600 ns simulation because two CVs values effectively diffused over the simulation (Figure 5.3A). Specifically, the height of the biased potential reached zero (Figure 5.3B) and there was no significant change in free energy surface shape or the structure of the minimum over the last 50 ns (Figure 5.4).

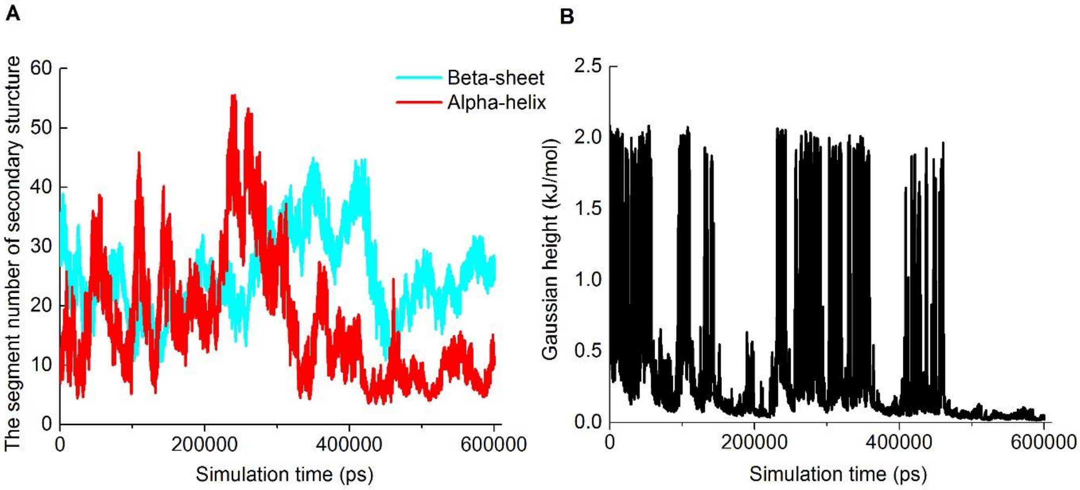

Figure 5.3 Time evolution of the CVs and Gaussian height over 600 ns of WT-metadynamics simulation of silk structure in water.

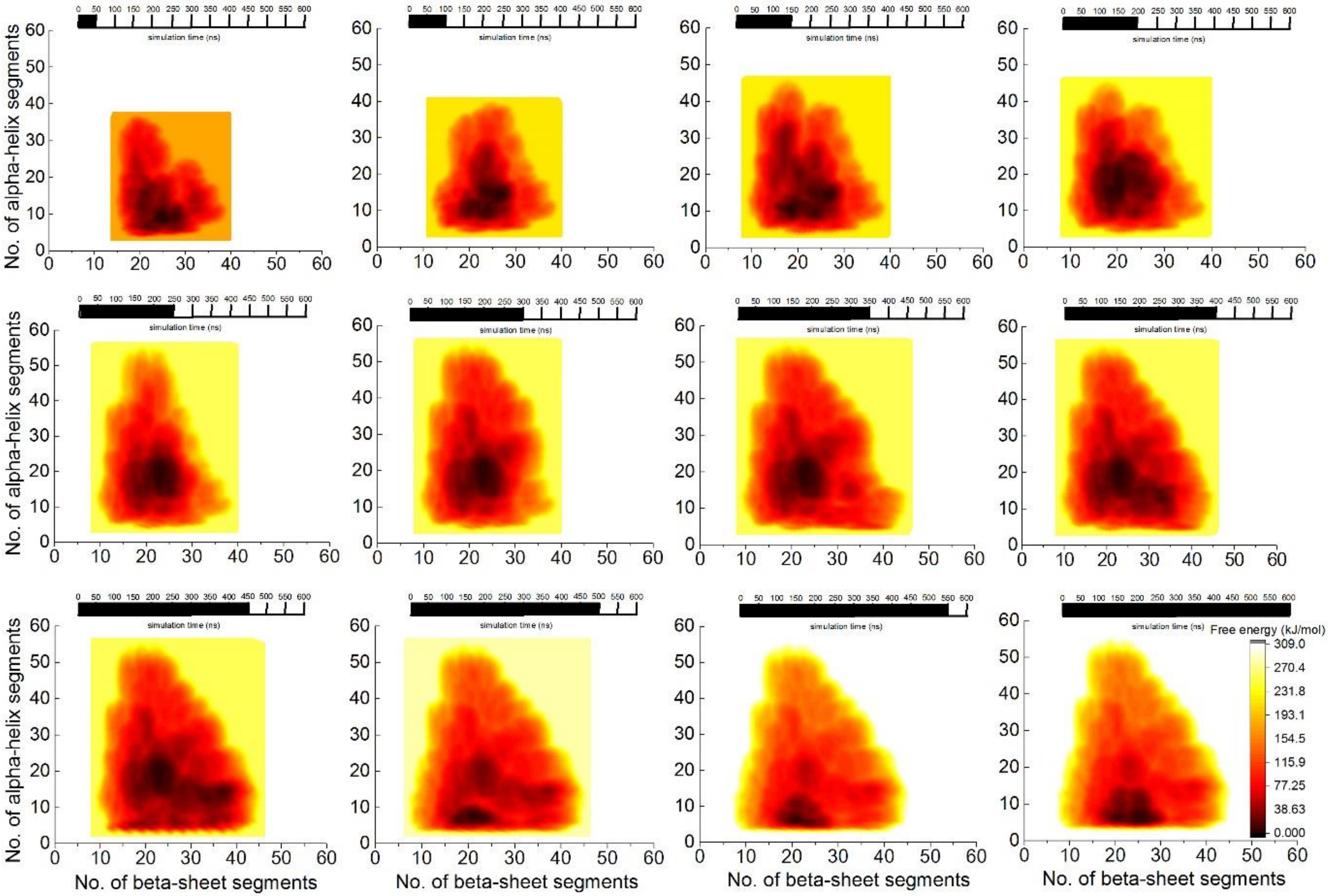

Figure 5.4 Time evolution of the free energy landscapes over 600 ns of WT-metadynamics simulation of silk structure in water.

Next, it was possible to extract the most interesting silk structures from the free energy surface at 600 ns, for example the most stable structure at the global minimum (Figure 5.5 point 2) as well as the relevant structures containing either the highest α-helix segments or the highest β-sheet segments (Figure 5.5 point 1 and 3, respectively). Silk I*, the ordered regions of silk I, represents the solution silk structure present in the middle silk gland and is described as the type II β-turn structure which is a nucleus for silk II formation (Asakura et al., 2015). Experimental evidence indicates that 55-58% of GAGSGAGA sequence in silk I adopts the Silk I* structure and the rest is a random coil (Asakura et al., 2015). To validate the simulation described in this chapter, the 14 repetitive GAGSGAGA sequences from the most stable silk structure were extracted (Figure 5.5B) and analysed by (i) plotting torsion angles phi and psi on a Ramachandran plot and (ii) examining the type II β-turn structure patterns.

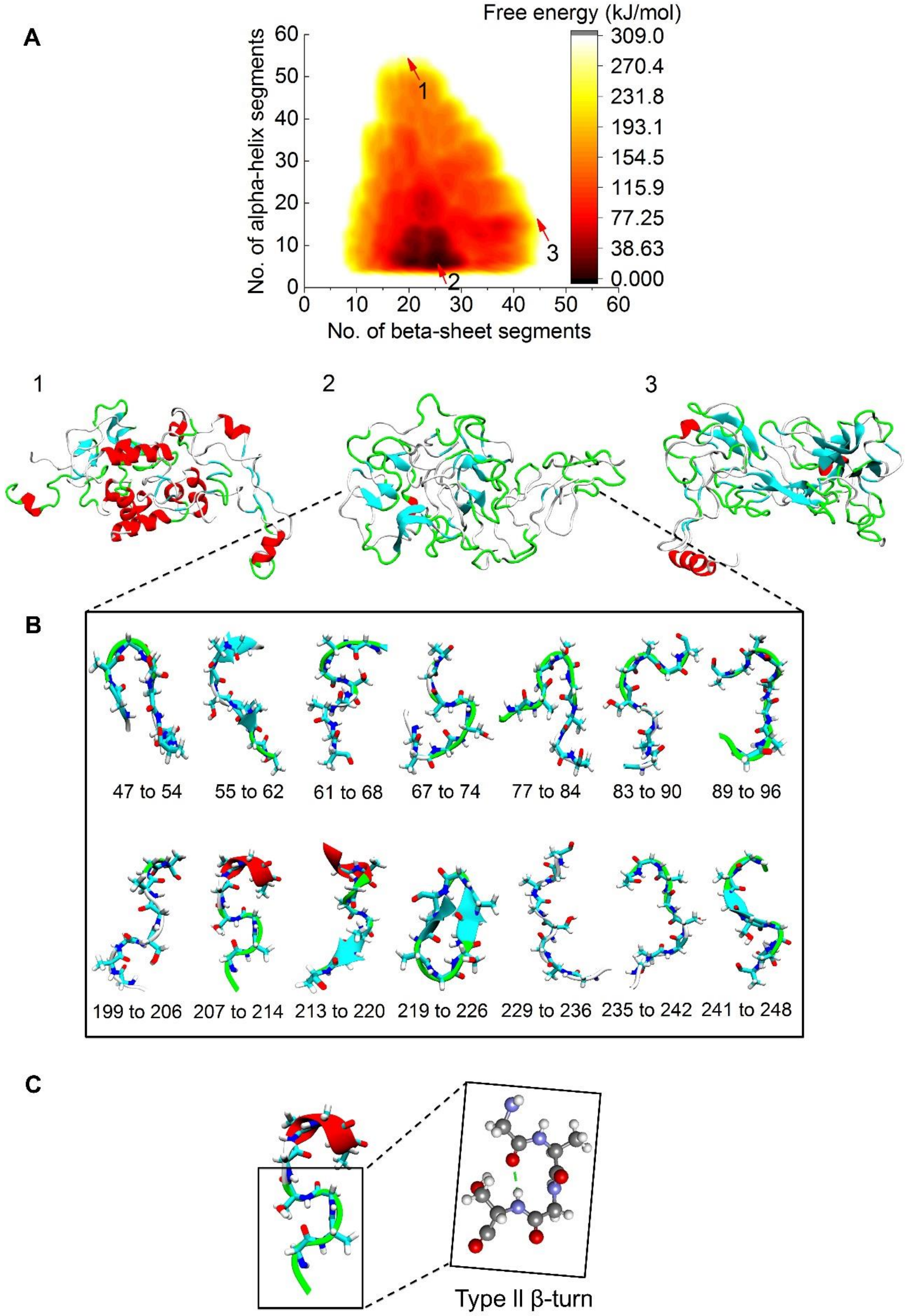

Figure 5.5 The converged free energy surface of silk structure in water with relevant structures and 14 repetitive sequence motifs GAGSGAGA in silk structure. (A) The free energy profile with three relevant silk structures; (1) the silk structure contains the

highest α-helix segments, (2) the most stable silk structure at global minimum and (3) the silk structure contains the highest β-sheet segments. (B) The 14 repetitive sequence motifs GAGSGAGA extracted from the most stable structure after WT-metadynamics simulation for 600 ns. The number is the residue number of GAGSGAGA in the silk structure. (C) The repetitive sequence motif GAGSGAGA (at residue number 207 to 214) of silk structure and its first four residues (GAGS) represented type II β-turn structure with hydrogen bond (green dash line). The silk structures were coloured with VMD: α-helix = red, β-sheet = cyan, turn = green, random-coil = white.

Solid state NMR data for soluble silk has been reported (i.e. silk stored in the silkworm middle gland) and the torsion angles of silk structure were plotted (Figure 5.1B) adopting a type II β-turn structure model (Figure 5.1C) (Suzuki et al., 2014). These literature torsion angles were then compared to the angles obtained from the silk structure after WT-metadynamics simulations. Here, 38% of GAGSGAGA from the respective sequence aligned in the area of ideal torsion angles (red circles) (Figure 5.6A). All angles of GAGSGAGA from the residue number 207 to 214 were located within this area. These data were corroborated by analysing the hydrogen bond and structural pattern in VMD. This revealed a type II β-turn structure with one hydrogen bond between the C=O of the glycine (i) and the H-N of the serine (i+3) (Asakura et al., 2015) (Figure 5.5C). Therefore, the silk model described in this chapter supports the current Silk I* conformation (i.e. the type II β-turn structure) previously proposed by NMR. Nonetheless, the modelling also yielded some residues that formed unstructured segments not described previously.

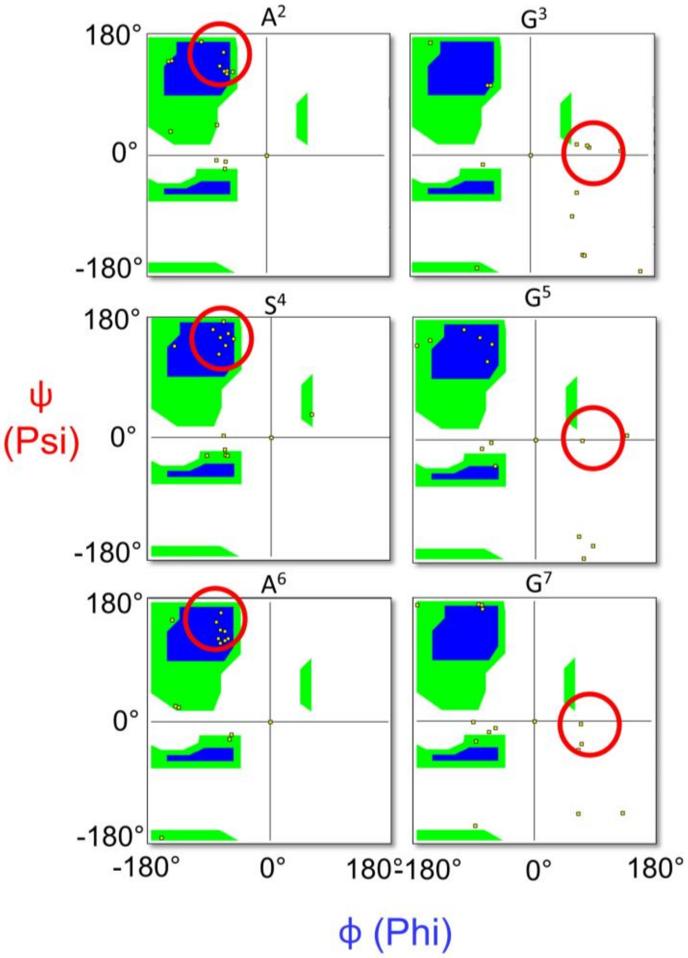

Figure 5.6 Ramachandran plot for repetitive sequence motifs $G_1A_2G_3S_4G_5A_6G_7A_8$ of silk structure after WT-metadynamics. The yellow dots represent torsion angles of each residue. The red circles indicate area of torsion angles of ideal type II β-turn structure from Asakura et al., 2015.

.5.3.2 pH-dependent silk-doxorubicin interactions

Previous work (Seib, Jones, et al., 2013; Wongpinyochit et al., 2015; Totten et al., 2017) and Chapter 2 detailed the manufacture of silk nanoparticles; these were examined for drug loading and release as well as their internalization and trafficking in breast cancer cells. These studied showed that doxorubicin loading could be accomplished by simple solution adsorption. In addition drug release was pH dependent with fastest release at an acidic pH (e.g. lysosomal pH (pH = 4.5)) (Seib, Jones, et al., 2013; Wongpinyochit et al., 2015). Nonetheless the underlying mechanism of doxorubicin interaction with silk and the subsequent impact of pH on drug release has not been studied.

Studies reported that MD simulations is a powerful tool to demonstrate the binding mechanism between doxorubicin and drug carrier molecules such as nanodiamond (Adnan et al., 2011), graphene oxides (Mahdavi et al., 2016) and chitosan oligosaccharide (Shan et al., 2014). These studies also suggested that Van der Waals, electrostatic interaction and hydrogen bonding are key to enabling doxorubicin carrier binding. Thus, this chapter used the silk structures extracted from WT-metadynamics simulations to study the pH-dependent interaction of doxorubicin with silk. The selected silk structures were (i) the most stable silk structure, (ii) the highest α-helix content silk (i.e. Silk I) and (iii) silk with the highest β-sheet content (i.e. Silk II dominating silk nanoparticles). Furthermore the N-terminal domain structure was also included because it contains a pH-responsive region required for silk self-assembly (He et al., 2012).

5.3.2.1 Calculation of pKa of ionisable amino acids

To mimic experimental studies, the silk structure models were subjected to pH values of 7.4 and 4 that mimic loading solution and lysosomes, respectively. The silk structure models used in this chapter contained five ionisable amino acids, most importantly: aspartic acid, glutamic acid and tyrosine in the amorphous-crystalline domain. In contrast the N-terminal domain contained aspartic acid, glutamic acid, tyrosine, lysine and arginine (Figure 5.7). The pKa of ionisable residues can be shifted depending on surrounding environment (e.g. solvent, pH etc.) impacting the resulting protein conformations (e.g. hiding/exposing ionisable groups in the structure etc) (Pace et al., 2009). Therefore, the initial step was to calculate the pKa of the ionisable amino acids in the silk models to modify the protonation states at pH 4 and pH 7.4 using DS software.

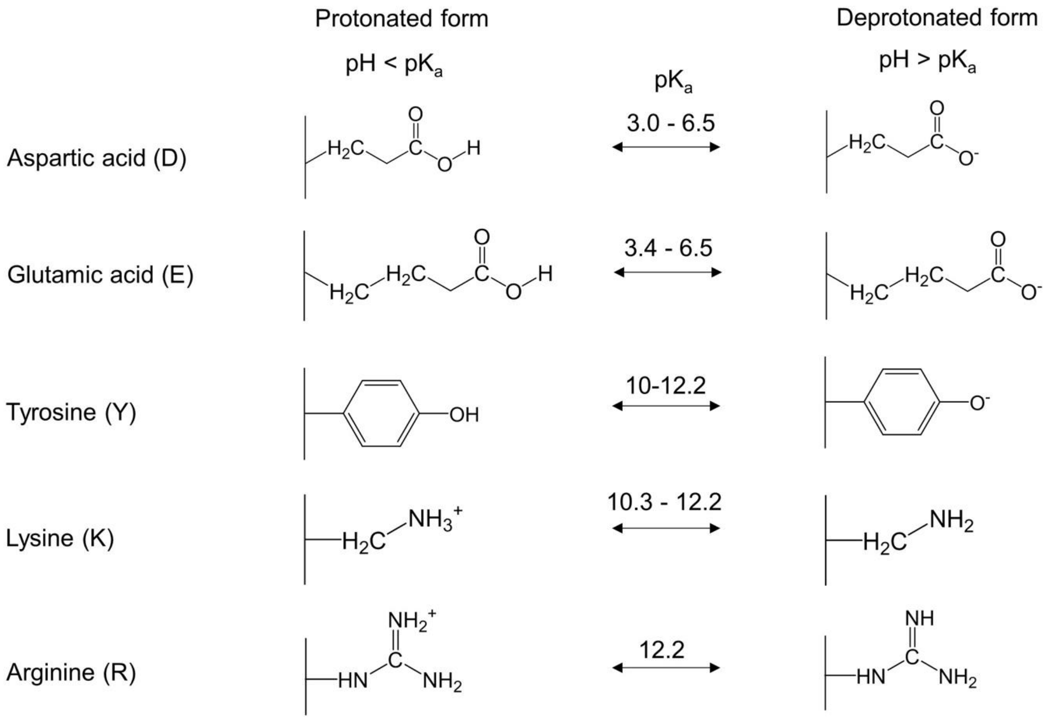

Figure 5.7 Calculated pKa from Discovery Studio and ionisable side chain of amino acids.

The calculated pKa values for ionisable residues can then be used to estimate the total net charges at pH 4 and pH 7.4 (Table 5.1-5.4). For the amorphous-crystalline domain of the model silk structure, the total net charge at pH 4 was less negative than at pH 7.4 (-2 to -4 at pH 4 and -12 at pH 7.4). In contrast, the N-terminal domain of the silk model contained a large amount of ionisable amino acids, the total net charges of N-terminal domain at pH 4 and pH 7.4 were significantly different (+6 at pH 4 and -17 at pH 7.4) (Table 5.4). Overall, glutamic acid contributed to the total net charge of all the silk structure models studied here.

Table 5.1 Calculated pKa values of ionisable amino acids in the highest beta-sheet content of silk structure and their charges in pH 4 and pH 7.4.

Silk model	Residue name	Residue number	Calculated pKa	Charges at pH	
				4	7.4
The highest beta-sheet content	Aspartic acid (D)	39, 146, 191, 298	3.96, 3.67, 3.89, 3.86	- 4	- 4
	Glutamic acid (E)	31, 37, 138, 144, 183, 189, 290, 296	4.32, 5.62, 4.55, 4.50, 5.00, 4.90 ,4.75, 4.80	0	- 8
	Tyrosine (Y)	21, 27, 30, 32, 98, 128, 134, 137, 139, 173, 179, 182, 250, 280, 286, 289, 291	12.20, 10.80, 10.00, 12.20, 10.63, 10.77, 12.20, 11.96, 10.56, 12.20, 11.06, 11.28, 10.50, 12.20, 11.59, 10.84, 10.37, 10.65	0	0
			Total charges	- 4	- 12

Table 5.2 Calculated pKa values of ionisable amino acids in the most stable silk structure in water and their charges in in pH 4 and pH 7.4.

Silk model	**Residue name**	**Residue number**	**Calculated pKa**	**Charges at pH**	
				4	**7.4**
The most stable structure in water	Aspartic acid (D)	39, 146, 191, 298	4.09, 3.90, 3.70, 3.61	- 3	- 4
	Glutamic acid (E)	31, 37, 138, 144, 183, 189, 290, 296	5.38, 4.59, 4.46, 4.99, 5.11, 5.10 ,4.80, 4.71	0	- 8
	Tyrosine (Y)	21, 27, 30, 32, 98, 128, 134, 137, 139, 173, 179, 182, 250, 280, 286, 289, 291	12.2, 12.2, 11.86, 10.02, 12.20, 10.41, 12.20, 12.20, 10.43, 12.20, 10.81, 11.69, 10.27, 10.69, 10.67, 10.73, 12.20, 12.20	0	0
			Total charges	**- 3**	**- 12**

Table 5.3 Calculated pKa values of ionisable amino acids in the highest α-helix content of silk structure and their charges in pH 4 and pH 7.4.

Silk model	**Residue name**	**Residue number**	**Calculated pKa**	**Charges at pH**	
				4	**7.4**
The highest α-helix content	Aspartic acid (D)	39, 146, 191, 298	4.25, 4.11, 3.79, 3.98	- 2	- 4
	Glutamic acid (E)	31, 37, 138, 144, 183, 189, 290, 296	5.00, 4.83, 4.50, 4.63, 4.95, 4.76, 4.49, 4.95	0	- 8
	Tyrosine (Y)	21, 27, 30, 32, 98, 128, 134, 137, 139, 173, 179, 182, 250, 280, 286, 289, 291	10.40, 10.65, 10.77, 10.35, 12.20, 10.40, 11.78, 11.79, 10.69, 12.20, 11.33, 11.37, 10.433, 12.2, 10.37, 12.20, 10.26, 12.20	0	0
			Total charges	**- 2**	**- 12**

Table 5.4 Calculated pKa values of ionisable amino acids in N-terminal domain of silk structure and their charges in pH 4 and pH 7.4.

Silk model	**Residue name**	**Residue number**	**Calculated pKa**	**Charges at pH**	
				4	**7.4**
N-terminus	Aspartic acid (D)	3, 5, 10, 20, 25, 61, 63, 72, 80, 85, 87, 98, 103, 133, 135, 144, 152	3.54, 3.81, 3.16, 4.60, 4.20, 3.94, 3.49, 5.54, 3.48, 4.14, 6.52, 5.31, 3.42, 3.77, 3.67, 4.25, 3.63	- 10	- 17
	Glutamic acid (E)	4, 21, 32, 33, 50, 66, 70, 71, 88, 99, 110, 111, 122, 138, 142, 143	5.11, 5.18, 5.52, 6.53, 5.36, 4.82, 6.49, 5.34, 5.31, 4.84, 6.36, 5.16, 4.61, 4.73, 5.99, 5.04	0	- 16
	Tyrosine (Y)	6	12.20	0	0
	Lysine (K)	38, 39, 43, 48, 51, 54, 76, 116, 117, 123, 126, 148	12.20, 11.41, 11.59, 10.31, 11.43, 12.20, 12.20, 11.58, 11.77, 11.22, 11.99, 12.20	12	12
	Arginine (R)	24, 42, 102, 120	12.20, 12.20, 12.20, 12.20	4	4
			Total charges	**6**	**-17**

The difference of the total net charges of the silk structures can be visualised by generating the distribution of charged amino acid residues on the surfaces (Figure 5.8). The proportion of negatively charged amino acids in the silk structure at pH 7.4 was higher than the proportion of charges present at pH 4. There were extra negative charges for the amorphous-crystalline silk structure at pH 7.4 due to the presence of glutamic acid (residue number 37, 290, 296) and aspartic acid (residue number 39) (Figure 5.8A). For the N-terminal domain, the surface charge distribution at pH 4 and pH 7.4 was already visually different (Figure 5.8B) due to high positive charges at pH 4 (+ 6) and high negative charges at pH 7.4 (-17) (Table 5.4).

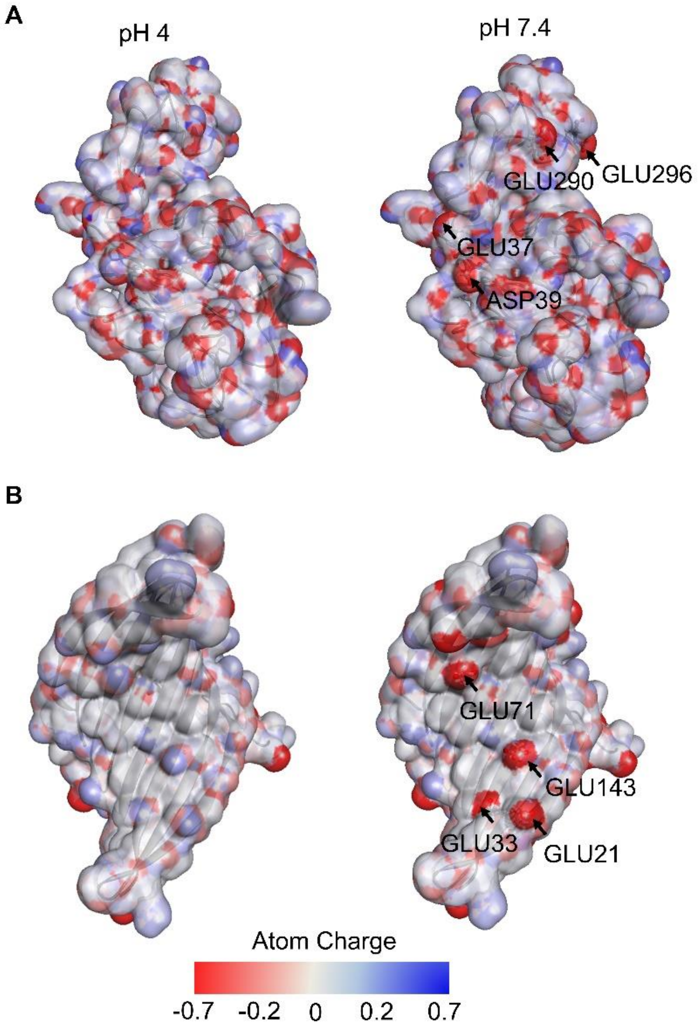

Figure 5.8 Surface charge distribution of the most stable silk structure in water (A) and N-terminal domain of silk (B) at pH 4 and pH 7.4. The labelled amino residues are examples of unprotonated residues at pH 7.4, which resulted in negative charges (red).

5.3.2.2 Molecular dynamics simulation: post-processing analysis

The model system consisted of modified protonation states of the model silk structure (four separated models system), 20 doxorubicin molecules and water. The molecular dynamics simulations of all systems were run for 50 ns in GROMACS packages. Firstly, this chapter analysed the spatial distribution of 20 doxorubicin molecules around the silk model structures during the start and the last frame of 50 ns (Figure 5.9). Overall, the number of doxorubicin with a close proximity to the silk model at pH 7.4 was higher than those in the systems at pH 4. This indicated that doxorubicin had a higher binding affinity for silk at pH 7.4 compared to the acidic pH. Interestingly, the N-terminus-doxorubicin system at pH 4 showed a significantly higher number of doxorubicin molecules at a long distance from the silk structure (>2 nm) than at the neural pH. This result suggests that the N-terminal domain is an important structural element influencing doxorubicin release.

The intermolecular hydrogen bonds formed between doxorubicin and each silk structure model were calculated because the number of hydrogen bonds between the drug and the carriers has previously been showed as a key feature to modulate drug loading (Subashini et al., 2011). The intermolecular hydrogen bond cut-off distance was set at 0.35 nm with 30° cut-off angle (Van Der Spoel et al., 2005). Overall, the number of hydrogen bonds in the pH 7.4 systems was higher than those in the pH 4 systems which indicated high drug loading efficacy at pH 7.4 (Figure 5.9). Additionally, the number of hydrogen bonds between doxorubicin and N-terminal domain of silk at pH 7.4 was substantially higher than at pH 4 (Figure 5.9). Therefore, this result confirmed that the N-terminal domain had a substantial influence on the drug loading and drug release behaviour.

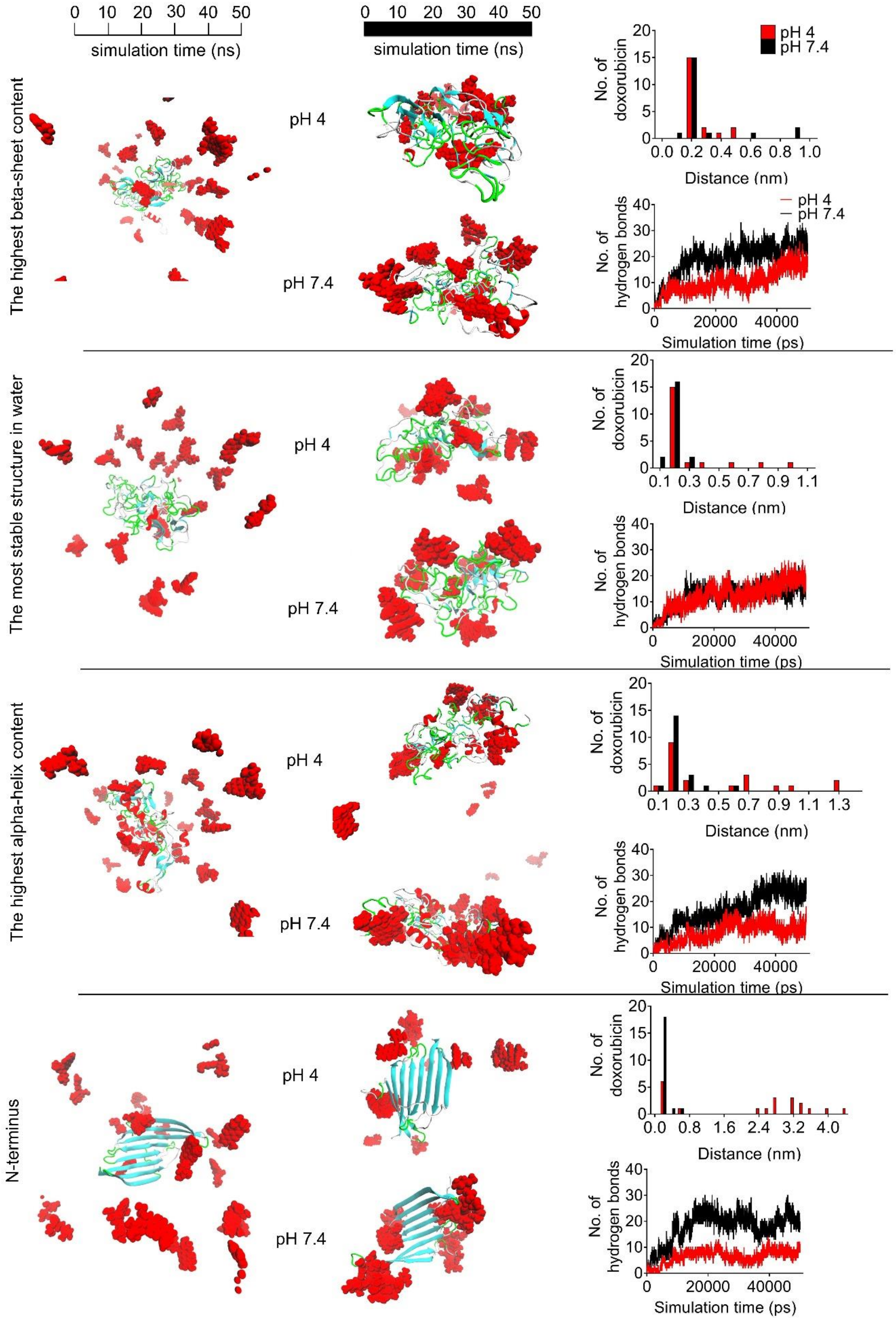

Figure 5.9 Snapshots of doxorubicin distribution to silk structure at 0 and 50 ns MD simulations at the indicated pH of 4 and pH 7.4. The post-processing analysis of silk-

doxorubicin system was presented as the number of doxorubicin molecules distribution in different distance (nm) from silk structures at 50 ns and the number of hydrogen bonds of all silk-doxorubicin systems over 50 ns simulation time. The doxorubicin and silk structures were coloured by VMD; α-helix = red, β-sheet = cyan, turn = green, random-coil = white and doxorubicin = red molecules.

The interaction energies were calculated to determine binding strength and the types of intermolecular interactions between doxorubicin and silk. The three prominent intermolecular forces can be classified in the following rank order: electrostatic interaction > hydrogen bonding > van der Waals interactions (Dhotel et al., 2013). Overall, the total interaction energies for the pH 7.4 systems were higher than at pH 4 indicating greater doxorubicin-silk interactions at pH 7.4 (Figure 5.10). Electrostatic interactions were also important at pH 7.4, especially for the N-terminal-doxorubicin pair (Figure 5.10D) due to the high number of hydrogen bonds than 20 (Figure 5.9). Therefore, the electrostatic interaction energy and the number of hydrogen bonds were plotted to determine the relationship between these values. The number of hydrogen bonds strongly correlated with the electrostatic interaction between silk and doxorubicin and correlated well with previous work of doxorubicin-chitosan oligosaccharide interactions (Shan et al., 2014). An increasing electrostatic interaction energy lead to a greater number of hydrogen bonds (Figure 5.11).

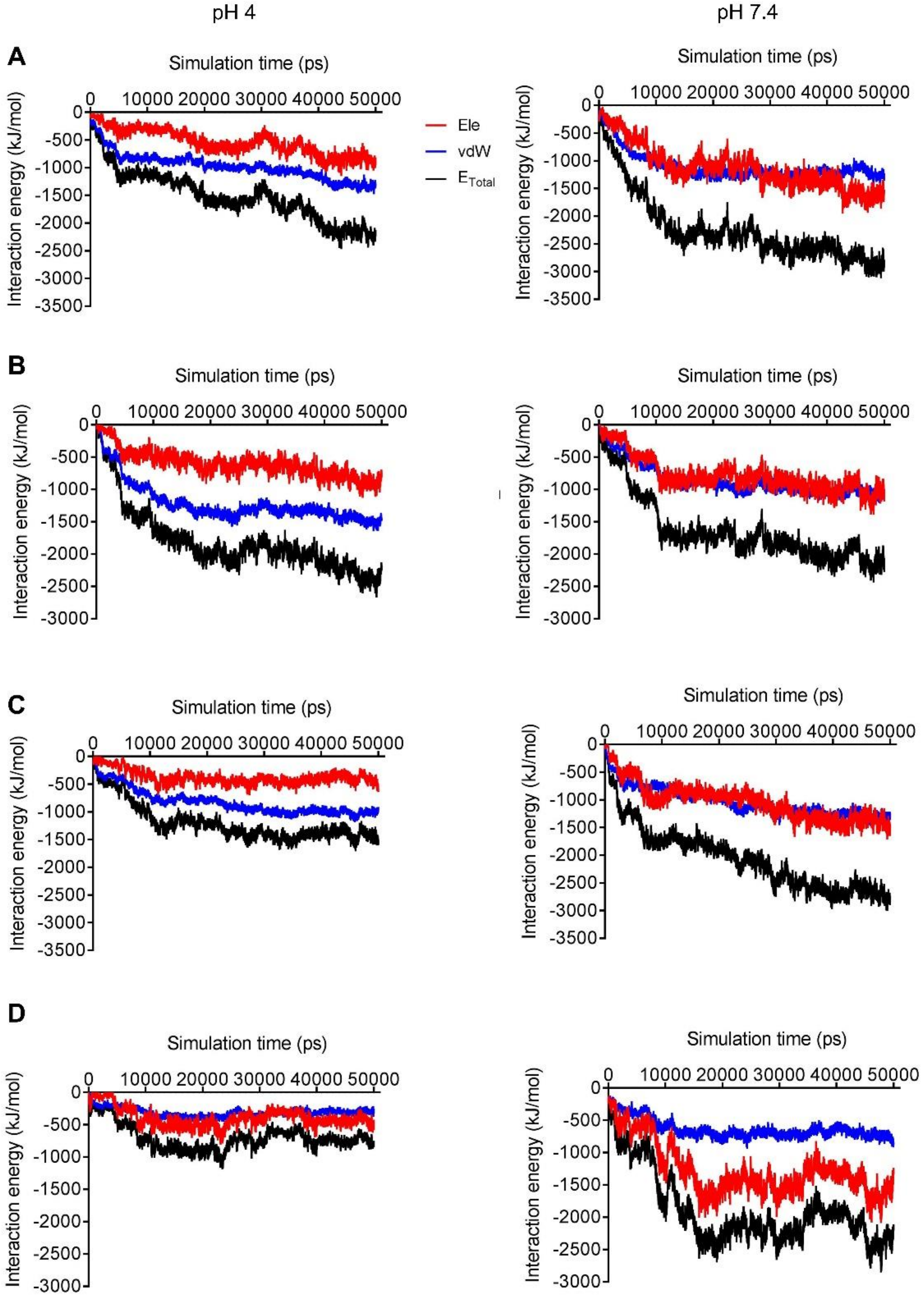

Figure 5.10 The interaction energies including electrostatic (Ele), van der Waals (vdW) and the total interaction energies (E_{total}) between doxorubicin and the model silks at pH 4

and pH 7.4. (A) the highest β-sheet content, (B) the most stable structure in water, (C) the highest amorphous content and (D) N-terminal domain.

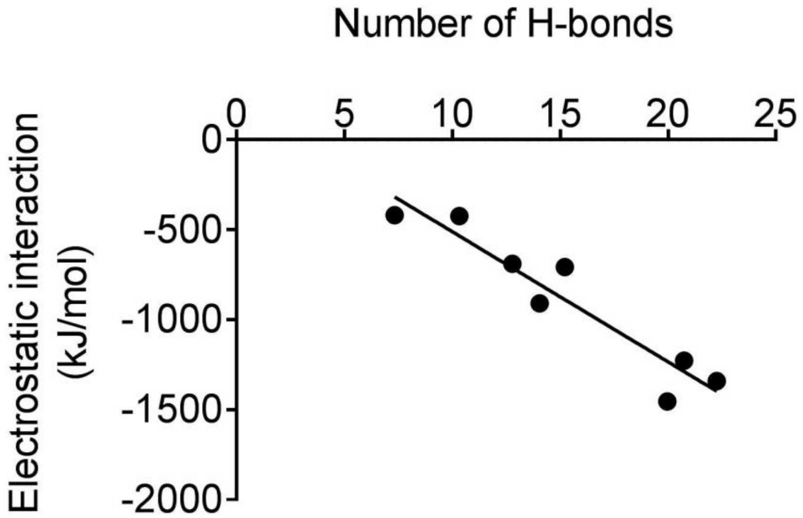

Figure 5.11 Linear relationship between the number of hydrogen bonds and electrostatic interaction energy of silk-doxorubicin system. Equation is Y = -72.3*X + 212 and R^2 = 0.8928.

Next, LIGPLOT and DS were used to generate 2D interactions diagram and to monitor the amino acids of silk that interacted with doxorubicin at 50 ns. The 2D diagram of the LIGPLOT detailed hydrogen bonds (green lines) and hydrophobic interactions (grey arcs) between silk and doxorubicin (Figure 5.12). The doxorubicin molecule in LIGPLOT was selected from those that showed the highest interaction energies with the silk model at 50 ns. Overall, the number of hydrogen bonds and number of amino acids responsible for the silk doxorubicin interaction at pH 7.4 were higher than those at pH 4 (Figure 5.12 and

Table 5.5). For the highest β-sheet content silk structure, the interaction between silk and doxorubicin at pH 4 was dominated by hydrophobic interaction (Figure 5.12A), while the interactions at pH 7.4 was dominated by hydrogen bonds. For other silk-doxorubicin model systems, the 2D diagram from LIGPLOT did not show significant differences in response to pH.

Overall pH influenced the doxorubicin binding affinity towards silk because ionisable amino acid residues (especially glutamic and aspartic acid) provided negative charges at pH 7.4 compared to pH 4 (shown in red Table 5.5). This correlates well with previous wet lab experiments (Seib and Kaplan, 2012; Seib, Jones, et al., 2013; Wongpinyochit et al., 2015; Totten et al., 2017).

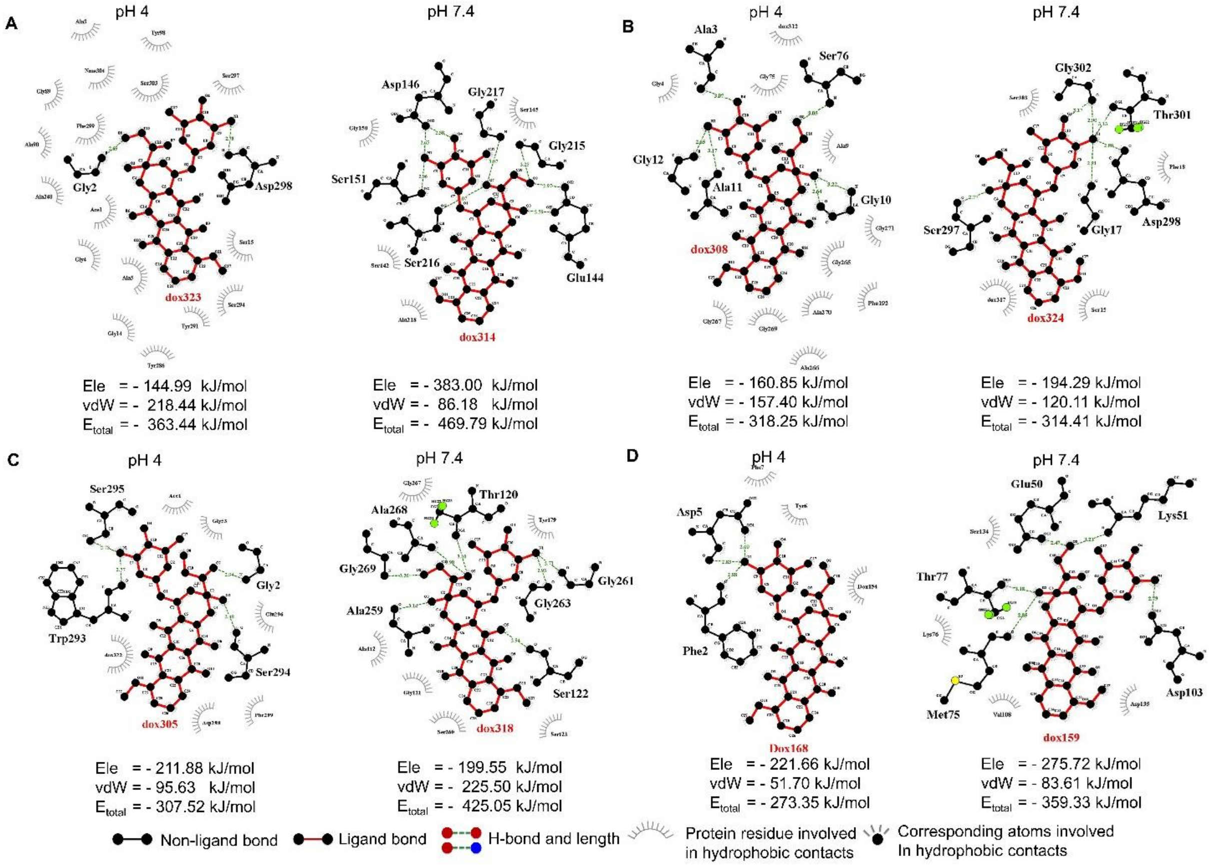

Figure 5.12 Schematic representation of 2D doxorubicin structure with the H-bonds and hydrophobic interactions between amino acid residues of silk structure at pH 4 and pH 7.4 at 50 ns. (A) the highest β-sheet content, (B) the most stable structure in water, (C) the highest amorphous content and (D) N-terminal domain.

Table 5.5 List of amino acid residues in each model silk structure interacted to doxorubicin at pH 4 and pH 7.4 at 50 ns. Red represents the negatively charged amino acids.

Model silk	**pH**	**Protein residues (residue number)**
The highest β-sheet content	4	ALA(40, 90), ASP(146, 298), GLY(2, 4), SER(145, 294, 303), THR(149), TYR(21, 286, 289)
	7.4	ALA(88, 264), ASP(39, 146, 191), GLU(31, 144, 296), GLY(6, 12, 14, 103, 195, 207, 209, 215, 217, 269), PHE(125), SER(76, 145, 151, 216, 244, 256), THR(13, 272)
The most stable structure in water	4	ALA(3, 11, 90, 206, 208, 220, 224, 240), GLY(10, 12, 71, 85, 89, 132, 207, 241), SER(70, 76, 108, 135, 188, 294)
	7.4	ALA(60), ASN(283), ASP(191, 298), GLU(183, 290, 296), HIS(24), PHE(18, 192), GLY(10, 17, 19, 177, 302), SER(70, 297), THR(149, 194, 301), TYR(182)
The highest α-helix content	4	ALA(264), GLU(31, 296), GLY(2, 156, 263), SER(28, 70, 294, 295), TRP(293)
	7.4	ALA(3, 5, 54, 224, 236, 259, 268), ASP(146, 298), GLU(296), GLY(29, 148, 225, 261, 263, 269), SER(28, 35, 36, 122, 260, 275, 295, 297), THR(120, 149), TYR(291)
N-terminus	4	ASN(17), ASP(5, 98), ILE(45, 100), PHE(2)
	7.4	ASN(49), ASP(3, 5, 103, 63), GLU(32, 33, 50, 143), ILE(125), LYS(51, 123), MET(75), SER(134)

5.4 Conclusion

In summary, the WT-metadynamics simulation was a promising technique to explore amorphous-crystalline silk structures in water system. The free energy profile generated after the simulation provided useful silk conformations, including the silk I structure and silk structures after treatments. The silk I* structure correlated well with previous NMR studies (Asakura et al., 2015). The molecular interaction between silk and doxorubicin showed pH dependent effects that correlated well with experimental data. The N-terminal domain was confirmed as an important part of silk that control drug binding and release in response to pH. This pH switch was attributed to ionisable amino acid residues, especially glutamic acid. This chapter also reports that electrostatic interactions due to hydrogen bonds were of critical importance for drug loading and release. Overall, this chapter demonstrated structure function relationships that will help to develop recombinant silks with improved drug binding and release characteristics. However, coarse-grained molecular dynamics simulations can be applied to reduce simulation time and to simulate macromolecule systems such as nanoparticles formations (detailed in Chapter 6, section 6.2.4).

Chapter 6

Conclusions and future directions

6.1 Thesis conclusions

The foundation to this thesis originated from the work of Seib and co-workers, who showed that *B. mori* silk-based nanomedicines can be prepared by nanoprecipitation. More importantly, these nanoparticles showed promise as carriers for lysosomotropic drug delivery (Seib, Jones, et al., 2013). However, many factors were unknown. Therefore this thesis aimed to fill some of these gaps, especially in relation to the potential of silk-based nanoparticles for drug delivery using wet lab experiments and computational modelling. Here, silk nanoparticles were generated in both batch and microfluidic processes. These nanoparticles were amenable to surface modification. The drug loading, cytotoxicity, intracellular trafficking and biodegradation of these nanoparticles were studied (Wongpinyochit et al., 2015, 2016, 2018). Additionally, the molecular structure of silk was modelled to gain insight into conformational features and drug binding-release behaviours at the atomic level using molecular dynamics simulations. Overall, the results obtained from this thesis confirmed that silk is an interesting biopolymer for drug delivery applications, for example anticancer drug delivery.

First, silk nanoparticles were successfully generated. The silk nanoparticle surface was covalently modified using activated PEG. The native and PEGylated silk nanoparticles were 104 to 116 nm in diameter, showed a negative zeta potential (-56 to -46 mV) and a high β-sheet structure. The PEGylated silk nanoparticles had the ability to achieve a surface charge shielding effect, a higher stability in PBS and reduced macrophage recognition. Both the native and PEGylated silk nanoparticles showed the ability to adsorb drug from solution. This study also demonstrated that either a single drug or drug combination (propranolol and doxorubicin) significantly reduced cell viability and changed cell morphology. PEGylated silk nanoparticles also improved intracellular accumulation due to reduced nanoparticle aggregation in culture medium.

In Chapter 3 native and PEGylated silk nanoparticles were examined in relation to their biodegradation behaviour using selected proteolytic enzymes and *ex vivo* lysosomal enzymes. This study showed that PEGylated silk nanoparticles were slowly degraded compared to native silk nanoparticles due to the ability of PEG to shield the silk surface and reduce enzyme accessibility. In addition, degradation behaviour of native and PEGylated silk nanoparticles varied depending on the proteolytic enzyme (rank order: protease XIV > papain >> α-chymotrypsin). This study also included the first investigation of *ex vivo* lysosomal degradation, which showed the reduction of particle sizes after a 5-day enzyme treatment.

In Chapter 4 the manufacture of silk nanoparticles was refined using microfluidic-assisted technologies. This method enabled fine-tuning of silk nanoparticle characteristics by varying process parameters. This study showed that the total flow rate and the flow rate ratio were the two main parameters affecting particle properties. A slow flow rate of 1 mL/min and the solvent:aqueous total flow rate ratio of 5:1 gave the best yield, small spherical particles (110 nm) and high stability (>42 days at 37°C). The stable silk nanoparticles with a 2 fold difference in size were studies using culture macrophages. These silk nanoparticles were non-toxic over the studied concentration range but showed size-dependent cellular trafficking.

In chapter 5 computational modelling was applied to gain insight into the secondary silk structure in water. WT-metadynamics simulation was a promising technique to explore semi-crystalline silk structure; the results obtained from the *in silico* modelling was consistent with published NMR studies. First molecular dynamics simulation studies investigated the molecular interactions between silk and the model drug doxorubicin. The results showed that the N-terminal domain played an important role in controlling electrostatic drug binding and release at both pH 7.4 and pH 4.

6.2 Future directions

Although the aims of this thesis have been achieved, there are many areas that would benefit from further investigation using both wet lab experimental studies and computational modelling (Figure 6.1).

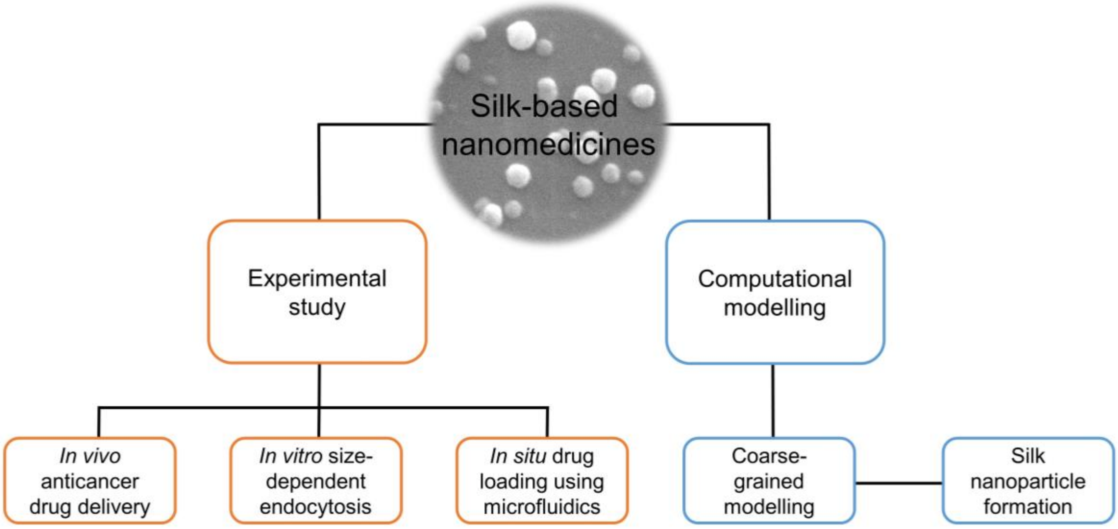

Figure 6.1 A schematic diagram of future directions.

6.2.1 *In vivo* anticancer drug delivery

In this thesis, native and PEGylated silk nanoparticles were investigated as a potential anticancer drug delivery system (Chapter 2). However, *in vitro* studies cannot recapitulate the EPR effect. Therefore, to demonstrate ERP-mediated tumour accumulation of silk nanoparticles, *in vivo* studies are required. This type of study would use a mouse xenograft model. The MDA-MB-231 human breast cancer model is a good choice because triple negative breast tumours are difficult to treat in humans and thus benefit from improved drug delivery. The following sets of studies are proposed for future studies. MDA-MB-231 cells, genetically engineered to carry the luciferase gene, will be injected into mammary fat pads of female mice. Tumours will be allowed to reach a volume of 200 mm^3. Next, the mice will be injected with freely diffusible drug (e.g. doxorubicin and propranolol) or the equivalent amount of drug loaded into PEGylated silk nanoparticles. Native silk nanoparticles will be excluded from the study, because *in vitro* studies have demonstrated substantial aggregation. The anticancer activity will be determined by measuring the tumour volume with callipers, tumour cell-associated bioluminescence (using the IVIS imagines system) while also monitoring mice weights and survival rate (Seib, Pritchard, et al., 2013; Wang et al., 2016). The survival rate will be determined by performing body conditioning scoring to ensure that the mice do not exceed accepted limits in cancer research (Workman et al., 2010) Additionally, the biodistribution of the free drugs and drug loaded silk nanoparticles will be examined by collecting tissues (e.g. heart, liver, spleen, lung, kidney and tumours) at several time points. The distribution of fluorescently labelled silk nanoparticle will be monitored using fluorescent images with the IVIS system; drug levels will be determined using HPLC analysis by extracting tissues. Similar biodistribution studies have been reported that could serve as a guide (Liu et al., 2012; Colombo et al., 2016).

6.2.2 *In vitro* size-dependent endocytosis

In Chapter 4 the optimised 110 nm and 215 nm silk nanoparticles showed size-dependent intracellular distributions, in particular in early endosomes (Figure 4.10). Therefore, future work is required to explain the endocytic pathway and to validate the size-dependent uptake mechanism. For this work RAW 264.7 cells will be preincubated with putative pharmacological inhibitors such as chlorpromazine and methyl-β-cyclodextrin for clathrin-mediated and caveolae-mediated endocytosis inhibition, respectively (Ivanov, 2008) (Note that a better experimental approach would be genetic knock-down studies but they are more difficult to conduct). The cells will then be incubated in medium containing both inhibitor and labelled silk nanoparticles. Next, the fluorescence intensities of nanoparticles will be analysed using flow cytometry and supported by live cell confocal microscopy. For example, a reduction in cell-associated fluorescence for the 110 nm silk nanoparticle population after chlorpromazine treatment would suggest that these silk nanoparticles use the clathrin-mediated endocytosis pathway to enter macrophages (Wang et al., 2017).

6.2.3 *In situ* drug loaded silk nanoparticles using microfluidics

Native and PEGylated silk nanoparticles were successfully loaded with drugs by drug adsorption to preformed nanoparticles (Chapter 2). However, no *in situ* drug loading was attempted. Furthermore, the drug carrying capacity for silk nanoparticles was found to be low. Therefore studies are needed to improve drug loading. Microfluidics was shown to generate silk nanoparticles with controlled particle characteristics (Chapter 4). Over the past 5 years, microfluidics has emerged as a promising tool for *in situ* drug encapsulation during particle manufacture as a single-step production process (Hood et al., 2014; Bains et al., 2017; Feng et al., 2017). Therefore, the next step would be to improve the silk nanoparticle drug loading capacity by exploiting *in situ* loading using microfluidics. To achieve this the payload will be mixed in either an aqueous silk solution or organic solvent. The pilot study will use a model drug (e.g. rhodamine B); rhodamine B has similar physiochemical properties as many small molecular weight drugs. Furthermore, rhodamine B is fluorescent and is thus easy to detected and measured. Based on the results reported in Chapter 4, the total flow rate and the solvent:aqueous total flow rate ratio will be used initially and fixed at 1 mL/min and 5:1, respectively. In this study, many parameters could be studied including the impact of the processing parameters on encapsulation efficiency, particle stability and drug release. Ultimately, this work will reduce preparation time of drug loaded silk nanoparticle formulations.

6.2.4 Coarse-grained molecular dynamics

While silk nanoparticles have been manufactured and characterised experimentally, the underling self-assembly mechanism of silk structure into nanoparticles has not been studied. Therefore, it will be meaningful to investigate silk nanoparticle formation to help the design of future silk-based nanomedicines. Coarse-grained molecular dynamics simulations can be applied by grouping atoms throughout the simulations into larger ‘pseudo’ atoms, which enables the simulation of large and complex systems such as protein aggregation, protein-protein interactions and membrane protein complexes (Baaden and Marrink, 2013; Kmiecik et al., 2016). According to the highly repetitive sequence (GAGAGS) of silk heavy chain and the molecular information detailed in Chapter 5, silk structure can be mapped as repeated blocks and into beads using MARTINI modelling (Marrink and Tieleman, 2013). This model can then be applied to reveal silk nanoparticle formation in different solvents such as acetone and isopropanol to complement experimental studies.

Appendix

Publications, presentations, placement and activities

Peer-reviewed publications

(i) Ibrahim, O. A. S., Gorenkova, N., McKittrick, C. M., **Wongpinyochit, T.**, Goudie, A., Seib, P. & Carswell, H. (2018) '*In vitro* studies on space-conforming self-assembling silk hydrogels as a mesenchymal stem cell-support matrix suitable for minimally invasive brain application', *Scientific Reports*. (Accepted).

(ii) **Wongpinyochit, T**., Johnston, B. F. and Seib, F. P. (2018) 'Degradation Behavior of Silk Nanoparticles—Enzyme Responsiveness', *ACS Biomaterials Science & Engineering*, 4(3), pp. 942–951. doi: 10.1021/acsbiomaterials.7b01021.

(iii) Maitz, M. F., Sperling, C., **Wongpinyochit, T**., Herklotz, M., Werner, C. and Seib, F. P. (2017) 'Biocompatibility assessment of silk nanoparticles: Hemocompatibility and internalization by human blood cells', *Nanomedicine: Nanotechnology, Biology and Medicine*, 13(8), pp. 2633–2642. doi: 10.1016/j.nano.2017.07.012.

(iv) Totten, J. D., **Wongpinyochit, T.** and Seib, F. P. (2017) 'Silk nanoparticles: proof of lysosomotropic anticancer drug delivery at single-cell resolution', *Journal of Drug Targeting,* 25(9–10), pp. 865–872. doi: 10.1080/1061186X.2017.1363212.

(v) Saborano, R., **Wongpinyochit, T**., Totten, J. D., Johnston, B. F., Seib, F. P. and Duarte, I. F. (2017) 'Metabolic Reprogramming of Macrophages Exposed to Silk, Poly(lactic-co-glycolic acid), and Silica Nanoparticles', *Advanced Healthcare Materials*, 6(14), p. 1601240. doi: 10.1002/adhm.201601240.

(vi) **Wongpinyochit, T**., Johnston, B. F. and Seib, F. P. (2016) ‘Manufacture and Drug Delivery Applications of Silk Nanoparticles’, *Journal of Visualized Experiments*, 116(116), p. e54669. doi: 10.3791/54669.

(vii) **Wongpinyochit, T**., Uhlmann, P., Urquhart, A. J. and Seib, F. P. (2015) ‘PEGylated Silk Nanoparticles for Anticancer Drug Delivery’, *Biomacromolecules*, 16(11), pp. 3712–3722. doi: 10.1021/acs.biomac.5b01003.

Papers in preparation/review

(i) **Wongpinyochit, T.**, Totten, J. D., Johnston, B. F. and Seib, F. P. ‘Microfluidic-assisted silk nanoparticle tuning’. (Submitted)

(ii) **Wongpinyochit, T.**, Mushrif, S.H., Johnston, B. F. and Seib, F. P. ‘Exploring native amorphous-crystalline silk structures and molecular binding behaviour in response to pH’. (In preparation)

Conference attendances and poster presentations

(i) **Wongpinyochit, T.**, Mushrif, S.H., Johnston, B.F., Seib, F. P. (2017) ‘Modelling the intracellular degradation of silk nanoparticles and applying WT-Metadynamics to explore silk structure space’. Poster presentation at 2017 UKICRS Workshop & Symposium (University of Strathclyde, UK).

(ii) **Wongpinyochit, T.**, Johnston, B.F., Seib, F. P. (2016) ‘Manufacture of *Bombyx mori* silk nanoparticles’. Poster presentation at 7th APS International PharmSci (University of Strathclyde, UK).

(iii) **Wongpinyochit, T.**, Johnston, B.F., Seib, F. P. (2016) ‘Understanding Silk nanoparticles - *In silico* modelling and *ex-vivo* degradation studies’. Poster presentation at Nanomaterials for Technology workshop (University of Strathclyde, UK).

(iv) **Wongpinyochit, T.**, Johnston, B.F., Urquhart, A.J., Seib, F. P. (2015) 'PEGylated silk nanoparticles for anticancer drug delivery'. Accepted abstract and poster presentation at CRS Annual Meeting & Exposition (Edinburgh, UK).

International placement

NTU Placement from 1st January – 8th March 2017

School of Chemical and Biomedical Engineering, Nanyang Technological University, Singapore

As part of my collaborative international PhD programme, I was in a placement within Assoc Prof Samir Hemant Mushrif's group. The technique I learned includes enhanced sampling method called well-tempered metadynamics for molecular dynamics simulations which accelerate systems to explore rare events and generate free energy landscape of protein structure.

Research activities

(i) European Researchers' Night (Explorathon) 2016 in Glasgow Science Centre, Glasgow, UK, 30th September 2016.

(ii) The Science Lates-Innovate event in Glasgow Science Centre, Glasgow, UK, 7th July 2017. The topic for this event was "Silk: An emerging high-tech material for medical applications".

(iii) European Researchers' Night (Explorathon) 2017 in Glasgow Science Centre, Glasgow, UK, 29th September 2017.

(iv) Glasgow Science Festival 2018 in Kelvingrove Art Gallery and Museum, Glasgow, UK, 17th June 2018.

References

Abriata, L. A. and Peraro, M. D. (2015) ‘Assessing the potential of atomistic molecular dynamics simulations to probe reversible protein-protein recognition and binding’, *Scientific Reports*, 5, p. 10549. doi: 10.1038/srep10549.

Adcock, S. A. and McCammon, J. A. (2006) ‘Molecular dynamics: Survey of methods for simulating the activity of proteins’, *Chemical Reviews*, 106(5), p. 1589–1615. doi: 10.1021/cr040426m.

Adnan, A., Lam, R., Chen, H., Lee, J., Schaffer, D. J., Barnard, A. S., Schatz, G. C., Ho, D. and Liu, W. K. (2011) ‘Atomistic simulation and measurement of pH dependent cancer therapeutic interactions with nanodiamond carrier’, *Molecular Pharmaceutics*, 8(2), p. 368–374. doi: 10.1021/mp1002398.

Alder, B. J. and Wainwright, T. E. (1957) ‘Phase transition for a hard sphere system’, *The Journal of Chemical Physics*, 27(5), p. 1208–1209. doi: 10.1063/1.1743957.

Altman, G. H., Diaz, F., Jakuba, C., Calabro, T., Horan, R. L., Chen, J., Lu, H., Richmond, J. and Kaplan, D. L. (2003) ‘Silk-based biomaterials’, *Biomaterials*, 24(3), p. 401–416. doi: 10.1016/S0142-9612(02)00353-8.

Appelqvist, H., Wäster, P., Kågedal, K. and Öllinger, K. (2013) ‘The lysosome: From waste bag to potential therapeutic target’, *Journal of Molecular Cell Biology*, 5(4), p. 214–226. doi: 10.1093/jmcb/mjt022.

Arinaminpathy, Y., Sansom, M. S. P. and Biggin, P. C. (2002) ‘Molecular dynamics simulations of the ligand-binding domain of the ionotropic glutamate receptor GluR2’, *Biophysical Journal*, 82(2), p. 676–683. doi: 10.1016/S0006-3495(02)75430-1.

Asakura, T., Okushita, K. and Williamson, M. P. (2015) ‘Analysis of the structure of Bombyx mori silk fibroin by NMR’, *Macromolecules*, 48, p. 2345–2357. doi: 10.1021/acs.macromol.5b00160.

Baaden, M. and Marrink, S. J. (2013) ‘Coarse-grain modelling of protein–protein interactions’, *Current Opinion in Structural Biology*, 23(6), p. 878–886. doi: 10.1016/j.sbi.2013.09.004.

Bae, Y. H. and Park, K. (2011) ‘Targeted drug delivery to tumors: myths, reality and possibility.’, *Journal of Controlled Release*, 153(3), p. 198–205. doi: 10.1016/j.jconrel.2011.06.001.

Baftizadeh, F., Biarnes, X., Pietrucci, F., Affinito, F. and Laio, A. (2012) ‘Multidimensional view of amyloid fibril nucleation in atomistic detail’, *Journal of the American Chemical Society*, 134(8), p. 3886–3894. doi: 10.1021/ja210826a.

Bains, A., Cao, Y., Kly, S., Wulff, J. E. and Moffitt, M. G. (2017) ‘Controlling structure and function of polymeric drug delivery nanoparticles using microfluidics’, *Molecular Pharmaceutics*, 14(8), p. 2595–2606. doi: 10.1021/acs.molpharmaceut.7b00177.

Bancos, S., Stevens, D. L. and Tyner, K. M. (2015) ‘Effect of silica and gold nanoparticles on macrophage proliferation, activation markers, cytokine production, and phagocytosis in vitro', *International Journal of Nanomedicine*, 10, p. 183–206. doi: 10.2147/IJN.S72580.

Barducci, A., Bonomi, M. and Parrinello, M. (2011) 'Metadynamics', *Wiley Interdisciplinary Reviews: Computational Molecular Science*, 1(5), p. 826–843. doi: 10.1002/wcms.31.

Barducci, A., Bussi, G. and Parrinello, M. (2008) 'Well-tempered metadynamics: A smoothly converging and tunable free-energy method', *Physical Review Letters*, 100(2), p. 1–4. doi: 10.1103/PhysRevLett.100.020603.

Bealing, C., Martonák, R. and Molteni, C. (2009) 'Pressure-induced structural phase transitions in CdSe: A metadynamics study', *Journal of Chemical Physics*, 130, p. 124712. doi: 10.1063/1.3086043.

Beck, D. A. C. and Daggett, V. (2004) 'Methods for molecular dynamics simulations of protein folding/unfolding in solution', *Methods*, 34(1), p. 112–120. doi: 10.1016/j.ymeth.2004.03.008.

Berman, H. M., Westbrook, J., Feng, Z., Gilliland, G., Bhat, T. N., Weissig, H., Shindyalov, I. N. and Bourne, P. E. (2000) 'The protein data bank', *Nucleic Acids Research*, 28(1), p. 235–242.

Berthiaume, E. P., Medina, C. and Swanson, J. A. (1995) 'Molecular size-fractionation during endocytosis in macrophages', *The Journal of Cell Biology*, 129(4), p. 989–998. doi: 10.1083/jcb.129.4.989.

Betancourt, T., Doiron, A., Homan, K. A. and Brannon-Peppas, L. (2009) 'Controlled release and nanotechnology', in *Nanotechnology in Drug Delivery*, p. 283–312. doi: 10.1007/978-0-387-77667-5_10.

Bonomi, M., Branduardi, D., Bussi, G., Camilloni, C., Provasi, D., Raiteri, P., Donadio, D., Marinelli, F., Pietrucci, F., Broglia, R. A. and Parrinello, M. (2009) 'PLUMED: A portable plugin for free-energy calculations with molecular dynamics', *Computer Physics Communications*, 180(10), p. 1961–1972. doi: 10.1016/j.cpc.2009.05.011.

Borkner, C. B., Elsner, M. B. and Scheibel, T. (2014) 'Coatings and films made of silk proteins', *ACS Applied Materials and Interfaces*, 6(18), p. 15611–15625. doi: 10.1021/am5008479.

Bratzel, G. and Buehler, M. J. (2012a) 'Molecular mechanics of silk nanostructures under varied mechanical loading', *Biopolymers*, 97(6), p. 408–417. doi: 10.1002/bip.21729.

Bratzel, G. and Buehler, M. J. (2012b) 'Sequence-structure correlations in silk: Poly-Ala repeat of N. clavipes MaSp1 is naturally optimized at a critical length scale', *Journal of the Mechanical Behavior of Biomedical Materials*, 7, p. 30–40. doi: 10.1016/j.jmbbm.2011.07.012.

Breslauer, D. N., Muller, S. J. and Lee, L. P. (2010) 'Generation of monodisperse silk microspheres prepared with microfluidics', *Biomacromolecules*, 11, p. 643–647.

Brown, J., Lu, C. L., Coburn, J. and Kaplan, D. L. (2015) ‘Impact of silk biomaterial structure on proteolysis’, *Acta Biomaterialia*, 11(1), p. 212–221. doi: 10.1016/j.actbio.2014.09.013.

Buchete, N. V. and Hummer, G. (2008) ‘Peptide folding kinetics from replica exchange molecular dynamics’, *Physical Review E - Statistical, Nonlinear, and Soft Matter Physics*, 77(3), p. 1–4. doi: 10.1103/PhysRevE.77.030902.

Buehler, M., Keten, S. and Ackbarow, T. (2008) ‘Theoretical and computational hierarchical nanomechanics of protein materials: Deformation and fracture’, *Progress in Materials Science*, 53(8), p. 1101–1241. doi: 10.1016/j.pmatsci.2008.06.002.

Cao, Y. and Wang, B. (2009) ‘Biodegradation of silk biomaterials.’, *International journal of molecular sciences*, 10(4), p. 1514–1524. doi: 10.3390/ijms10041514.

Cavalli, A., Spitaleri, A., Saladino, G. and Gervasio, F. L. (2015) ‘Investigating drug-target association and dissociation mechanisms using metadynamics-based algorithms’, *Accounts of Chemical Research*, 48, p. 277–285. doi: 10.1021/ar500356n.

Chen, C., Yao, T., Tu, S., Xu, W., Han, Y. and Zhou, P. (2016) ‘In situ microscopic studies on the structures and phase behaviors of SF/PEG films using solid-state NMR and Raman imaging’, *Physical Chemistry Chemical Physics*, 18(24), p. 16353–16360. doi: 10.1039/C6CP03314H.

Chen, T., Song, J. and Chan, H. S. (2015) ‘Theoretical perspectives on nonnative interactions and intrinsic disorder in protein folding and binding’, *Current Opinion in Structural Biology*, 30, p. 32–42. doi: 10.1016/j.sbi.2014.12.002.

Cheng, Y., Koh, L.-D., Li, D., Ji, B., Han, M.-Y. and Zhang, Y.-W. (2014) ‘On the strength of β-sheet crystallites of Bombyx mori silk fibroin’, *Journal of the Royal Society, Interface*, 11, p. 20140305.

Cheng, Y., Koh, L.-D., Li, D., Ji, B., Zhang, Y., Yeo, J., Guan, G., Han, M.-Y. and Zhang, Y.-W. (2015) ‘Peptide–Graphene Interactions Enhance the Mechanical Properties of Silk Fibroin’, *ACS Applied Materials & Interfaces*, 7(39), p. 21787–21796. doi: 10.1021/acsami.5b05615.

Cho, H. J. and Um, I. C. (2010) ‘The effect of dissolution condition on the yield , molecular weight , and wet- and electro-spinnability of regenerated silk fibroins prepared by LiBr aqueous solution’, *International Journal of Industrial Entomology*, 20(2), p. 99–105.

Chou, T.-C. (2006) ‘Theoretical basis, experimental design, and computerized simulation of synergism and antagonism in drug combination studies.’, *Pharmacological reviews*, 58(3), p. 621–681. doi: 10.1124/pr.58.3.10.

Colombo, M., Fiandra, L., Alessio, G., Mazzucchelli, S., Nebuloni, M., De Palma, C., Kantner, K., Pelaz, B., Rotem, R., Corsi, F., Parak, W. J. and Prosperi, D. (2016) ‘Tumour homing and therapeutic effect of colloidal nanoparticles depend on the number of attached antibodies’, *Nature Communications*, 7, p. 13818. doi: 10.1038/ncomms13818.

Comitani, F., Melis, C. and Molteni, C. (2015) ‘Elucidating ligand binding and channel gating mechanisms in pentameric ligand-gated ion channels by atomistic simulations’, *Biochemical Society Transactions,* 43(2), p. 151–156. doi: 10.1042/BST20140259.

Cortes, J. E., Goldberg, S. L., Feldman, E. J., Rizzeri, D. A., Hogge, D. E., Larson, M., Pigneux, A., Recher, C., Schiller, G., Warzocha, K., Kantarjian, H., Louie, A. C. and Kolitz, J. E. (2015) ‘Phase II, multicenter, randomized trial of CPX-351 (cytarabine:daunorubicin) liposome injection versus intensive salvage therapy in adults with first relapse AML’, *Cancer,* 121(2), p. 234–242. doi: 10.1002/cncr.28974.

Cossio, P., Trovato, A., Pietrucci, F., Seno, F., Maritan, A. and Laio, A. (2010) ‘Exploring the universe of protein structures beyond the protein data bank’, *PLoS Computational Biology,* 6(11), p. e1000957. doi: 10.1371/journal.pcbi.1000957.

Dama, J. F., Parrinello, M. and Voth, G. A. (2014) ‘Well-tempered metadynamics converges asymptotically’, *Physical Review Letters,* 112(24), p. 240602. doi: 10.1103/PhysRevLett.112.240602.

Davis, M. E., Chen, Z. G. and Shin, D. M. (2008) ‘Nanoparticle therapeutics: an emerging treatment modality for cancer.’, *Nature reviews. Drug discovery,* 7(9), p. 771–782. doi: 10.1038/nrd2614.

Dhotel, A., Chen, Z., Delbreilh, L., Youssef, B., Saiter, J.-M. and Tan, L. (2013) ‘Molecular motions in functional self-assembled nanostructures’, *International Journal of Molecular Sciences,* p. 2303–2333. doi: 10.3390/ijms14022303.

Dou, H. and Zuo, B. (2014) ‘Effect of sodium carbonate concentrations on the formation and mechanism of regenerated silk fibroin nanofibers by electrospinning’, *Journal of Nanomaterials,* 2014, p. 1–9. doi: 10.1080/00405000.2014.919065.

Duncan, R. (2006) ‘Polymer conjugates as anticancer nanomedicines’, *Nature Reviews Cancer,* 6, p. 688–701. doi: 10.1038/nrc1958.

Duncan, R. (2009) ‘Development of HPMA copolymer-anticancer conjugates: Clinical experience and lessons learnt’, *Advanced Drug Delivery Reviews,* 61(13), p. 1131–1148. doi: 10.1016/j.addr.2009.05.007.

Duncan, R. and Gaspar, R. (2011) ‘Nanomedicine(s) under the microscope’, *Molecular Pharmaceutics,* 8(6), p. 2101–2141. doi: 10.1021/mp200394t.

Duncan, R. and Richardson, S. C. W. (2012) ‘Endocytosis and intracellular trafficking as gateways for nanomedicine delivery: Opportunities and challenges’, *Molecular Pharmaceutics,* 9(9), p. 2380–2402. doi: 10.1021/mp300293n.

Duncan, R. and Vicent, M. J. (2013) ‘Polymer therapeutics-prospects for 21st century: The end of the beginning’, *Advanced Drug Delivery Reviews,* 65(1), p. 60–70. doi: 10.1016/j.addr.2012.08.012.

Durrant, J. D. and McCammon, J. A. (2011) ‘Molecular dynamics simulations and drug discovery’, *BMC Biology,* 9(1), p. 71. doi: 10.1186/1741-7007-9-71.

De Duve, C., De Barsy, T., Poole, B., Trouet, A., Tulkens, P. and Van Hoof, F.

(1974) ‘Lysosomotropic agents’, *Biochemical Pharmacology*, 23(18), p. 2495–2531. doi: 10.1016/0006-2952(74)90174-9.

Ensing, B., De Vivo, M., Liu, Z., Moore, P. and Klein, M. L. (2006) ‘Metadynamics as a tool for exploring free energy landscapes of chemical reactions’, *Accounts of Chemical Research*, 39, p. 73–81. doi: 10.1021/ar040198i.

Fang, J., Nakamura, H. and Maeda, H. (2011) ‘The EPR effect: Unique features of tumor blood vessels for drug delivery, factors involved, and limitations and augmentation of the effect.’, *Advanced Drug Delivery Reviews*, 63(3), p. 136–151. doi: 10.1016/j.addr.2010.04.009.

Feng, Q., Liu, J., Li, X., Chen, Q., Sun, J., Shi, X., Ding, B., Yu, H., Li, Y. and Jiang, X. (2017) ‘One-step microfluidic synthesis of nanocomplex with tunable rigidity and acid-switchable surface charge for overcoming drug resistance’, *Small*, 13(9), p. 1603109. doi: 10.1002/smll.201603109.

Florczak, A., Mackiewicz, A. and Dams-Kozlowska, H. (2014) ‘Functionalized spider silk spheres as drug carriers for targeted cancer therapy’, *Biomacromolecules*, 15(8), p. 2971–2981. doi: 10.1021/bm500591p.

Fu, C., Shao, Z. and Fritz, V. (2009) ‘Animal silks: their structures, properties and artificial production’, *Chemical Communications*, (43), p. 6515. doi: 10.1039/b911049f.

Gdowski, A., Johnson, K., Shah, S., Gryczynski, I. and Vishwanatha, J. (2018) ‘Optimization and scale up of microfluidic nanolipomer production method for preclinical and potential clinical trials’, *Journal of Nanobiotechnology*, 16(1), p. 12. doi: 10.1186/s12951-018-0339-0.

Gholami, A., Tavanai, H. and Moradi, A. R. (2011) ‘Production of fibroin nanopowder through electrospraying’, *Journal of Nanoparticle Research*, 13, p. 2089–2098. doi: 10.1007/s11051-010-9965-7.

Giesa, T., Arslan, M., Pugno, N. M. and Buehler, M. J. (2011) ‘Nanoconfinement of spider silk fibrils begets superior strength, extensibility, and toughness.’, *Nano letters*, 11(11), p. 5038–5046. doi: 10.1021/nl203108t.

Goodman, J. M. (1998) *Chemical application of molecular modelling*. Cambridge: The Royal Society of Chemistry.

Graham, J. M. (1993) ‘The identification of subcellular fractions from mammalian cells’, in Graham, J. M. and Higgins, J. A. (eds) *Methods in molecular biology, biomembrane protocols: I. Isolation and analysis*. Totowa: Humana Press Inc, p. 1–18.

Granata, D., Camilloni, C., Vendruscolo, M. and Laio, A. (2013) ‘Characterization of the free-energy landscapes of proteins by NMR-guided metadynamics’, *Proceedings of the National Academy of Sciences*, 110(17), p. 6817–6822. doi: 10.1073/pnas.1218350110.

Greenwald, R. B., Choe, Y. H., McGuire, J. and Conover, C. D. (2003) ‘Effective drug delivery by PEGylated drug conjugates’, *Advanced Drug Delivery Reviews*, 55(2), p. 217–250. doi: 10.1016/S0169-409X(02)00180-1.

Guimarães, M., Correia, S., Briuglia, M. L., Niosi, F. and Lamprou, D. A. (2017) ‘Microfluidic manufacturing of phospholipid nanoparticles: Stability, encapsulation efficacy, and drug release’, *International Journal of Pharmaceutics*, 516, p. 91–99. doi: 10.1016/j.ijpharm.2016.11.025.

Gupta, V., Aseh, A., Ríos, C. N., Aggarwal, B. B. and Mathur, A. B. (2009) ‘Fabrication and characterization of silk fibroin-derived curcumin nanoparticles for cancer therapy.’, *International journal of nanomedicine*, 4, p. 115–122.

Gustafson, H. H., Holt-Casper, D., Grainger, D. W. and Ghandehari, H. (2015) ‘Nanoparticle uptake: The phagocyte problem’, *Nano Today*, 10(4), p. 487–510. doi: 10.1016/j.nantod.2015.06.006.

Ha, S.-W., Gracz, H. S., Tonelli, A. E. and Hudson, S. M. (2005) ‘Structural study of irregular amino acid sequences in the heavy chain of Bombyx mori silk fibroin.’, *Biomacromolecules*, 6, p. 2563–2569. doi: 10.1021/bm050294m.

Hakimi, O., Knight, D. P., Vollrath, F. and Vadgama, P. (2007) ‘Spider and mulberry silkworm silks as compatible biomaterials’, *Composites Part B: Engineering*, 38, p. 324–337. doi: 10.1016/j.compositesb.2006.06.012.

Hamelberg, D., Mongan, J. and McCammon, J. A. (2004) ‘Accelerated molecular dynamics: A promising and efficient simulation method for biomolecules’, *J Chem Phys*, 120(24), p. 11919–11929. doi: 10.1063/1.1755656.

He, Y. X., Zhang, N. N., Li, W. F., Jia, N., Chen, B. Y., Zhou, K., Zhang, J., Chen, Y. and Zhou, C. Z. (2012) ‘N-terminal domain of Bombyx mori fibroin mediates the assembly of silk in response to pH decrease’, *Journal of Molecular Biology*, 418, p. 197–207. doi: 10.1016/j.jmb.2012.02.040.

Heim, M., Keerl, D. and Scheibel, T. (2009) ‘Spider silk: From soluble protein to extraordinary fiber’, *Angewandte Chemie - International Edition*, 48(20), p. 3584–3596. doi: 10.1002/anie.200803341.

Holland, C., Numata, K., Rnjak-Kovacina, J. and Seib, F. P. (2018) ‘The biomedical use of silk: Past, present, future’, *Advanced Healthcare Materials*, p. 1800465. doi: 10.1002/adhm.201800465.

Holland, C., Terry, A. E., Porter, D. and Vollrath, F. (2007) ‘Natural and unnatural silks’, *Polymer*, 48(12), p. 3388–3392. doi: 10.1016/j.polymer.2007.04.019.

Holliday, D. L. and Speirs, V. (2011) ‘Choosing the right cell line for breast cancer research’, *Holliday and Speirs Breast Cancer Research*, 13, p. 215. doi: 10.1186/bcr2889.

Hood, R. R., Vreeland, W. N. and DeVoe, D. L. (2014) ‘Microfluidic remote loading for rapid single-step liposomal drug preparation’, *Lab on a chip*, 14(17), p. 3359–3367. doi: 10.1039/c4lc00390j.

Hrkach, J. et al. (2012) ‘Preclinical development and clinical translation of a PSMA-targeted docetaxel nanoparticle with a differentiated pharmacological profile’, *Science Translational Medicine*, 4, p. 128–139. doi: 10.1126/scitranslmed.3003651.

Hu, X., Kaplan, D. and Cebe, P. (2006) ‘Determining beta-sheet crystallinity in fibrous proteins by thermal analysis and infrared spectroscopy’, *Macromolecules*, 39(18), p. 6161–6170. doi: 10.1021/ma0610109.

Humphrey, W., Dalke, A. and Schulten, K. (1996) ‘VMD: Visual molecular dynamics’, *Journal of Molecular Graphics*, 14(1), p. 27–28. doi: 10.1016/0263-7855(96)00018-5.

Inoue, S., Tanaka, K., Arisaka, F., Kimura, S., Ohtomo, K. and Mizuno, S. (2000) ‘Silk fibroin of Bombyx mori is secreted, assembling a high molecular mass elementary unit consisting of H-chain, L-chain, and P25, with a 6:6:1 molar ratio’, *Journal of Biological Chemistry*, 275(51), p. 40517–40528. doi: 10.1074/jbc.M006897200.

Isralewitz, B., Gao, M. and Schulten, K. (2001) ‘Steered molecular dynamics and mechanical functions of proteins’, *Current Opinion in Structural Biology*, 11(2), p. 224–230. doi: 10.1016/S0959-440X(00)00194-9.

Ivanov, A. I. (2008) ‘Pharmacological inhibition of endocytic pathways: Is it specific enough to be useful?’, *Methods in Molecular Biology*, 440, p. 15–33. doi: 10.1007/978-1-59745-178-9_2.

Ivens, I. A., Achanzar, W., Baumann, A., Brändli-Baiocco, A., Cavagnaro, J., Dempster, M., Depelchin, B. O., Irizarry Rovira, A. R., Dill-Morton, L., Lane, J. H., Reipert, B. M., Salcedo, T., Schweighardt, B., Tsuruda, L. S., Turecek, P. L. and Sims, J. (2015) ‘PEGylated biopharmaceuticals’, *Toxicologic Pathology*, 43, p. 959–983. doi: 10.1177/0192623315591171.

Jewell, M., Daunch, W., Bengtson, B. and Mortarino, E. (2015) ‘The development of SERI® Surgical Scaffold, an engineered biological scaffold’, *Annals of the New York Academy of Sciences*, 1358(1), p. 44–55. doi: 10.1111/nyas.12886.

Ji, Y., Chen, S., Xiao, X., Zheng, S. and Li, K. (2012) ‘β-blockers: a novel class of antitumor agents’, *OncoTargets and therapy*, 5, p. 391–401. doi: 10.2147/OTT.S38403.

Jin, H.-J. and Kaplan, D. L. (2003) ‘Mechanism of silk processing in insects and spiders.’, *Nature*, 424(6952), p. 1057–1061. doi: 10.1038/nature01809.

Joshi, S., Hussain, M. T., Roces, C. B., Anderluzzi, G., Kastner, E., Salmaso, S., Kirby, D. J. and Perrie, Y. (2016) ‘Microfluidics based manufacture of liposomes simultaneously entrapping hydrophilic and lipophilic drugs’, *International Journal of Pharmaceutics*, 514(1), p. 160–168. doi: 10.1016/j.ijpharm.2016.09.027.

Kastner, E., Kaur, R., Lowry, D., Moghaddam, B., Wilkinson, A. and Perrie, Y. (2015) ‘High-throughput manufacturing of size-tuned liposomes by a new micro fl uidics method using enhanced statistical tools for characterization’, *International Journal of Pharmaceutics*, 477(1–2), p. 361–368. doi: 10.1016/j.ijpharm.2014.10.030.

Keten, S. and Buehler, M. J. (2010) ‘Nanostructure and molecular mechanics of spider dragline silk protein assemblies’, *Journal of the Royal Society, Interface / the Royal Society*, 7, p. 1709–1721. doi: 10.1098/rsif.2010.0149.

Keten, S., Xu, Z., Ihle, B. and Buehler, M. J. (2010) ‘Nanoconfinement controls stiffness, strength and mechanical toughness of β-sheet crystals in silk’, *Nature Materials*, 9(4), p. 359–367. doi: 10.1038/nmat2704.

Klemm, A. R., Young, D. and Lloyd, J. B. (1998) ‘Effects of polyethyleneimine on endocytosis and lysosome stability’, *Biochemical Pharmacology*, 56(1), p. 41–46. doi: 10.1016/S0006-2952(98)00098-7.

Kmiecik, S., Gront, D., Kolinski, M., Wieteska, L., Dawid, A. E. and Kolinski, A. (2016) ‘Coarse-grained protein models and their applications’, *Chemical Reviews*, 116(14), p. 7898–7936. doi: 10.1021/acs.chemrev.6b00163.

Koh, L.-D., Cheng, Y., Teng, C.-P., Khin, Y.-W., Loh, X.-J., Tee, S.-Y., Low, M., Ye, E., Yu, H.-D., Zhang, Y.-W. and Han, M.-Y. (2015) ‘Structures, mechanical properties and applications of silk fibroin materials’, *Progress in Polymer Science*, 46, p. 86–110. doi: 10.1016/j.progpolymsci.2015.02.001.

Kreuter, J. (2007) ‘Nanoparticles-a historical perspective’, *International journal of pharmaceutics*, 331(1), p. 1–10. doi: 10.1016/j.ijpharm.2006.10.021.

Kundu, J., Chung, Y.-I., Kim, Y. H., Tae, G. and Kundu, S. C. (2010) ‘Silk fibroin nanoparticles for cellular uptake and control release.’, *International journal of pharmaceutics*, 388(1–2), p. 242–250. doi: 10.1016/j.ijpharm.2009.12.052.

Kusaka, T., Nakayama, M., Nakamura, K., Ishimiya, M., Furusawa, E. and Ogasawara, K. (2014) ‘Effect of silica particle size on macrophage inflammatory responses.’, *PloS One*, 9(3), p. e92634. doi: 10.1371/journal.pone.0092634.

de la Zerda, A., Bodapati, S., Teed, R., May, S. Y., Tabakman, S. M., Liu, Z., Khuri-Yakub, B. T., Chen, X., Dai, H. and Gambhir, S. S. (2012) ‘Family of enhanced photoacoustic imaging agents for high-sensitivity and multiplexing studies in living mice’, *ACS Nano*, 6(6), p. 4694–4701. doi: 10.1021/nn204352r.

Laio, A. and Gervasio, F. L. (2008) ‘Metadynamics: A method to simulate rare events and reconstruct the free energy in biophysics, chemistry and material science’, *Reports on Progress in Physics*, 71, p. 126601. doi: 10.1088/0034-4885/71/12/126601.

Laio, A. and Parrinello, M. (2002) ‘Escaping free-energy minima’, *Proceedings of the National Academy of Sciences of The United States of America*, 99(20), p. 12562–12566. doi: 10.1073/pnas.202427399.

Lammel, A. S., Hu, X., Park, S.-H., Kaplan, D. L. and Scheibel, T. R. (2010) ‘Controlling silk fibroin particle features for drug delivery’, *Biomaterials*, 31(16), p. 4583–4591. doi: 10.1016/j.biomaterials.2010.02.024.

Lammel, A., Schwab, M., Hofer, M., Winter, G. and Scheibel, T. (2011) ‘Recombinant spider silk particles as drug delivery vehicles.’, *Biomaterials*, 32(8), p. 2233–40. doi: 10.1016/j.biomaterials.2010.11.060.

Leach, A. R. (2001) *Molecular modelling principles and applications*. Second Edi. Essex: Pearson Education Limited.

Lefèvre, T., Rousseau, M.-E. and Pézolet, M. (2007) ‘Protein secondary structure and orientation in silk as revealed by raman spectromicroscopy', *Biophysical Journal,* 92(8), p. 2885–2895. doi: 10.1529/biophysj.106.100339.

Leva, F. S. Di, Tomassi, S., Maro, S. Di, Reichart, F., Notni, J., Dangi, A., Marelli, U. K., Brancaccio, D., Merlino, F., Wester, H. J., Novellino, E., Kessler, H. and Marinelli, L. (2018) 'From a helix to a small cycle: metadynamics-inspired αvβ6 integrin selective ligands', *Angewandte Chemie - International Edition,* 57(44), p. 14645–14649. doi: 10.1002/anie.201803250.

Lewars, E. G. (2011) *Computational chemistry Introduction to the theory and applications of molecular and quantum mechanics*. Second Edi. Peterborough: Springer Science.

Li, A. B., Kluge, J. A., Guziewicz, N. A., Omenetto, F. G. and Kaplan, D. L. (2015) 'Silk-based stabilization of biomacromolecules', *Journal of Controlled Release,* 219, p. 416–430. doi: 10.1016/j.jconrel.2015.09.037.

Lim, J.-M., Bertrand, N., Valencia, P. M., Rhee, M., Langer, R., Jon, S., Farokhzad, O. C. and Karnik, R. (2014) 'Parallel microfluidic synthesis of size-tunable polymeric nanoparticles using 3D flow focusing towards in vivo study', *Nanomedicine: Nanotechnology, Biology, and Medicine,* 10(2), p. 401–409. doi: 10.1016/j.nano.2013.08.003.

Liu, G., Yang, X., Li, Y., Yang, Z., Hong, W. and Liu, J. (2015) 'Continuous flow controlled synthesis of gold nanoparticles using pulsed mixing microfluidic system', *Advances in Materials Science and Engineering,* p. 160819. doi: 10.1155/2015/160819.

Liu, Y., Tseng, Y. and Huang, L. (2012) 'Biodistribution studies of nanoparticles using fluorescence imaging: A qualitative or quantitative Method?', *Pharmaceutical Research,* 29(12), p. 3273–3277. doi: 10.1007/s11095-012-0818-1.

Lozano-Perez, A. A., Montalban, M. G., Aznar-Cervantes, S. D., Cragnolini, F., Cenis, J. L. and Villora, G. (2015) 'Production of silk fibroin nanoparticles using ionic liquids and high-power ultrasounds', *Journal of Applied Polymer Science*, p. 41702. doi: 10.1002/app.41702.

Lu, Q., Huang, Y., Li, M., Zuo, B., Lu, S., Wang, J., Zhu, H. and Kaplan, D. L. (2011) 'Silk fibroin electrogelation mechanisms', *Acta Biomaterialia,* 7, p. 2394–2400. doi: 10.1016/j.actbio.2011.02.032.

Lu, Q., Zhang, B., Li, M., Zuo, B., Kaplan, D. L., Huang, Y. and Zhu, H. (2011) 'Degradation mechanism and control of silk fibroin', *Biomacromolecules,* 12, p. 1080–1086. doi: 10.1021/bm101422j.

Lu, S., Wang, X., Lu, Q. and Hu, X. (2009) 'Stabilization of enzymes in silk films', *Biomacromolecules,* 10(5), p. 1032–1042. doi: 10.1021/bm800956n.Stabilization.

Lu, S., Wang, X., Uppal, N., Kaplan, D. L. and Li, M. (2009) 'Stabilization of horseradish peroxidase in silk materials', *Frontiers of Materials Science in China,* 3(4), p. 367–373. doi: 10.1007/s11706-009-0058-4.

Ma, M., Zhong, J., Li, W., Zhou, J., Yan, Z., Ding, J. and He, D. (2013) 'Comparison of four synthetic model peptides to understand the role of modular motifs in the self-assembly of silk fibroin', *Soft Matter*, 9, p. 11325. doi: 10.1039/c3sm51498f.

Maeda, H., Nakamura, H. and Fang, J. (2013) 'The EPR effect for macromolecular drug delivery to solid tumors: Improvement of tumor uptake, lowering of systemic toxicity, and distinct tumor imaging in vivo', *Advanced Drug Delivery Reviews*, 65(1), p. 71–79. doi: 10.1016/j.addr.2012.10.002.

Magee, G. A., Halbert, G. W. and Wilmott, N. (1995) 'Effect of process variables on the in-vitro degradation of protein microspheres', *Journal of Controlled Release*, 37(1–2), p. 11–19. doi: 10.1016/0168-3659(95)00040-F.

Magee, G. A., Willmott, N. and Halbert, G. W. (1993) 'Development of a reproduceable in vitro method for assessing the biodegradation of protein microspheres', *Journal of Controlled Release*, 25(3), p. 241–248. doi: 10.1016/0168-3659(93)90082-G.

Mahdavi, M., Rahmani, F. and Nouranian, S. (2016) 'Molecular simulation of pH-dependent diffusion, loading, and release of doxorubicin in graphene and graphene oxide drug delivery systems', *Journal of Materials Chemistry B*, 4(46), p. 7441–7451. doi: 10.1039/C6TB00746E.

Mains, J., Lamprou, D. A., McIntosh, L., Oswald, I. D. H. and Urquhart, A. J. (2013) 'Beta-adrenoceptor antagonists affect amyloid nanostructure; amyloid hydrogels as drug delivery vehicles', *Chemical Communications*, 49(44), p. 5082–5084. doi: 10.1039/C3CC41583J.

Maitz, M. F., Sperling, C., Wongpinyochit, T., Herklotz, M., Werner, C. and Seib, F. P. (2017) 'Biocompatibility assessment of silk nanoparticles: Hemocompatibility and internalization by human blood cells', *Nanomedicine: Nanotechnology, Biology and Medicine*, 13(8), p. 2633–2642. doi: 10.1016/j.nano.2017.07.012.

Makadia, H. K. and Siegel, S. J. (2011) 'Poly Lactic-co-Glycolic Acid (PLGA) as biodegradable controlled drug delivery carrier', *Polymers*, 3(3), p. 1377–1397. doi: 10.3390/polym3031377.

Mantovani, A., Marchesi, F., Malesci, A., Laghi, L. and Allavena, P. (2017) 'Tumour-associated macrophages as treatment targets in oncology', *Nature Reviews Clinical Oncology*, 14(7), p. 399–416. doi: 10.1038/nrclinonc.2016.217.

Marrink, S. J. and Tieleman, D. P. (2013) 'Perspective on the martini model', *Chemical Society Reviews*, 42(16), p. 6801–6822. doi: 10.1039/c3cs60093a.

Mathur, A. B. and Gupta, V. (2010) 'Silk fibroin-derived nanoparticles for biomedical applications.', *Nanomedicine*, 5(5), p. 807–820. doi: 10.2217/nnm.10.51.

Matsumura, Y. and Maeda, H. (1986) 'A new concept for macromolecular therapeutics in cancer chemotherapy: mechanism of tumoritropic accumulation of proteins and the antitumor agent Smancs', *Cancer Research*, 46, p. 6387–6392.

McCammon, J. A. (1976) 'Molecular dynamics study of the bovin pancreatic trypsin inhibitor', in Berendsen, H. J. C. (ed.) *Models for Protein Dynamics*. Orsay, France: CECAM, Universite´ de Paris IX, p. 137–152.

Meinel, L., Hofmann, S., Karageorgiou, V., Kirker-Head, C., McCool, J., Gronowicz, G., Zichner, L., Langer, R., Vunjak-Novakovic, G. and Kaplan, D. L. (2005) ‘The inflammatory responses to silk films in vitro and in vivo’, *Biomaterials,* 26(2), p. 147–155. doi: 10.1016/j.biomaterials.2004.02.047.

Montalban, M. G., Coburn, J. M., Lozano-Perez, A. A., Cenis, J. L., Villora, G. and Kaplan, D. L. (2018) ‘Production of curcumin-loaded silk fibroin nanoparticles for cancer therapy’, *Nanomaterials,* 8, p. 126. doi: 10.3390/nano8020126.

Monti, P., Taddei, P., Freddi, G., Asakura, T. and Tsukada, M. (2001) ‘Raman spectroscopic characterization of Bombyx mori silk fibroin : Raman spectrum of Silk I’, *Journal of Raman Spectroscopy,* 32, p. 103–107.

Mottaghitalab, F., Farokhi, M., Shokrgozar, M. A., Atyabi, F. and Hosseinkhani, H. (2015) ‘Silk fibroin nanoparticle as a novel drug delivery system’, *Journal of Controlled Release,* 206, p. 161–176. doi: 10.1016/j.jconrel.2015.03.020.

Murphy, A. R. and Kaplan, D. L. (2009) ‘Biomedical applications of chemically-modified silk fibroin’, *Journal of materials chemistry,* 19(36), p. 6443–6450. doi: 10.1039/b905802h.

Myung, S. J., Kim, H., Kim, Y., Chen, P. and Jin, H. (2008) ‘Fluorescent silk fibroin nanoparticles prepared using a reverse microemulsion’, *Macromolecular Research,* 16(7), p. 604–608.

Nakamura, H., Fang, J. and Maeda, H. (2015) ‘Development of next-generation macromolecular drugs based on the EPR effect: challenges and pitfalls’, *Expert Opinion on Drug Delivery,* 12(1), p. 53–64. doi: 10.1517/17425247.2014.955011.

Natfji, A. A., Ravishankar, D., Osborn, H. M. I. and Greco, F. (2017) ‘Parameters affecting the enhanced permeability and retention effect: The need for patient selection’, *Journal of Pharmaceutical Sciences*, 106(11), p. 3179–3187. doi: 10.1016/j.xphs.2017.06.019.

Nativo, P., Prior, I. A. and Brust, M. (2008) ‘Uptake and intracellular fate of surface-modified gold nanoparticles’, *ACS Nano*. American Chemical Society, 2(8), p. 1639–1644. doi: 10.1021/nn800330a.

Nova, A., Keten, S., Pugno, N. M., Redaelli, A. and Buehler, M. J. (2010) ‘Molecular and nanostructural mechanisms of deformation, strength and toughness of spider silk fibrils’, *Nano Letters,* 10, p. 2626–2634. doi: 10.1021/nl101341w.

Numata, K., Cebe, P. and Kaplan, D. L. (2010) ‘Mechanism of enzymatic degradation of beta-sheet crystals’, *Biomaterials*, 31(10), p. 2926–2933. doi: 10.1016/j.biomaterials.2009.12.026.

Numata, K. and Kaplan, D. L. (2010) ‘Silk-based delivery systems of bioactive molecules’, *Advanced Drug Delivery Reviews,* 62(15), p. 1497–1508. doi: 10.1016/j.addr.2010.03.009.

Omenetto, F. G. and Kaplan, D. L. (2010) ‘New opportunities for an ancient material’, *Science*, 329(5991), p. 528–531. doi: 10.1126/science.1188936.

Onuchic, J. N., Luthey-Schulten, Z. and Wolynes, P. G. (1997) ‘Theory of protein folding: the energy landscape perspective', *Annual Review of Physical Chemistry,* 48(1), p. 545–600. doi: 10.1146/annurev.physchem.48.1.545.

Owens, D. E. and Peppas, N. A. (2006) 'Opsonization, biodistribution, and pharmacokinetics of polymeric nanoparticles', *International Journal of Pharmaceutics,* 307(1), p. 93–102. doi: 10.1016/j.ijpharm.2005.10.010.

Pace, C. N., Grimsley, G. R. and Scholtz, J. M. (2009) 'Protein ionizable groups: pK values and their contribution to protein stability and solubility', *The Journal of Biological Chemistry,* 284(20), p. 13285–13289. doi: 10.1074/jbc.R800080200.

Padaki, N. V., Das, B. and Basu, A. (2015) 'Advances in understanding the properties of silk', in Basu, A. (ed.) *Advances in Silk Science and Technology*. Cambridge, UK: Woodhead Publishing, p. 3–16. doi: 10.1016/B978-1-78242-311-9.00001-X.

Pantziarka, P., Bouche, G., Meheus, L., Sukhatme, V. and Sukhatme, V. P. (2015) 'Repurposing drugs in your medicine cabinet: Untapped opportunities for cancer therapy?', *Future Oncology,* 11(2), p. 181–184. doi: 10.2217/fon.14.244.

Pasquier, E., Ciccolini, J. and Carre, M. (2011) 'Propranolol potentiates the anti-angiogenic effects and anti-tumor efficacy of chemotherapy agents: implication in breast cancer treatment', *Oncotarget,* 2(10), p. 797–809. doi: 10.18632/oncotarget.343.

Pasut, G. and Veronese, F. M. (2012) 'State of the art in PEGylation: The great versatility achieved after forty years of research', *Journal of Controlled Release,* 161(2), p. 461–472. doi: 10.1016/j.jconrel.2011.10.037.

Pelton, J. T. and McLean, L. R. (2000) 'Spectroscopic methods for analysis of protein secondary structure', *Analytical Biochemistry,* 277(2), p. 167–176. doi: 10.1006/abio.1999.4320.

Pereira, R. F. P., Silva, M. M. and de Zea Bermudez, V. (2015) 'Bombyx mori silk Fibers: An outstanding family of materials', *Macromolecular Materials and Engineering,* 300(12), p. 1171–1198. doi: 10.1002/mame.201400276.

Perez-Rigueiro, J., Elices, M., Llorca, J. and Viney, C. (2001) 'Tensile properties of silkworm silk obtained by forced silking', *Journal of Applied Polymer Science,* 82(8), p. 1928–1935. doi: 10.1002/app.2038.

Pietrucci, F. and Laio, A. (2009) 'A collective variable for the efficient exploration of protein beta-sheet structures: Application to SH3 and GB1', *Journal of Chemical Theory and Computation,* 5(9), p. 2197–2201. doi: 10.1021/ct900202f.

Pondman, K. M., Sobik, M., Nayak, A., Tsolaki, A. G., Jäkel, A., Flahaut, E., Hampel, S., ten Haken, B., Sim, R. B. and Kishore, U. (2014) 'Complement activation by carbon nanotubes and its influence on the phagocytosis and cytokine response by macrophages', *Nanomedicine: Nanotechnology, Biology and Medicine,* 10(6), p. 1287–1299. doi: https://doi.org/10.1016/j.nano.2014.02.010.

Price, R., Poursaid, A. and Ghandehari, H. (2014) 'Controlled release from recombinant polymers', *Journal of Controlled Release,* 190, p. 304–313. doi:

10.1016/j.jconrel.2014.06.016.

Pritchard, E. M., Dennis, P. B., Omenetto, F., Naik, R. R. and Kaplan, D. L. (2012) ‘Review physical and chemical aspects of stabilization of compounds in silk’, *Biopolymers*, 97(6), p. 479–98. doi: 10.1002/bip.22026.

Pritchard, E. M., Hu, X., Finley, V., Kuo, C. K. and Kaplan, D. L. (2013) ‘Effect of silk protein processing on drug delivery from silk films’, *Macromolecular Bioscience*, 13(3), p. 311–320. doi: 10.1002/mabi.201200323.

Qin, G. and Kaplan, D. L. (2011) ‘Silk-based biomaterials biology, properties, and clinical applications’, in Hollinger, J. O. (ed.) *An introduction to biomaterials*. Second, p. 421–431.

Qu, J., Wang, L., Hu, Y., You, R. and Li, M. (2013) ‘Preparation of silk fibroin microspheres and its cytocompatibility’, *Journal of Biomaterials and Nanobiotechnology*, 4, p. 84–90. doi: 10.4236/jbnb.2013.41011.

Rabanel, J.-M., Hildgen, P. and Banquy, X. (2014) ‘Assessment of PEG on polymeric particles surface, a key step in drug carrier translation’, *Journal of Controlled Release*, 185, p. 71–87. doi: 10.1016/j.jconrel.2014.04.017.

Rajak, S. N., Habtamu, E., Weiss, H. a, Kello, A. B., Gebre, T., Genet, A., Bailey, R. L., Mabey, D. C. W., Khaw, P. T., Gilbert, C. E., Emerson, P. M. and Burton, M. J. (2011) ‘Absorbable versus silk sutures for surgical treatment of trachomatous trichiasis in ethiopia: A randomised controlled trial’, *PLoS Medicine*. Edited by S. Lewallen, 8(12), p. e1001137. doi: 10.1371/journal.pmed.1001137.

Rajkhowa, R., Hu, X., Tsuzuki, T., Kaplan, D. L. and Wang, X. (2012) ‘Structure and biodegradation mechanism of milled Bombyx mori silk particles’, *Biomacromolecules*, 13(8), p. 2503–2512. doi: 10.1021/bm300736m.

Rajkhowa, R., Wang, L. and Wang, X. (2008) ‘Ultra-fine silk powder preparation through rotary and ball milling’, *Powder Technology*, 185, p. 87–95. doi: 10.1016/j.powtec.2008.01.005.

Rhinehardt, K. L., Srinivas, G. and Mohan, R. V. (2015) ‘Molecular dynamics simulation analysis of anti-MUC1 aptamer and mucin 1 peptide binding’, *Journal of Physical Chemistry B*, 119, p. 6571–6583. doi: 10.1021/acs.jpcb.5b02483.

Rickwood, D. (1992) ‘Appendix 4: Marker enzymes and chemical assays for the analysis of subcellular fractions’, in Rickwood, D. (ed.) *Preparative centrifugation: A practical approach*. Oxford: Oxford University Press, p. 369–387.

Rockwood, D. N., Preda, R. C., Yücel, T., Wang, X., Lovett, M. L. and Kaplan, D. L. (2011) ‘Materials fabrication from Bombyx mori silk fibroin’, *Nature Protocols*, 6(10), p. 1612–1631. doi: 10.1038/nprot.2011.379.

Ryckaert, J.-P., Ciccotti, G. and Berendsen, H. J. . (1977) ‘Numerical integration of the cartesian equations of motion of a system with constraints: molecular dynamics of n-alkanes’, *Journal of Computational Physics*, 23(3), p. 327–341. doi: 10.1016/0021-9991(77)90098-5.

Rygula, A., Majzner, K., Marzec, K. M., Kaczor, A., Pilarczyk, M. and Baranska, M.

(2013) ‘Raman spectroscopy of proteins: A review’, *Journal of Raman Spectroscopy*, 44(8), p. 1061–1076. doi: 10.1002/jrs.4335.

Saborano, R., Wongpinyochit, T., Totten, J. D., Johnston, B. F., Seib, F. P. and Duarte, I. F. (2017) ‘Metabolic reprogramming of macrophages exposed to silk, poly(lactic-co-glycolic acid), and silica nanoparticles’, *Advanced Healthcare Materials*, 6(14), p. 1601240. doi: 10.1002/adhm.201601240.

Schneider, C. A., Rasband, W. S. and Eliceiri, K. W. (2017) ‘NIH image to ImageJ : 25 years of image analysis’, *Nature Methods*, 9(7), p. 671–675.

Seib, F. P. (2017a) ‘Silk hydrogels for drug and cell delivery’, in Singh, T. R. R., Laverty, G., and Donnelly, R. (eds) *Hydrogels: Design, Synthesis and Application in Drug Delivery and Regenerative Medicine*. Taylor & Francis Group, p. 208–227.

Seib, F. P. (2017b) ‘Silk nanoparticles—an emerging anticancer nanomedicine’, *AIMS Bioengineering*, 4(2), p. 239–258. doi: 10.3934/bioeng.2017.2.239.

Seib, F. P. (2018) ‘Reverse-engineered silk hydrogels for cell and drug delivery’, *Therapeutic Delivery*, 9(6), p. 469–487. doi: 10.4155/tde-2018-0016.

Seib, F. P., Jones, A. T. and Duncan, R. (2006) ‘Establishment of subcellular fractionation techniques to monitor the intracellular fate of polymer therapeutics I. Differential centrifugation fractionation B16F10 cells and use to study the intracellular fate of HPMA copolymer-doxorubicin’, *Journal of Drug Targeting*, 14(6), p. 375–390. doi: 10.1080/10611860600833955.

Seib, F. P., Jones, A. T. and Duncan, R. (2007) ‘Comparison of the endocytic properties of linear and branched PEIs, and cationic PAMAM dendrimers in B16f10 melanoma cells’, *Journal of Controlled Release*, 117(3), p. 291–300. doi: 10.1016/j.jconrel.2006.10.020.

Seib, F. P., Jones, G. T., Rnjak-Kovacina, J., Lin, Y. and Kaplan, D. L. (2013) ‘pH-Dependent anticancer drug release from silk nanoparticles’, *Advanced Healthcare Materials*, 2(12), p. 1606–1611. doi: 10.1002/adhm.201300034.

Seib, F. P. and Kaplan, D. L. (2012) ‘Doxorubicin-loaded silk films: drug-silk interactions and in vivo performance in human orthotopic breast cancer.’, *Biomaterials*, 33(33), p. 8442–50. doi: 10.1016/j.biomaterials.2012.08.004.

Seib, F. P. and Kaplan, D. L. (2013) ‘Silk for drug delivery applications: Opportunities and challenges’, *Israel Journal of Chemistry*, 53(9–10), p. 756–766. doi: 10.1002/ijch.201300083.

Seib, F. P., Pritchard, E. M. and Kaplan, D. L. (2013) ‘Self-assembling doxorubicin silk hydrogels for the focal treatment of primary breast cancer’, *Advanced Functional Materials*, 23(1), p. 58–65. doi: 10.1002/adfm.201201238.

Shan, P., Shen, J.-W., Xu, D.-H., Shi, L.-Y., Gao, J., Lan, Y.-W., Wang, Q. and Wei, X.-H. (2014) ‘Molecular dynamics study on the interaction between doxorubicin and hydrophobically modified chitosan oligosaccharide’, *RSC Advances*, 4(45), p. 23730–23739. doi: 10.1039/C4RA01199F.

Shen, Y. and Bax, A. (2013) ‘Protein backbone and sidechain torsion angles predicted from NMR chemical shifts using artificial neural networks', *Journal of Biomolecular NMR*, 56(3), p. 227–241. doi: 10.1007/s10858-013-9741-y.

Sheridan, C. (2012) 'Proof of concept for next-generation nanoparticle drugs in humans', *Nature Biotechnology*, 30(6), p. 471–473. doi: 10.1038/nbt0612-471.

Shimanovich, U., Ruggeri, F. S., Genst, E. De, Adamcik, J., Barros, T. P., Porter, D., Muller, T., Mezzenga, R., Dobson, C. M., Vollrath, F., Holland, C. and Knowles, T. P. J. (2017) 'Silk micrococoons for protein stabilisation and molecular encapsulation', *Nature Communications*, 8(15902), p. 1–9. doi: 10.1038/ncomms15902.

Smith, A., Duan, H., Mohs, A. and Nie, S. (2008) 'Bioconjugated quantum dots for in vivo molecular and cellular imaging', *Advanced Drug Delivery Reviews*, 60(11), p. 1226–1240. doi: 10.1016/j.addr.2008.03.015.

Soenen, S. J., Manshian, B. B., Abdelmonem, A. M., Montenegro, J.-M., Tan, S., Balcaen, L., Vanhaecke, F., Brisson, A. R., Parak, W. J., De Smedt, S. C. and Braeckmans, K. (2014) 'The cellular interactions of PEGylated gold nanoparticles: Effect of PEGylation on cellular uptake and cytotoxicity', *Particle & Particle Systems Characterization*, 31(7), p. 794–800. doi: 10.1002/ppsc.201300357.

Spassov, V. and Yan, L. (2008) 'A fast and accurate computational approach to protein ionization', *Protein Science*, p. 1955–1970. doi: 10.1110/ps.036335.108.porary.

Spiess, K., Lammel, A. and Scheibel, T. (2010) 'Recombinant spider silk proteins for applications in biomaterials', *Macromolecular Bioscience*, 10(9), p. 998–1007. doi: 10.1002/mabi.201000071.

Van Der Spoel, D., Lindahl, E., Hess, B., Groenhof, G., Mark, A. E. and Berendsen, H. J. C. (2005) 'GROMACS: Fast, flexible, and free', *Journal of Computational Chemistry*, 26(16), p. 1701–1718. doi: 10.1002/jcc.20291.

Stoka, V., Turk, B. and Turk, V. (2005) 'Lysosomal cysteine proteases: Structural features and their role in apoptosis', *IUBMB Life*, 57(4–5), p. 347–353. doi: 10.1080/15216540500154920.

Stolnik, S., Dunn, S. E., Garnett, M. C., Davies, M. C., Coombes, A. G. A., Taylor, D. C., Irving, M. P., Purkiss, S. C., Tadros, T. F., Davis, S. S. and Illum, L. (1994) 'Surface modification of poly(lactide-co-glycolide) nanospheres by biodegradable poly(lactide)-poly(ethylene glycol) copolymers', *Pharmaceutical Research*, 11(12), p. 1800–1808. doi: 10.1023/A:1018931820564.

Strebhardt, K. and Ullrich, A. (2008) 'Paul Ehrlich's magic bullet concept: 100 Years of progress', *Nature Reviews Cancer*, 8(6), p. 473–480. doi: 10.1038/nrc2394.

Stroock, A. D. (2002) 'Chaotic mixer for microchannels', *Science*, 295(5555), p. 647–651. doi: 10.1126/science.1066238.

Subashini, M., Devarajan, P. V., Sonavane, G. S. and Doble, M. (2011) 'Molecular dynamics simulation of drug uptake by polymer', *Journal of Molecular Modeling*, 17(5), p. 1141–1147. doi: 10.1007/s00894-010-0811-8.

Subia, B. and Kundu, S. C. (2013) ‘Drug loading and release on tumor cells using silk fibroin-albumin nanoparticles as carriers.’, *Nanotechnology*, 24(3), p. 035103. doi: 10.1088/0957-4484/24/3/035103.

Sugita, Y. and Okamoto, Y. (1999) ‘Replica-exchange molecular dynamics method for protein folding’, *Chemical Physics Letters*, 314(1–2), p. 141–151. doi: 10.1016/S0009-2614(99)01123-9.

Suzuki, Y., Yamazaki, T., Aoki, A., Shindo, H. and Asakura, T. (2014) ‘NMR study of the structures of repeated sequences, GAGXGA (X = S, Y, V), in bombyx mori liquid silk’, *Biomacromolecules*, 15(1), p. 104–112. doi: 10.1021/bm401346h.

Talati, C. and Lancet, J. E. (2018) ‘CPX-351: changing the landscape of treatment for patients with secondary acute myeloid leukemia’, *Future Oncology*, 14(12), p. 1147–1154. doi: 10.2217/fon-2017-0603.

Tarakanova, A. and Buehler, M. J. (2012) ‘A Materiomics Approach to Spider Silk: Protein Molecules to Webs’, *The Journal of The Minerals, Metals & Materials Society*, 64(2), p. 214–225. doi: 10.1007/s11837-012-0250-3.

Teh, S.-Y., Lin, R., Hung, L.-H. and Lee, A. P. (2008) ‘Droplet microfluidics’, *Lab Chip*, 8, p. 198–220. doi: 10.1039/b715524g.

Termonia, Y. (1994) ‘Molecular modeling of spider silk elasticity’, *Macromolecules*, 27, p. 7378–7381. doi: 10.1021/ma00103a018.

Teule, F., Miao, Y.-G., Sohn, B.-H., Kim, Y.-S., Hull, J. J., Fraser, M. J., Lewis, R. V. and Jarvis, D. L. (2012) ‘Silkworms transformed with chimeric silkworm/spider silk genes spin composite silk fibers with improved mechanical properties’, *Proceedings of the National Academy of Sciences*, 109(3), p. 923–928. doi: 10.1073/pnas.1109420109.

Thierry, B. and Griesser, H. J. (2012) ‘Dense PEG layers for efficient immunotargeting of nanoparticles to cancer cells’, *Journal of Materials Chemistry*. The Royal Society of Chemistry, 22(18), p. 8810–8819. doi: 10.1039/C2JM30210A.

Thomas, V., Halloran, B. A., Ambalavanan, N., Catledge, S. A. and Vohra, Y. K. (2012) ‘In vitro studies on the effect of particle size on macrophage responses to nanodiamond wear debris’, *Acta Biomaterialia*, 8(5), p. 1939–1947. doi: 10.1016/j.actbio.2012.01.033.

Thurber, A. E., Omenetto, F. G. and Kaplan, D. L. (2015) ‘In vivo bioresponses to silk proteins’, *Biomaterials*, 71, p. 145–157. doi: 10.1016/j.biomaterials.2015.08.039.

Tian, Y., Jiang, X., Chen, X., Shao, Z. and Yang, W. (2014) ‘Doxorubicin-loaded magnetic silk fibroin nanoparticles for targeted therapy of multidrug-resistant cancer’, *Advanced Materials*, 26(43), p. 7393–7398. doi: 10.1002/adma.201403562.

Toprakcioglu, Z., Levin, A. and Knowles, T. P. J. (2017) ‘Hierarchical biomolecular emulsions using 3-D microfluidics with uniform surface chemistry’, *Biomacromolecules*, 18(11), p. 3642–3651. doi: 10.1021/acs.biomac.7b01159.

Torchilin, V. (2011) ‘Tumor delivery of macromolecular drugs based on the EPR effect’, *Advanced Drug Delivery Reviews*, 63(3), p. 131–135. doi:

10.1016/j.addr.2010.03.011.

Torrie, G. M. and Valleau, J. P. (1977) ‘Nonphysical sampling distributions in Monte Carlo free-energy estimation: Umbrella sampling’, *Journal of Computational Physics*, 23(2), p. 187–199. doi: 10.1016/0021-9991(77)90121-8.

Totten, J. D., Wongpinyochit, T. and Seib, F. P. (2017) ‘Silk nanoparticles: proof of lysosomotropic anticancer drug delivery at single-cell resolution’, *Journal of Drug Targeting*, 25(9–10), p. 865–872. doi: 10.1080/1061186X.2017.1363212.

Tudora, M.-R., Zaharia, C., Stancu, I.-C., Vasile, E., Trusca, R. and Cincu, C. (2013) ‘Natural silk fibroin micro- and nanoparticles with potential uses in drug delivery systems’, *UPB Scientific Bulletin, Series B,* 75(1), p. 43–52.

Turecek, P. L., Bossard, M. J., Schoetens, F. and Ivens, I. A. (2016) ‘PEGylation of biopharmaceuticals: A review of chemistry and nonclinical safety information of approved drugs’, *Journal of Pharmaceutical Sciences*, 105(2), p. 460–475. doi: 10.1016/j.xphs.2015.11.015.

Turk, B., Turk, V. and Turk, D. (1997) ‘Structural and functional aspects of papain-like cysteine proteinases and their protein inhibitors’, *Biological Chemistry,* 378(3–4), p. 141–50.

Uchegbu, I. F. and Siew, A. (2013) ‘Nanomedicines and nanodiagnostics come of age’, *Journal of Pharmaceutical Sciences*, 102(2), p. 305–310. doi: 10.1002/jps.23377.

Veiseh, O., Tang, B. C., Whitehead, K. A., Anderson, D. G. and Langer, R. (2015) ‘Managing diabetes with nanomedicine: Challenges and opportunities’, *Nature Reviews Drug Discovery,* 14(1), p. 45–57. doi: 10.1038/nrd4477.

Vepari, C. and Kaplan, D. L. (2007) ‘Silk as a biomaterial’, *Progress in polymer science*, 32(8–9), p. 991–1007. doi: 10.1016/j.progpolymsci.2007.05.013.

Vepari, C., Matheson, D., Drummy, L., Naik, R. and Kaplan, D. L. (2010) ‘Surface modification of silk fibroin with poly(ethylene glycol) for antiadhesion and antithrombotic applications.’, *Journal of biomedical materials research. Part A*, 93(2), p. 595–606. doi: 10.1002/jbm.a.32565.

Veronese, F. M. and Pasut, G. (2005) ‘PEGylation, successful approach to drug delivery’, *Drug Discovery Today,* 10(21), p. 1451–1458. doi: 10.1016/S1359-6446(05)03575-0.

Wallace, A., Laskowski, R. and Thornton, J. (1995) ‘LIGPLOT: A program to generate schematic diagrams of protein-ligand interactions’, *Protein Engineering,* 8(2), p. 127–134.

Wang, F., Cao, T.-T. and Zhang, Y.-Q. (2015) ‘Effect of silk protein surfactant on silk degumming and its properties’, *Materials Science and Engineering: C*, 55, p. 131–136. doi: 10.1016/j.msec.2015.05.041.

Wang, R. (2013) ‘Nanoparticles influence droplet formation in a T-shaped microfluidic’, *Journal of Nanoparticle Research,* 15, p. 2128. doi: 10.1007/s11051-013-2128-x.

Wang, T., Wang, L., Li, X., Hu, X., Han, Y., Luo, Y., Wang, Z., Li, Q., Aldalbahi, A., Wang, L., Song, S., Fan, C., Zhao, Y., Wang, M. and Chen, N. (2017) 'Size-dependent regulation of intracellular trafficking of polystyrene nanoparticle-based drug-delivery systems', *ACS Applied Materials and Interfaces*, 9(22), p. 18619–18625. doi: 10.1021/acsami.7b05383.

Wang, X., Yucel, T., Lu, Q., Hu, X. and Kaplan, D. L. (2010) 'Silk nanospheres and microspheres from silk/pva blend films for drug delivery.', *Biomaterials*, 31(6), p. 1025–1035. doi: 10.1016/j.biomaterials.2009.11.002.

Wang, Y., Rudym, D. D., Walsh, A., Abrahamsen, L., Kim, H. J., Kim, H. S., Kirker-Head, C. and Kaplan, D. L. (2008) 'In vivo degradation of three-dimensional silk fibroin scaffolds', *Biomaterials*, 29(24–25), p. 3415–3428. doi: 10.1016/j.biomaterials.2008.05.002.

Wang, Y., Zhang, L., Zhang, X., Wei, X., Tang, Z. and Zhou, S. (2016) 'Precise polymerization of a highly tumor microenvironment-responsive nanoplatform for strongly enhanced intracellular drug release', *ACS Applied Materials & Interfaces*. American Chemical Society, 8(9), p. 5833–5846. doi: 10.1021/acsami.5b11569.

Wartlick, H., Michaelis, K., Balthasar, S., Strebhardt, K., Kreuter, J. and Langer, K. (2004) 'Highly specific HER2-mediated cellular uptake of nntibody-modified nanoparticles in tumour cells', *Journal of Drug Targeting*, 12(7), p. 461–471. doi: 10.1080/10611860400010697.

Webster, R., Didier, E., Harris, P., Siegel, N., Stadler, J., Tilbury, L. and Smith, D. (2006) 'PEGylated proteins: Evaluation of their safety in the absence of definitive metabolism studies', *Drug Metabolism and Disposition*, 35(1), p. 9–16. doi: 10.1124/dmd.106.012419.

Wenk, E., Merkle, H. P. and Meinel, L. (2011) 'Silk fibroin as a vehicle for drug delivery applications.', *Journal of Controlled Release*, 150(2), p. 128–141. doi: 10.1016/j.jconrel.2010.11.007.

Wenk, E., Wandrey, A. J., Merkle, H. P. and Meinel, L. (2008) 'Silk fibroin spheres as a platform for controlled drug delivery.', *Journal of Controlled Release*. Elsevier B.V., 132(1), p. 26–34. doi: 10.1016/j.jconrel.2008.08.005.

Werner, V. and Meinel, L. (2015) 'From silk spinning in insects and spiders to advanced silk fibroin drug delivery systems', *European Journal of Pharmaceutics and Biopharmaceutics*, 97, p. 392–399. doi: 10.1016/j.ejpb.2015.03.016.

Wilhelm, S., Tavares, A. J., Dai, Q., Ohta, S., Audet, J., Dvorak, H. F. and Chan, W. C. W. (2016) 'Analysis of nanoparticle delivery to tumours', *Nature Reviews Materials*, 1(5), p. 16014. doi: 10.1038/natrevmats.2016.14.

Williams, D. F. (2008) 'On the mechanisms of biocompatibility.', *Biomaterials*, 29(20), p. 2941–53. doi: 10.1016/j.biomaterials.2008.04.023.

Wilson, D., Valluzzi, R. and Kaplan, D. (2000) 'Conformational transitions in model silk peptides', *Biophysical journal*, 78(5), p. 2690–701. doi: 10.1016/S0006-3495(00)76813-5.

Wong, J., Chan, H. and Chrzanowski, W. (2014) ‘Silk for pharmaceutical and cosmeceutical applications’, in Kundu, S. C. (ed.) *Silk Biomaterials for Tissue Engineering and Regenerative Medicine*. Cambridge: Woodhead Publishing Limited, p. 519–545. doi: 10.1533/9780857097064.3.519.

Wongpinyochit, T. (2014) *Silk nanoparticles for drug delivery applications*. University of Strathclyde.

Wongpinyochit, T., Johnston, B. F. and Seib, F. P. (2016) ‘Manufacture and drug delivery applications of silk nanoparticles’, *Journal of Visualized Experiments*, 116(116), p. e54669. doi: 10.3791/54669.

Wongpinyochit, T., Johnston, B. F. and Seib, F. P. (2018) ‘Degradation behavior of silk nanoparticles—enzyme responsiveness’, *ACS Biomaterials Science & Engineering*, 4(3), p. 942–951. doi: 10.1021/acsbiomaterials.7b01021.

Wongpinyochit, T., Uhlmann, P., Urquhart, A. J. and Seib, F. P. (2015) ‘PEGylated silk nanoparticles for anticancer drug delivery’, *Biomacromolecules*, 16(11), p. 3712–3722. doi: 10.1021/acs.biomac.5b01003.

Workman, P., Aboagye, E. O., Balkwill, F., Balmain, A., Bruder, G., Chaplin, D. J., Double, J. A., Everitt, J., Farningham, D. A. H., Glennie, M. J., Kelland, L. R., Robinson, V., Stratford, I. J., Tozer, G. M., Watson, S., Wedge, S. R. and Eccles, S. A. (2010) ‘Guidelines for the welfare and use of animals in cancer research’, *British Journal of Cancer*, 102(11), p. 1555–1577. doi: 10.1038/sj.bjc.6605642.

Xia, X.-X., Qian, Z.-G., Ki, C. S., Park, Y. H., Kaplan, D. L. and Lee, S. Y. (2010) ‘Native-sized recombinant spider silk protein produced in metabolically engineered Escherichia coli results in a strong fiber’, *Proceedings of the National Academy of Sciences of the United States of America*, 107(32), p. 14059–63. doi: 10.1073/pnas.1003366107.

Xia, X.-X., Wang, M., Lin, Y., Xu, Q. and Kaplan, D. L. (2014) ‘Hydrophobic drug-triggered self-assembly of nanoparticles from silk-elastin-like protein polymers for drug delivery’, *Biomacromolecules*, 15(3), p. 908–914. doi: 10.1021/bm4017594.

Xiao, L., Lu, G., Lu, Q. and Kaplan, D. L. (2016) ‘Direct Formation of Silk Nanoparticles for Drug Delivery’, *ACS Biomaterials Science & Engineering*, 2, p. 2050–2057. doi: 10.1021/acsbiomaterials.6b00457.

Xiao, S., Stacklies, W., Cetinkaya, M., Markert, B. and Gräter, F. (2009) ‘Mechanical response of silk crystalline units from force-distribution analysis’, *Biophysical Journal*, 96(10), p. 3997–4005. doi: 10.1016/j.bpj.2009.02.052.

Xiao, S., Xiao, S. and Gräter, F. (2013) ‘Dissecting the structural determinants for the difference in mechanical stability of silk and amyloid beta-sheet stacks’, *Physical Chemistry Chemical Physics*, 15(22), p. 8765. doi: 10.1039/c3cp00067b.

Xie, M.-B., Li, Y., Zhao, Z., Chen, A.-Z., Li, J.-S., Hu, J.-Y., Li, G. and Li, Z. (2015) ‘Solubility enhancement of curcumin via supercritical CO2 based silk fibroin carrier’, *The Journal of Supercritical Fluids*, 103, p. 1–9. doi: 10.1016/j.supflu.2015.04.021.

Xie, R.-J., Wu, H.-Y., Xu, J.-M. and Deng, Q.-M. (2008) ‘The preparation of silk fibroin drug-loading microspheres’, *Journal of Fiber Bioengineering and Informatics*, 1(1), p. 73–80. doi: 10.3993/jfbi06200810.

Xu, G., Gong, L., Yang, Z. and Liu, X. Y. (2013) ‘What makes spider silk fibers so strong? From molecular-crystallite network to hierarchical network structures’, *Soft Matter*, 10(13), p. 2116–2123. doi: 10.1039/C3SM52845F.

Xu, Z., Lu, C., Riordon, J., Sinton, D. and Moffitt, M. G. (2016) ‘Microfluidic manufacturing of polymeric nanoparticles: Comparing flow control of multiscale structure in single-phase staggered herringbone and two-phase reactors’, *Langmuir*, 32(48), p. 12781–12789. doi: 10.1021/acs.langmuir.6b03243.

Yang, H., Yang, S., Kong, J., Dong, A. and Yu, S. (2015) ‘Obtaining information about protein secondary structures in aqueous solution using Fourier transform IR spectroscopy’, *Nature Protocols*. Nature Publishing Group, a division of Macmillan Publishers Limited. All Rights Reserved., 10(3), p. 382–396. doi: 10.1038/nprot.2015.024.

Yin, H., Kanasty, R. L., Eltoukhy, A. A., Vegas, A. J., Dorkin, J. R. and Anderson, D. G. (2014) ‘Non-viral vectors for gene-based therapy’, *Nature Reviews Genetics*, 15(8), p. 541–555. doi: 10.1038/nrg3763.

Yucel, T., Lovett, M. L. and Kaplan, D. L. (2014) ‘Silk-based biomaterials for sustained drug delivery’, *Journal of Controlled Release*, 190, p. 381–397. doi: 10.1016/j.jconrel.2014.05.059.

Zhang, J., Pritchard, E., Hu, X., Valentin, T., Panilaitis, B., Omenetto, F. G. and Kaplan, D. L. (2012) ‘Stabilization of vaccines and antibiotics in silk and eliminating the cold chain’, *Proceedings of the National Academy of Sciences*, 109(30), p. 11981–11986. doi: 10.1073/pnas.1206210109.

Zhang, L., Zhang, Z., Jasa, J., Li, D., Cleveland, R. O., Negahban, M. and Jérusalem, A. (2017) ‘Molecular dynamics simulations of heterogeneous cell membranes in response to uniaxial membrane stretches at high loading rates’, *Scientific Reports*, 7(1), p. 1–12. doi: 10.1038/s41598-017-06827-3.

Zhang, Y.-Q., Shen, W.-D., Xiang, R.-L., Zhuge, L.-J., Gao, W.-J. and Wang, W.-B. (2007) ‘Formation of silk fibroin nanoparticles in water-miscible organic solvent and their characterization’, *Journal of Nanoparticle Research*, 9(5), p. 885–900. doi: 10.1007/s11051-006-9162-x.

Zhang, Y. S., Zhao, T. F., Zhao, A. C. and Nakagaki, M. (2011) ‘Stably express spider flagelliform silk protein in Bombyx mori cell line by piggyBac transposon-derived vector’, *Advanced Materials Research*, 332–334, p. 779–782. doi: 10.4028/www.scientific.net/AMR.332-334.779.

Zhao, B., Stuart, M. A. C. and Hall, C. K. (2017) ‘Navigating in foldonia: Using accelerated molecular dynamics to explore stability, unfolding and self-healing of the β-solenoid structure formed by a silk-like polypeptide’, *PLoS Computational Biology*, 13(3), p. 1–22. doi: 10.1371/journal.pcbi.1005446.

Zhao, H. P., Feng, X. Q., Yu, S. W., Cui, W. Z. and Zou, F. Z. (2005) ‘Mechanical properties of silkworm cocoons’, *Polymer*, 46(21), p. 9192–9201. doi: 10.1016/j.polymer.2005.07.004.

Zhao, Z., Chen, A., Li, Y., Hu, J., Liu, X., Li, J., Zhang, Y., Li, G. and Zheng, Z. (2012) ‘Fabrication of silk fibroin nanoparticles for controlled drug delivery’, *Journal of Nanoparticle Research*, 14(4), p. 736. doi: 10.1007/s11051-012-0736-5.

Zhao, Z., Li, Y., Chen, A. Z., Zheng, Z. J., Hu, J. Y., Li, J. S. and Li, G. (2013) ‘Generation of silk fibroin nanoparticles via solution-enhanced dispersion by supercritical CO2’, *Industrial and Engineering Chemistry Research*, 52(10), p. 3752–3761. doi: 10.1021/ie301907f.

Zhao, Z., Li, Y. and Xie, M.-B. (2015) ‘Silk fibroin-based nanoparticles for drug delivery’, *International Journal of Molecular Sciences*, 16(3), p. 4880–4903. doi: 10.3390/ijms16034880.

Zhao, Z., Xie, M., Li, Y., Chen, A., Li, G., Zhang, J., Hu, H., Wang, X. and Li, S. (2015) ‘Formation of curcumin nanoparticles via solution-enhanced dispersion by supercritical CO2’, *International Journal of Nanomedicine*, 10, p. 3171. doi: 10.2147/IJN.S80434.

Zhigaltsev, I. V, Belliveau, N., Hafez, I., Leung, A. K. K., Huft, J., Hansen, C. and Cullis, P. R. (2012) ‘Bottom-up design and synthesis of limit size lipid nanoparticle systems with aqueous and triglyceride cores using millisecond microfluidic mixing’, *Langmuir*, 28(7), p. 3633–3640. doi: 10.1021/la204833h.

Zhou, C.-Z., Confalonieri, F., Jacquet, M., Perasso, R., Li, Z.-G. and Janin, J. (2001) ‘Silk fibroin: Structural implications of a remarkable amino acid sequence’, *Proteins: Structure, Function, and Genetics*, 44(2), p. 119–122. doi: 10.1002/prot.1078.

Zhou, C.-Z., Confalonieri, F., Medina, N., Zivanovic, Y., Esnault, C., Yang, T., Jacquet, M., Janin, J., Duguet, M., Perasso, R. and Li, Z.-G. (2000) ‘Fine organization of Bombyx mori fibroin heavy chain gene’, *Nucleic Acids Research*, 28(12), p. 2413–2419. doi: 10.1093/nar/28.12.2413.

Zhou, P., Li, G., Shao, Z., Pan, X. and Yu, T. (2001) ‘Structure of Bombyx mori silk fibroin based on the DFT chemical shift calculation’, *The Journal of Physical Chemistry B*, 105(50), p. 12469–12476. doi: 10.1021/jp0125395.